Physicochemical evolution of an active plate boundary fault; the Alpine Fault, New Zealand: insight from the Deep Fault Drilling Project

Thesis submitted in accordance with the requirements of the University of Liverpool for the degree of Doctor of Philosophy by

Michael John Allen

September 2017

Abstract

The Alpine Fault, a transpressional plate boundary between the Australian and Pacific plates, bounding the western edge of the Southern Alps on New Zealand's South Island, accommodates over 70 % of the relative motion between the colliding Australian and Pacific Plates with dextral-reverse movement offsetting basement rocks laterally by ~470 km. This motion manifests itself as quasi-periodical ruptures of large magnitude earthquakes (M_w ~8), with the fault currently thought to be nearing the end of its most recent interseismic period. Seismicity in the upper crust occurs due to frictional instabilities on faults; with earthquake nucleation, propagation, and inhibition governed by the properties of the fault zone and the tectonic forces acting upon it.

The Deep Fault Drilling Project (DFDP) is an ongoing international effort, undertaken in order to provide insight into the current geological and seismological state of a plate boundary fault at the end of its latest seismic cycle. The first phase of the DFDP comprised two vertical pilot holes (DFDP-1A and DFDP-1B) drilled into an active thrust segment of the Alpine Fault Zone at Gaunt Creek, Westland in January – February 2011. The boreholes reached depths of 100.6 m and 151.4 m, respectively, sampling a range of fault lithologies including ultramylonites, cataclasites and gouges from both the hanging wall and footwall of the fault; including multiple fault principal slip zones. This was followed by diverse down-hole observations and the installation of sensors for long-term in situ monitoring. Drilling revealed the presence of a ~30 m thick alteration zone overprinting the fault core and transition into the damage zone. This alteration zone was defined based on a distinctive, light green colour in drill core and in field outcrop, produced by elevated concentrations of alteration minerals (e.g., phyllosillicates and carbonates) above regional levels.

This thesis presents a multidisciplinary approach of experimental physical property measurement, microstructural observations and fine-scale spatially resolved geochemical analyses performed with the aim to characterise and define the behaviour of a major plate boundary fault throughout its seismic cycle, with particular focus on fluids within the fault and the impact they have on fault processes. The study includes: the measurement of permeability and seismic velocity anisotropy of heavily cataclased and altered fault rock, in order to characterise the properties of the fault at the end of an interseismic period; the

microstructural and geochemical observations of carbonate-mineralised fractures within the fault core / alteration zone, in order to better understand sealing processes and fluid-rock interactions within heavily cataclased rock; and a study of the occurrence of frictional melt and ultracataclasis within the fault, with focus on the inter-relations of these processes as fault properties and fluid behaviour varies throughout the seismic cycle. These analyses were performed on Alpine Fault lithologies collected from the field and the DFDP.

Our suite of experimental permeability and seismic velocity measurements, conducted with pore fluid (H_2O) pressure held at 5 MPa over an effective pressure range of 5 – 105 MPa, show a zone of low permeability, from 10^{-17} to 10^{-21} m^2, and low seismic velocity, *P-wave:* 4400 to 5900 m/s; *S-wave:* 3900 to 4200 m/s, material bounding the PSZ of the central Alpine Fault, i.e. the fault core / alteration zone, under conditions approximating depths of 5 – 6 km. Measurements performed on protolith lithologies show lower permeabilities and higher seismic velocities than the fault-damaged rock owing to their intact, unfractured nature. Low permeabilities at low experimental pressures are explained by the presence of fine grained alteration products, carbonate precipitation and highly variable cataclastic structures within the fault zone. The PSZ, being composed of ultrafine-grained alteration products, acts as a barrier to cross-fault fluid flow postseismicity. This is in agreement with other petrophysical studies on other mature faults subjected to extensive comminution and fluid-rock alteration.

Using SEM-based electron backscatter diffraction and optical cathodoluminescence together with secondary ion mass spectroscopy, we present fine-scale, quantitative microstructural and spatially resolved geochemical observations on the alteration zone carbonate-sealed fractures. We have shown that the hanging wall alteration zone is pervasively mineralised by carbonate precipitation, while the footwall is relatively devoid. This mineralisation is generated through a protracted cycle of fracturing and sealing, with ambient conditions fluctuating during exhumation and seismicity, as evidenced by variation in calcite trace element chemistry and deformation microstructures across vein generations. The vast majority of veins appear to be filled by blocky-equant calcite crystals with uniform chemistry, indicating that the veins were rapidly sealed by a single fluid pulse. Subsequent fluid-rock interaction and deformation has resulted in modification of vein microstructures and chemistry. These findings reflect the transient nature of permeability

on the Alpine Fault, highly permeable co- and immediately post-seismically, and reduced to its current state in the late interseismic period.

The evolution of fault rock microstructure with seismic shear and subsequent interseismic fluid-rock interaction has a great effect on the hydraulic and elastic properties of fault zones. This evolution is complex and cyclical, potentially promoting rupture via dynamic coseismic processes such as thermal pressurization. During interseismic periods fluid flow is likely concentrated upon pervasive, unconsolidated gouge-filled fracture networks at the contact of the fault core / alteration zone and the relatively unaltered damage zone in the hanging wall, allowing the flow of fluid along the fault and to the surface, as observed by abundant hydrothermal springs southeast of the fault.

Using SEM-based microstructural observations and geochemical analyses, including: backscatter electron imaging; electron backscatter diffraction; and energy dispersive spectroscopy, presented is a study on the occurrence of pseudotachylytes and nanoparticulates within the fault zone. The focus is on the setting of these features, as well as the extent of mechanical reworking, chemical alteration and/or preservation they have undergone throughout the seismic cycle. It is shown that pseudotachylytes occur throughout the fault core / alteration zone cataclasites, predominantly as reworked, disassociated clasts, with intact pseudotachylyte veins constrained to the fault core / damage zone contact in the fractured ultramylonites. Frictional melt appears to occur in the presence of fluid, as evidenced by the cataclasis of calcite veins associated with, amygdules within and veins overprinting pseudotachylytes. With the lack of intact pseudotachylyte veins within and in the immediate vicinity of the principal slip zone it can be inferred that frictional melt did not occur during the most recent high magnitude Alpine Fault slip event. It is more likely that the pseudotachylytes observed are reworked relicts from older Alpine Fault ruptures below the Brittle – Viscous Transition, or rather, smaller magnitude earthquakes that have produced pseudotachylytes that have been subsequently incorporated into the widening alteration zone with exhumation. The presence of preserved nanoparticles within clasts in the principal slip zone could indicate that the Alpine Fault produced nanoparticulates during increments of slip at greater depths without the production of melt. This could indicate a transition in slip weakening mechanisms with exhumation; frictional melting may occur in the more competent rock close to the Brittle – Viscous Transition, nanoparticulate-aided slip may be important at intermediate depths, aided by thermal pressurisation, while cataclasis dominates at shallower crustal levels.

Acknowledgments

Many thanks go to my supervisors Elisabetta Mariani and Daniel Faulkner for their support and guidance throughout my PhD. It has been an honour to have had the opportunity to work alongside both in the Rock Deformation and Electron Microscopy Laboratories at Liverpool as well as in the field and during the drilling in Whataroa. I have learned so much from them in past few years.

I would like to thank everyone who has been involved in the research, including Carolyn Boulton, Catriona Menzies and Virginia Toy for valuable discussions on the Alpine Fault Zone, working together over in New Zealand and for taking me around and about the West Coast for geology and tramping. Thanks to Dan Tatham for his help and feedback on the experimental work in this thesis. And I'm grateful for the opportunity to have had time working at the NERC Ion Microprobe Facility with John Craven and Richard Hinton.

Working in the department in Liverpool has been entertaining and interesting, with particular thanks to John Bedford and Gary Coughlan for putting up with my blathering at lunchtimes and general doings in the Rock Def Lab. Thanks to my office mates Joe Gardner, Joe Aslin and Teo Nagy for company throughout the PhD, particularly in the final stages. Finally, special thanks to my petit pois, Henri Leclère for experimental and body language expertise.

The Whataroa River, Central Westland, New Zealand

Contents

Physicochemical evolution of an active plate boundary fault; the Alpine Fault, New Zealand: insight from the Deep Fault Drilling Project 1

Abstract 2

Acknowledgments 5

Contents 7

Preface 13

i. Thesis structure 13

ii. Status of manuscripts and co-author contribution 14

iii. Funding information 16

List of figures and tables 17

1. Introduction 27

1.1. Shear zones in the crust 27

1.2. Rheology of the crust 27

1.3. Deformation of the crust 29

1.4. Structure of brittle fault zones 32

1.5. Fluids in the crust and how fault zones influence their behaviour 34

1.6. The Alpine Fault, New Zealand 36

1.6.1. Historic and paleoseismicity 38

1.6.2. Fluids in the Southern Alps 38

1.6.3. The Deep Fault Drilling Project 40

1.6.4. The lithologies of the Alpine Fault and the nature of the alteration zone 41

1.7. Thesis aims 51

2. Methods 53

2.1. Introduction 53

2.2. Drilling operations 53

2.2.1. Deep Fault Drilling Project-2: onsite operations summary 57

2.2.2. Observations and findings of Deep Fault Drilling Project-2 59

2.3. Sample preparation for experiments and laboratory analyses 61

2.3.1. Experimental sample preparation 61

2.3.2. Thin section preparation 63

2.3.3. Sample preparation for trace element and stable isotope analyses 64

2.4. Overview of experimental apparatus 64

2.4.1. Permeability and seismic wave velocity measurements 65

2.5. Methods for microstructural and chemical analyses 70

2.5.1. X-ray computed tomography 70

2.5.2. Optical cold-cathode cathodoluminescence 72

2.5.3. Scanning Electron Microscopy 73

2.6. Geochemical study 88

2.6.1. Secondary ion mass spectrometry 88

2.6.2. Instrumentation and operational conditions 89

2.7. Supplementary material 94

2.7.1. DFDP-2: Thin section preparation protocol 94

2.7.2. Permeability calculation spreadsheet 97

2.7.3. Ultrasonic velocity conversion script – isf to csv. 99

2.7.4. Secondary ion mass spectrometry carbonate standards 100

3. Permeability and seismic velocity and their anisotropy across the Alpine Fault, New Zealand: an insight from laboratory measurements on core from the Deep Fault Drilling Project 101

Key Points 101

Abstract 101

3.1. Introduction 102

3.2. The Alpine Fault, New Zealand, and DFDP Drilling 104

3.3. Methods 106

3.3.1. Sample selection and preparation 106

3.3.2. Experimental procedure 110

3.4. Results 113

3.4.1. Permeability Measurements 113

3.4.2. Seismic velocity measurements 115

3.4.3. Specimen Microstructural Variation 119

3.5. Discussion 122

3.5.1. Microstructural controls on physical properties 122

3.5.2. Correlation with other studies 125

3.5.3. Implications for fault zone properties during the seismic cycle 127

3.6. Conclusion 128

3.7. Supplementary material 130

4. Cycles of fault zone sealing and restrengthening from the structure and chemistry of vein networks in the Alpine Fault, New Zealand 132

Key points 132

Abstract 132

4.1. Introduction 134

4.1.1. Fluids in fault zones and fluid-rock interactions 134

4.1.2. The Alpine Fault Zone, New Zealand 136

4.2. Methods 138

4.2.1. The Deep Fault Drilling Project 138

4.2.2. Petrology of core lithologies 139

4.2.3. Techniques 141

4.2.4. Sample preparation 143

4.3. Results 144

4.3.1. An introduction to fracture and vein classification 144

4.3.2. Microstructural and chemical variation with proximity to the PSZ 145

4 4. Discussion 161

4.4.1. Classification of the Alpine Fault alteration zone carbonate veins 161

4.4.2. The microstructure of vein calcite in the Alpine Fault 162

4.4.3. Controls on trace element variation 168

4.4.4. Implications for fault zone processes 175

4.4. Conclusions 179

4.5. Further work 180

4.6. Supplementary material 182

5. Occurrence and nature of pseudotachylyte and ultracomminution within the Alpine Fault, New Zealand: insight from the Deep Fault Drilling Project.....193

Key points..... 193

Abstract..... 193

5.1. Occurrence of melt and ultracomminution within fault zones 195

5.2. Geological Setting 198

5.2.1. The Alpine Fault, New Zealand 198

5.2.2. Occurrence of pseudotachylyte in the Alpine Fault Zone..... 199

5.3. Methods..... 200

5.3.1. The Deep Fault Drilling Project 200

5.3.2. Petrology of core lithologies 201

5.3.3. Sample preparation 202

5.3.4. Techniques..... 204

5.4. Results..... 206

5.4.1. Pseudotachylyte within the Alpine Fault core 206

5.4.2. Principal Slip Zone ultracomminuted gouges of the Alpine Fault..... 223

5.5. Discussion..... 229

5.5.1. Melt behaviour and subsequent alteration and reworking of pseudotachylytes 229

5.5.2. The nature and behaviour of the principal slip zone 233

5.5.3. Implications for fault processes 239

5.6. Conclusions 242

5.7. Further work 243

5.8. Supplementary material 243

5.8.1. Additional tables and figures 243

5.8.2. Grain shape analyses..... 251

6. Conclusions 254

7. Future work.....258

8. References.....260

Preface

i. Thesis structure

Chapter 1 outlines the background, motivation, and aims of this thesis*, Chapter 2* describes the techniques and methods utilised throughout the course of this project, *Chapters 3, 4* and *5* contain the original research that was undertaken for this thesis. *Chapters 3*, *4 and 5* were written as stand-alone manuscripts and for this reason they will contain some repetitions of the key techniques and Alpine Fault related concepts that underpin this research. The content of these chapters is as follows:

Chapter 3 **–** presents permeability and seismic velocity measurements performed in multiple orientations on fault rock from core retrieved during the Deep Fault Drilling Project. These data are then analysed to assess the degree of anisotropy present in the Alpine Fault Zone and the microstructural controls on physical property variation are explored.

Chapter 4 **–** presents microstructural observations and geochemical analyses on the carbonate vein infill of the Alpine Fault alteration zone. The influence of fluid-rock interactions and sealing mechanisms are explored in light of these data sets.

Chapter 5 **–** presents microstructural observations and geochemical analyses on fault gouges and pseudotachylytes generated on the Alpine Fault. These observations are then interpreted in regard to melt and nanoparticle generation and mineral alteration. Two process based models are proposed and implications for seismic cycle processes are discussed.

All references are consolidated into one list that can be found at the end of the thesis while supplementary materials, abbreviated as *SM*, follow each respective chapter or in the Digital Supplementary Material.

A summary of the thesis and the main conclusions are provided in *Chapter 6*.

ii. Status of manuscripts and co-author contribution

Chapter 3: M.J. Allen[1], D. Tatham[1], D.R. Faulkner[1], E. Mariani[1], and C. Boulton[12]. Permeability and seismic velocity and their anisotropy across the Alpine Fault, New Zealand: an insight from laboratory measurements on core from the Deep Fault Drilling Project phase 1 (DFDP-1). *Journal of Geophysical Research: Solid Earth.*

Submitted: 25th April 2017

Status: Published.

Co-author contribution:

Michael John Allen – Principal investigator, primary author, data collection, analysis and interpretation.

Daniel Tatham – Data collection, manuscript review, discussion.

Daniel Faulkner – Data interpretation, manuscript review, discussion.

Elisabetta Mariani – Manuscript review, discussion.

Carolyn Boulton – Manuscript review, discussion.

Chapter 4: M.J. Allen[1], E. Mariani[1], D.R. Faulkner[1], C. Boulton[12] and C.D. Menzies[3]. Cycles of fault zone sealing and restrengthening from the structure and chemistry of vein networks in the Alpine Fault, New Zealand.

Status: Near completion, to be submitted to the Journal of Structural Geology.

Co-author contribution:

Michael John Allen – Principal investigator, primary author, data collection, analysis and interpretation.

Elisabetta Mariani – Data collection, analysis and interpretation, manuscript review, discussion.

Daniel Faulkner – Manuscript review, discussion.

Carolyn Boulton – Discussion.

Catriona Menzies – Discussion.

Chapter 5: M.J. Allen[1], E. Mariani[1], D.R. Faulkner[1] and C. Boulton[12]. Occurrence and nature of pseudotachylyte and other seismic cycle microstructures within the Alpine Fault, New Zealand: insight from the Deep Fault Drilling Project.

Status: In preparation.

Co-author contribution:

Michael John Allen – Principal investigator, primary author, data collection, analysis and interpretation.

Elisabetta Mariani – Data analysis and interpretation, manuscript review, discussion.

Daniel Faulkner – Manuscript review, discussion.

Carolyn Boulton – Data collection, discussion.

Co-author affiliations:

[1] Department of Earth Ocean and Ecological Sciences, University of Liverpool, Liverpool, UK.

[2] School of Geography, Environment, and Earth Sciences, Victoria University of Wellington, Wellington, New Zealand.

[3] Ocean and Earth Science, National Oceanography Centre Southampton, University of Southampton, UK.

Publication co-authorship of thesis author

Through involvement with the drilling operations and data collection of Deep Fault Drilling Project Phase 2 (DFDP-2) the thesis author is included as co-author in the following peer-

reviewed publications, with published manuscripts included in the thesis Digital Supplementary Material.

R. Sutherland, J. Townend, V. Toy, P. Upton, J. Coussens, **M.J. Allen**, et al., (2017) Extreme hydrothermal conditions at an active plate-bounding fault. *Nature*, (546)7656, 137 – 140.

V. Toy, R. Sutherland, J. Townend, **M.J. Allen**, et al., (2017) Bedrock Geology of DFDP-2B, Central Alpine Fault, New Zealand. *New Zealand Journal of Geology and Geophysics*. (60)4, 497 – 518.

J. Townend, R. Sutherland, V. Toy, M. Doan, B. Celerier, C. Massiot, J. Coussens, T. Jeppson, L. Janku-Capova, L. Remaud, P. Upton, D. Schmitt, P. Pezard, J. Williams, **M.J. Allen**, et al., (2017) Petrophysical, geochemical, and hydrologic evidence for extensive fracture mediated fluid and heat transport in the Alpine Fault's hanging-wall damage zone. *Geochemistry, Geophysics, Geosystems. (1*8)12, 4709 – 4732.

Included in the Digital Supplementary Material of this thesis are a selected number of conference posters and presentations the thesis author has delivered throughout the PhD studies. These include: posters concerning *Chapter 3* of this thesis, presented at the Gordon Research Conference – Rock Deformation 2014 and the American Geophysical Union Fall Meeting 2015; poster concerning *Chapter 4* of this thesis, presented at the American Geophysical Union Fall Meeting 2016; and an oral presentation slide show concerning *Chapter 4* of this thesis presented at the Tectonic Studies Group – Volcanic and Magmatic Studies Group – British Geophysical Association Joint Assembly 2017.

iii. Funding information

This work was supported by the Natural Environment Research Council (NERC) grants NE/J024449/1: Evolution of the physical, geochemical and mechanical properties of the Alpine Fault Zone: A journey through an active plate boundary, to D.R. Faulkner and E. Mariani; and NE/H012486/1: The evolution of deformation mechanisms, physical conditions and physical properties in the seismogenic Alpine Fault zone: a pilot study, to D. Prior, E. Mariani and D.R. Faulkner.

List of figures and tables

SM – supplementary materials

Figure 1.1 – The 'Sibson – Scholz' conceptual fault zone model. 28

Figure 1.2 – Conceptual model of fault zone structure. 33

Figure 1.3 – Satellite image of New Zealand's South Island with the Alpine Fault. 37

Figure 1.4 – Schematic diagram of the fluid flow regime and isotherms in the Southern Alps. 39

Figure 1.5 – Generalized geology map of the South Island, New Zealand and a digital elevation model image of the central South Island. 42

Figure 1.6 – Schematic cross-section of an oblique thrust segment within the central section of the Alpine Fault. 43

Figure 1.7 – Photomicrographs and backscatter electron images of protolith lithologies; the Alpine Schist and a quartzofeldspathic ultramylonite. 44

Figure 1.8 – Flow chart of the alteration reactions occurring in the Alpine Fault alteration zone. 50

Figure 1.9 – Flow diagram of the factors influencing fault zone structure, composition and behaviour. 52

Table 1.1 – Mineralogies of the schist and mylonite protoliths for the Alpine Fault ultramylonites / cataclasites and gouges. 46

Table 1.2 – Description of lithological units recovered in the Deep Fault Drilling Project-1. 49

Figure 2.1 – Photographs of the Deep Fault Drilling Project Phase 1 and Phase 2 drill sites. 54

Figure 2.2 – The Revolution XT Ring Saw, used for sample preparation. 62

Figure 2.3 – Schematic cross-section and diagrams of the triaxial experimental apparatus. 66

Figure 2.4 – Photograph of the triaxial experimental apparatus. 67

Figure 2.5 – Schematic and photograph of the seismic sample assembly configuration with test specimen set-up. 69

Figure 2.6 – Illustration of the theory for the pulse transient decay method of measuring permeability. 71

Figure 2.7 – Illustration of a scanning electron microscope primary electron beam and how it interacts with the atoms within a sample. 75

Figure 2.8 – Illustration of a calcite rhomb with trigonal crystal system and illustration of electron beam scattering pattern generation. 78

Figure 2.9 – Photograph and schematic cross-section of the CAMSCAN X500 CrystalProbe field emission gun scanning electron microscope. 80

Figure 2.10 – Electron backscatter diffraction reference frame vs. scanning electron microscope reference frame conventions. 86

Figure 2.11 – Schematic plan view of the CAMECA IMS-1270 microprobe used in the trace element analyses. 90

Figure 2.12 – Schematic plan view of the CAMECA IMS-4f microprobe used in the stable isotope analyses. 91

Figure 2.13 – Schematic cross-section and plan view of the sample holders used in the microprobes. 92

Table 2.1 – Location information for the Deep Fault Drilling Project Phase 1 and 2. 57

Table 2.2 – Complete sampling summary for both phases of the Deep Fault Drilling Project. 60

Sheet SM 2.1 – Water pore fluid properties. 97

Table SM 2.1 – Water properties with temperature and varying pressure. 97

Table SM 2.2 – Water properties with temperature and varying pressure. 97

Figure SM 2.1 – Graph of viscosity variation with pressure. 97

Figure SM 2.2 – Graph of compressibility variation with pressure. 97

Table SM 2.3 – Calculated values for compressibility from pressure and density. 97

Figure SM 2.3 – Graph of density variation with pressure. 97

Figure SM 2.4 – Graph of volume variation with pressure. 97

Sheet SM 2.2 – Triaxial Apparatus Pressure system reservoirs volumes. 97

Table SM 2.4 – Three Way Valves / Two Pressure Connections information. 97

Table SM 2.5 – High Pressure Elbows information. 97

Table SM 2.6 – High Pressure Tees information. 97

Table SM 2.7 – Triaxial experimental apparatus pore pressure system pipe work volumes. 97

Table SM 2.8 – Seismic sample assembly pipe work volumes. 97

Table SM 2.9 – Honeywell Pressure Transducer information. 97

Table SM 2.10 – Triaxial apparatus pore fluid reservoir volume breakdown. 97

Table SM 2.11 – Circle to square and porous spacer volume breakdown. 98

Sheet SM 2.3 – Worksheet containing parameters for permeability calculations. 98

Sheet SM 2.4 – Worksheet for calculating permeability. 98

Figure SM 2.5 – Example of a batch file used to convert seismic velocity data. 99

Table SM 2.12 – University of Edinburgh NERC Ion Microprobe facility standards for carbonate trace element and $\delta^{18}O$ stable isotope analyses. 100

Figure 3.1 – Map of the South Island, New Zealand with location of Alpine Fault, major towns and rivers marked, including a schematic borehole section of Deep Fault Drilling Project – 1. 105

Figure 3.2 – Photomicrographs of cataclastic microstructures from the Alpine Fault hanging wall and footwall. 107

Figure 3.3 – The Revolution XT Ring Saw, used for sample preparation. 109

Figure 3.4 – Schematic illustrations and photographs of the triaxial experimental apparatus, including the Seismic sample assembly and sample configuration. 111

Figure 3.5 – Graphs showing permeability, *P-wave* velocity and *S-wave* velocity measurements as a function of effective pressure. 114

Figure 3.6 – Graphs showing permeability and seismic velocity ranges for material from DFDP-1A and DFDP-1B with depth and field derived protolith lithologies. 116

Figure 3.7 – Graphs showing permeability and seismic velocity anisotropy with depth. 118

Figure 3.8 – Backscatter electron images of hanging wall and footwall cataclasites. 120

Figure SM 3.1 – Graphs showing the hysteresis effect observed in both the permeability and seismic wave velocity measurements. 130

Table SM 3.1 – Seismic velocity values reported in Figures 3.5 and 3.6. 131

Table SM 3.2 – Permeability values reported in Figures 3.5 and 3.6. 131

Table SM 3.3 – Anisotropy values reported in Figures 3.7. 131

Video SM 3.1 – nanoCT tomographic reconstruction of an Alpine Fault hanging wall cataclasite. 131

Video SM 3.2 – nanoCT tomographic reconstruction of an Alpine Fault footwall cataclasite. 131

Figure 4.1 – Schematic borehole section showing the lithologies encountered during DFDP-1A and 1B and sampling for *Chapter 4*. 140

Figure 4.2 – Microstructural observations of a sheared calcite vein in a hanging wall ultramylonite (*1B-99.3m-A* – Unit 2), including; photomicrographs, cathodoluminescence images, electron backscatter diffraction analyses and geochemical measurements. 147

Figure 4.3 – Microstructural observations of cataclased calcite vein in a hanging wall ultramylonite (*1B-99.3m-B* – Unit 2), including; photomicrographs, cathodoluminescence images, electron backscatter diffraction analyses and geochemical measurements. 150

Figure 4.4 – Microstructural observations of an en-échelon calcite vein structure in a hanging wall cataclasite (*1B-118.64m-A* – Unit 3), including; photomicrographs, cathodoluminescence images, electron backscatter diffraction analyses and geochemical measurements. 152

Figure 4.5 – Microstructural observations of an oscillatory chemically zoned calcite vein a hanging wall cataclasite (*1B-118.64m-B* – Unit 3), including; photomicrographs, cathodoluminescence images, electron backscatter diffraction analyses and geochemical measurements. 155

Figure 4.6 – Microstructural observations of a multigenerational calcite clast in a principal slip zone gouge (*1A-90.74m-A* – Unit 5), including; photomicrographs, cathodoluminescence images, electron backscatter diffraction analyses and geochemical measurements. 157

Figure 4.7 – Microstructural observations of a multigenerational calcite clast in a principal slip zone gouge (*1A-142.2m* – Unit 5), including; photomicrographs and cathodoluminescence images. 158

Figure 4.8 – Graph showing carbonate trace element Mg and Fe concentrations in part per million with depth. 160

Figure 4.9 – Graph showing a principal component analysis plot of all trace element measurements, Fe, Mn, Mg, Sr, Ba and Ce, made in this study. 173

Figure 4.10 – Summary schematic illustration of various vein calcite mineralisation mechanisms. 176

Table 4.1 – Classification and description of calcite twin morphology variation with increasing temperature. 165

Figure SM 4.1 – Microstructural observations of a multigenerational calcite vein in a hanging wall cataclasite (*1A-89.4m* – Unit 3), including; photomicrographs and cathodoluminescence images. 182

Figure SM 4.2 – Microstructural observations of an ankerite vein in a hanging wall cataclasite (*1A-111m-A* – Unit 4), including; photomicrographs, cathodoluminescence images, electron backscatter diffraction and geochemical measurements. 183

Figure SM 4.3 – Microstructural observations of a multigenerational calcite vein in a hanging wall cataclasite (*1A-111m-B* – Unit 4), including; photomicrographs, cathodoluminescence and electron backscatter diffraction analyses. 184

Figure SM 4.4 – Microstructural observations of an en-échelon calcite vein structure in a hanging wall cataclasite (*1B-118.64m-C* – Unit 3), including; photomicrographs, cathodoluminescence images, electron backscatter diffraction analyses and geochemical measurements. 185

Figure SM 4.5 – Microstructural observations of a calcite vein in a hanging wall cataclasite (*1B-123.15m* – Unit 3), including; photomicrographs, cathodoluminescence images, electron backscatter diffraction analyses and geochemical measurements. 187

Figure SM 4.6 – Microstructural observations of a multigenerational calcite clast in a principal slip zone gouge (*1A-90.74m-B* – Unit 5), including; photomicrographs, cathodoluminescence images and electron backscatter diffraction analyses. 188

Figure SM 4.7 – Microstructural observations of a calcite vein in a footwall cataclasite (*1B-133m* – Unit 6), including; photomicrographs, cathodoluminescence images and geochemical measurements. 189

Figure SM 4.8 – A Stereographic projection of calcite showing key planes and directions. 190

Figure SM 4.9 – Graph showing carbonate trace element Mg and Fe concentrations in part per million with depth. Symbol variation denotes separate generations. 191

Figure SM 4.10 – Photomicrographs and backscatter electron images of Alpine Fault garnets. 192

Table SM 4.1 – Table detailing all the vein types observed and identified in this study. 183

Workbook SM 4.1 – Microsoft Excel workbook containing all carbonate trace element and $\delta^{18}O$ measurement data and workings for Principal Component Analysis (PCA). 183

Figure 5.1 – Schematic borehole section showing the lithologies encountered during DFDP-1A and 1B and sampling for *Chapter 5*. 203

Figure 5.2 – Microstructural observations of melt segregation in a hanging wall ultramylonite pseudotachylyte (*1B-99.3m-A* – Unit 2), including; photomicrographs and backscatter electron image. 208

Figure 5.3 – Microstructural observations of melt segregation and ultracataclasite-melt transition in a hanging wall ultramylonite pseudotachylyte (*1B-99.3m-A* – Unit 2), including; photomicrographs and backscatter electron image. 209

Figure 5.4 – Microstructural observations of melt segregation in a hanging wall ultramylonite pseudotachylyte (*1B-99.3m-A* – Unit 2), including; photomicrographs, backscatter electron image and energy dispersive spectroscopy maps. 210

Figure 5.5 – Microstructural observations of melt segregation and calcite veining in a hanging wall ultramylonite pseudotachylyte (*1B-99.3m-B* – Unit 2), including;

photomicrographs backscatter electron image and energy dispersive spectroscopy maps. 212

Figure 5.6 – Cathodoluminescence of amygdules and other mineralised voids in a hanging wall ultramylonite pseudotachylyte (*1B-99.3m-B* – Unit 2). 214

Figure 5.7 – Cathodoluminescence of calcite veining in a hanging wall ultramylonite pseudotachylyte (*1B-99.3m-B* – Unit 2). 215

Figure 5.8 – Backscatter electron image and energy dispersive spectroscopy maps of calcite veining and pseudotachylyte matrix alteration in a hanging wall ultramylonite pseudotachylyte (*1B-99.3m-B* – Unit 2). 216

Figure 5.9 – Microstructural observations of pseudotachylyte in a hanging wall ultramylonite (*1A-68.36m* – Unit 2), including; photomicrographs, quantitative evaluation of minerals by scanning electron microscopy map, backscatter electron images and energy dispersive spectroscopy maps. 218

Figure 5.10 – Microstructural observations of fragmented pseudotachylyte in a hanging wall cataclasite (*1B-118.64m* – Unit 3), including; photomicrographs, backscatter electron images and energy dispersive spectroscopy maps. 219

Figure 5.11 – Microstructural observations of irregularly shaped pseudotachylyte in a hanging wall cataclasite (*1B-123.15m* – Unit 3), including; photomicrographs, backscatter electron images and energy dispersive spectroscopy maps. 221

Figure 5.12 – Photomicrographs of pseudotachylyte in a footwall cataclasite (*1B-132.2m* – Unit 6). 222

Figure 5.13 – Hand specimen images of the principal slip zones from DFDP-1 A/B with lithological key. 224

Figure 5.14 – Microstructural observations of a feldspathic fragment in a principal slip zone gouge (*1A-90.74m* – Unit 5), including; photomicrographs, backscatter electron images and electron backscatter diffraction analyses. 226

Figure 5.15 – Microstructural observations of a feldspathic fragments in a principal slip zone gouge (*1B-143.85m* – Unit 5), including; photomicrographs, backscatter electron and cathodoluminescence images. 227

Figure 5.16 – Microstructural observations of a polygonal clast in a principal slip zone gouge (*1A-90.74m* – Unit 5), including; photomicrographs, EBSD analyses and backscatter electron images. 228

Figure 5.17 – Block diagram illustrating the proposed formation mechanism of the polygonal feldspathic clasts. 238

Figure 5.18 – Schematic illustration of the Alpine Fault Zone in the upper crust, showing the fault rock lithological sequence, geothermal gradient and pseudotachylyte occurrence. 241

Figure SM 5.1 – Energy dispersive spectroscopy maps of clasts detailed in Figure 5.14. 244

Figure SM 5.2 – Energy dispersive spectroscopy maps of clasts detailed in Figure 5.16. 245

Figure SM 5.3 – Microstructural observations of pseudotachylyte matrix in a hanging wall metabasic mylonite (field sample), including; photomicrographs, backscatter electron images and energy dispersive spectroscopy maps. 246

Figure SM 5.4 – Microstructural observations of secondary minerals associated with pseudotachylyte in a hanging wall metabasic mylonite (field sample), including; photomicrographs, backscatter electron images and energy dispersive spectroscopy maps. 247

Figure SM 5.5 – Microstructural observations of a calcite vein cross-cutting host-rock and pseudotachylyte margin, including; backscatter electron image and EBSD analyses. 248

Figure SM 5.6 – Microstructural observations of calcite veining and a quartz survivor clast within a pseudotachylytes matrix, including; backscatter electron image and EBSD analyses. 250

Figure SM 5.7 – Image analyses of backscatter electron images of pseudotachylyte survivor clast grain shapes. 252

Figure SM 5.8 – Image analyses of backscatter electron images of pseudotachylyte survivor clast grain shapes. 253

Table SM 5.1 – Table detailing all the pseudotachylyte and gouge microstructures observed and identified in this study. 243

Table SM 5.2 – Table detailing preliminary grain shape analyses of pseudotachylyte survivor clasts shown in Figures SM 5.5 and 5.6. 251

1. Introduction

1.1. Shear zones in the crust

Movement within the Earth, from global to microscopic scales, occurs along discrete zones of displacement which, depending on their setting in the crust, may be viscous or brittle – viscous shear zones or brittle faults. The largest of these structures occur at the contacts between tectonic plate boundaries. Accommodating significant motion and very large displacements, these features extend far into the lithosphere, sometimes into the lower crust and mantle, and are the focus for either the burial or exhumation of vast amounts of geological material, processes that have great influence on climatic, oceanic and biological Earth systems [*Snoke et al.*, 1998; *Tikoff et al.*, 2001; *Mooney, W. D., Beroza, G. C., and Kind*, 2009]. At shallow depths in the crust, between 2 – 15 km in a region known as the seismogenic zone, plate boundary faults often rupture periodically with large magnitude earthquakes. The rapid release of elastic strain energy from the fault during slip is radiated through the crust as earthquake waves causing massive shaking and represent significant economic and societal threat.

1.2. Rheology of the crust

Shear zones form a broad continuum of geological structures in which strain is localised in the Earth, transitioning from broad, distributed, viscous shear zones in the lower crust to brittle faults in the upper crust. This transition in rheological response to stress does not occur at a specific depth but rather occurs over a transitional zone within which brittle – viscous processes coexist [*Kohlstedt et al.*, 1995]. The onset of plasticity (or, conversely, cataclasis) is dependent on a number of factors such as the geothermal gradient, pressure (both overburden and fluid), the bulk strain rate and the stress field orientation [*Simpson*, 1985]. Other factors include the mineral composition of the rock, grain size and pre-existing textures or fabrics. Fault structure and varied responses to deformation with depth have been studied in both ancient and modern shear zones using geological field techniques and remote sensing. The resulting conceptual model initially formed by *Sibson* [1977] and further developed by *Scholz* [1988] is widely known as the 'Sibson – Scholz fault zone model', illustrated in Figure 1.1.

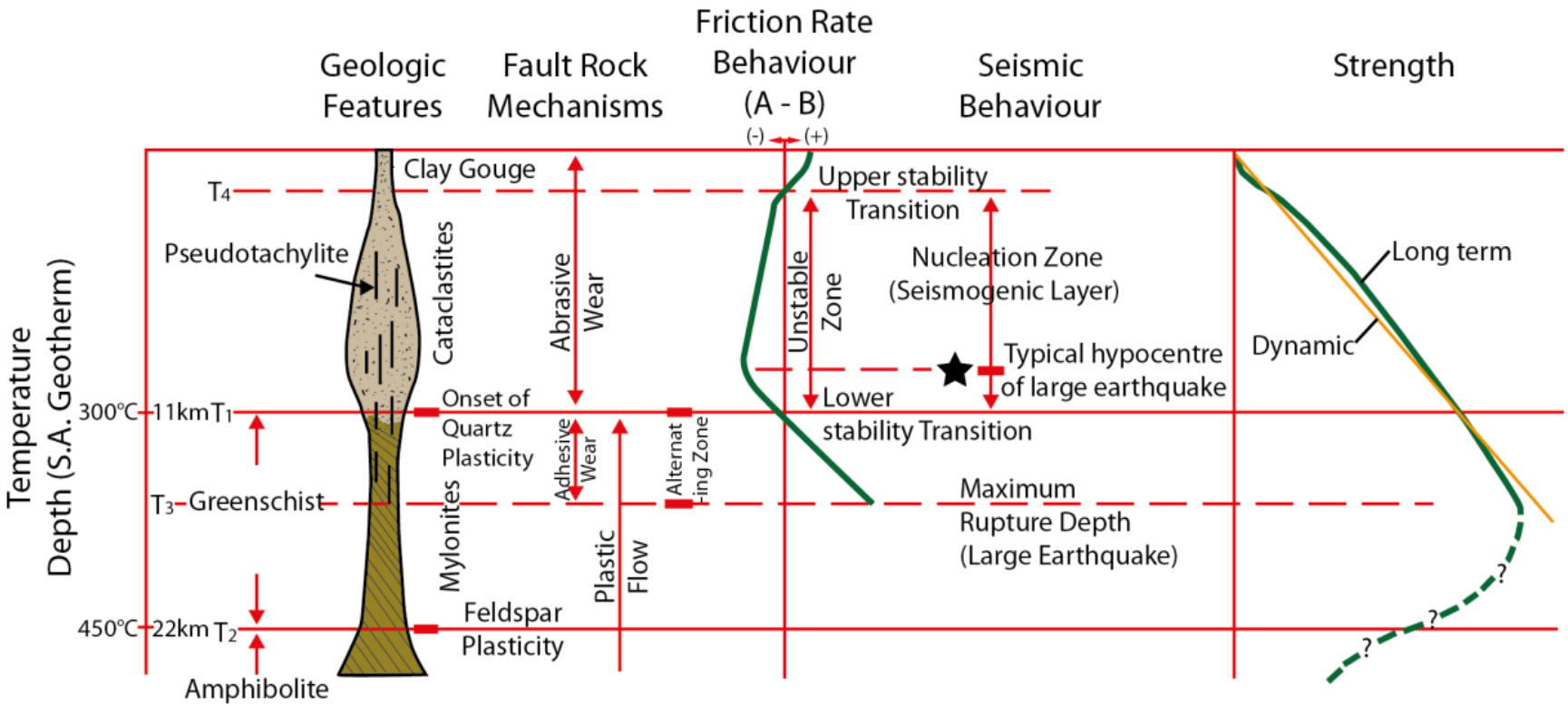

Figure 1.1 – *The 'Sibson – Scholz' conceptual fault zone model for a vertical fault in a quartzofeldspathic crust, after Scholz, [1988] and Imber et al., [2001]. The geothermal gradient is based on that at the San Andreas Fault, California, USA (S.A).*

1.3. Deformation of the crust

To a first approximation the variation in deformation mechanisms within the crust corresponds to variations in ambient conditions, particularly the systematic change of temperature, via the Earth's geothermal gradient and pressure, via gravity, with crustal depth. These changes in ambient conditions alter the material properties of minerals and thus how they respond to an applied stress. A materials response to stress can be divided into the following behaviours: *elastic*; *inelastic*, which can be sub-divided into *plastic* and *viscous*; and *brittle*. *Elastic* behaviour is exhibited in materials that can undergo deformation that is instantaneously recoverable once stress is removed. *Inelastic* materials can behave *viscously*, when a material undergoes non-recoverable deformation in which the bulk strain rate is directly proportional to the applied stress; or *plastically*, in which a material will only deform once its yield stress has been exceeded. In *inelastic* materials permanent strain is accommodated without losing the ability to resist the load (or stress). *Brittle* behaviour is when a material undergoes non-recoverable deformation and its ability to resist load decreases with permanent strain [*Blenkinsopp*, 2000; *Jaeger et al.*, 2007].

Viscous behaviour is characterised by deformation mechanisms such as intracrystalline plasticity and solid-state diffusive mass transfer at grain boundaries. These occur at deeper crustal levels and are sensitive to strain rate but insensitive to pressure and strongly promoted by high temperatures. Brittle behaviour is characterised by deformation through cataclasis, involving the fracture and sliding of rock, and is supressed by pressure but insensitive to temperature, and so is favoured in the upper crust [*Blenkinsopp*, 2000; *Jaeger et al.*, 2007].

Minerals at high temperatures and pressures deform by crystal-plasticity. This is facilitated by the movement of dislocations, and/or vacancies in a crystal lattice, through a crystal as it responds to an applied stress. This can occur by *dislocation glide*, in which slip occurs on the defect planes, or *dislocation climb* when defects move out of their respective crystallographic plane to overcome obstacles. The combination of *dislocation glide* and *climb* is known as *dislocation creep*. If *dislocation glide* operates without sufficient *dislocation climb* dislocations can tangle, causing work hardening of the crystal. This can result in brittle failure even at low strain rates. When *climb* occurs dislocations are able to move out of their slip planes and into subgrain boundaries, this can be similarly achieved by

the movement of boundaries, which can collect isolated dislocations. Formation of subgrain boundaries and grain boundary migration are dynamic recrystallisation processes that aid the grain-size reduction of rock and allow deformation to continue resulting in the generation of mylonites [*Blenkinsopp*, 2000].

Diffusive mass transfer (*DMT*) processes, which involves the removal, transportation and deposition of material without distortion of the crystal lattice or fracturing, can occur by the diffusion of atoms in a solution at the grain boundaries of a crystal or the solid-state diffusion of atoms through the crystal lattice, i.e. *Nabarro-Herring creep,* or along the grain boundaries of a crystal, i.e. *Coble Creep* [*Poirier*, 1985; *Wheeler*, 1992; *Blenkinsopp*, 2000]. *DMT* is grain-size sensitive creep, driven by stress and/or chemical gradients around the crystal boundaries, induced by macroscopically homogenous differential load [*Poirier*, 1985; *Wheeler*, 1992]. It is the general consensus that, in nature, up to amphibolite facies conditions, the majority of *DMT* occurs via solution due to the large time-scales of solid-state diffusion at these temperatures [*Rutter*, 1983], while above amphibolite facies conditions solid-state diffusion is favoured.

Conditions within the upper crust are generally of low temperature and low lithostatic pressures, and facilitate the failure of rock through brittle fracture and cataclasis during frictional sliding at high strain rates. The fracture of material, particularly the generation of microfractures, was recognised and described by *Griffith*, [1921], after whom the Murrel – Griffith macroscopic failure criterion was formulated;

$$\tau^2 = 4\sigma_n' T_0 + 4T_0^2 \qquad (1)$$

where T_0 is the tensile strength of intact rock, σ_n' is the effective stress normal to the failure plane and τ is the shear stress perpendicular to that plane [*Price and Cosgrove*, 1990]. *Griffith*, [1921] and *Brace*, [1960] formulated a scheme of fracture classification which relates the displacement of the wall rock relative to the fracture plane and edge and is divided into three end members as follows. Mode I – extensional fractures that form perpendicular to the least principal compressive stress σ_3'; at the fracture tips of these extensional fractures the stress field is perturbed, concentrating stress between neighbouring, en-échelon fractures and allowing them to link, forming through going

structures which can accommodate shear. These are classified as Mode II (sliding) and Mode III (tear or shear) fractures. Fractures that exhibit both shear and extension modes of failure are classified as hybrid fractures [e.g., *Ramsey and Chester*, 2004]. Experimental evidence from *Kohlstedt et al.*, [1995] suggests that, at confining pressures of 600 – 800 MPa, Mode I fracturing is supressed and only Mode II and III shear fractures can form. However *Scambelluri et al.*, [1998] reports evidence of Mode I fracturing in the eclogites of the Italian alps, suggesting formation at 1100 – 1300 MPa and 450 – 550°C.

When elastic strain is accumulated in a rock mass encompassing a fracture or fault plane, the stored energy can be released suddenly through slip upon the fault contact, causing sudden displacement of the rock mass and generating an earthquake. The timing, magnitude and severity of the earthquake depend on variety of factors including the frictional strength of a fracture surface. This process is described by Amontons' Law where further deformation on a fracture can be accommodated by sliding on the cohesionless fracture plane;

$$\tau = \mu\sigma_n' \qquad (2)$$

where the shear stress, τ, is proportional to the normal stress, σ_n', via the coefficient of friction, μ. This is the ratio of shear stress to normal stress required to: 1) initiate a sliding surface (*internal friction)*; 2) initiate sliding on a pre-existing surface (*static friction)*; and 3) maintain sliding on a surface (*dynamic friction)*. The frictional behaviour of a surface and a system's overall stiffness governs whether a steady-state or a stick-slip form of sliding is observed [*Leeman et al.*, 2015]. Stick-slip behaviour is characterised by a rapid transition from a static state to dynamic slip on a fracture plane; it is controlled by a system's compliance and can occur at rates of 0.1 – 2 ms^{-1}, releasing a large amount of energy in the form of seismic waves. As well as compliance (or stiffness) the recurrence of stick-slip behaviour at all scales is influenced by the composition of material upon the fracture / fault plane and weakening processes that occur within the zone surrounding the fracture / fault, modifying compliance through time. The initiation and duration of shear on a fracture / fault is controlled by the *velocity weakening* or *velocity strengthening* behaviour of the rock [*Dieterich*, 1978, 1979; *Ruina*, 1983; *Tse and Rice*, 1986; *Chester et al.*, 1993; *Marone*, 1998]. In *velocity weakening* materials the resistance to sliding decreases with increased velocity allowing the generation of earthquakes, while in *velocity strengthening* materials sliding

upon fractures and faults is stable, aseismic and steady-state, a behaviour thought to be favoured at higher temperatures [*Shimamoto*, 1989; *Chester et al.*, 1993]. Stick slip behaviour is also controlled by the rate of loading, with increased loading rates supressing stick slip and their accompanying stress drops [*Karner and Marone*, 2000].

1.4. Structure of brittle fault zones

The generation of fractures and their coalescence into a localised plane is the precursor stage to the development of a fault. As a fault accommodates progressive deformation, via seismic slip or aseismic creep, its structure evolves, scaling with fault displacement and increasing in length and width. A conceptual model for fault zone structure divides the fault zone into two primary features; the fault core, where most strain is localised, and a damage zone comprised of distributed fractures and faulting, both of which are hosted within a country rock protolith, as shown in Figure 1.2 [*Caine et al.*, 1996; *Wibberley and Shimamoto*, 2002; *Faulkner et al.*, 2010]. The fault core typically contains at least one principal slip zone (PSZ) composed of fine-grained and/or amorphous material such as ultracomminuted gouges, cataclasites and pseudotachylytes [*Caine et al.*, 1996; *Chester and Chester*, 1998; *Sibson*, 2003]. As most strain is localised in the fault core and this is also where the majority of coseismic displacement takes place, the material within the fault core is interpreted to be generated from grain-size reduction by fragmentation, abrasion and comminution with some translation and rotation [*Chester and Logan*, 1986; *Chester and Chester*, 1998; *Sibson*, 2003; *Boulton et al.*, 2017b]. Fault cores are commonly nested within damage zones, regions of rock consisting of fractures and subsidiary faults over a wide range of length scales generated as a result of off-fault damage during seismicity. A generalised view of off-fault damage is illustrated in Figure 1.2, showing an increase in fracture density with proximity to the principal slip zone, where fracture density then dramatically decreases due to the fine-grained nature of the fault core, enhancing compaction and the closure of fractures. Fault zones, comprising a high strain fault core and lower strain damage zone vary in thickness between 10 – 10^3 m [*Sibson*, 1986; *Caine et al.*, 1996; *Faulkner et al.*, 2010].

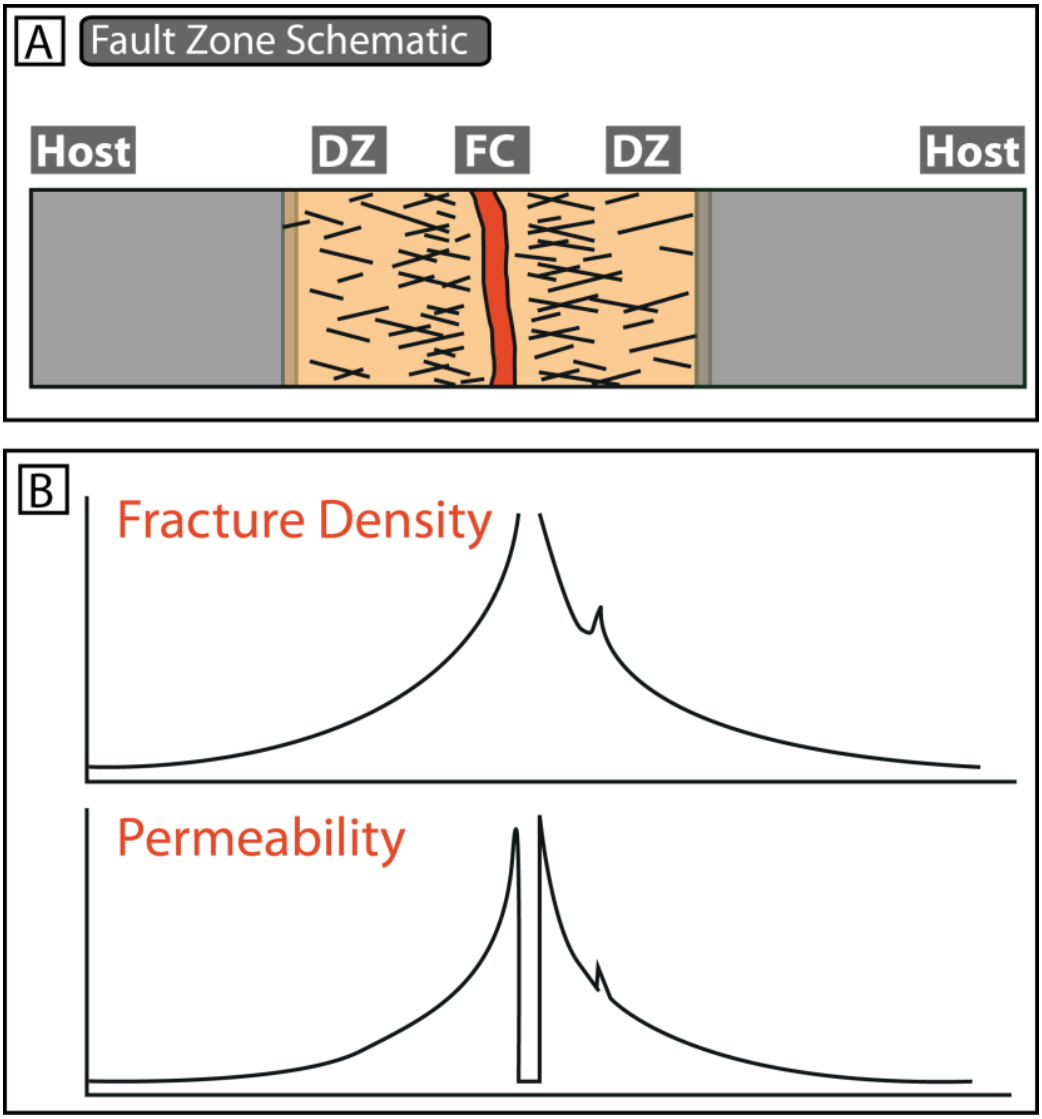

Figure 1.2 – [A] *A schematic illustration of a fault zone; a fault core (FC) typically composed of gouge, cataclasite and ultracataclasite, where most of the strain is localised and a damage zone (DZ) a distributed zone of fractures and subsidiary faulting on a range of length scales.* ***[B]*** *Some physical properties, particularly permeability, are related to fault structures such as fracture density, which increases exponentially from the host country rock protolith to the FC. Within the FC fractures are healed and sealed by compaction of ultracomminuted material and fluid-rock interaction. Modified after Faulkner et al., [2010].*

1.5. Fluids in the crust and how fault zones influence their behaviour

Fluids are ubiquitous throughout the Earth's crust and have a significant effect on rock strength, influencing deformation behaviour through mechanical and fluid-rock interaction processes. Fluids facilitate the transport of mass at a range of scales, via diffusive mass transfer [*Rutter*, 1983] and stress corrosion [*Carter et al.*, 1990] processes, can reduce effective stresses [*Murrell*, 1963] and are able to cause hydrolytic weakening [*Kronenberg and Tullis*, 1984]. These processes aid the localisation of strain in the crust, and the generation of brittle and viscous shear zones depending on the crustal depth setting and geothermal gradient. Localised deformation on shear zones, coupled with bulk rock flow and the activity of pervasive and dynamic fluid-rock interactions, govern the rheology of the lithosphere [*Carter et al.*, 1990].

Sources of crustal fluids are determined by geological setting and are broadly defined as follows. Sedimentary fluids are derived from the burial of wet sediments where compaction expels the majority of pore fluids, with buried sediments typically retaining ~ 2 wt.% water, or <10 wt. % if the sediment is clay-rich [*Yardley*, 1997]. Metamorphic fluids may develop through mineral dewatering and devolatilisation during burial and heating, making available volatiles such as CO_2, H_2O, CH_4 and others [*Yardley*, 1997]. During prograde metamorphism hydrous minerals may undergo transformations to denser, dehydrated minerals stable at higher temperatures and pressures. Up to greenschist facies metamorphism water originating from detrital clays are assimilated into newly formed hydrous phases such as chlorite and muscovite for example. With further metamorphism up to amphibolite facies, chlorite reacts to form biotite, garnet and amphibole, a reaction that produces excess fluids of up to 5 wt. % of the rock (H_2O and CO_2) [*Walther and Orville*, 1982]. Magmatic fluids are generated through aqueous fractionation during melt crystallisation and are mobilised through hydrothermal fluid flow from the igneous bodies' heat. These fluids generally contain higher concentrations of dissolved solids and have higher salinity than metamorphic fluids. Meteoric fluids, derived from surface precipitation, have been observed to penetrate as far down as the Brittle-Viscous Transition Zone [e.g. *Jenkin et al.*, 1994; *Upton et al.*, 1995; *Menzies et al.*, 2014]. Their movement is driven by the topographic and thermal structure of the crust, that facilitate descent into the crust by flow up temperature gradients, gain heat and then ascend once fluids have become sufficiently buoyant [*Koons and Craw*, 1991].

As temperatures and confining pressures increase with depth, compaction and cementation reduce permeability and limit fluid mobility, potentially allowing fluid pressures to reach or exceed lithostatic pressures in certain circumstances. The movement of fluid in the crust can be described by two end-member states, pervasive and focussed, with commonly observed overlap between these two states [*Oliver*, 1996]. As described by *Oliver* [1996], focussed fluid flow involves the passage of fluid through high-permeability conduits that may include: shear zones, lithological contacts, boudin necks and permeable lithologies. Pervasive flow involves the distributed passage of fluids around individual mineral grains and may be initiated by the creation of regions of low fluid pressure by means of focussed flow for example, resulting in pervasive flow characterising volumes of low pressure.

Darcy's law describes the pervasive flow of fluids in a porous permeable material;

$$q_x = -\frac{k}{\mu} \cdot \left(\frac{\partial [P + \rho_f g Z}{\partial x} \right) \qquad (3)$$

where q_x is the magnitude of the fluid flux, k is the intrinsic permeability of the medium, μ is the fluid viscosity, P is the fluid pressure, ρf is fluid density, g is the gravitational acceleration and Z is the elevation above a defined point. The energy gradient for fluid flow along a pathway x is defined through $\partial(P + \rho_f g Z)/\partial c$ [*Ague*, 2003]. A fluid flux can be increased by decreasing the fluid viscosity μ, increasing the intrinsic permeability k or by increasing the fluid pressure gradient.

Permeability of rock varies considerably, with gravel and highly fractured rocks measuring at ~ 10^{-7} m^2 to crystalline igneous and metamorphic rocks yielding permeabilities as low as ~10^{-22} m^2 [*Bear*, 1972; *Ague*, 2003]. These latter values can be considered the intact, matrix permeabilities of a rock and can be drastically increased as a function of the concentration, orientation and connectivity of fractures and faults.

The dynamic nature of fault zones means that faults, though occupying a relatively small volume of the lithosphere, can act as conduits or barriers to fluid flow, influencing the distribution of heat and chemical changes depending on their tectonic setting, maturity and composition [*Chester and Logan*, 1986; *Caine et al.*, 1996; *Faulkner et al.*, 2010]. Where faults act as favourable conduits to fluid flow they are sites of enhanced dissolution and

precipitation. The permeability of a fault zone is thought to be dynamic, evolving from highly permeable immediately post-earthquake rupture, due to seismically induced fracture damage, to becoming effectively sealed by the precipitation of minerals in pore spaces and fractures and the compaction of clay-rich, ultrafine-grained fault gouges [*Blanpied et al.*, 1992; *Gratier et al.*, 2002].

1.6. The Alpine Fault, New Zealand

The Alpine Fault Zone (AFZ), bounding the western edge of the Southern Alps on New Zealand's South Island from Arthur's Pass to Milford Sound, accommodates over 70 % of the relative motion between the colliding Australian and Pacific Plates, see Figure 1.3 [*Norris and Toy*, 2014]. The ramping of the Pacific plate over the Australian plate is accommodated through a transpressional dextral-reverse movement, offsetting basement rocks laterally by ~470 km, with Quaternary horizontal displacement rates estimated at 2 – 27 mm yr^{-1} [*Norris and Cooper*, 2001; *Lamb et al.*, 2015]. The mean plane of the fault dips at 40 – 60° southeast to a depth of 15 km, at which it begins to shallow downwards into a lower crustal detachment at 35 km depth [*Norris and Cooper*, 2007; *Stern et al.*, 2007; *Sutherland et al.*, 2012]. Uplift across the fault is rapid, exhuming crustal rocks from depths of 20 to 30 km at a rate of ~6 – 9 mm yr^{-1} [*Little et al.*, 2002b]. Accompanying this rapid uplift is the advection of the regional geothermal gradient. Quartz fluid inclusion microthermometry places the gradient at 40 °C/km [*Toy et al.*, 2010], while titanium thermobarometry of quartz shows a gradient of 45 °C/km [*Cross et al.*, 2015] and recent shallow borehole measurements report a gradients of 62.6 ± 2.1 and 125 ± 55 °C/km attributed to rapid uplift on the fault and the topographically-driven movement of fluids concentrating heat in valleys [*Sutherland et al.*, 2012, 2017].

The Alpine Fault originated during the Oligocene – Miocene as a broad zone of dextral crustal shearing <100 km wide, [*Carter and Norris*, 1976; *Cooper et al.*, 1987; *Sutherland*, 1999a; *Little and Mortimer*, 2001] with an additional convergent component relative to the Pacific – Australian plate motions [*Sutherland*, 1995; *Walcott*, 1998; *Cande and Stock*, 2004]. Deformation was progressively localised on the current fault trace forming a linear feature along the South Island West Coast. Much of the deformation is localised in a clay-rich gouge zone, approximately 25 cm thick, known as the Principal Slip Zone (PSZ), this zone is nested within a cataclasite zone ranging from 10 – 50 m thick which transitions into

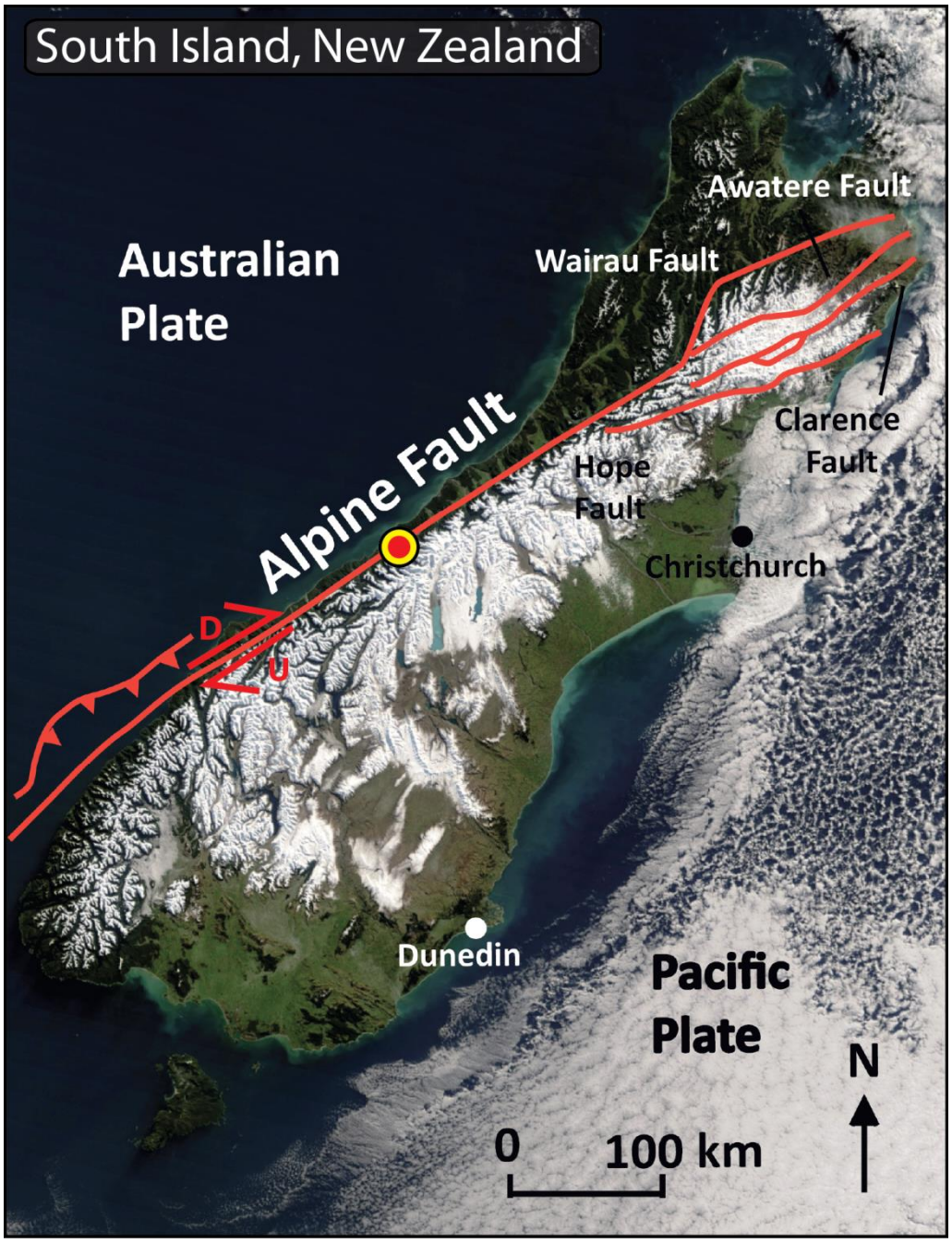

Figure 1.3 – *Satellite image of New Zealand's South Island with the Alpine Fault, image from Google. Red / yellow point marks the region of study in this thesis.*

a mylonitic rock sequence of approximately 1 – 1.5 km thickness that has been exhumed from <35 km depth in the last 5 – 8 Ma [*Norris and Cooper*, 2007; *Toy et al.*, 2008]. This viscous to brittle fault rock sequence is sourced from non-mylonitised amphibolite facies schist protoliths that are predominantly quartzofeldspathic, with dykes of metabasic composition [*Holm et al.*, 1989; *Grapes and Watanabe*, 1992; *Little et al.*, 2002a].

1.6.1. Historic and paleoseismicity

Palaeoseismic evidence has indicated that the Alpine Fault has had numerous geologically recent rupture episodes at 1717 ± 25, 1630 ± 25 and 1460 ± 25 A.D., estimated to have moment magnitudes of 7.9 ± 0.3, 7.6 ± 0.3, and 7.9 ± 0.4, respectively [*Wells et al.*, 1999; *Rhoades and Van Dissen*, 2003; *Langridge et al.*, 2012], with these ruptures propagating along nearly the entire ~600 km length of the fault. Recent seismicity patterns, geodetic strain records, and inferred high pore fluid pressures from regional seismic P- and S-wave velocity ratios and gravity surveys deep in the fault zone, suggest that the fault is locked above 6 – 12 km depth and that it is in the late stages of its earthquake cycle [*Eberhart-Phillips*, 1995; *Eberhart-Phillips and Bannister*, 2002; *Sutherland et al.*, 2007; *De Pascale and Langridge*, 2012; *Lamb and Smith*, 2013]. There has been no evidence for aseismic creep on the fault, though these observations are limited to the past 50 years. The global significance of the Alpine Fault in the study of major fault zones and crustal processes is considerable; the opportunity to study a locked continental plate boundary fault thought to be late in the earthquake cycle will yield insight into the pre-rupture conditions of a major fault and the nature of the interseismic physico-chemical processes that have taken place. It is to be noted that rock retrieved from the surface or shallow depths will yield incomplete information on the locked sections of the fault at depth, where elastic strain energy is stored and earthquake nucleation occurs.

1.6.2. Fluids in the Southern Alps

The origin, behaviour and compositions of fluids around the Alpine Fault, and the Southern Alps as a whole, have been the focus of many studies, covering warm springs [*Barnes et al.*, 1978; *Allis and Shi*, 1995; *Menzies et al.*, 2014, 2016], hydrothermally altered rock and vein assemblages [*Jenkin et al.*, 1994; *Vry et al.*, 2001], borehole fluid temperature observations [*Sutherland et al.*, 2012, 2017] as well as geophysical imaging

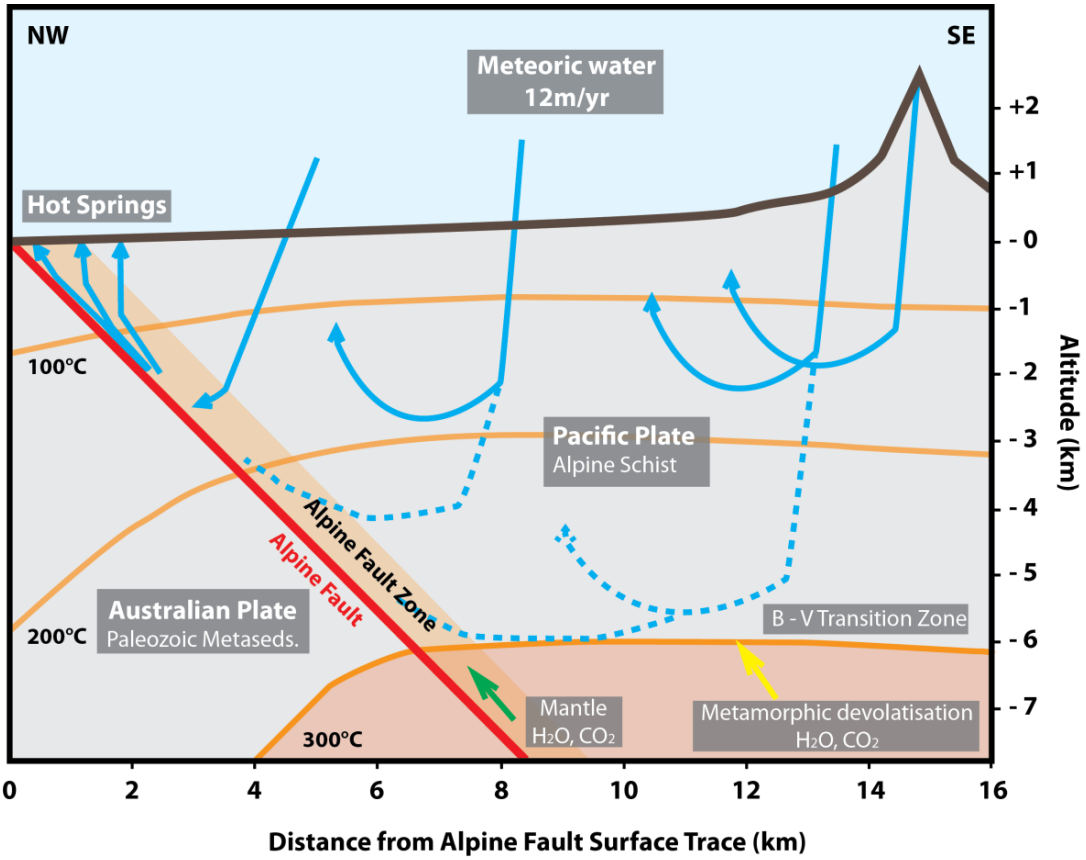

Figure 1.4 – *Schematic of the fluid flow regime in the Southern Alps, adapted from Menzies et al., [2014] with isotherms adapted from Toy et al., [2010]. Meteoric water permeates through the Alpine Fault hanging wall and is focused up along the fault to the surface as hot springs. A small component also reaches the Brittle – Viscous Transition and is incorporated into vein-infill. Metamorphic and mantle derived fluid also have a small input into the overall fluid composition.*

[*Stern et al.*, 2001; *Wannamaker et al.*, 2002]. These studies indicate the presence of an extensive, advective hydrothermal system at depth, east of the Alpine Fault beneath the Southern Alps [*Koons et al.*, 1998; *Cox et al.*, 2015; *Menzies et al.*, 2016]. This hydrothermal system is driven by a variety of factors including: abundant rainfall, elevated isotherms and steep topography [*Barnes et al.*, 1978; *Koons and Craw*, 1991; *Sutherland et al.*, 2017], a small component of metamorphic overpressured fluids [*Vry et al.*, 2001; *Craw and Campbell*, 2004; *Menzies et al.*, 2016] and fluctuations in permeability at the Brittle – Viscous Transition [*Upton et al.*, 1995; *Vry et al.*, 2010; *Menzies et al.*, 2014]. A simplified schematic of the fluid behaviour in the Southern Alps is presented in Figure 1.4.

Thermal springs, a result of the elevated geotherm, are common in the fault hanging wall, extending from 1 – 20 km south east of the Alpine Fault [*Allis et al.*, 1979; *Koons*, 1987; *Allis and Shi*, 1995; *Beavan et al.*, 2010]. The influence of seismicity on fluid flow on the fault, and across the Southern Alps, appears substantial, with work by *Cox et al.*, [2015] showing that large distal earthquakes across the South Island of New Zealand, including a M_w 7.8 in south-western Fiordland in 2009 and a M_w 7.1 in eastern Canterbury in 2010, caused variation in temperature and fluid chemistry in a monitored spring in the western Southern Alps, at a distance of 350 km and 180 km respectively.

The fluids within the Southern Alps are dominantly derived from meteoric waters, with a small component of metamorphic fluid [*Vry et al.*, 2001; *Craw and Campbell*, 2004; *Menzies et al.*, 2016]. Magmatic fluids do not feature in the Alpine Fault zone as there have been no large scale igneous intrusions into the hanging wall Alpine Schists and there are no known magma repositories at depth beneath the fault.

1.6.3. The Deep Fault Drilling Project

In order to study the Alpine Fault at depth at in situ conditions away from surface weathering and processes, and to provide a continuous transect across the Alpine Fault rock sequence, the Deep Fault Drilling Project (DFDP) was initiated. DFDP is an ongoing international effort, being undertaken in order to provide insight into the current geological and seismological state of the Alpine Fault. DFDP has currently performed two phases of drilling operations, sampling the Alpine Fault lithologies including the principal slip zone of the fault, performing down-hole observations and installing sensors for long term in situ

monitoring. Both phases of drilling took place in the central section of the Alpine Fault with the first, DFDP-1, taking place at Gaunt Creek, a tributary to the Wanganui River, and the second, DFDP-2, taking place in the Whataroa River valley (see Figure 1.5B). An account of the drilling operations and findings of DFDP is detailed in Section 2.2 of this thesis.

1.6.4. The lithologies of the Alpine Fault and the nature of the alteration zone

The sequence of lithologies present in the Alpine Fault Zone can be divided into five main groups; protoliths, mylonites, cataclasites, ultracomminuted gouges and pseudotachylytes. This section provides a brief review of these lithologies based on previous work in the region. Figure 1.5A shows the broad geological terranes present in the South Island, New Zealand and Figure 1.5B showing the main focus of this thesis, the central section of the Alpine Fault. A schematic cross-section of the Alpine Fault lithological sequence is also illustrated in Figure 1.6 after *Norris and Cooper*, [2007].

1.6.4.1. Protoliths

The basement terranes of New Zealand can be divided into two main groups, the Western Province and the Eastern Province, broadly separated by the Alpine Fault trace across the South Islands west coast, as shown in Figure 1.5 [*Sutherland*, 1999b]. Within the central section of the Alpine fault, the area that is the focus of this thesis, the fault is bounded to the southeast by metamorphosed metasediments and to the northwest by a number of formations belonging to the Western Province, including: Palaeozoic granites and gneisses, metasediments and Cretaceous granitoids [*Muir et al.*, 1998; *Toy*, 2007].

The predominant lithology in the Eastern Province group is the Haast schists, derived from a variety of sediments including volcanoclastic greywacke and argillite, transitioning into pelitic schists, metacherts and mafic metavolcanics [*Mortimer and Roser*, 1992]. These rock types were metamorphosed and deformed during the Mesozoic, forming the Otago Schist and Alpine Schist subgroups within the Haast Schist [*Mortimer*, 2000], with the Alpine Schists as the main protolith lithology of fault lithologies in the central Alpine Fault. The Alpine Schists are quartzofeldspathic schists grading from greenschist facies (quartz – albite – muscovite – chlorite) to amphibolite facies (biotite – albite – oligoclase – garnet) with proximity to the fault, with estimated burial depths of ~40 km in the Mesozoic

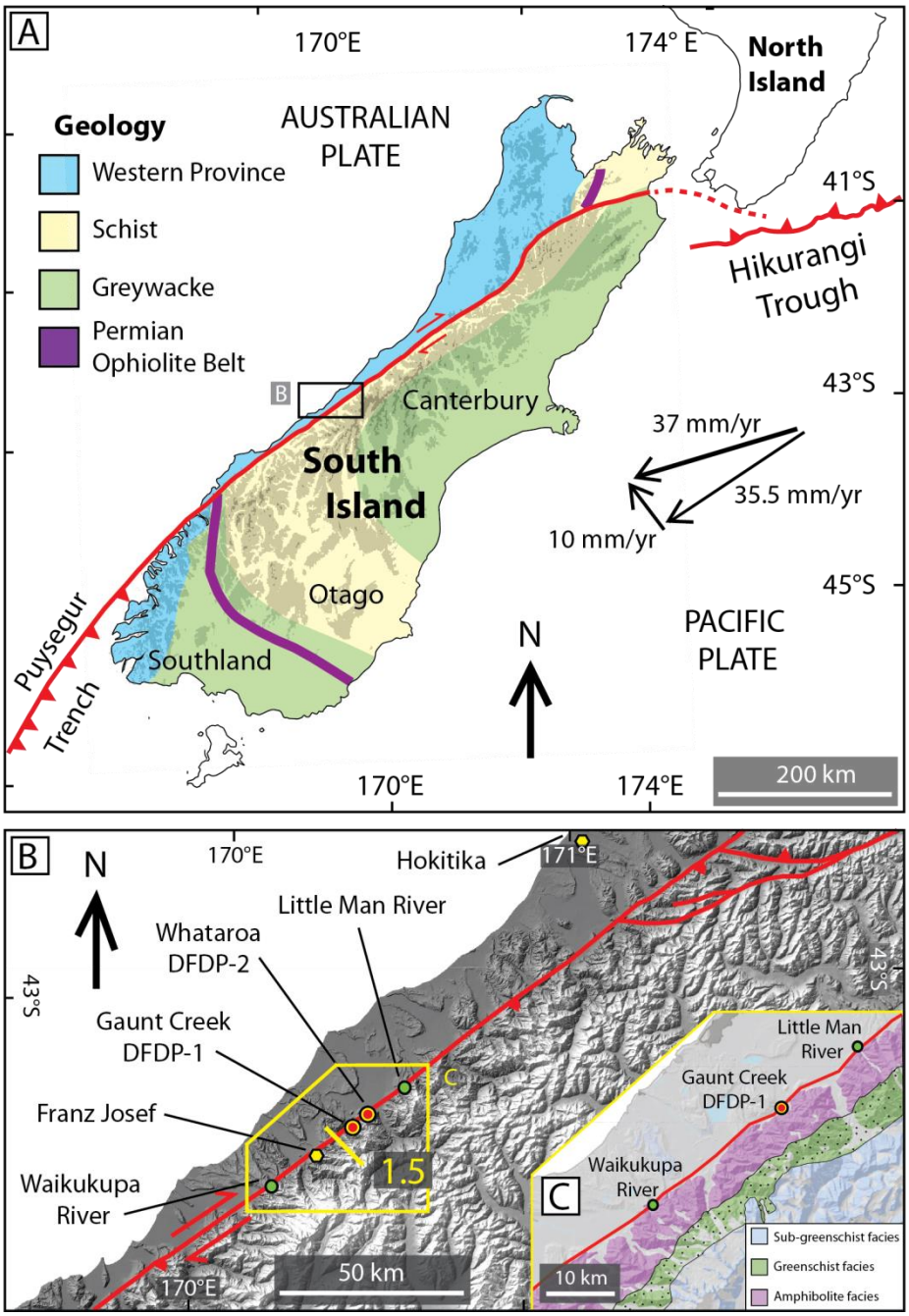

Figure 1.5 – [A] *Generalized geology map of South Island, New Zealand with the main features of the Australian – Pacific plate boundary, including Alpine Fault, Puysegur trench, and Hikurangi trough, adapted from Norris and Cooper, [2003]. Arrows show the interplate velocity vector of the South Island and its components parallel and perpendicular to the Alpine Fault (Nuvel 1A; DeMets et al., [1994]). Shading, light grey >800 m and dark grey >1800 m elevation.* ***[B]*** *A digital elevation model (DEM) image of the central South Island highlighted in (**A**) [Barth et al., 2013]. The location of the Alpine Fault is shown with locations of the DFDP-1 and DFDP-2 drill sites and sites where field specimens were collected are marked.* ***[C]*** Metamorphic facies map after [*Menzies et al.*, 2014].

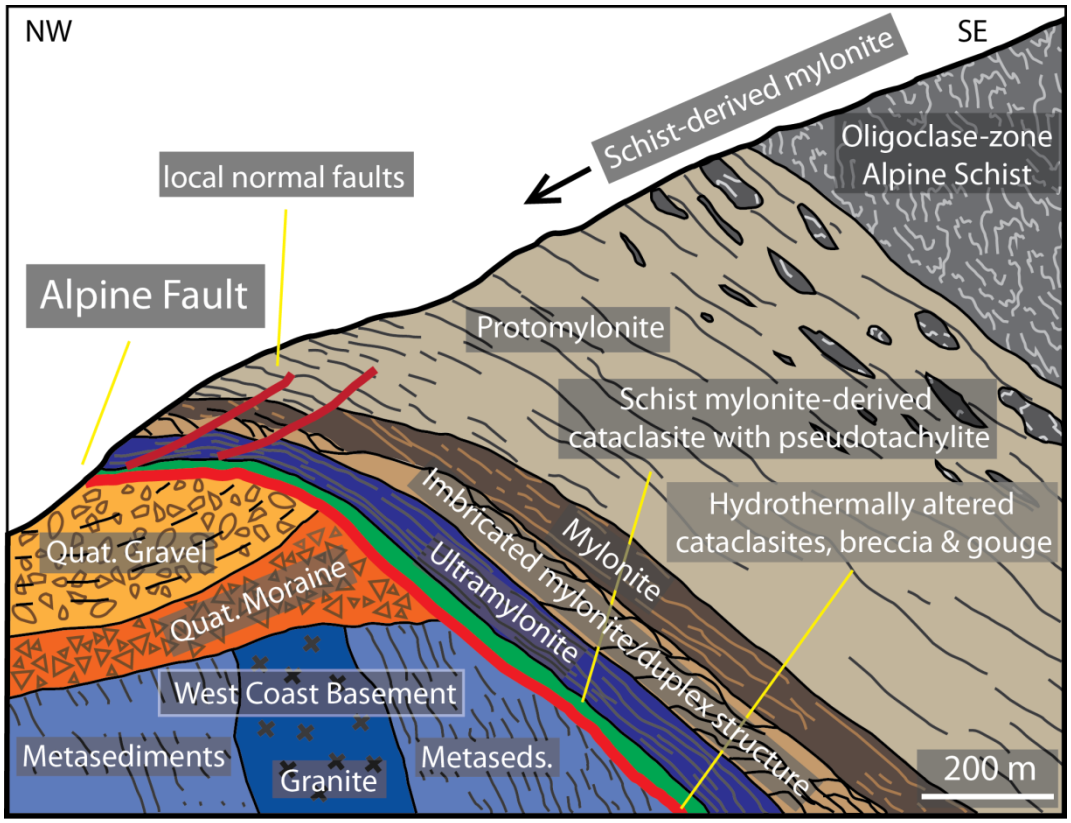

Figure 1.6 – *Schematic cross-section of an oblique thrust segment within the central section of the Alpine Fault, section line highlighted in Figure 1.5B, adapted from Norris and Cooper, [2007].*

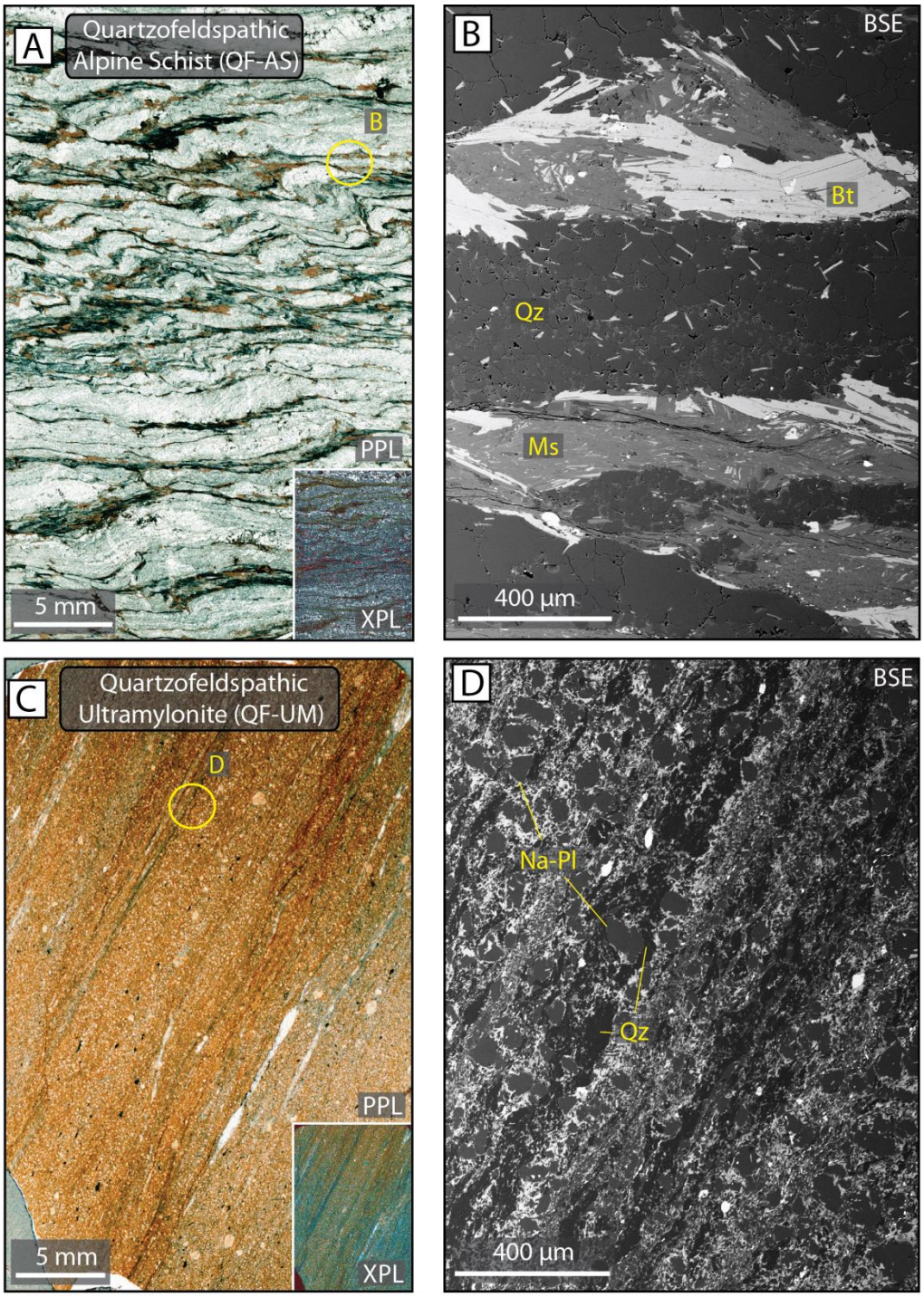

Figure 1.7 – [A and B] *Quartzofeldspathic Alpine Schist (QF-AS), the protolith for many of the mylonite sequence rock in the Alpine Fault hanging wall.* ***[C and D]*** *Quartzofeldspathic ultramylonite (QF-UM) derived from the QF-AS, one of the most common mylonite sequence rocks in the Alpine Fault hanging wall.*

[*Grapes and Watanabe*, 1992]. Intercalated within the Alpine Schist are bands of metabasic and metachert lithologies forming limited horizons within the hanging wall sequence. Figure 1.7 shows the characteristic textures and microstructures of the Alpine Schist and Table 1.1 details the typical mineralogies of the hanging wall protolith schists.

1.6.4.2. Mylonites

Mylonites are foliated rocks that have undergone considerable deformation within high strain zones at conditions favourable for the viscous deformation of their constituent minerals. Viscous deformation may result in grain size reduction (through dynamic recrystallisation during dislocation creep, for example) and the generation of strong, planar fabrics which, if present, wrap around porphyroclasts of resistant minerals, usually garnets and feldspars. The mylonite classification used most widely for the Alpine Fault is based on percentage of matrix material compared to porphyroclasts [*Sibson*, 1977; *Schmid and Handy*, 1991; *Scholz*, 2002], in which rocks with 10 – 50 % matrix are classified as protomylonites; those with 50 – 90 % matrix as mylonites and those over 90 % as ultramylonites. Pre-mylonitic schist structures are retained in protomylonites and are not preserved in mylonites and ultramylonites.

The hanging wall mylonites derived from the Alpine Schist can be divided into four, broad sub zones transitioning from the non-mylonitic schist to protomylonites, mylonites and ultramylonites, as established by *Norris and Cooper*, [2003]**.** These mylonites have been studied extensively since their first description by *Reed*, [1964] and comprise a 1 – 1.5 km thick zone to the southeast of the fault, in which the ultramylonites compose ~150 m thick zone in closest proximity to the fault, with the upper ~500 – 600 m comprised of progressively less deformed mylonites to protomylonites that preserve Mesozoic fabrics [*Little et al.*, 2002a, 2016; *Norris and Cooper*, 2007; *Toy et al.*, 2012, 2013].

These mylonites are again similarly intercalated with metabasic, metachert and metapelitic lithologies though are dominantly quartzofeldspathic in composition. An example of a quartzofeldspathic mylonite is shown in Figure 1.7C and Table 1.1 details the typical mineralogies of the various hanging wall mylonite sequence lithologies.

Alpine Schist		Mylonites	
Lithology	**Mineralogy**	**Lithology**	**Mineralogy**
Quartzofeldspathic schist [Campbell, 2002]	Qz + Pl + Ms + Grt + Bt + Ilm + Ap ± Chl ± Ep ± Gr ± Rt ± Zrn	Quartzofeldspathic mylonite [Toy, 2007]	Qz + Pl + Bt ± Ms ± Gr ± Chl ± Ep ± Cal ± Spn ± Ap ± sulfides ± Gr ± Tur ± Zrn
Metabasic schist [Campbell, 2002]	Hbl + Pl + Bt + Grt + Ttn + Czo + Ap + Opq ± Qz ± Ms ± sulphides	Metabasic mylonite [Prior, 1988]	Hbl + Pl + Qz + Ilm + Ttn ± Grs Grt ± Ep ± Cal ± Ank ± Chl ± Bt if transitional to pelite
Metachert schist [Cooper, 1970]	Qz + Grt (often Sps) ± Ab ± Ms ± Bt ± Rt ± Ttn ± Chl ± Ap ± Mag ± Opq	Metachert mylonite [Prior, 1988]	Qz ± Ms ± Sps Grt ± Pl ± Bt ± Ilm

Table 1.1 – *Mineralogies of the schist and mylonite protoliths for the Alpine Fault ultramylonites / cataclasites and gouges analysed in this thesis [Cooper, 1970; Prior, 1988; Campbell, 2002; Toy, 2007].*

1.6.4.3. Pseudotachylytes

Pseudotachylytes, a fine-grained, cohesive, sometimes glassy but often devitrified, fault rock that generally occurs as veins, are thought to be derived from frictional heating along fault planes producing melt [*Magloughlin and Spray*, 1992]. Numerous studies have been undertaken on Alpine Fault pseudotachylytes, first described by *Reed*, [1964] with further, more recent work by *Sibson et al.*, [1981] and *Toy et al.*, [2011] documenting their occurrence across the entire Alpine Fault rock sequence. A more comprehensive description on these features and their occurrence in the study area can be found in *Chapter 5* of this thesis.

1.6.4.4. Cataclasites and gouges

Fault rocks derived from brittle processes can be divided into incohesive and cohesive sub-groups. Incohesive brittle fault rocks can be further subdivided into incohesive breccias, incohesive cataclasites and fault gouge with breccias containing >30 % visible fragments of >2 mm diameter; cataclasites containing 50 – 90 % matrix of <0.1 mm diameter and fault gouge containing <30 % visible fragments of >2 mm diameter [*Woodcock and Mort*, 2008]. These incohesive brittle fault rocks are commonly associated with shallow crustal levels, while material generated at greater depths becomes increasingly cohesive. Cohesive brittle

fault rocks are subdivided into cohesive breccias, cohesive cataclasites and pseudotachylytes. This cohesion is due to the cementation of brittle fault rocks by precipitation of secondary minerals such as calcite, quartz, epidote and chlorite, and, if fluid infiltration is limited and the precipitating solution is highly alkaline, K-feldspar may form [*Wintsch*, 1975; *Wintsch et al.*, 1995; *Passchier and Trouw*, 2005].

Cataclastic rocks within the Alpine Fault Zone occur throughout the mylonites as breaks in the fault rock sequence by subsidiary faulting [*Reed*, 1964; *Sibson et al.*, 1981]. The transition from mylonitic to cataclastic rocks was further investigated by *White and White*, [1983] who attributed the generation of these features to the cyclic operation of brittle and viscous mechanisms with accompanying pervasive retrogressive alteration. Within the central Alpine Fault Zone *Cooper and Norris*, [1994] described the cataclasites immediately above the Alpine Fault at Gaunt Creek as being composed of a sequence of ultracataclasite, cataclastic mylonite and pseudotachylyte transitioning into intact mylonite. This sequence comprises the lithologies sampled during the Deep Fault Drilling Project Phase 1 (DFDP-1) and is the focus of this study; Table 1.2 outlines the main lithologies sampled during DFDP-1 and the nomenclature that will be used throughout the thesis.

1.6.4.5. Retrogression and alteration within the Alpine Fault cataclasites

In the hanging wall of the Alpine Fault, overprinting the fault core and the transition into the damage zone, is a distinct ~20 to 30 m thick zone of hydrothermally altered rock, containing elevated concentrations of hydrous alteration minerals and cements (phyllosillicates and carbonates) [*Sutherland et al.*, 2012; *Townend et al.*, 2013; *Toy et al.*, 2015b; *Boulton et al.*, 2017a].

This alteration takes the form of retrograde mineral assemblages as first outlined by *Warr and Cox*, [2001] and further explored by *Toy et al.*, [2015] and *Boulton et al.*, [2017a]. This alteration is understood to occur during exhumation from sub-greenschist facies conditions, with the first occurrence of retrogressed minerals within the ultramylonites ~ 30 m above the principal slip zone (PSZ). The extent of alteration increases with proximity to the PSZ within hanging wall cataclasites. *Warr and Cox*, [2001] identified two stages of chemical alteration. The first stage occurs at conditions near or at the Brittle – Viscous Transition in which non-oxidised metasomatic alteration reactions at <400 °C replace

feldspars with muscovite, sericite or sausserite, while biotite (phlogopite), epidote and actinolite react to form chlorite (clinochlore) via hydrous chloritization, see Figure 1.8C. A second stage of alteration occurs at temperatures of <120 °C. This, depending on redox conditions, alters primary minerals such as chlorite, albite / feldspar and muscovite to kaolinite, smectite and/or pyrite or smectite, kaolinite, Fe-hydroxide (goethite) and/or carbonate (see Figure 1.8A and B) [*Warr and Cox*, 2001; *Boulton et al.*, 2017a]. *Boulton et al.*, [2017a] identified the presence of low temperature clay minerals montmorillonite and kaolinite in the PSZ gouges of the fault, and inferred that the gouges are the most altered rock within the fault core. This degree of alteration found in the fault core has been attributed to cyclical, seismically induced fracture damage and comminution facilitating the infiltration of fluids into the fault, promoting fluid-rock interaction, resulting in carbonate and phyllosilicate precipitation and the gradual reduction of fault porosity and permeability [*Boulton et al.*, 2017a].

Lithologic Unit	Name	Description	Dominant Microstructures	Grain Size (mm)	Mineralogy
Unit 1	Grey and dark green ultramylonites	Planar-foliated mylonite to ultramylonite	Segregations of Qz + Pl and Ms + Bt ± Ep ± Chl with locally abundant Pl-augen trains, mm-spaced continuous foliation	>0.03 – >1	Qz + Pl + Bt + Ms ± Cal ± Amp ± Ep ± Chl ± Ilm ± Ttn
Unit 2	Brown-green-black ultramylonites	Planar-foliated ultramylonite	Indistinct mm-spaced foliation defined by opaque seams and parallel mica grains which form a locally dilatant disjunctive cleavage; Pl-augen common	<0.05 – <0.2	Qz + Pl + Bt + Ms ± Chl ± Cal ± Ep ± Amp ± Ilm ± Ttn
Unit 3	Upper unfoliated cataclasites	Unfoliated cataclasites derived from Units 1 and 2	Angular clasts of Units 1 and 2 in a variably calcite-cemented ultrafine-grained matrix (<0.1 mm grains)	<0.01 – <0.1 with <100 clasts	Qz + Pl + Bt + Ms ± Chl ± Cal ± Ep ± Amp ± Ilm ± Ttn
Unit 4	Upper foliated cataclasites	Foliated cataclasites derived from Units 1-3	Foliation defined by micro-shears, anastomosing seams of opaques, and/or locally aligned phyllosilicates; e-twinned veins and clasts of calcite	<0.01 – <0.1	Qz + Pl + Ms + Chl ± Cal ± Bt ± Ep ± Amp ± Ilm ± Ttn
Unit 5	Gouges	Cemented to uncemented gouges with variable mineralogy	Predominantly random fabric with rare locally aligned phyllosilicates; e-twinned calcite clasts; gouge and cataclasite clasts common	<0.001 – <0.01	Qz + Pl + Ms + Chl + Cal ± Ksp ± Sme(Mnt) ± Kln ± Gth ± Mn ± Ilm ± Ttn ± Zrn ± Ap
Unit 6	Lower cataclasites – *divided into 4 subunits*	6a- white to cream-colored ccl with granitoid and gneissic clasts; 6b- greenish grey foliated protocataclasite; 6c- greenish grey to black ultracataclasite to gouge with gneiss, Qz-Pl- Fsp, and rare mylonite clasts; 6d- a mixture of 6a - 6c.	6a - random fabric, granitoid clasts contain myrmekite and antiperthite textures, gneissic clasts contain ribbon Qz; 6b - foliations comprise muscovite and chlorite; 6c - random fabric; 6d - interlayered mixture of 6a - 6c containing numerous micro to mesoscale faults	<<0.03 – >>0.1	Qz + Ksp + Pl + Ms ± Bt ± Chl ± Zrn ± Ap ± Ttn
Unit 7	Breccias	Protocataclasite to breccia composed of black mylonite-gneiss clasts	Remnant mylonitic-gneissic foliation with Pl-augen or Qz segregations; phyllosilicate foliations wrap porphyroclasts	<1 – >10	Qz + Ksp + Pl + Ms + Bt + Chl + Ep + Ap + Ttn + Gr
Unit 8	Gravels	Quaternary gravels composed primarily of Alpine Schist clasts	Locally imbricated	0.25 – >10	Qz + Pl + Bt + Ms ± Cal ± Amp ± Ep ± Chl ± Ilm ± Ttn

Table 1.2 – *Description of the lithological units recovered in DFDP-1, modified from Toy et al.*, [2015] and *Boulton et al.*, [2017].

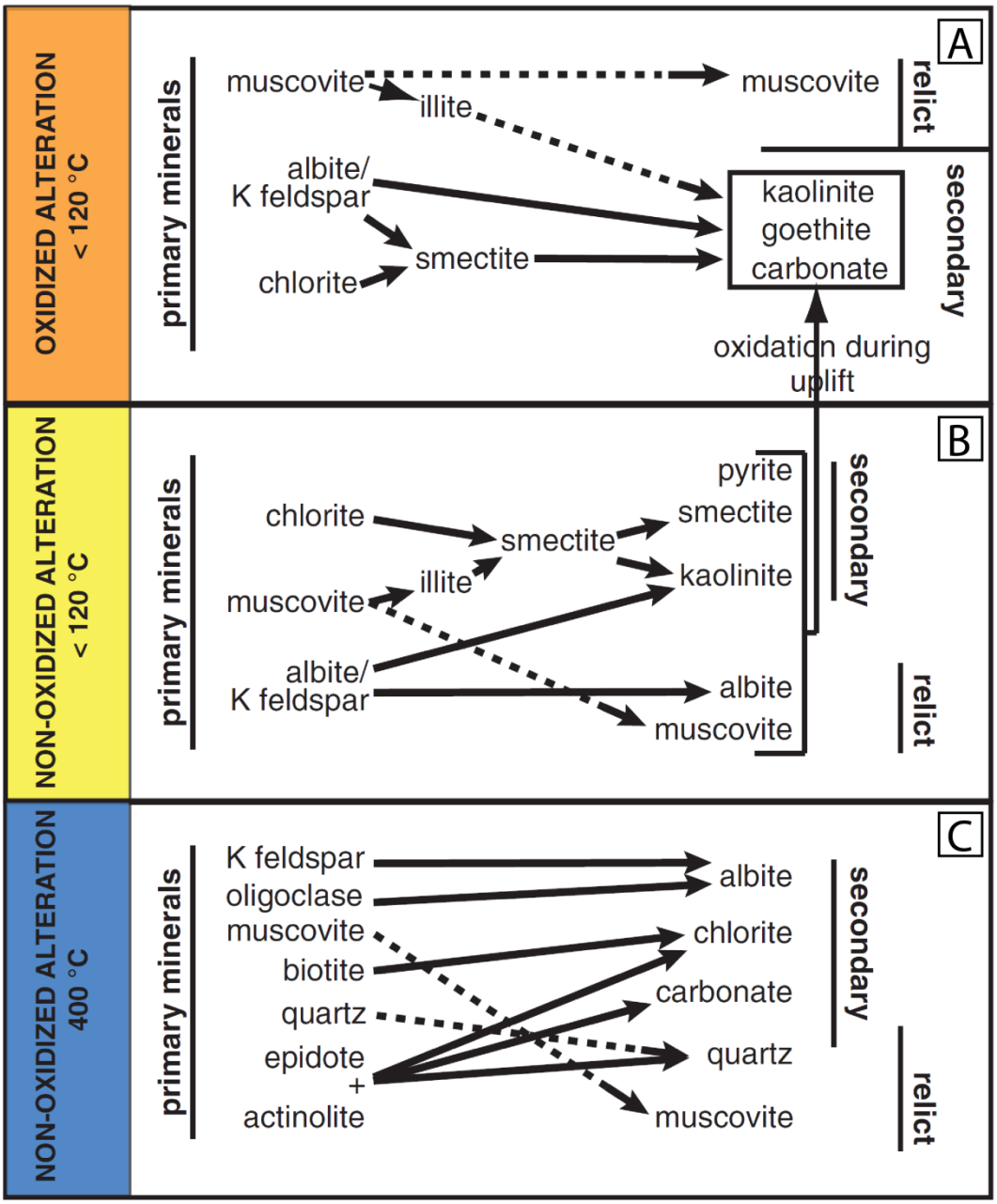

Figure 1.8 *– Retrogressive reactions occurring in the Alpine Fault alteration zone, after Boulton et al., [2017]. As the Alpine Fault cataclasites and gouges have been exhumed from subgreenschist facies conditions they have undergone multiple phases of alteration. Primary nonoxidized and oxidized alteration reactions are outlined, after Chamberlain et al., [1999] and Warr and Cox, [2001].*

1.7. Thesis aims

The behaviour and nature of faults is a product of a variety of interrelated factors that can be divided into three main aspects: fault structure, fluid flow and mechanics, with a number of sub-factors, all feeding into the umbrella term of "fault zone composition" [*Faulkner et al.*, 2010] (Figure 1.9). The research reported in this thesis is focused on fluid-rock interactions and fluid flow on faults and on related sub-topics of permeability, alteration reactions and mode of failure. Insight on such factors was gained through investigation of the physicochemical processes that occur within rock from core of the Alpine Fault Zone, with the following aims:

1 – To constrain the interseismic permeability and seismic velocities of the Alpine Fault core experimentally, and investigate the extent and causes of physical property anisotropy in heavily cataclased and altered fault rock, exploring potential implications on fault zone processes.

2 – To investigate the sealing behaviour of fracture damage generated during seismicity within the Alpine Fault core by constraining fracture generation mechanisms, fluid-rock interactions and mineral precipitation processes through quantitative microstructural and fine-scale, spatially resolved, geochemical analyses.

3 – To investigate the occurrences of frictional melt and nanoparticulates within the Alpine Fault fault core / alteration zone by examining their setting, extent of cataclastic reworking, chemical alteration and/or preservation through the many seismic cycles of the Alpine Fault.

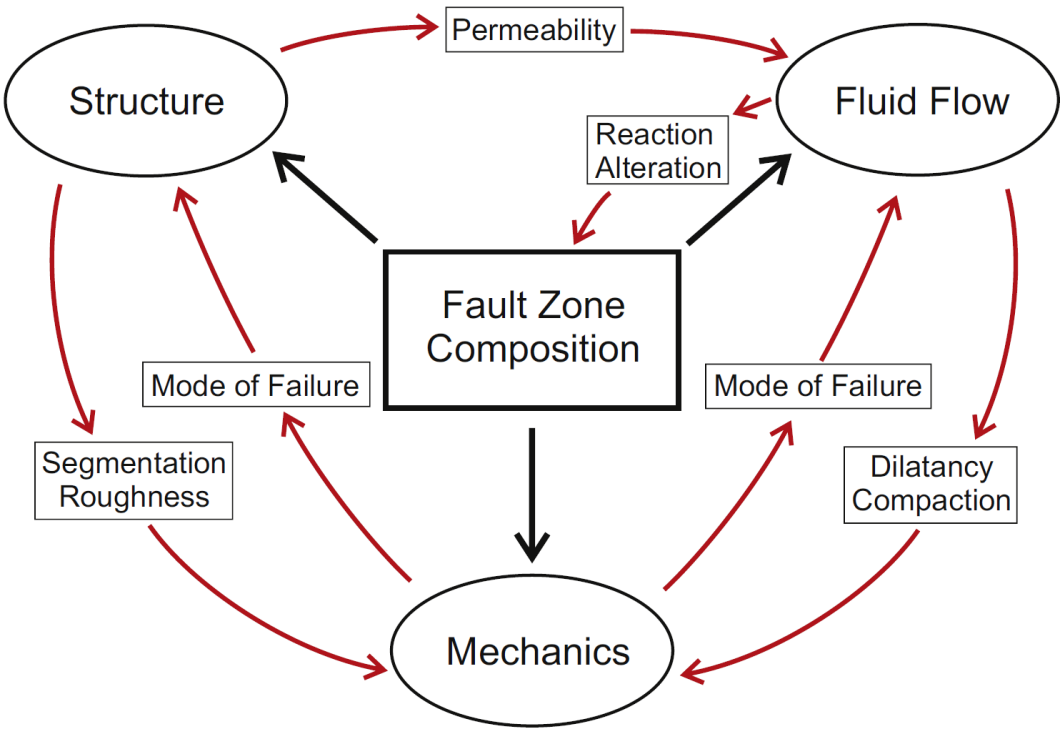

Figure 1.9 – *Flow diagram showing the inter-relationships among the three main aspects of structure, mechanics and fluid flow. Mode of failure refers to whether or not seismic slip occurs or not. The focus of this thesis is in fluid flow and its related sub-topics of permeability, reaction alteration and mode of failure. Diagram after Faulkner et al.*, [2010].

2. Methods

2.1. Introduction

This chapter details all techniques and methods utilised during the course of this project. These include the drilling operations of the Alpine Fault Deep Drilling Project Phase 1 and Phase 2 (DFDP-1 and DFDP-2); sample preparation techniques for fragile drill core material; the experimental apparatus and procedures used for the measurement of fault rock physical properties; and the analytical equipment and methods used for microstructural and geochemical investigations of deformation microstructures.

All drilling operations aiming to sample the Alpine Fault Zone (AFZ) took place in Westland, South Island, New Zealand through the combined efforts of a multinational team of scientists, see Figure 2.1. Seismic velocity and permeability measurements were undertaken using a triaxial high pressure apparatus and ultrasonic seismic sample assembly in the Rock Deformation Laboratory, at the University of Liverpool. All microstructural observations were performed in the Electron Microscopy Laboratory (Liverpool Earth Sciences) using a Camscan X500 CrystalProbe and Philips XL30 Scanning Electron Microscopes (SEM) for Electron Backscatter Diffraction (EBSD) and Energy Dispersive Spectroscopy (EDS). Optical Cathodoluminescence (CL) analyses were undertaken at the University of Liverpool's Central Teaching Laboratory. Secondary Ion Mass Spectroscopy (SIMS) was performed at the University of Edinburgh's NERC Ion Micro-Probe Facility using a Cameca IMS-4f for trace element analyses and a Cameca IMS-1270 for stable isotope analyses. X-ray Computed Tomography (CT) was performed at the Delft University of Technology, Netherlands by Ludmila Adams and Auke Baarnhorn (University of Auckland, New Zealand and Delft University of Technology). Quantitative evaluation of minerals by scanning electron microscopy (QEMSCAN®) analyses were performed at the Intellection Pty Ltd, Milton, Australia by Alan Butcher (Intellection Pty Ltd). All mineral abbreviations used in this thesis are after *Whitney and Evans*, [2010].

2.2. Drilling operations

The only way to determine ambient conditions directly, measure physical and chemical properties in situ and collect geological material away from surface weathering effects is

Figure 2.1 – [A] *Drill site of DFDP-1 at Gaunt Creek, a tributary to the Wanganui River, Westland, South Island, New Zealand, photo courtesy of E. Mariani.* ***[B]*** *Drill site of DFDP-2 in the Whataroa River valley, Westland, South Island, New Zealand, photo courtesy of J. Thompson.*

through scientific drilling. Drilling programs have been performed on a number of active fault zones globally, usually after the occurrence of a large magnitude earthquake. Some major examples are the drilling projects that took place on the Tohoku-Oki fault and Nojima fault, Japan after a M_w 9.1 and 6.9 earthquake; the Chelungpu fault, Taiwan after a M_w 7.7 earthquake; the Wenchuan fault, China after a M_w 7.9 earthquake and on the creeping section of the San Andreas Fault, USA [*Fulton et al.*, 2004, 2013; *Ma et al.*, 2006; *Kitagawa et al.*, 2007; *Xue et al.*, 2013].

In regard to the Alpine Fault, the Deep Fault Drilling Project (DFDP) is an ongoing international effort, undertaken in order to provide insight into the current geological and seismological state of a plate boundary fault thought to be nearing the end of its latest interseismic state [*Townend et al.*, 2013]. The broad science objectives of DFDP include determining how and why earthquakes happen and how slip occurs on a large scale tectonic boundary, investigated through borehole collection of rock, fluid and gas samples, diverse down-hole observations and the installation of sensors for long-term in situ monitoring. The long-term strategy of DFDP is to drill to progressively greater depths along the exhumation trajectory of the Alpine Fault in order to identify how the ambient conditions and processes change on the fault with depth. While the drilling operations planned so far have been completed, there are plans to continue this multinational project in the future.

The first phase of the Deep Fault Drilling Project (DFDP-1) comprised two vertical pilot holes (DFDP-1A and DFDP-1B) drilled into an active thrust segment of the Alpine Fault Zone (AFZ) at Gaunt Creek, Westland in January – February 2011. For locations of drill sites see Figure 1.5 and Table 2.1. The boreholes reached depths of 100.6 m and 151.4 m, respectively, through percussion drilling in the upper borehole sections followed by wireline coring. A range of fault lithologies from both the hanging wall and footwall were recovered including ultramylonites, cataclasites and gouges. The Principal Slip Zone (PSZ) of the Alpine Fault Zone was reached at 90.74 m depth in DFDP-1A and 128.3 m in DFDP-1B, marking the boundary between the Australian and Pacific Plates, with a second PSZ recorded in DFDP-1B at 143.85 m [*Toy et al.*, 2015b]. Both slip zones are composed of clay-rich gouge [*Sutherland et al.*, 2012]. For full details on sampling in DFDP-1 see Table 2.2. Once core collection, wireline logs and hydraulic observations were completed a downhole

observatory was installed to monitor seismicity, temperature, fluid pressure and chemistry [*Sutherland et al.*, 2012; *Carpenter et al.*, 2014].

The drilled core diameter was 85 mm (PQ wireline bit size) and supplied for sample preparation as 200 – 300 mm length intact core rounds and half rounds. These core sections were oriented with respect to the borehole axis, however due to core rotation during retrieval the horizontal orientation could not be preserved [*Sutherland et al.*, 2011; *Toy et al.*, 2015]. Subsampling of material recovered in DFDP-1 for this thesis was performed by supervisors Elisabetta Mariani, Daniel Faulkner and Daniel Tatham using detailed core logs and individual observations.

Findings from the DFDP-1 drilling operations combined with finite element models, LIDAR studies on river terraces [*Barth et al.*, 2012; *Langridge et al.*, 2014] and a 640-channel seismic-reflection survey [*Lay et al.*, 2016] informed the decision to perform the second phase of drilling in the lower Whataroa valley, see Figures 1.3, 1.5 and Table 2.1 for location information. This site was further investigated with a 96 – channel (stacked hammer source) seismic line, a gravity survey and potentiometric groundwater survey in order to confirm the location of the fault, the thickness of the overlying sediment and the elevation of the unconfined water table surface. These pre-drilling analyses concluded with the aim to intersect the fault at ~1 km depth, with a target total depth of 1.3 km and a contingency to reach 1.5 km. Initially destructive drilling was to take place through Holocene river gravel (estimated depth 0 – 8 m), post-glacial pebbly gravel containing cobbles and boulders (est. 8 – 80 m), cohesive silt with interbedded sand or gravel layers containing scattered cobbles or boulders (est. 80 – 100 m) and Alpine Schist and mylonite (est. 100 – 950 m). Coring of the brittle fault rock sequence, as detailed in the Section 1.6.4 of this thesis, was estimated to occur at 950 – 1000 m sampling both the hanging wall and footwall damage zone / fault core. The footwall protolith lithologies (est. 1000 – 1300 m) composed of fractured granite, gneiss, and metaquartzite were also marked for sampling due to the poor exposure of these rocks at the surface northwest of the fault [*Sutherland et al.*, 2015].

As the primary objectives of the drilling project lay in the bottom ~500 m of the borehole the following goals were set out for the project [*Sutherland et al.*, 2015];

1. Grout (full annulus) steel casing in place to secure the borehole above 800 m depth.
2. Collect core with minimum diameter 61 mm (HQ3 bit size), ideally 83 mm (PQ bit size), via triple-tube wire-line to below 800 m.
3. Use wire-line geophysical tools to log the open borehole (as completely as possible).
4. Make hydraulic/stress observations using a downhole packer tool.
5. Install permanent instruments to create a fault zone observatory.

DFDP – Borehole locations		
DFDP-1A	Latitude, longitude (WGS84)	43.316031°S, 170.325925°E
	NZTM coordinates	1383121.61 m east, 5200611.2 m north
DFDP-1B	Latitude, longitude (WGS84)	43.315886°S, 170.326657°E
	NZTM coordinates	1383221.7 m east, 5200621.3 m north
DFDP-2A	Latitude, longitude (WGS84)	43.29065°S, 170.40661°E
	NZTM coordinates	1389611.5 m east, 5203642.6 m north
DFDP-2B	Latitude, longitude (WGS84)	43.29065°S, 170.40646°E
	NZTM coordinates	1389599.2 m east, 5203641.9 m north

Table 2.1 *– Location information for the phases of the Deep Fault Drilling Project (DFDP) detailed in this thesis.*

2.2.1. Deep Fault Drilling Project-2: onsite operations summary

Drilling operations for DFDP-2 took place from August 2014 to January 2015 and involved an international group of seventy one scientists along with the drilling team and support staff. Prior to the start of drilling the thesis author attended a course on drilling operations and technology run by the International Ocean Drilling Programme (IODP) and held in Franz Josef, South Island, New Zealand. Afterwards work began in the Whataroa valley drilling site with the author taking part in the full duration of the drilling operations. Work was organised in shifts running 24/7. The author's contribution, including a team-leading role in the preparation of thin sections, is described in detail in Section 2.2.2. Throughout the drilling operations the following data sets were collected: drill rig data, wireline geophysical observations, geological sampling and observations, gas sampling and observations, mud sampling and observations and seismological observations.

Two phases of drilling took place for the first bore hole, DFDP-2A. The first phase consisted of drilling and casing through the Quaternary sediments to provide a stable platform for deeper operations into the bedrock. A *Washington drill rig* using dual rotary air or water drilling was used during the installation of a 12" welded casing to 29 m followed by 10" welded casing to 126 m depth, with a total depth of 212.6 m reached. DFDP-2A was abandoned as drilling large boulders alternating to fine till in fluvial and glacial deposits proved challenging. To optimise chances of success it was decided larger casing was required in the upper bore hole to drill more effectively to further depths.

DFDP-2B was located ~12.5 m to the east of DFDP-2A with the *Washington drill rig* used to install 16" welded casing to 78 m, open hole drilling at 14" was performed to 197 m followed by the installation of 12" welded casing to 237 m after which 10" welded casing was installed and seated to bedrock at 243 m and continued down to 264.93 m. A 9.5" open hole was drilled to 275.91 m to ensure the bedrock had been reached. The second phase of drilling in the DFDP-2B borehole was conducted with a *Hanjin D&B-45D* using tungsten carbide bits with water / drilling mud lubricant. The aim was to perform 8.5" open hole drilling in order to rapidly progress to the region of interest, followed by the installation of Anchor Casing and then by wireline coring. However, due to technical problems this stage of drilling did not go to plan with 8.5" drilling and casing continued to 893.2 m (818 m true vertical depth) after which drilling ceased.

The technical problems encountered during the project included: deviation of the borehole, with a spontaneous tilt of <4° by 275 m, increasing to 12° by 121 m, to 21° by 526 m and then to 44° by 893.2 m depth. The bottom hole assembly (BHA), which consisted of the drill bit and stabilizers, was lost and recovered on two separate occasions postponing operations; and finally a failure in the thread-coupling between casings at 436 m and 439.6 m resulted in the loss of the borehole, due to cement flooding the hole during the grouting of casing. A combination of the above problems resulted in the cessation of drilling operations. The deviation of the borehole was attributed to the heavily foliated schist-protomylonite sequence which was proposed to be leading the drilling equipment away from vertical, while the loss of the BHA and casing failure were attributed to mechanical failure of equipment. A full report on the DFDP-2 operations is available in *Sutherland et al.*, [2015].

2.2.2. Observations and findings of Deep Fault Drilling Project-2

Although the drilling project failed to achieve some of its intended goals, sample collection and observations were performed throughout the duration of the project. Sampling of the boreholes in the form of rock cuttings, cores, drilling mud and gas extracted from the drilling mud were performed during drilling. Full details on sampling depths and intervals are shown in Table 2.2. During breaks in drilling, wireline observations were performed in the borehole fluids and on the borehole walls prior to casing installation. These included: fluid temperature and conductivity, flow measurement, natural / spectral gamma rays, magnetic susceptibility, electrical induction, full waveform sonic logs, calliper diameter measurements (3 arms) and acoustic borehole imaging. For details on tool specifications see *Sutherland et al.*, [2015].

The author of this thesis spent 52 days on the DFDP-2 drill site, aiding in the construction of the 'science block' which comprised of four shipping containers housing a gas lab, a geophysical logging facility, a thin section lab and a *DMT* core scanner / photography lab. The author worked principally as part of a team focused on the collection, preparation and analysis of rock cuttings during the drilling operations. This role involved the preparation of high quality thin sections in a short period of time in order to keep up with the rhythm of drilling and the recovery of cuttings. These thin sections were then analysed through optical microscopy to inform drilling procedure on the distance to the principal slip zone of the fault, predominantly through the analysis of mylonitic quartz grain size and modal abundances. For full details on this procedure see Section SM 2.7.1. Other tasks fulfilled by the author included crafting thin sections and polished blocks of field specimens during lulls in drilling for comparative work with borehole sampling, optical microscope point analyses of cutting material to determine mica abundance with proximity to the PSZ, field excursions for sample collection as well as taking part in a number of outreach events with local residents and school children.

While core could not be recovered, the main successes of DFDP-2 where in valuable wireline measurements, and the analysis of fluids from mud. This resulted in a high profile publication in Nature regarding the enhanced geothermal gradient observed at depth within the Whataroa Valley attributed to rapid exhumation of the fault and topographic focusing of groundwater, published by *Sutherland et al.*, [2017]. Many more publications

Borehole	Type of sample	Location	Age	Purpose	Total	Depth range (m) Top	Bottom	Spacing (m)	Notes
DFDP-1A	Cuttings	Onsite	Quaternary	Geological description	#	0	9		
	Cuttings	Onsite	Basement	Geological description	#	9	30		
	Core	Onsite	Basement	Geological description	#	31	96		
DFDP-1B	Cuttings	Onsite	Quaternary	Geological description	#	0	19		
	Cuttings	Onsite	Basement	Geological description	#	19	36		
	Core	Onsite	Basement	Geological description		36	46		
	Cuttings	Onsite	Basement	Geological description	#	46	93		
	Core	Onsite	Basement	Geological description	#	93	151.4		
DFDP-2A	Cuttings	Onsite	Quaternary	Geological description	127	0	126	1	
	Fossil	Onsite	Quaternary	Dating	4	58	61.5	0.9	Spacing is an average
	Core	Onsite	Quaternary	Geological description	37	125.5	212.6		
DFDP-2B	Cuttings	Onsite	Quaternary	Geological description	80	0	238.5	3	
	Fossil	Onsite	Quaternary	Dating	24	19.9	238	9.1	Spacing is an average
	Cuttings	Onsite	Basement	Geological description	334	238.5	893.18	2	
	Drilling mud	Onsite	Quaternary and Basement	Geological analyses	153	47	893.2	5.5	
	Fossil	Onsite	Quaternary	Dating	1	235.9	236		
	Core	Onsite	Basement	Geological description	80	437	478.3		Total core length = 32.22 m; Mostly cement
	Cuttings	Onsite	Basement	Thin Section	265	238.5	893.18	4.9	One quartz-rich separate and one whole rock sample at each depth
	Unwashed cuttings	Offsite	Basement	Thin Section or geochemical analyses	22	280.1	893.18		Unwashed cutting samples were mostly only taken when insufficient washed sample was available for the analyses so the depth interval is not systematic.
	Unwashed cuttings	Offsite	Basement	Mechanical tests	4	299	886		299, 814, 866, 886 m.
	Washed cuttings	Offsite	Basement	Thin Section or geochemical analyses	202	243.5	884	3.2	
	Carbonaceous material	Offsite	Quaternary	Dating	23	20	233	9.3	Spacing is an average
	Gas extracted from drill mud	Onsite	Quaternary and Basement	Chemical analysis	36	236	892	18.2	Average spacing; it actually ranges from 0 to 65 m

Table 2.2 *– Complete sampling summary for both phases of the Deep Fault Drilling Project, adapted from Sutherland et al., [2011] and [2015].*

are in preparation regarding the geological and geophysical observations made during both DFDP-1 and DFDP-2.

For more information on both DFDP-1 and DFDP-2 drilling operations see, *Sutherland et al.*, [2011] and *Sutherland et al.*, [2015].

2.3. Sample preparation for experiments and laboratory analyses

Due to the friable nature of many of the recovered lithologies, traditional methods of sample preparation such as water-lubricated coring, sawing and grinding proved catastrophic, causing washout of the finer grain-size fractions and often total disaggregation. Therefore, in order to overcome these challenges AFZ core presented us with, we developed new preparation techniques that could be used to produce high-quality specimens for all experimental measurements, microstructural observations and chemical analyses. These new procedures are described below.

2.3.1. Experimental sample preparation

The experimental measurement of physical properties and permeability required the preparation of 15 x 15 x 15 mm cubic specimens. To obtain suitable specimens AFZ core was first wrapped in thin plastic wrap (to protect it from plaster contamination) followed by the application of three to four layers of modroc® (gypsum plaster bandages). The original core orientation was recorded throughout the wrapping process and once plaster bandages had fully hardened it was scribed onto the final plaster covering. Cutting the material was accomplished through the use of an annular saw (Revolution XT Ring Saw®), see Figure 2.2. The annular saw blade is 5 mm thick with a total diameter of 254 mm and a blade width of 1.5 mm; it is fabricated from pressed powder and diamond ensuring uniform sharpness and hardness throughout the blade lifespan. The configuration of the annular blade means that only the actively cutting portion of the blade is in contact with the sample, reducing grain plucking and disaggregation. Some cooling and lubricating fluid (tap water) is required during cutting; this was applied by a moist sponge to the blade edge. The saw also operates at low revolutions per minute (RPM) and high torque, further improving the quality of the cut.

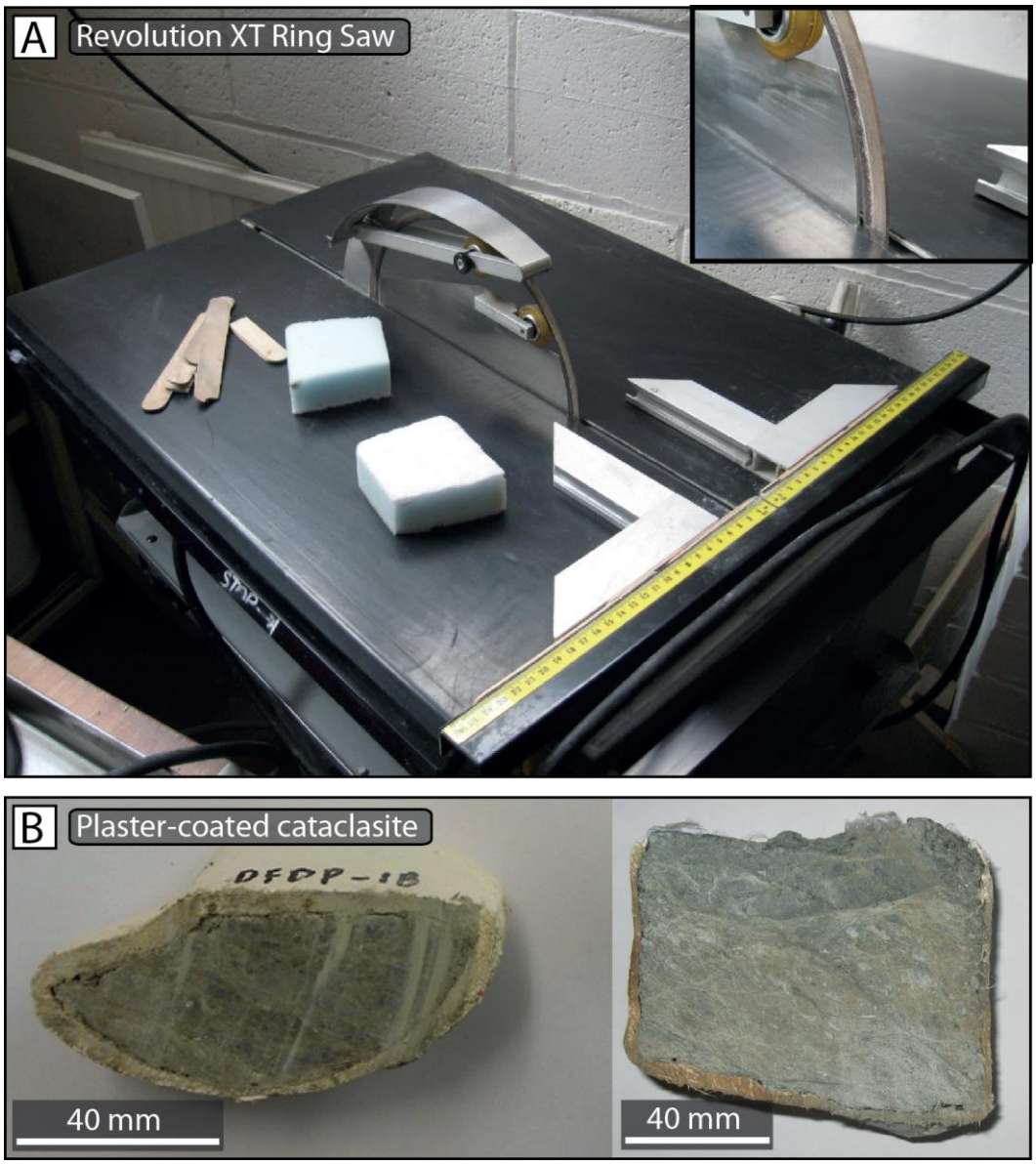

Figure 2.2 – [A] *The Revolution XT Ring Saw, developed by Gemini Saw Company, used in shaping the study specimens. Sponges and wooden shims were used for lubrication and securing sample during cutting.* ***[B]*** *Examples of clean cut surfaces of cataclasites bound in ModRoc® bandages.*

A first cut through the bandaged core exposed a surface that was again covered by plastic wrap and modroc following the above procedure. A second cut perpendicular to the first surface exposed a second face that was then wrapped and the operation was repeated until the required 15 x 15 x 15 mm experimental specimen was produced, unwrapped, mounted in the sample assembly and loaded in the experimental apparatus. The orientation of the vertical borehole axis was transferred on the cubic specimen obtained, which also had two faces orthogonal to the core surface and cut according to any relevant microstructural fabric if present, i.e., foliations, calcite veins and fractures. A final step, if the specimen proved sufficiently robust, involved hand grinding the cube surfaces with dry, fine (2000 grit) emery paper to provide a smooth flat surface to maximise acoustic wave and fluid transmission from the sample assembly to the sample cube.

2.3.2. Thin section preparation

Rock billets for thin sections (of dimensions 20 x 15 x 5 mm) were prepared following the wrapping and cutting procedure described above with a final stage of epoxy impregnation, using a low viscosity epoxy (Buehler EpoThin™) and a vacuum chamber. This was required in order to increase specimen strength for transport to an external thin section workshop. Thin sections were prepared using standard petrographic thin section techniques, if robust enough, using tap water and progressively finer grit size to polish the sample surface to a finish of 0.5 µm alumina grit. Friable material was prepared using 'dry' polishing techniques and was carried out using numerous non-aqueous fluids, a 50:50 mixture of Ethylene Glycol and Methylated spirit for the lapping slurry and a solvent based diamond suspension for polishing. EBSD analyses require a high-quality surface polish which eliminates any residual amorphous layer on the surface of interest; therefore final chemo-mechanical polishing was performed on thin sections using SYTON – colloidal silica consisting of particles of grit size 0.005 – 0.006 µm dispersed in an alkaline solution. Depending on the mineral under investigation SYTON polishing time varied; calcite was polished for 20 minutes while quartz and feldspars were polished for 2 hours. SYTON polishing was conducted at the Electron Microscopy Laboratory (Liverpool Earth Sciences) and thin sections made by Paul Hands of Hands on Thin Sections Ltd.

2.3.3. Sample preparation for trace element and stable isotope analyses

After optical and SEM analyses key areas for trace element and stable isotope measurements were located. For use in the Cameca microprobes thin section dimensions had to be altered by coring and sampling the key areas using specialist glass cutting techniques, see Figure 2.12 for specimen set up schematics. For the Cameca IMS-4f a standard diamond-tipped hand glass cutter and diamond grit grinder were used to shape a 25 mm diameter disc containing the area of interest to fit into the sample holder for trace element analysis. For use in the Cameca IMS-1270 the specimen had to be further altered, involving the coring of 2.5 mm diameter cores using a Gatan™ (Model 601) ultrasonic cutter using boron-carbide slurry. These small diameter cores along with the chemical standards (see Section SM 2.7.4 for more details) were then set and pressed into an indium mount, housed within an aluminium base, using an Enerpac™ (P142) hand press, up to 200 bars. For both analyses gold coating was required. Separate sample preparations were required for each analysis due to limitations in sample carrying capacity of the microprobe equipment. The Cameca IMS-4f is fitted with an eight sample airlock system, allowing more samples to be accommodated and measurements to be made without the need to vent the apparatus and switch samples. The Cameca IMS-1270 however does not have such a system and thus requires all samples and standards to be housed in a single sample holder.

2.4. Overview of experimental apparatus

The triaxial experimental apparatus, used to undertake permeability and seismic velocity measurements, and illustrated and detailed in Figures 2.3 and 2.4, was first described in *Faulkner and Armitage*, [2013]. This apparatus is capable of triaxial deformation under confining pressures up to 250 MPa, which is applied using silicon oil confining medium (at 20 cSt viscosity). A differential stress can be imposed with a servo-controlled axial loading system, this was not utilised in this thesis. This apparatus is capable of measuring permeability down to 10^{-22} m^2 and resolving sample volume changes of less than 0.1 mm^3 in samples with porosities lower than 1 % [*Mitchell and Faulkner*, 2008]. The upstream pore pressure system is servo-controlled and the downstream end of the sample is connected to a low-volume reservoir. The transducers (Honeywell Pressure Transducer – TJE) used to monitor the controlled values of confining and pore fluid pressures have a resolution of 7000 Pa. Pressure measurements from the transducers are sent in millivolt form to an amplifier to boost the signal to a ±10 V range for the CompactRio (NI9024) data logging

module. The signal is then sent to a 4-channel, 16-Bit analogue input modules (NI 9215). Working set points (WSPs) for the pressure systems are input into a LabVIEW program on the apparatus computer and sent to the CompactRio wherein a servo-loop compares them to the signals being received by the analogue input modules. If the input signal and WSP do not match, a signal is sent from the 4-channel, 16-bit analogue voltage output module (NI 9263) to the servo-control box, the magnitude of which is controlled by user entered PID parameters (Proportional gain, Integral gain, and Derivative gain). A servo-amplifier within the control box then amplifies the signal to a higher voltage and current which is then used to drive the actuators / motors that control the confining and pore pressure systems and the axial load, within the apparatus [*Bedford*, 2017]. The workings of this servo-control system are summarised in Figure 2.3D

The pressure data recorded in the experiments, and used in this thesis for permeability calculation, are logged as raw voltage values by using National Instruments CompactRio and a LabVIEW program designed by Daniel Faulkner installed on the apparatus computer. This is programmed to use equations, obtained from instrumental calibrations, to convert raw voltage outputs from the confining and pore pressure gauges, the force gauge and the linear variable differential transformer (LVDT measuring displacement – note that the latter two devices were not utilised in this study) into mega pascals (MPa) and millimetres (mm). Instrumental calibrations take place by measuring a gauge output against that of a pre-calibrated, high resolution device such as a Heise gauge for pressure or a load cell of known calibration for force. These calibrations are repeated annually or when a component of the apparatus is altered or replaced.

2.4.1. Permeability and seismic wave velocity measurements

Before experimental measurement of permeability and ultrasonic wave velocities the specimen must first be mounted in the experimental sample assembly as follows. Once prepared into its cubic form, as described in Section 2.3.1, the specimen is jacketed in heat-shrink polyolefin and PVC tubing along with porous steel spacers (SIKA R-AX) and housed within a seismic sample assembly, configured to supply de-ionised water pore fluid to each end of the specimen via the upstream and downstream platens, see Figure 2.5A – C. Porous steel spacers were used in order to stop any fine-grained material entering into the pore fluid pipe work of the apparatus and to distribute the pore fluid across the entire specimen

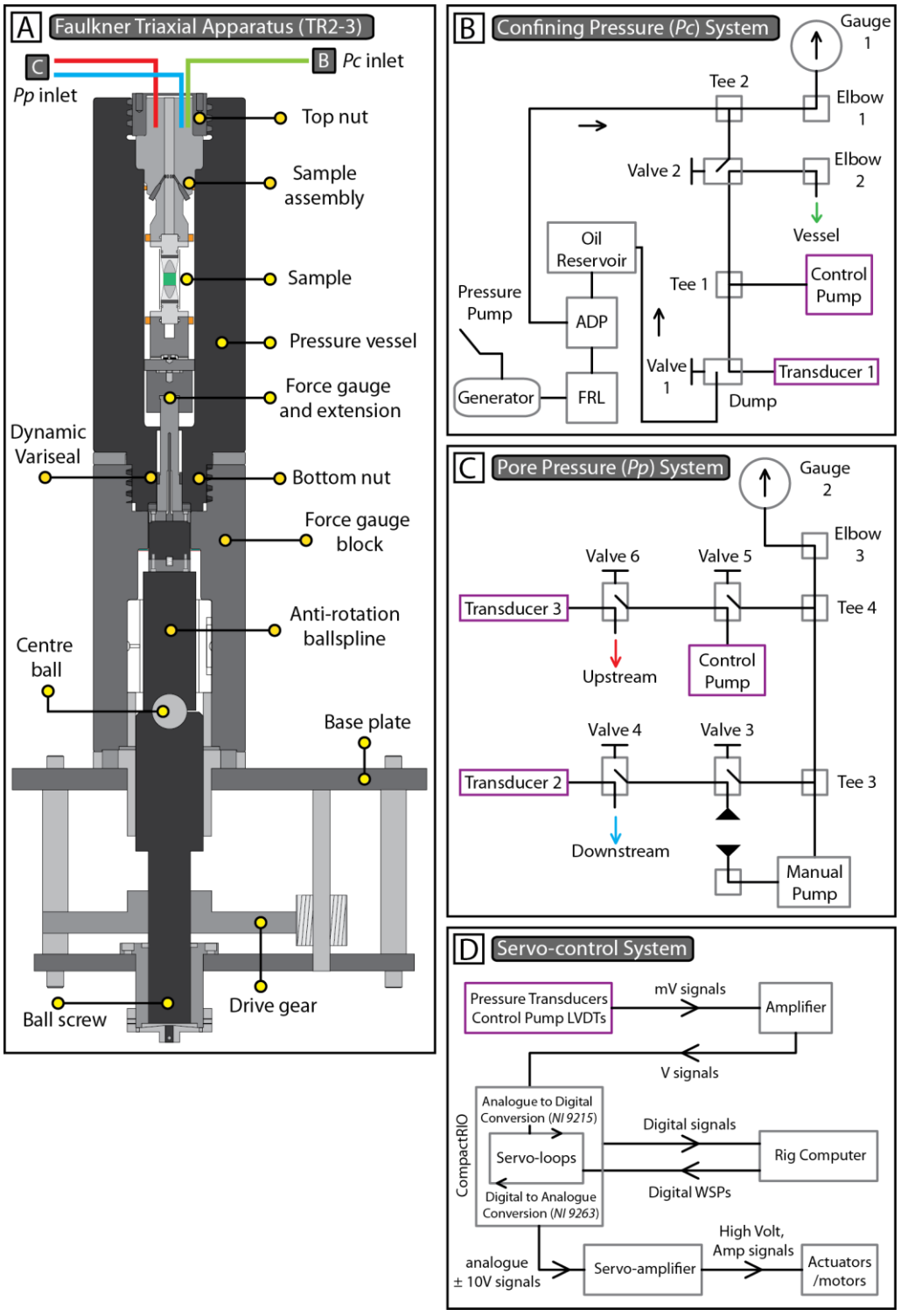

Figure 2.3 – [A] *Faulkner Triaxial Experimental Apparatus (TR2-3) schematic cross-section at the Rock Deformation Laboratory, University of Liverpool.* ***[B and C]*** *Schematic diagrams of the confining (P_c) and pore pressure (P_p) systems in TR2-3. FRL = filter regulator lubricator; ADP = Air Differential Pressure Switches.* ***[D]*** *Schematic diagram of the servo-control system showing the conversions of instrument signals. The purple highlight corresponds to the sensors highlighted in (**B**) and (**C**). WSPs = working set points; NI = National Instruments.*

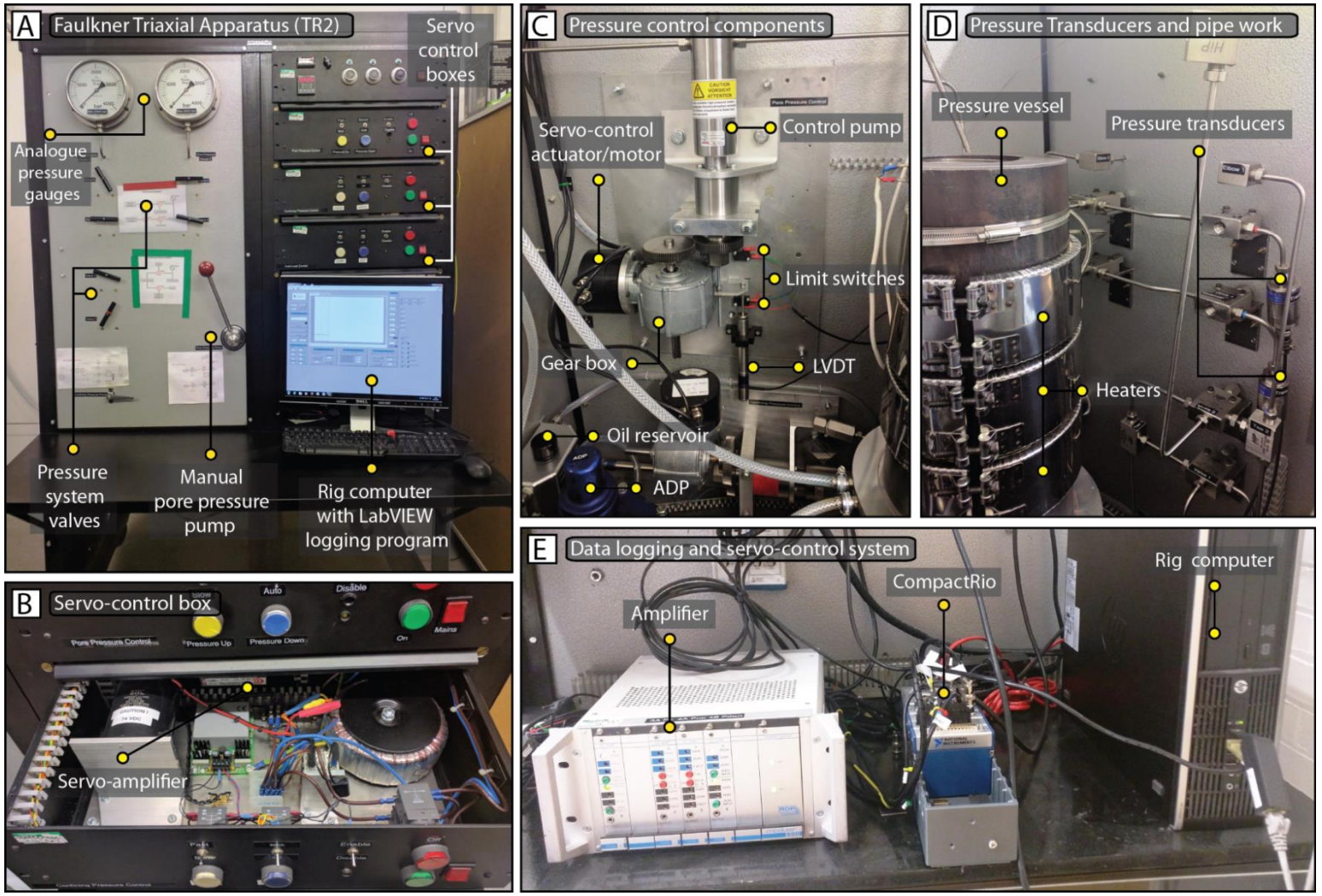

Figure 2.4 *– caption overleaf.*

Figure 2.4 – *(above)* ***[A]*** *Faulkner Triaxial Experimental Apparatus (TR2) at the Rock Deformation Laboratory, University of Liverpool.* ***[B]*** *The servo-control box used to send high voltage / current signals to the actuators driving the pressure control systems.* ***[C]*** *The pressure control components used to control the P_p and P_c systems. LVDT = Linear variable differential transformer; ADP = Air Differential Pressure Switches.* ***[D]*** *Pressure transducers and pipework monitoring and containing the P_p and P_c systems. Also shown are the vessel heaters which were not used in this thesis.* ***[E]*** *Data logging and signal processing equipment for the servo-control system detailed in Figure 2.3D.*

face. For improved coupling between the square cross-section of the specimen and the circular fluid-flow platens, a circle to square spacer is required. The assembly is loaded into the pressure vessel, the required confining pressure (P_c) is applied slowly, and finally the specimen is allowed to saturate and equilibrate with the pore fluid pressure (P_f) at low effective pressures (~5 MPa) for a time determined by the estimated permeability of the test specimen. This ranged between 12 – 24 hours.

Piezoelectric ceramics (PZT-5H, with fundamental frequency set at 1.5 MHz) with different polarisation directions are secured in each upstream and downstream platen, with silver-loaded epoxy adhesive and copper plate backing see Figure 2.5D for schematic illustration. These ceramics are used to produce and record ultrasonic P and S waves that travel through the specimen. Ultrasonic velocities are measured with the through-transmission method, using the travel times and specimen length [*Birch*, 1960] after correction for the travel time through the loading platens. Due to the high frequencies involved in ultrasonic measurements the electrical cabling used can alter the final recorded value through attenuation of the signal through the cable material. To minimize these effects high frequency coaxial cable is used (attenuation at 100 MHz: 3.61 dB, capacitance per metre: 105 pF). The resistance of this high frequency coaxial cable should equal the output of the pulser / receiver set up used in the measurement. In the case of this study a resistance of 50 Ohms is used to reduce internal reflections at connections between components [*Blake*, 2011].

Ultrasonic velocity data was collected using a Tektronix TDS 3032B oscilloscope, with 300 MHZ bandwidth and time based accuracy of 20 ppm time based accuracy. The signals were summed or ‘stacked’ 512 times to improve the signal to noise ratio and were collected in

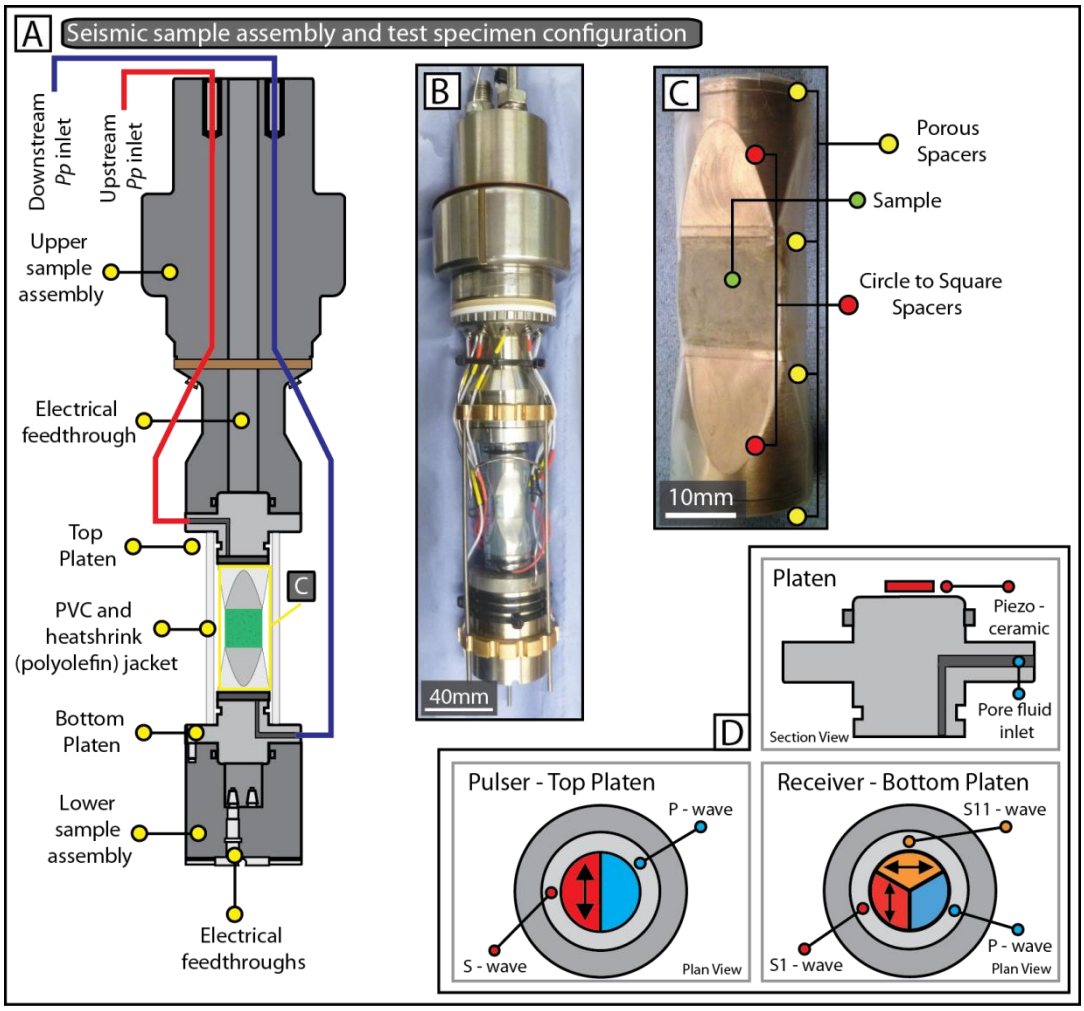

Figure 2.5 – [A] *Schematic illustration of the seismic sample assembly showing specimen position and platen configuration.* ***[B]*** *Photograph of (**A**).* ***[C]*** *A cube-shaped specimen set between porous steel spacers (both square and circle) and a circle to square adapter to allow coupling with the circular assembly platens.* ***[D]*** *Schematic illustration of the seismic sample assembly top and bottom platens with configuration of piezoelectric ceramics shown for each platen.*

the .isf file format and later converted to .csv file format, see Section SM 2.7.3 for conversion script. Data processing and analysis were carried out in a LabVIEW program as described above.

Permeability measurements were achieved using the transient-pulse decay method [*Brace et al.*, 1968] in hydrostatic conditions. The method involves the separation of an upstream and downstream pore fluid reservoir by the rock specimen. The upstream reservoir is subjected to a small (<1 MPa), instantaneous pressure increase, exposing the top of the rock specimen to a higher pore fluid pressure than the bottom. This pressure difference then decays at a rate proportional to the permeability of the sample. See Figure 2.6 for an illustration of this process.

Equation 4 after *Brace et al.*, [1968] was used to calculate permeability through an algorithm reported in the spreadsheet detailed in SM Section 2.7.2;

$$k = \lambda / (1/v1 + 1/v2) * (\eta \beta L)/A \qquad (4)$$

where k is permeability, λ is the gradient calculated from the ln (Upstream Pore pressure – Calculated Equilibrium), v_1 and v_2 are the upstream and downstream pore volumes, respectively, η is the pore fluid viscosity, β is the pore fluid compressibility, L is the sample length and A is the sample area.

2.5. Methods for microstructural and chemical analyses

2.5.1. X-ray computed tomography

Computed tomography (CT) is a technique that utilises X-ray equipment to obtain images of the internal structure of an object at various angles and from these then form detailed 3-dimensional cross-sectional or tomographic images through computer processing. This technique was used to visualise, non-destructively, the connectivity and extent of fractures present within the specimens used for experimental physical property measurements. These analyses were performed by Ludmila Adams and Auke Baarnhorn (University of Auckland, New Zealand and Delft University of Technology.

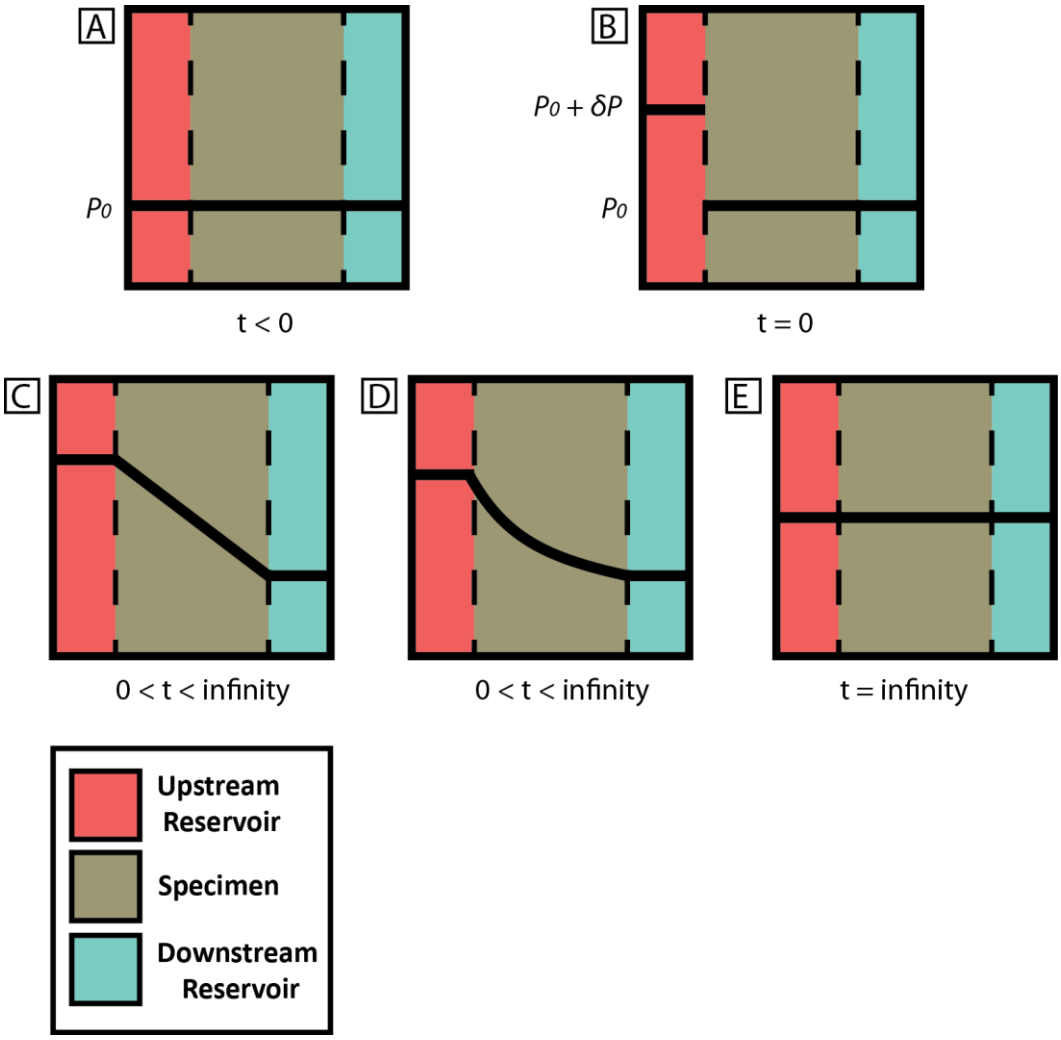

Figure 2.6 – *Illustration of the theory for the Pulse Transient Decay (PTD) method of measuring permeability, showing the assumed and real pressure variations across a sample during a PTD measurement, adapted from Childs, [1986] and Faulkner, [1997].* ***[A]*** *Initial conditions (P_0) where pressure is equal in both upstream and downstream reservoirs and test specimen.* ***[B]*** *A sudden increase in pressure (δP) in the upstream reservoir at time = 0.* ***[C]*** *The assumed variation of pressure across the specimen.* ***[D]*** *The true variation in pressure across the specimen.* ***[E]*** *The final equilibration of pressure in both reservoirs and specimen.*

The instrumentation used in this study was a Phoenix Nanotom nano-CT scanner at the Delft University of Technology, Netherlands. The analysis is performed with a micro-focus X-ray source, operating at 180 kV / 15 W, illuminating the specimen; the projected X-rays are then collected by a planar X-ray detector upon which they are magnified. As the specimen rotates during data acquisition a large number of X-ray images or 'slices' are collected; these slices are synthesised into a stack of virtual cross-section images of the specimen. As the X-rays pass through a material they are attenuated according to the materials atomic number (Z) and density, however the original strength of the X-ray energy itself can influence the degree of attenuation [*Ketcham and Carlson*, 2001]. These variations in X-ray attenuation allow the differentiation of various phases and open pore spaces in the test specimens. In post-processing the raw intensity data of the detected X-rays are linearly converted into a CT number, which in this study relates to a 12-bit Hounsfield Unit (HU) scale. 2-dimensional images are then constructed using the CT numbers as a greyscale with voids in the sample appearing black and the minerals varying shades of grey depending on their density. More details on this method can be found in *Ketcham and Carlson*, 2001 and *Cnudde and Boone*, 2013.

2.5.2. Optical cold-cathode cathodoluminescence

Optical cathodoluminescence (CL) is a technique that permits the optical examination and imaging of a sample through the attachment of an evacuated CL-stage to an optical microscope. This stage makes use of an attached cathode gun which bombards the sample with a high-energy electron beam resulting in the luminescence of a mineral, i.e., the emission of photons of a characteristic wavelength. This luminescence is the result of the transformation of various energy types into visible light, through emissive transition of molecules, anions or the transition of a crystal from excited electronic states to lower energy or ground states [*Marfunin*, 1979]. Luminescence in solids is controlled by the transition of electrons between conduction and valence bands, this transition is influenced by defects in a material's crystal lattice which form luminescence centres by the addition of energy levels within the conduction – valence band gap [*Pagel et al.*, 2000; *Götze and Kempe*, 2009]. Variation in a materials luminescence highlight subtle compositional and microstructural variations that are not visible using standard optical microscopy, as well as other more sophisticated techniques such as the SEM-based EDS and BSE imaging. This is

the case for many minerals, in this study particularly calcite and quartz, as the CL activating, sensitising or quenching trace elements are within parts per million concentrations.

This study used a cold-cathode CL apparatus, wherein an electron beam is generated by the discharge between a negative high voltage cathode and an anode at ground potential within ionized gas. The electron beam is produced within a moderate vacuum of ~10^{-2} Torr, resulting in a relatively low-intensity CL. In cold-cathode CL the specimen does not require a conductive coating due to the presence of positive ions with the electron beam which neutralises any surface charge build up [*Marshall*, 1991; *Waychunas*, 2014].

Cold-cathode CL can be viewed through a microscope objective lens or digital camera; this study used a Nikon Eclipse Ci microscope with a CITL Mk5-2 cold stage and Nikon DS-Fi1c camera, working at beam conditions of 10.8 Kv and 390 μA in a vacuum of 0.047-33 Torr, suitable for analysis of carbonate minerals. CL observations were made on polished thin sections prior to performing any SEM analyses. This precaution was taken to avoid compromising cold-cathode CL observations and interpretations due to the damage that a specimen surface would undergo during interaction with the electron beam in the SEM.

2.5.3. Scanning Electron Microscopy

This section will described the scanning electron microscopes (SEM) and the various SEM-based techniques used throughout this thesis.

2.5.3.1. CamScan X500 CrystalProbe field emission gun SEM

The CamScan X500 Crystal Probe field-emission gun (FEG) SEM was purposely designed by Obducat CamScan Ltd and Professor Dave Prior for the optimised performance of electron backscatter diffraction (EBSD) analyses of all Earth and engineering materials and for in situ experimentation (hot static and deformation tests). This specially designed SEM is one of only two ever built worldwide [*Seward et al.*, 2004].

The X500 CrystalProbe was used in this study for the acquisition of orientation contrast images (OCI), all EBSD data and qualitative EDS analyses. This SEM features a thermionic field emission warm cathode source, formed by a tungsten single crystal tip coated with

ZrO_2 that generates a highly focussed (coherent) electron beam thus enabling high resolution imaging. Conventional SEM configurations for EBSD analyses involve the specimen / stage being tilted at a high angle, 160° corresponding to 70° specimen tilt, to the incident electron beam. As illustrated in Figure 2.7 the X500 CrystalProbe SEM the column and electron-optic axis is inclined at an angle of 70° to the conventional vertical position allowing the specimen / stage to remain horizontal whilst allowing the ideal specimen-beam geometry for EBSD analysis. This configuration allows greater accuracy in specimen positioning and enhanced stage speed by removing the vertical component of movement for automated EBSD analysis. The tilted column geometry also allows a division of the SEM chamber into two domains: a lower domain for the sample and stage, and an upper domain for the detectors, particularly the large forescatter detector array for orientation contrast imaging (described below). Two main advantages are that: 1) particularly large samples (up to 12 x 12 cm) can be analysed using EBSD without issues of sample stability due to the action of gravity, and 2) in situ experiments (not performed in this study) are devoid of issues such as the gravitational flow of material out of its location on the stage (again due to gravity when the stage is tilted) [*Prior et al.*, 1999; *Seward et al.*, 2004; *Mariani and Ghassemieh*, 2010; *Dempsey et al.*, 2011].

EBSD analyses were performed using the F+ Nordlys EBSD detector mounted on the X500 CrystalProbe SEM in combination with the AZtec Oxford Instrument acquisition system. EBSD patterns (EBSPs) are collected using a phosphor screen which is mounted in front of a CCD camera, with 1344 x 1024 resolution, that digitises the EBSPs imaged on the phosphor screen at a speed of 640 Hz (equivalent to 640 patterns per second). EDS analyses are performed using an Oxford Instruments X-Max 50 mm^2 silicon drift detector (SDD), also combined with the AZtec Oxford Instrument acquisition system. SDD detectors are cooled using the Peltier method and do not require the traditional liquid nitrogen cooling system, thus permitting data acquisition at speeds that are comparable and exceed that of the Nordlys F+ detector. EBSD and EDS can therefore be acquired simultaneously at speeds of 640 Hz covering whole thin sections areas in a matter of 1 – 2 hours at 10 µm step sizes. The typical operating parameters for this study were 20 kV accelerating voltage, 20 – 30 nA beam current, and 5.5 nm spot size.

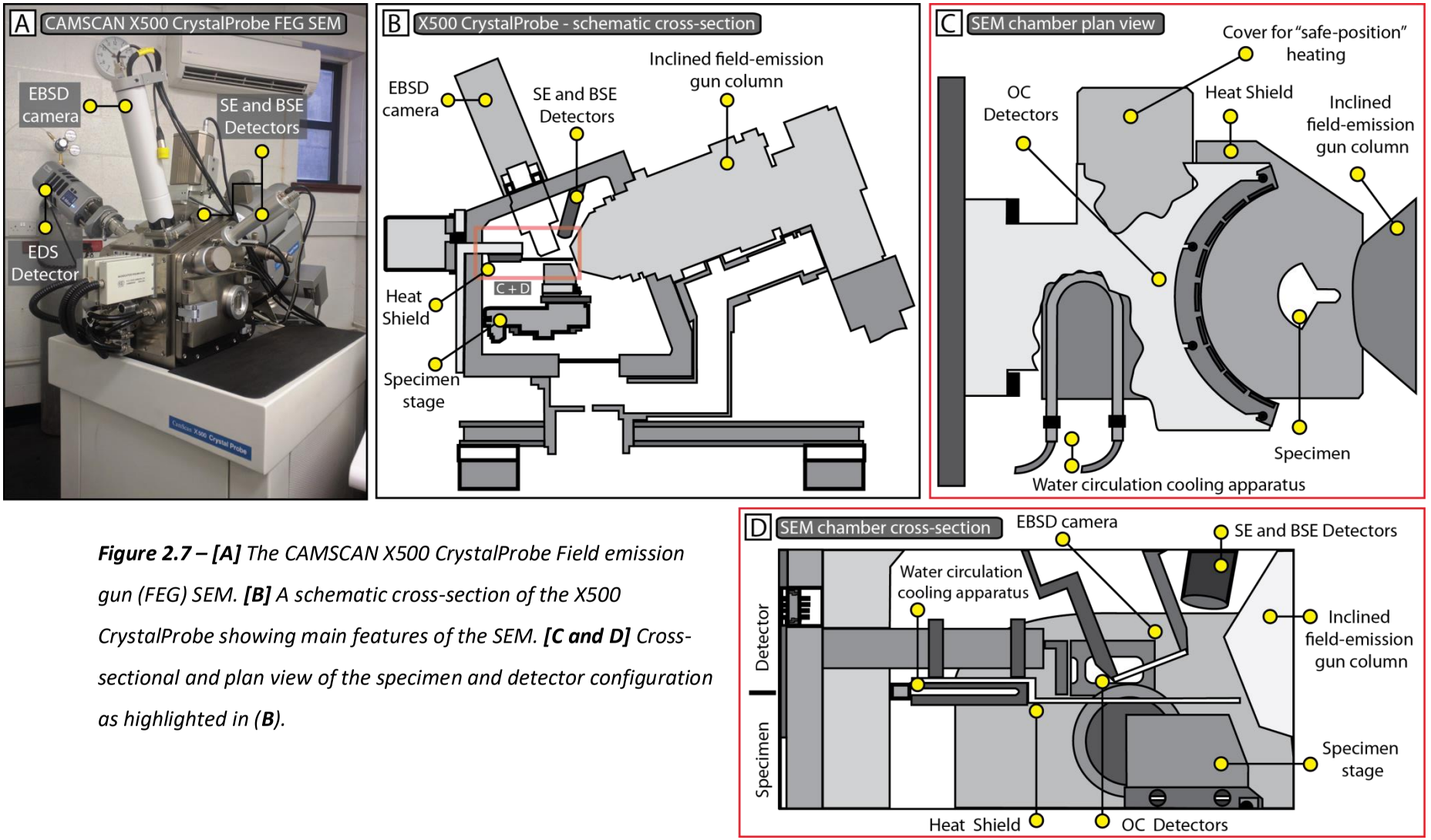

Figure 2.7 – [A] *The CAMSCAN X500 CrystalProbe Field emission gun (FEG) SEM.* ***[B]*** *A schematic cross-section of the X500 CrystalProbe showing main features of the SEM.* ***[C and D]*** *Cross-sectional and plan view of the specimen and detector configuration as highlighted in (**B**).*

The X500 CrystalProbe is also equipped with an Everhart-Thornley secondary electron detector, a KE industries solid-state backscattered electron (BSE) detector (K.E. Developments Ltd), an array of nine solid-state detectors for OC imaging and a four-axis stepping motor driven stage with high precision encoders. In terms of imaging capabilities the Philips XL30 SEM is better equipped for standard secondary electron imaging (SE), for observation of topographic surface features, and backscatter electron imaging (BSE), for qualitative assessment of atomic number contrast (Z), which gives information on mineralogy. The X500 CrystalProbe SEM is a cutting edge research SEM that, in addition to being optimised for the EBSD and EDS techniques described above, can provide information on crystallographic orientation using orientation contrast images (OCI) acquired with nine forward-mounted (with respect to electron beam and the diffracted electrons) backscatter detectors. These are mounted in an arc around the specimen. Signal from any combination of forescatter detectors can be processed via three separate analogue channels. As the central three detectors are at the smallest scattering angle from the incident beam, they receive the greatest component of crystallite orientation signal [*Prior et al.*, 1999]. As the perimeter angle from specimen to the detector increases, a greater amount of Z-contrast is incorporated into the signal, which weakens the OC signal. Orientation contrast images complement EBSD studies due to ability of rapidly identifying even subtle differences in crystallographic orientation. OC images can be directly compared and complement collected EBSD maps.

CHANNEL 5 HKL software was used for EBSD data acquisition and data processing and analysis; see Section 2.5.3.4 for details on data presentation.

2.5.3.2. Philips XL30 Tungsten filament SEM

The Philips XL30 SEM is a conventional, tungsten filament SEM with an adjustable stage for tilt between 0 – 70°. The Philips XL30 is fitted with backscatter electron (BSE), secondary electron (SE) and cathodoluminescence (CL) detectors; is capable of electron backscatter diffraction (EBSD) analyses using an Nordlys EBSD detector and Energy Dispersive X-Ray Spectroscopy (EDS) analyses using an Oxford Instruments x-act 10 mm^2 silicon drift detector (SDD); both EBSD and EDS are used in combination with the AZtec Oxford Instrument acquisition system.

The Philips XL30 SEM was utilised for BSE imaging and EDS analyses, operating at 20 kV accelerating voltage, 60 – 80 µA beam current and a 5 nm spot size.

2.5.3.3. Electron Backscatter Diffraction

Electron backscatter diffraction (EBSD) is a predominantly SEM based technique (but is also used in transmission electron microscopy – TEM) that measures the absolute crystallographic orientation of minerals with respect to the (known) SEM reference frame. EBSD uses the interactions between the electron beam and the surface of a crystalline sample favourably oriented at low angle to the beam (incidence angle 70° - see Figure 2.8); to form a divergent source of fore-scattered electrons close to the sample surface. Some of the scattered electrons diffract on atomic planes, satisfying Bragg's equation;

$$n\lambda = 2dsin\vartheta \qquad (5)$$

where *n* is an integer, λ is the wavelength of the electrons, *d* is the spacing of the diffracting plane and ϑ the angle of incidence of the electrons on the diffracting plane [*Randle*, 1992]. These electrons are diffracted to form a set of paired large-angle cones that correspond to each diffracting plane and are received by a phosphor screen; which fluoresces with an image containing characteristic Kikuchi bands (cone traces on a 2-dimensional surface), which are then viewed using a sensitive lens distortion correction (LDC) camera. These bands are formed where the regions of enhanced electron intensity intersect the phosphor screen, see Figure 2.9B [*Nishikawa and Kikuchi*, 1928].

The image of a particular set of Kikuchi bands collected on the phosphor screen is referred to as electron backscatter diffraction pattern (EBSP) and is characteristic of the structure and orientation of a crystalline material in the small volume (a few μm^3) of sample that returns that image. EBSPs are photographed by a LDC high resolution camera and then saved to a PC where specialised software (commercially available – Oxford Instruments HKL Software) can index each pattern as long as the mineral phase of interest and its crystallography are known. EBSPs can be used to determine the crystal orientation of grains, discriminate between crystallographically different phases (polymorphs), characterise grain boundaries (misorientation >10°) and the relationship between grains across such boundaries

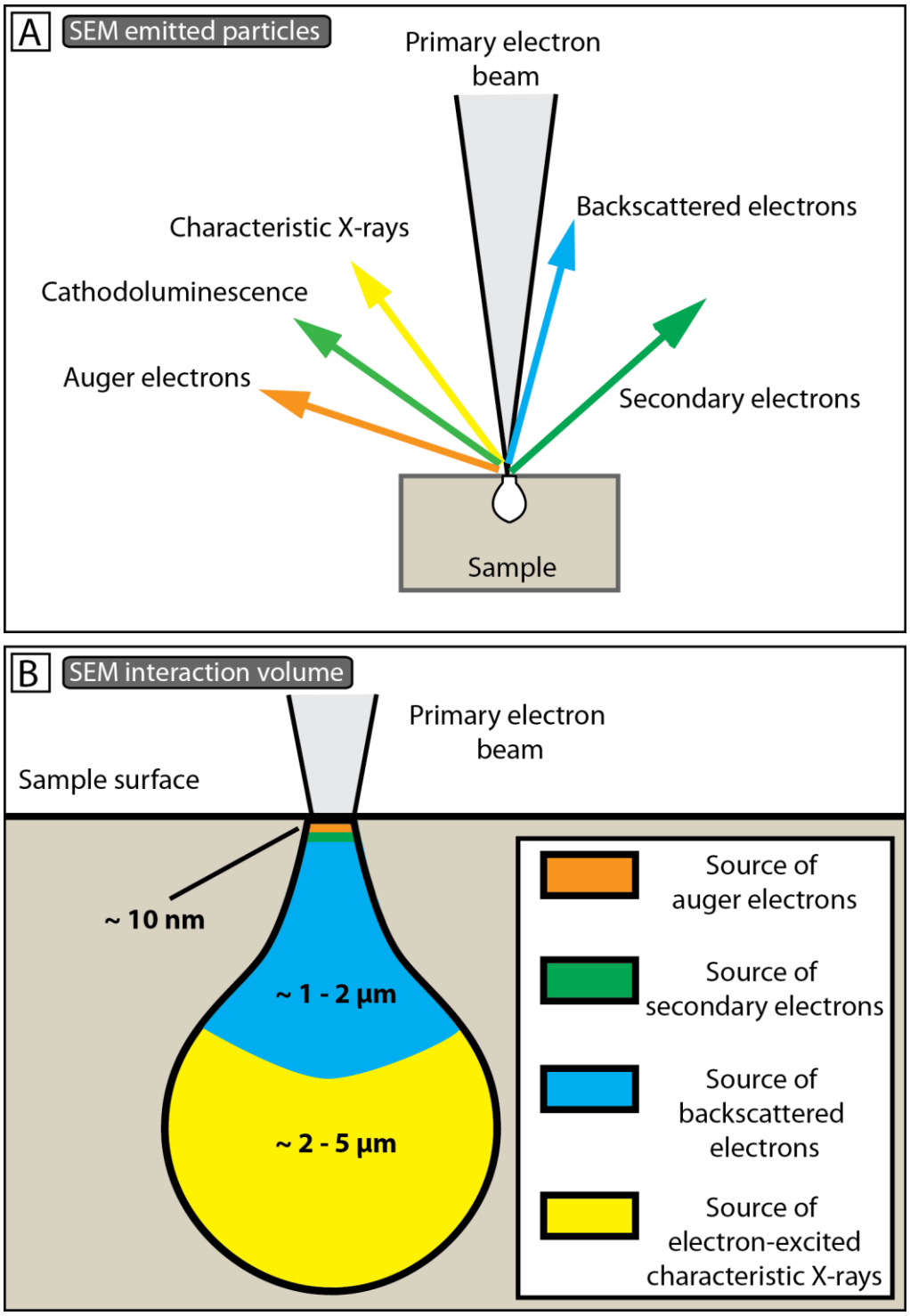

Figure 2.8 – [A] *Illustration of an SEM primary electron beam and how it interacts with the atoms within a sample. Some electrons are ejected from the sample, i.e. backscattered electrons, while some collide with atoms causing the generation of secondary electrons. Other products of these interactions are X-rays, light and heat.* ***[B]*** *The interaction volume generated within the sample surface by the primary electron beam. Illustration shows the depths at which the different interactions and thus products are generated.*

characterise sub-structure (sub-grain walls and sub-grain boundaries (misorientation <10°) and provide information about the local crystalline perfection. EBSPs are collected in a grid fashion, whereby the area and spacing (step size) of the grid are chosen by the user. Indexed EBSPs are then most commonly visualised as orientation maps and stereographic projections (pole figures and/or inverse pole figures). In this thesis EBSD is used to determine the crystallographic orientation of calcite, ankerite, quartz and K-feldspar (orthoclase), with particular focus on calcite, a schematic of its typical crystal system is illustrated in Figure 2.9A.

As the phase and orientation at each pixel in an EBSD map is known, visualisation of the data can be achieved in a number of ways, each chosen as the best means to communicate effectively the relevant scientific message. Post-processing and analysis of EBSD data was performed using the Oxford Instruments *HKL Channel 5* software. Channel5 provides a range of software modules including; *Tango,* which allows the presentation and manipulation of data via a suite of orientation maps, permitting a variety of post-processing and data analysis techniques to be applied including; a noise-reduction facility, multiple grain size analyses and misorientation profiles. *Mambo* software is a pole figure plotting program that allows the analysis of a specimen's crystallographic preferred orientation (CPO) and presentation as pole figure figures (PF), and inverse pole figures (IPF).The different types of orientation maps and pole figures used in this thesis are described below.

A Band Contrast (BC) map is an image of the EBSP quality factor, determined from the Hough transform, which describes the average intensity of the Kikuchi bands with respect to the overall intensity within the EBSP. The values are scaled and mapped to a greyscale range (byte range 0 to 255) and give a realistic representation of the microstructures analysed, with dark BC indicating no or poor EBSP quality (fuzzy EBSP image with poor contrast and definition) , while light BC indicates good quality EBSPs (bright, sharp image with high Kikuchi band definition).

All-Euler (AE) maps visualise orientation through use of an Euler angle-based colour scale. Euler angles are a set of three angles ($\phi 1$, Φ, and $\phi 2$) used to describe the crystallographic orientation of crystals relative to a reference coordinate system; defined by the primary SEM stage axes. The value of each Euler angle, reflecting the magnitude of the 3 rotations necessary to determine a rotation path from the SEM reference frame to that of the crystal

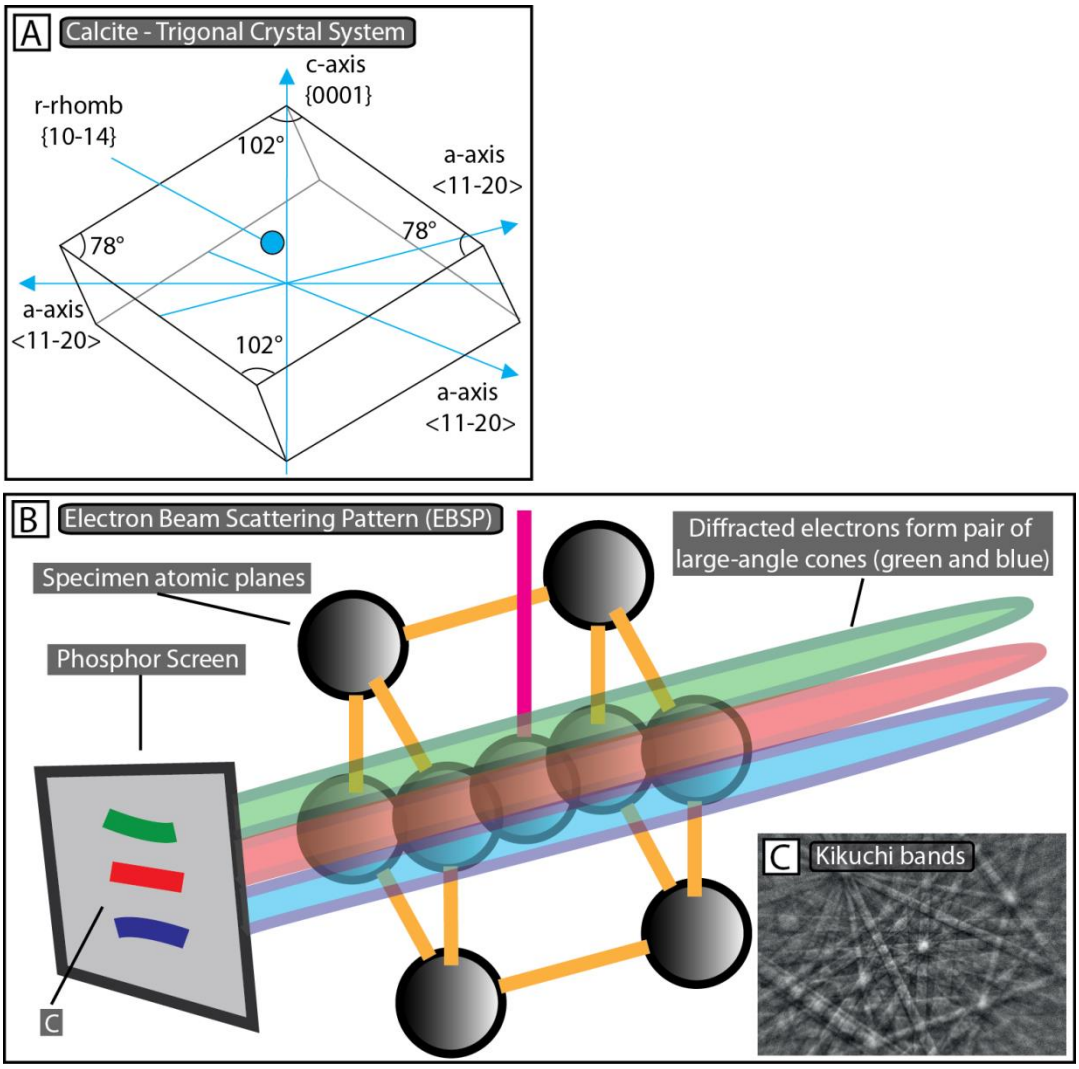

Figure 2.9 – [A] *Calcite rhomb with trigonal crystal system, [0001] c-axis, <11-20> a-axis and {10-14} r-rhomb face shown.* ***[B]*** *The electron beam scattering pattern (EBSP) is generated through the interaction of electrons within the specimen when exposed to an electron beam. Cones are generated by the electrons from divergent sources that satisfy the Bragg equation on a single lattice plane. The generated cones are projected onto the EBSD camera's phosphor screen forming Kikuchi bands (**C**).*

analysed, is individually set to a colour scale (red, green and blue for Euler angles ϕ1, Φ, and ϕ2, respectively) which are then combined into a single RGB colour that represents the observed crystallographic orientation. AE maps display microstructures quantitatively, using colour schemes in which similar colours indicate similar crystallographic orientations, thus enabling for example the determination of intracrystalline distortion within grains and the fabric (or texture in the Materials Science terminology) strength of the aggregate. However, the AE component contains a 'wraparound' effect caused by one or more of the Euler angles reaching their respective limit, resulting in the RGB value to vary between minimum and maximum, potentially resulting in colour speckling even when little to no orientation variation between grains exists.

This limitation of AE map can be mitigated by complementing data analysis with Inverse Pole Figure (IPF) orientation maps. In this case a RGB colouring scheme is fitted to the data using an inverse pole figure scheme, whereby the colouring of pixels is relative to the chosen projection-parallel crystallographic axis only, independent of the other 2 axis in the reference frame. This technique is useful for displaying preferred orientations parallel to a particular sample direction. However, the user must bear in mind that in IPF maps, grains with identical axes parallel to a specified IPF projection direction will have the same colour in the IPF-based scheme, but may be in significantly different orientations. With this in mind IPF maps must be viewed in multiple orientations (X, Y and Z for example) to determine the full orientation properties of the aggregate.

Texture component (TC) maps display orientation using a user-determined orientation colouring scheme relative to a specific orientation of interest that can be selected as a reference point. Each pixel on the map is coloured relative to the misorientation between the orientation at that pixel and the reference point. This reference point can be a crystallographic definition (plane / direction pair), a fibre-texture definition or a set of Euler angles. This visualisation is particularly useful when comparing a parent grain orientation to recrystallised daughter grains for example.

Stereographic projections of pole figures (PFs) allow the visualisation of 3-dimensional orientation information in 2-dimensions, showing the projected positions of a chosen set of crystallographic planes or directions in which the poles to the plane / normals or the directions are projected onto a sphere and visualised in 2-dimensions as intersections onto

the circle representing the equatorial plane of the sphere. There are two main projection techniques that PF employ, the stereographic and equal area projection which can be shown as upper or lower hemisphere depending on conventions in a given discipline. In Earth Sciences stereographic projections are generally shown as lower hemisphere while crystallographers tend to show upper hemisphere projections. Inverse Pole Figures (IPFs) plot specific directions of interest, such as the stress direction for example, on a projection using crystallographic coordinates for the reference frame. Such coordinates will reflect the crystal system of the mineral of interest. For the data presented in this thesis a lower hemisphere equal area projection was used for PF plots, further details regarding this can be found in Section 2.5.3.4. In an equal area projection a random distribution of crystal orientations generates a uniform distribution of points in the whole projection area while in a stereographic projection a random distribution of crystal orientations results in a denser population of points in the centre of the PF, thinning towards the perimeter. The plotted points can be colour coded according to their respective Euler orientation and can be contoured according to their densities. In this thesis contouring is set to a half width of 20° and data clustering of 5°. In order to describe the intensity of the fabric shown in PFs a statistical method is used known as the multiple of uniform density (MUD), which is quantified using the maximum intensity of a contoured PF. MUD values of 1 indicate randomly orientated grains (uniform distribution) while a MUD >1 is indicative of a fabric or CPO, these values are illustrated alongside the PFs. MUD values, however, are only a qualitative approximation of CPO strength and cannot be used in direct comparison of different PFs as multiples of uniform density are calculated only relative to the dataset being analysed. More reliable quantitative measures of the strength of a CPO may be the J index and the m index (see e.g., *Skemer et al.*, 2005). These were not utilised in this thesis as no systematic comparison of CPOs across datasets was carried out. The notations used in the PFs to represent crystallographic orientations are: [hkil] and (hkil) for individual crystallographic axes and poles to planes, respectively, and <hkil> and {hkil} for families of axes and poles to planes, respectively. More information can be found in *Prior et al.*, [1999, 2009] and *Bestmann and Prior*, [2003], wherein they report the advent and evolution of EBSD in the Earth Sciences as well as some specific case studies.

2.5.3.4. EBSD reference frame vs. SEM reference frame conventions

In early 2016 it was brought to the attention of members of the EBSD community that inconsistences in EBSD orientation data in comparison with other techniques, e.g., U-stage data, existed for many research groups and labs. This inconsistency was discovered by performing EBSD measurements on an obliquely cut quartz single crystal reference sample in a number of Oxford EBSD / SEM systems. In these systems the derived crystal orientations are rotated with respect to the EBSD-map and scanning electron image.

In any EBSD-SEM system the "point of view" of the SEM (always looking down along the electron beam trajectory) is different from the "point of view" of the EBSD camera. This is represented in Figure 2.10B, where X_s, Y_s and Z_s are the axes of the sample reference frame. Therefore, when we look at the image generated by the SEM, in the plane of the image, X_s is horizontal and points to the left, while Y_s is vertical and points down. However, looking from the EBSD camera point of view (represented by a kikuchi pattern in Figure 2.10B), X_s and Y_s are rotated 180° around Z_s with respect to the SEM image. In other words, the crystallographic orientation measured when the EBSD software fits a best solution to the kikuchi pattern collected, is rotated 180° around Z_s with respect to the orientation of the studied crystal as seen in the SEM image. Constructing a convention that relates the SEM reference frame to the EBSD reference frame from first principles is non-trivial as this must account fully for the sample-EBSD camera-SEM column geometric relationships. While sample normal, EBSD camera and SEM column always lay within the same vertical plane, the angle at which the EBSD camera is set-up may vary in every different EBSD-SEM system. *Britton et al.*, [2016] provide a mathematical framework for an EBSD-SEM reference frame convention, suggest methods of testing the system using crystals of known orientation and make their code (written in Python and MATLAB) freely available to other users.

Generally, companies that provide commercial EBSD acquisition and processing software apply their own corrections to the system. So not only the geometry of each EBSD-SEM system might be different, but also each company might implement different software conventions. With ever increasing interdisciplinary collaborations between SEM laboratories it has clearly become paramount that each laboratory test their system and the commercial EBSD software of choice so to make sure that the correct crystallographic orientations are reported and that confusion and misinterpretation are avoided.

Recently Rüdiger Kilian and Michel Bestmann (personal communication), of the Geologisch-Paläontologisches Institut, Universität Basel and the GeoZentrum Nordbayern, University Erlangen-Nuremberg, respectively, tested the conventions used by HKL Channel-5 Flamenco and Oxford instruments AZtec software by indexing a quartz single crystal of known orientation. They found that, while the EBSD-map reference frame and scanning electron image remain consistent, pole figures (PF) plotted using this software display a 180° rotation around the normal to the sample surface / centre of the PF (Z_s) in relation to the SEM image and EBSD maps [*Kilian et al.*, 2016].

In the Liverpool Earth Science EBSD-SEM laboratory a kyanite single crystal of known orientation was used to test the reference frame convention when the system was first installed. However, further testing was carried out by myself and Joseph Gardner, a fellow PhD student at the University of Liverpool, using a quartz single crystal reference sample, this is reported below.

Firstly the EBSD reference frame was compared to the SEM reference frame; this was checked within the virtual AZtec chamber with the view from the EBSD camera along the horizontal plane. In the case of a standard SEM the sample is tilted at 70° around X_m and the electron beam is vertical, see Figure 2.10A. As detailed in Section 2.5.3.1, within the X500 CrystalProbe SEM system the sample is horizontal, the electron beam at 70° and EBSD camera at 110° to the sample surface, see Figure 2.10B. The collection of data occurs from the top left hand corner of the scanning electron image, rastering, in user-defined steps, to the right then down and left, rastering the next acquisition line to the wright again and so on. This beam movement builds a data collection grid from the top left corner of the SEM image and is referred to as 'scanning down' by Oxford Instruments.

In our test an idiomorphic quartz single crystal was used. A clear rhombohedral {r} plane was chosen and oriented to rest as the horizontal surface of interest in the SEM sample holder (Figure 2.10C). The quartz crystal was positioned so that its c-axis <0001> had a plunge of 165° and dip 38° towards southeast. Figure 2.10C shows the point of view of the EBSD camera, which, as discussed previously, is rotated 180° from the actual SEM image (see SE image of the rhombohedral quartz face in Figure 2.10D). X_s and Y_s reported here show a reference frame consistent with X_0, Y_0 of the AZtec virtual chamber in Figure 2.10A. In this configuration the c-axis <0001> will plot in the northwest quadrant of lower

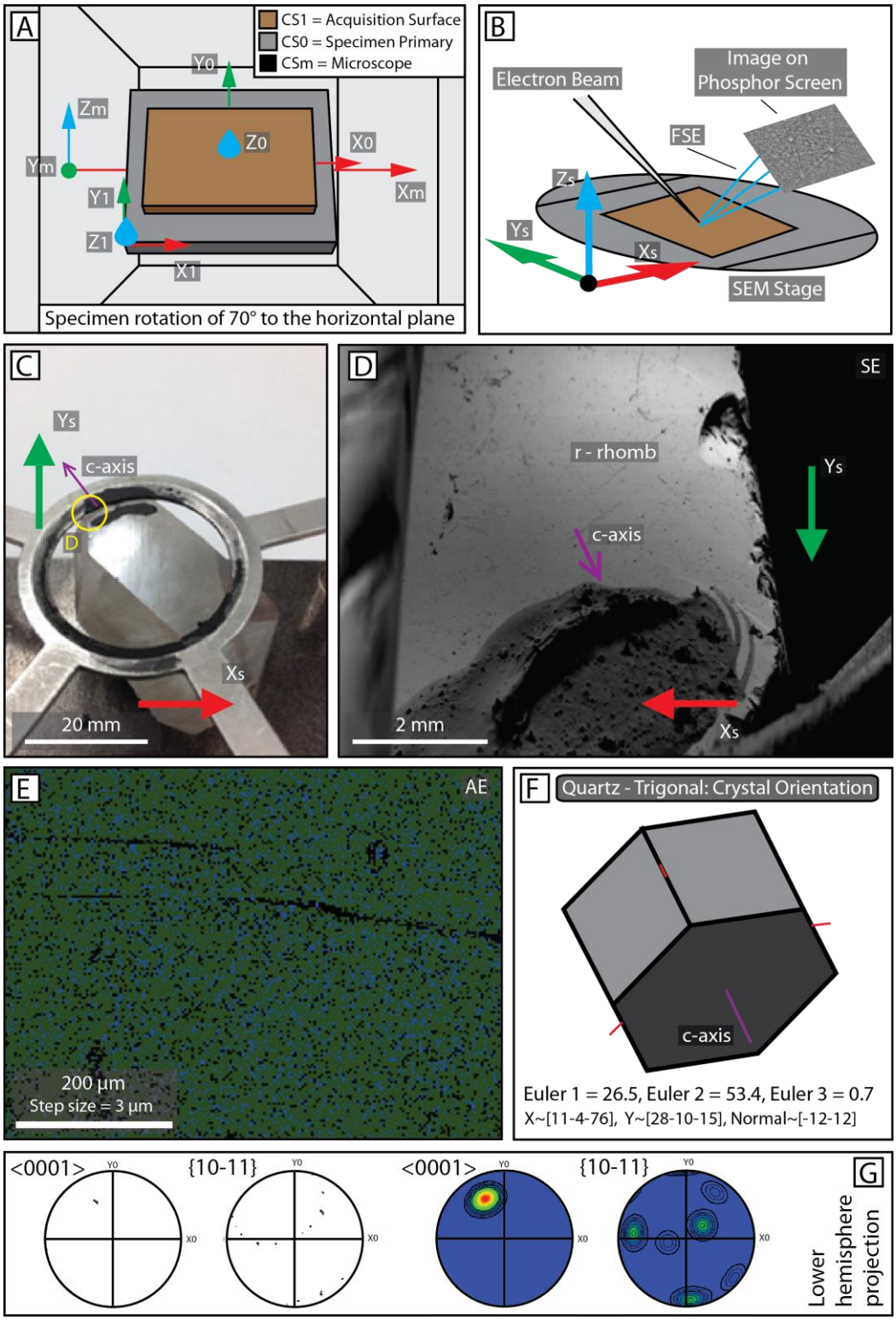

Figure 2.10 – *caption overleaf.*

Figure 2.10 – *(above) EBSD reference frame vs. SEM reference frame calibration procedure.* ***[A]*** *Virtual AZtec SEM chamber showing the SEM reference frame for a standard SEM with tilted sample for EBSD analysis.* ***[B]*** *Schematic diagram showing the configuration of the CamScan X500 CrystalProbe SEM chamber and the kikuchi pattern projection onto the EBSD detector phosphor screen. FSE = Forescattered electron.* ***[C]*** *Photograph of the quartz single crystal in the SEM sample holder.* ***[D]*** *Secondary electron image (SE) of the sample from the point of view of the EBSD camera.* ***[E]*** *An All-Euler (AE) EBSD map of the quartz single crystal r-rhomb face showing uniform orientation. Black are misindexed data points and blue pixels are due to the 'wraparound' effect.* ***[F]*** *CH5 3-dimensional crystal orientation tool of the region shown in (**E**), with c-axis pointing towards the southeast.* ***[G]*** *Pole figure plots of the orientation data in (**E**) showing the c-axis [0001] and r-rhomb face {10-11} orientations plotted as lower hemisphere projections. Note the c-axis plots to the northwest indicating a 180° rotation.*

hemisphere PF plot or the southeast quadrant of an upper hemisphere PF plot. A map of a small area on the {r} surface was acquired and it is shown in Figure 2.10E as an All-Euler map. Several pixels on this map were then selected and the CH5 3-dimensional crystal orientation tool was used to show the orientation of each pixel. All pixels consistently show the orientation reported in Figure 2.10F, where the orientation of the c-axis <0001> (purple) is consistent with <0001> in the SEM image (Figure 2.10D) i.e., with the sample orientation in the SEM as seen from the point of view of the electron beam. This indicates that AZtec software applies a 180° rotation to the acquired orientation data to bring such data into coincidence with the orientation of the SEM image when visualised as an EBSD map. Therefore here the convention utilised is consistent between the EBSD and SEM reference frames.

Following the same convention, in the equal area lower hemisphere PF reported in Figure 2.10G the c-axis <0001> should plot in the southeast quadrant. However, this is not the case and c plots in the northwest quadrant instead, indicating that there is a difference corresponding to a 180° rotation around Z_s between the c-axis measured with EBSD and the orientation of the c-axis in the SEM image.

As the crystal orientation reported in EBSD maps and that in SEM images are consistent with each other, we infer that there is consistency in the convention used during data

acquisition. However, the same convention is not applied to PFs plotted using AZtec and CH5 software. This is of course confusing and a consistent convention should be utilised by commercial suppliers of EBSD acquisition and processing software. For any data acquired in the Liverpool Earth Science EBSD-SEM laboratory we apply a rotation of 180° to any pole figures plotted using Aztec or CH5 (upper hemisphere PFs are in reality lower hemisphere ones). This has been done for all PFs reported in this thesis.

2.5.3.5. Energy dispersive spectroscopy

Energy Dispersive X-Ray Spectroscopy (EDS) is an SEM technique used to determine the chemical composition of a solid material. When bombarded by an electron beam, atoms in the specimen eject electrons. The resultant electron vacancies are filled by electrons from a higher energy state, with X-rays emitted as energy packages reflecting the energy difference between the two electrons' states. This X-ray energy is characteristic of the element from which it is emitted.

The EDS detector measures the relative abundance of the emitted X-rays versus their energy, whereby, when an incident X-ray is received by the detector, a charge pulse is generated proportional to the energy of the X-ray. The charge pulse is converted to a voltage pulse via the charge-sensitive preamplifier; the signal is then passed through a multichannel analyser in which pulses are sorted by voltage. After subtraction of the background signal, the spectrum of X-ray energy versus counts is then evaluated in order to determine the elemental composition of the sampled volume [*Agarwal*, 1991; *Goldstein et al.*, 2003].

EDS data acquisition can be qualitative or quantitative. Qualitative EDS consists of identifying the traces in the generated X-ray spectra, giving the elemental composition of the specimen. Quantitative EDS, in which the concentrations of the elements are acquired, requires measuring line intensities for each element in a specimen and to compare with a calibration standards that contain these elements [*Goldstein et al.*, 2003].

At the Electron Microscopy Laboratory (Liverpool Earth Sciences) semi-quantitative EDS is possible using the Philips XL30 SEM as a full set of geological standards is available for calibration. A full element standardization procedure is carried out regularly. Once the most

recent standardization files are created, these are used as a reference to quantify element weight % in minerals within research samples. When performing quantitative EDS analyses, a purposely made thin section holder with mounted standards (cobalt, kyanite and diopside) is used to carry out regular checks on beam stability, on the cobalt, and on the validity of the element weight % values obtained. The resolution of energy dispersive detectors limits the accuracy of analyses to within 2 % from the total elemental composition expected for a given mineral. In this study only qualitative EDS analyses were undertaken, using a Philips XL30 SEM.

2.5.3.6. Quantitative evaluation of minerals by SEM

Using similar methods as SEM EDS analyses the *quantitative evaluation of minerals by scanning electron microscopy* (QEMSCAN®) is an SEM technique developed by CSIRO to identify mineral species rapidly, automatically and non-destructively.

The technique consists of the automatic acquisition of EDS spectra and BSE images of a specimen surface which are then combined with one another to identify the mineral species within it, this achieved through comparison to a comprehensive mineral database incorporated into the QEMSCAN software [*Qian et al.*, 2015]. The technique requires standard polished thin sections or blocks with a surface coating of conductive material to avoid surface charging effects. This technique was used briefly in *Chapter 5* of this thesis on pseudotachylyte and cataclastic material by Alan Butcher of Intellection Pty Ltd, Milton, Australia who performed the analysis using a QEMSCAN® system.

2.6. Geochemical study

2.6.1. Secondary ion mass spectrometry

Secondary ion mass spectrometry (SIMS) is a technique used to analyse the surface compositions of solid material through the use of a focused primary ion beam. This ion beam when focused on a surface bombards it with heavy particles, resulting in the sputtering of secondary ions. The secondary ions ejected from the sample upon bombardment are collected and isolated within a mass analyser within the ion detection unit, which consists of a photographic plate, a Faraday cup, an electron multiplier or a charge coupled device (CCD) camera and image plate. This records the magnitude of the

secondary ion signal and measures their mass / charge ratios revealing the elemental, isotopic or molecular composition of the point of interest. The primary beam source, utilised for sample bombardment, is usually composed of O_2^+, O^-, Cs^+, Ar^+, Ga^+ at energies between 1 and 30 keV.

Secondary ions leave the sample from a volume approximately 1 – 2 nm below the surface; this coupled with the small volume of material sputtered, 100 – 1000 μm^3 for high energy and high primary beam densities, allows a high spatial resolution of 10 – 15 µm.

Elements from H to U can be detected, and most elements can be measured down to concentrations of 1 ppm or 1 ppb, with isotopic ratios to a precision of 0.5 – 0.05 %. However, the technique has some limitations. The sputtered material consists of both mono-atomic ions and molecular species which dominate the mass spectrum, making some elemental analysis impossible; these include for example the unresolvable equal mass ions such as Lu – Hf in zircon [*Benninghoven et al.*, 1987]. Also, the sputtering process is poorly understood, so that secondary ionisation processes cannot be predicted, as a result suitable standards and empirical corrections are required for quantitative information. The composition of the specimen and also the primary beam type used in the measurement have a strong effect on the element detection sensitivity; Therefore standards should have a major element composition as close to the unknown as possible. See Section SM 2.7.4 for details and compositions of the standards used in this study.

2.6.2. Instrumentation and operational conditions

The University of Edinburgh NERC Ion Microprobe Facility comprises two Cameca ion microprobes for SIMS analysis, the Cameca IMS-4f, used in this study for trace element measurements, and the Cameca IMS-1270, that was used for stable isotope measurements. The following section details the capabilities of these microprobes and the analytical protocols that are followed in order to obtain reliable SIMS measurements. See Figure 2.11, 2.12 and 2.13 for detailed schematics of the instruments and sample holders.

Both the IMS-4f and IMS-1270 microprobes are equipped with a Duoplasmatron and a Cs ion source. Duoplasmatron can operate with most gasses, including air, though oxygen is

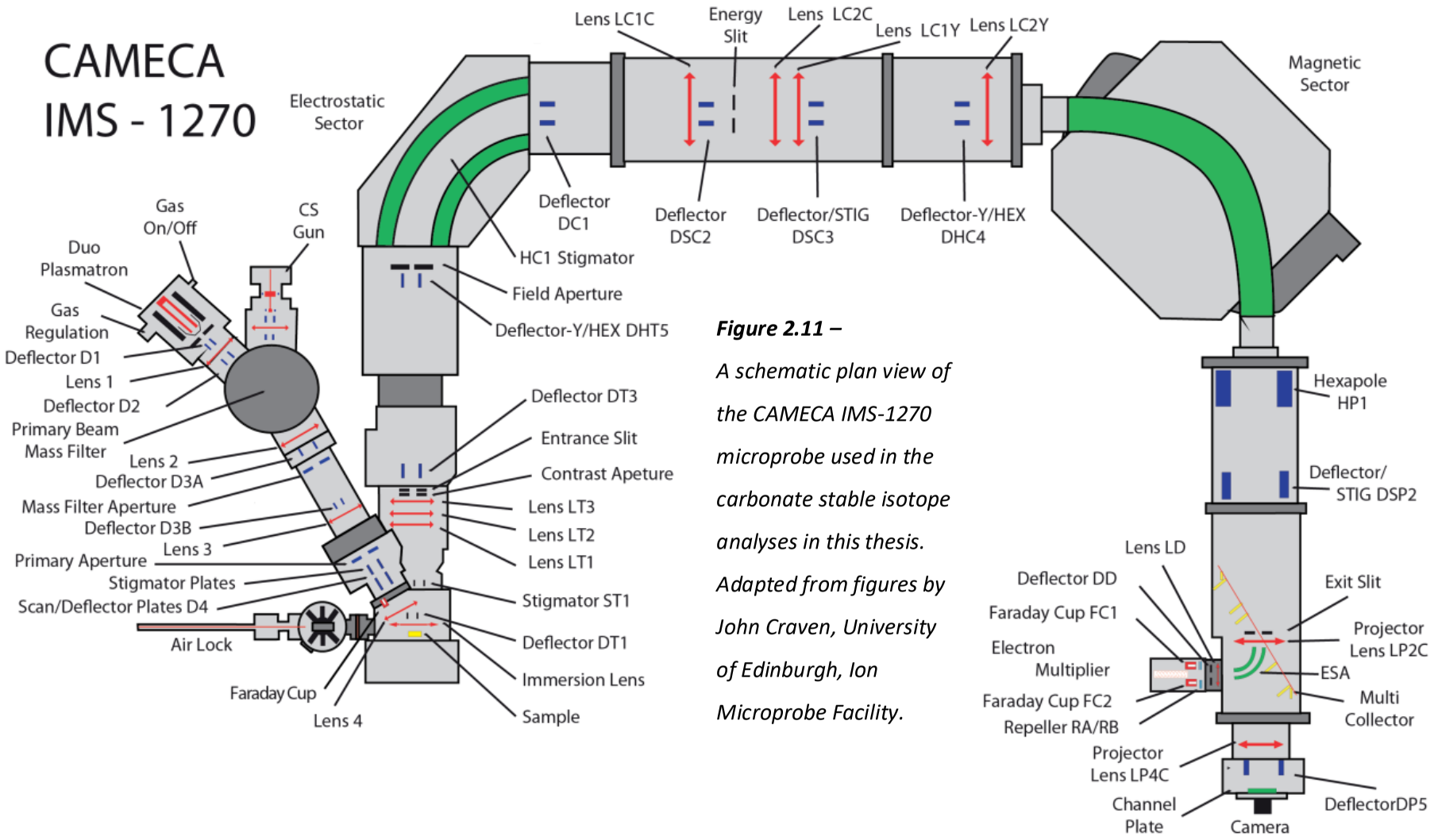

Figure 2.11 –

A schematic plan view of the CAMECA IMS-1270 microprobe used in the carbonate stable isotope analyses in this thesis. Adapted from figures by John Craven, University of Edinburgh, Ion Microprobe Facility.

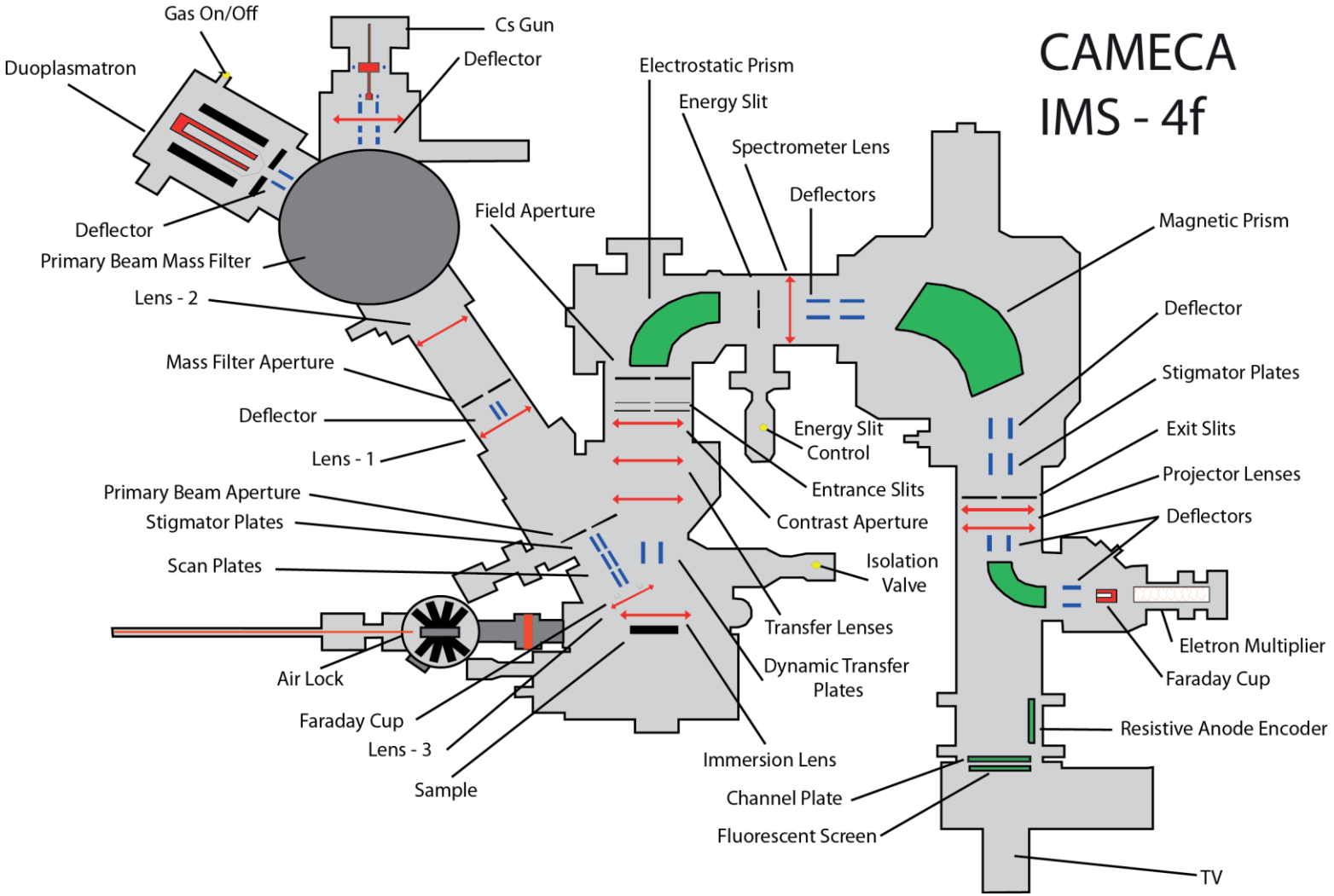

Figure 2.12 – *A schematic plan view of the CAMECA IMS-4f microprobe used in the carbonate trace element analyses in this thesis. Adapted from figures by John Craven, University of Edinburgh, Ion Microprobe Facility*

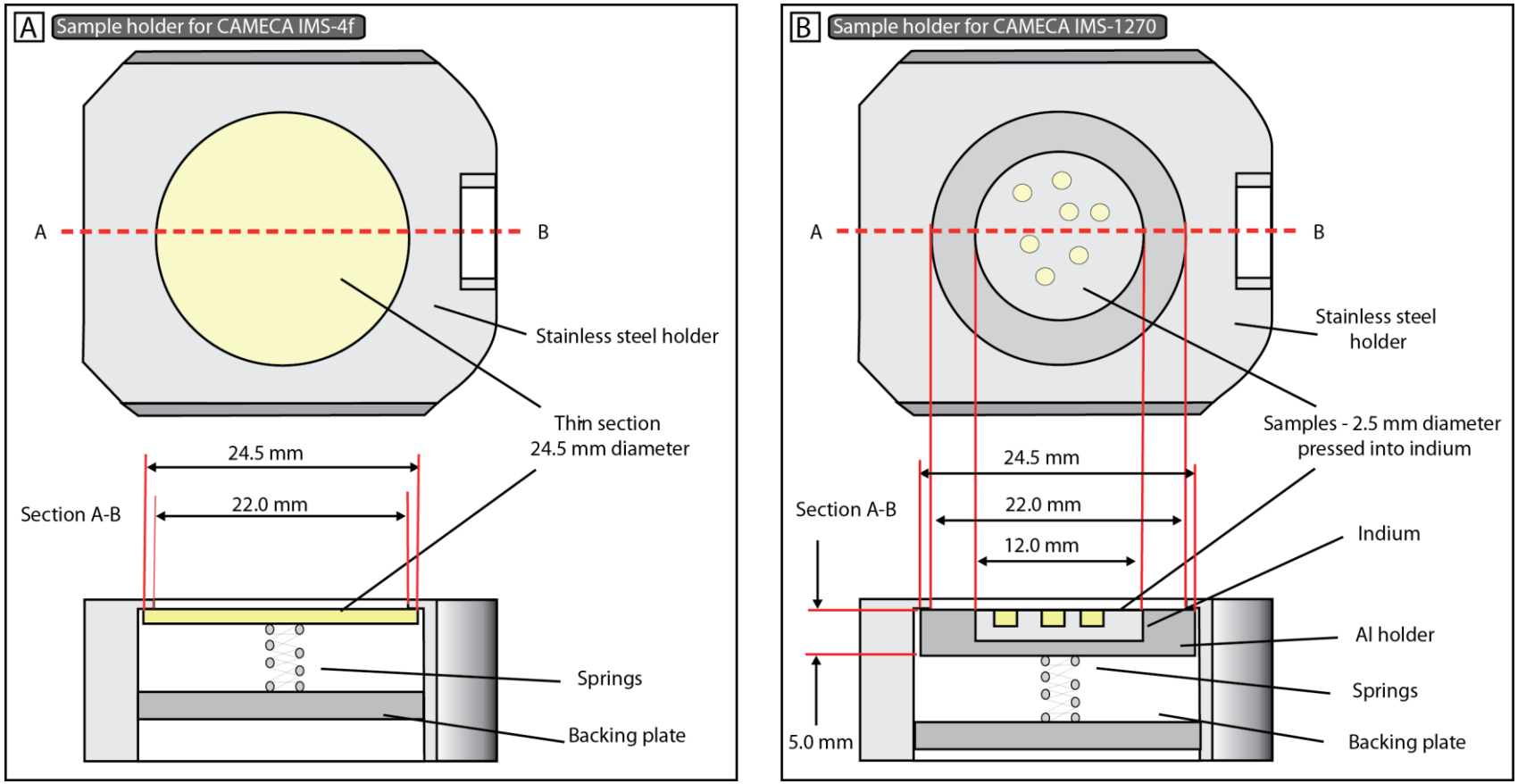

Figure 2.13 – *A schematic cross-section and plan view of the sample holders used in the SIMS portion on this thesis.* ***[A]*** *Sample holder for the CAMECA IMS-1270.* ***[B]*** *Sample holder for the CAMECA IMS-4f. Adapted from figures by John Craven, University of Edinburgh, Ion Microprobe Facility.*

commonly used as it enhances the yield of electropositive elements (Al, Si, REE etc.). It can be used to extract O^- O_2^- or O_2^+ depending on the electrical polarity set by the operator, whereby in negative polarity mode O^- is more abundant, while in positive mode O_2^+ are the most abundant ions. When the specimen is an electrical insulator, setting a negative mode (O^- ions) prevents charge build-up on the specimen surface. A Cs ion beam is used to enhance yields of electronegative elements (C, O and S etc.) and only operates in positive mode. This source generates smaller beams than the Duoplasmatron and sputters more effectively due to the greater ion mass. Due to the high operating expense the Cs source is used routinely only for O, S or C isotopic analysis.

Once the primary ion beam is generated it is passed through the primary column mass filter, the apertures, lenses and deflection plates, it reaches the sample surface and generates secondary ions. These ions are removed by an extraction / immersion lens and then transferred by a second electrostatic (transfer) lens into the mass spectrometer. For further details see *Hinton*, [1995].

The settings used on the IMS-4f microprobe during the carbonate trace element analyses for collection of species ^{23}Na, ^{26}Mg, ^{27}Al, ^{30}Si, ^{44}Ca, ^{54}Fe, ^{55}Mn, ^{88}Sr, ^{138}Ba and ^{140}Ce trace elements were as follows. A primary ion beam operating with O_2^- ions with a 20 µm spot size; within the microprobe a field of view of 825 µm, 25 µm image field, 150 µm field aperture and 150 µm contrast aperture. Measurements were collected using an offset of 75 volts with dwell times in seconds of 3 for ^{23}Na, 5 for ^{26}Mg, 2 for ^{27}Al, 2 for ^{30}Si, 2 for ^{44}Ca, 5 for ^{54}Fe, 5 for ^{55}Mn, 2 for ^{88}Sr, 5 for ^{138}Ba, 5 for ^{140}Ce and wait times in seconds of 1 for ^{23}Na, 0.2 for ^{26}Mg, 0.2 for ^{27}Al, 0.2 for ^{30}Si, 0.2 for ^{44}Ca, 0.2 for ^{54}Fe, 0.2 for ^{55}Mn, 0.2 for ^{88}Sr, 0.2 for ^{138}Ba, 0.2 for ^{140}Ce. The settings used on the IMS-1270 microprobe during the carbonate $\delta^{18}O$ analyses were as follows. A primary ion beam operating with Cs^+ ions at 10 kV with a 20 µm spot size; within the microprobe a field aperture of 3 mm, entrance slit at 60 µm, exit slit at 411 µm, energy slit of 81 µm, contrast aperture of 150 µm and a transfer lens of 30 µm were used.

2.7. Supplementary material

2.7.1. DFDP-2: Thin section preparation protocol

Two thin sections are to be prepared; **pure quartz cuttings (Q)** and **bulk rock cuttings (R)**
Notes: Wear personal protection equipment (PPE) appropriately; gloves are provided for handling epoxy, ear and eye protection for use of saw. Oven temperature should remain at 60 °C, avoid activating the timer function. Ensure water reservoir for saw is maintained, refill with water from the hose / creek.

Creating the block

1) Acquire cuttings and depths from cutting curators, should be dried and cleaned.
2) Separate as many pure quartz cuttings from the bulk rock cuttings as possible with tweezers / spatula.
3) Bond block moulds securely to glass plate with sticky back plastic – ensure mould bottoms are clean to prevent leaks.
4) Mix epoxy resin:hardener as 5:1. In order to fill a SINGLE mould 6 ml total of mix is required.
5) Cover the bottoms of each mould with a thin layer of epoxy.
6) Sprinkle grain cuttings into the mould, ensure cuttings are spread out evenly and are touching the glass base.
7) Fill mould with remaining epoxy and slam (gently) on the table to remove bubbles.
8) Cure in the oven at 60 °C for ~30 mins.
9) Remove from oven and check hardness, submerge in water to cool.
10) Use the arbor press set up to remove blocks from moulds.

Polishing the block

11) Use the lapper and 240 grit to expose the cuttings at the block base, ensure even pressure is applied and block is moved across plate surface. Try to expose as many grains as possible (all).
12) Once cuttings are exposed use 600 grit to give a final polish for ~2 mins, ensure the full surface of glass polishing block is used.
13) Wash and dry blocks.

Applying block to glass slide

14) Mix ~3 ml total of epoxy and apply a very thin layer to two fresh slides. Apply a small amount of epoxy to the polished block face and apply to the centre of the slide.
15) Place slides and blocks into oven ensuring they do not slide off, allow to cure for ~20 mins or until hard.
16) Remove from oven and allow to cool (make sure oven door is completely latched shut).

Removing excess block material

When using the saw ensure adequate PPE is used i.e., safety goggles and ear protection.

17) Mount the bottom of the slide into the right angle jig of the saw; support the slide / block against the side.
18) Ensure reservoir of saw is sufficiently filled and turn on taps to lubricate / cool the cut. Initiate saw at wall switch
19) Slowly push block into the path of the saw blade, cut ~1/2 way through block, return the jig to its original position and flip sample. Cut the remaining half retaining the removed block.

Polishing slide

20) Begin polishing the slide with 240 grit, move the slide across the lapper plate while polishing and apply pressure depending to varying thickness of slide. More pressure on thicker areas. Check slide very frequently with optical microscope to avoid over polishing.
21) Once blue to purple interference colours are visible in quartz switch to 600 grit until the majority of quartz cuttings show grey interference colours. Ensure sections do not get too thin as material will be lost and damage to the grains will occur. Interpretation will be comprised.
22) Dry and clean sections.

Finishing touches

23) Apply a thin strip of UV glue to surface of cuttings, cover with a single cover slip ensuring an even spread below slip.
24) Put under UV lamp for ~30 seconds, turn off after use.
25) Once cured wash slide with ethanol and paper towels.
26) If slide has excess cured epoxy on surface shave off with razor blade.
27) Label thin section and deliver to thin section describer.
    e.g., DFDP-2B_###_CU_(R)
    DFDP-2B_###_CU_(Q)
28) Put any excess material and block material into a labelled plastic bag and return to cutting curator.

2.7.2. Permeability calculation spreadsheet

The spreadsheet detailed in this section was adapted from an original spreadsheet designed by Daniel Faulkner and Peter Armitage and can be found in the Digital Supplementary Materials attached to the hard copy of this thesis.

Sheet SM 2.1 – *Water pore fluid properties*

Table SM 2.1 – *Water properties with temperature at 295.15 K (22 °C) and varying pressure (MPa) from The Engineering ToolBox, [2014]. C_V = Specific heat at a constant volume; C_P = Specific heat at a constant pressure.*

Table SM 2.2 – *Water properties with temperature at 295.15 K (22 °C) and varying pressure (MPa) from The Engineering ToolBox, [2014] required for permeability calculations.*

Figure SM 2.1 – *Graph of viscosity (Pa.S) variation with pressure (MPa).*

Figure SM 2.2 – *Graph of compressibility (Pa^{-1}) variation with pressure (MPa).*

Table SM 2.3 – *Calculated values for compressibility from pressure and density values.*

Figure SM 2.3 – *Graph of density (kg/m^3) variation with pressure (MPa).*

Figure SM 2.4 – *Graph of volume (m^3) variation with pressure (MPa).*

Sheet SM 2.2 – *Pressure system volumes (reservoirs) for Faulkner Triaxial Apparatus 2 (TR2), used to calculate permeability values. All pressure fitting dimensions and diagrams taken from The High Pressure Equipment Company, [2014].*

Table SM 2.4 – *Three Way Valves / Two Pressure Connections information.*

Table SM 2.5 – *High Pressure Elbows information.*

Table SM 2.6 – *High Pressure Tees information.*

Table SM 2.7 – *Triaxial apparatus pore pressure system pipe work volumes.*

Table SM 2.8 – *Seismic sample assembly pipe work volumes.*

Table SM 2.9 – *Honeywell Pressure Transducer (TJE) information.*

Table SM 2.10 – *Reservoir volume breakdown.*

Table SM 2.11 – *Circle to square and porous spacer volume breakdown.*

Sheet SM 2.3 – *Front sheet containing parameters for permeability calculations, calibrations for converting raw voltage data to pressure values and front graph / table to show permeability (m^2) variation with effective pressure (MPa).*

Sheet SM 2.4 – *Example sheet in which raw voltage data logged from the pressure transducers is loaded into the spreadsheet and converted to pressure values, equilibrium pressures are calculated and used to calculate the ln (Upstream Pore pressure – Calculated Equilibrium). The gradient from the ln (Upstream Pore pressure – Calculated Equilibrium) values is then used to finally calculate a permeability value. The time series cells are used to select the region of interest within the pressure log and the up calib (up calibration) is used to remove the calibration that allows the upstream and downstream pore pressure signals to be distinguished from one another in the Rig Computer LabVIEW Program.*

2.7.3. Ultrasonic velocity conversion script – isf to csv.

This program is used to convert the ultrasonic wave data that is saved from the Tektronix TDS 3032B oscilloscope in a .isf extension to a .csv extension. The follow command should be executed in MS-Dos: *cnvrtwfm.exe*. Executing this command generates a file called placeholdername.csv. In order to covert numerous .isf data files a batch script (.bat) file is used, see Figure SM 2.5 below for an example script. The batch file and files for conversion are placed in the same folder as the 'isf to csv' script when being executed.

```
@echo off
cnvrtwfm -l -8- p-p-M2-5.isf
cnvrtwfm -l -8- p-p-M2-15.isf
cnvrtwfm -l -8- p-p-M2-30.isf
cnvrtwfm -l -8- p-p-M2-40.isf
cnvrtwfm -l -8- p-p-M2-55.isf
cnvrtwfm -l -8- p-p-M2-65.isf
cnvrtwfm -l -8- p-p-M2-80.isf
cnvrtwfm -l -8- p-p-M2-90.isf
cnvrtwfm -l -8- p-p-M2-105.isf
cnvrtwfm -l -8- s-s-M2-5.isf
cnvrtwfm -l -8- s-s-M2-15.isf
cnvrtwfm -l -8- s-s-M2-30.isf
cnvrtwfm -l -8- s-s-M2-40.isf
cnvrtwfm -l -8- s-s-M2-55.isf
cnvrtwfm -l -8- s-s-M2-65.isf
cnvrtwfm -l -8- s-s-M2-80.isf
cnvrtwfm -l -8- s-s-M2-90.isf
cnvrtwfm -l -8- s-s-M2-105.isf
```

Figure SM 2.5 – *Example of a batch file. A text editor (Notepad or WordPad in Windows) can be used to create the batch file. The file extension of the file should be saved as .bat.*

2.7.4. Secondary ion mass spectrometry carbonate standards

	Haxby	OKA	LFC	NCC	DIS	UWC	M93	Dol
^{23}Na	2655	119	12	41	15	15	3195	26
^{26}Mg	18006	610	821	2657	528	472	1076	109475
^{27}Al	22	43	13	15	20	12	34	38
^{30}Si	28	102	18	31	40	17	45	1152
^{44}Ca	400220	400220	400220	400220	400220	400220	400220	218000
^{54}Fe	57	426	5966	15118	771	64	97	1137
^{55}Mn	1	1910	356	1461	433	75	2	79
^{88}Sr	2820	13363	542	909	484	394	8655	83
^{138}Ba	24	1801	0	5	0	286	4	8
^{140}Ce	0	715	0	5	4	1	0	4
δ^{18}O	-	-	19.029	20.366	17.348	23.28	25.93	-
^{16}O/^{18}O	-	-	0.0020434	0.0020460	0.0020400	0.0020519	0.0020572	-

Table SM 2.12 **–** University of Edinburgh NERC Ion Microprobe facility standards for carbonate trace element and δ^{18}O stable isotope analyses. Trace element values are reported in parts per million (ppm) with Ca artificially set at the stated values. Stable isotope standards are also reported. Standards were chosen to cover as wide a range of carbonate trace element concentrations as possible due to the highly variable nature of the Alpine Fault Zone carbonates.

Haxby**:** Deep Water coral, Haxby Ridge; used for its high ^{26}Mg content. See *Kasemann et al.*, 2009 (as PS69/318-1) for more details. ***OKA*****:** The Oka carbonatite complex, Quebec; used for their high ^{88}Sr, ^{138}Be and ^{140}Ce content. Provided by Blundy, J., University of Bristol. ***LFC, NCC*** **and** ***DIS*****:** Provided by Tony Dickson, University of Cambridge, United Kingdom; used for their high ^{54}Fe, ^{55}Mn and ^{88}Sr content. See *Swart*, 1990 for more details. ***UWC*****:** Inorganic calcite; sky blue marble from the Valentine Wollastonite Mine in the Adirondacks, USA, also known as University of Wisconsin Calcite; used for its high ^{88}Sr and ^{138}Ba content. See *Graham et al.*, 1998 for more details. ***M93*****:** also known as M93-T-FC1. Porites coral micro-atoll from the north coast of Papua New Guinea; used for its high ^{23}Na, ^{26}Mg and ^{88}Sr content. Provided by Allison, N., St Andrews University, United Kingdom. ***Dol*****:** Dolomite of unknown origin; used for its high ^{26}Mg content.

3. Permeability and seismic velocity and their anisotropy across the Alpine Fault, New Zealand: an insight from laboratory measurements on core from the Deep Fault Drilling Project

M.J. Allen, D. Tatham, D.R. Faulkner, E. Mariani, and C. Boulton
Published in Journal of Geophysical Research: Solid Earth

Key Points

- Low permeability and low seismic velocity is associated with the damage zone of the Alpine Fault Zone, New Zealand.
- The development of pervasive gouge-filled and calcite-filled fractures explains the low permeability and low seismic velocity.
- Seismic velocity anisotropy is low (<30 %) due to the lack of preferred orientation of the fracture network in the fault damage zone.

Abstract

The Alpine Fault, a transpressional plate boundary between the Australian and Pacific plates, is known to rupture quasiperiodically with large magnitude earthquakes (M_w ~8). The hydraulic and elastic properties of fault zones are thought to vary over the seismic cycle, influencing the nature and style of earthquake rupture and associated processes. We present a suite of laboratory permeability and P (V_p) and S (V_s) wave velocity measurements performed on fault lithologies recovered during the first phase of the Deep Fault Drilling Project (DFDP-1), which sampled principal slip zone (PSZ) gouges, cataclasites and fractured ultramylonites, with all recovered lithologies overprinted by abundant secondary mineralization, recording enhanced fluid-rock interaction. Core material was tested in three orthogonal directions, orientated relative to the down-core axis and, when present, foliation. Measurements were conducted with pore pressure (H_2O) held at 5 MPa over an effective pressure (P_{eff}) range of 5 – 105 MPa. Permeabilities and seismic velocities decrease with proximity to the PSZ with permeabilities ranging from 10^{-17} to 10^{-21} m^2 and V_p and V_s ranging from 4400 to 5900 m/s in the ultramylonites / cataclasites and 3900 to 4200

m/s at the PSZ. In comparison with intact country rock protoliths, the highly variable cataclastic structures and secondary phyllosilicates and carbonates have resulted in an overall reduction in permeability and seismic wave velocity, as well as a reduction in anisotropy within the fault core. These results concur with other similar studies on other mature, tectonic faults in their interseismic period.

3.1. Introduction

The quantitative characterization of the physical properties of fault zones, such as permeability and the transmission of seismic waves, is essential in order to understand the influence they have on fluid flow and seismicity in the brittle crust. Upper-crustal fault zones can be divided into three primary components: the fault core, the damage zone, and the host protolith. These components may be lithologically and structurally distinct and vary in proportion according to geological setting [*Chester and Logan*, 1986; *Caine et al.*, 1996; *Faulkner et al.*, 2010]. The fault core can consist of singular or multiple anastomosing slip surfaces and is where the highest strain and most displacement are accommodated [*Faulkner et al.*, 2003]. This core is usually nested within a damage zone, a region of kinematically related cracks and small faults, decreasing in density with distance from the core and transitioning into the local host protolith [*Anders and Wiltschko*, 1994; *Wilson et al.*, 2003; *Mitchell and Faulkner*, 2009].

The Alpine Fault in New Zealand is a major fault that forms the active plate boundary between the Pacific and Australian plates. The exhumation of the Alpine Fault hanging wall enables direct observations of the internal structure of a large plate-boundary fault, which is late in its seismic cycle and could therefore provide important information on the fault state at the time prior to an earthquake. The damage zone of the Alpine Fault of New Zealand is composed of diverse fault rock lithologies including clay-rich gouges, cataclasite, ultramylonites, and fault breccias, all overprinted, to different extents, by a geochemically altered zone, which, in this fault, masks evidence of a Brittle – Viscous Transition [*Sibson et al.*, 1981; *Caine et al.*, 1996; *Sutherland et al.*, 2012]

Fault zone architecture has a considerable influence on the hydraulic properties of the rock surrounding fault zones, with faults acting as either conduits or barriers for fluid flow or a combination of the two [*Caine et al.*, 1996; *Evans et al.*, 1997]. The determining factors are

dominantly the ratio of fault core (typically low permeability regions) to damage zone (high permeability regions), with the fault core acting as a barrier to flow across the fault and the damage zone acting as a conduit for fault-parallel flow [*Caine et al.*, 1996]. Furthermore, there may be inherent anisotropy within the rocks of both the fault core [*Faulkner and Rutter*, 1998; *Farrell et al.*, 2014] and the damage zone [*Faulkner and Armitage*, 2013]. This model is further complicated by the occurrence of fault-related alteration via fluid-rock interactions. This commonly leads to phase transformation, clay mineral generation, and cementation and hence variations in physical properties with time [e.g., *Wintsch et al.*, 1995; *Holdsworth*, 2004]

Investigation at a variety of scales requires quantification of the variables that control fault zone behaviour, for instance, whether slip is accommodated seismically or aseismically; whether a fault is a fluid conduit or barrier, can pore fluid overpressures develop, or will mineralization occur. Geophysical investigation techniques, such as seismic and electrical resistivity surveys, give broad regional information on fault structure [*Rietbrock*, 2001; *Eberhart-Phillips and Bannister*, 2002; *Hoffmann-Rothe et al.*, 2004; *Lay et al.*, 2016]. Direct observations of fault zones, and collection of samples for laboratory testing and microstructural analyses, are limited to faults that have been exhumed to the surface [e.g.,, *Wibberley and Shimamoto*, 2002] or that have been drilled and cored at depth [e.g., *Zoback et al.*, 2011]. Otherwise, only indirect measurements of some of the properties of faults at depth are possible through inference [e.g., *Faulkner et al.*, 2008; *Mitchell and Faulkner*, 2012].

In this paper, laboratory measurements of permeability and ultrasonic wave velocity are made on fault rock samples recovered from the central Alpine Fault Zone. These specimens were sampled from core collected from two shallow (<150 m depth) boreholes that were drilled as part of the Deep Fault Drilling Project (DFDP-1). These cores provide a unique opportunity to sample through a continuous section across the Alpine Fault Zone, uninterrupted by thick vegetation and relatively unaffected by surface weathering effects. First, a brief introduction to the Alpine Fault Zone and the DFDP project is given. Then the techniques used to prepare the delicate samples analysed are described. Finally, results of permeability, P and S wave velocity measurements, including their anisotropy, and microstructural controls, are described and their influence on fault zone processes during and after seismicity is discussed.

3.2. The Alpine Fault, New Zealand, and DFDP Drilling

The Alpine Fault Zone (AFZ), bounding the western edge of the Southern Alps on New Zealand's South Island, accommodates over 70 % of the relative motion between the colliding Australian and Pacific Plates [*Norris and Toy*, 2014]. The ramping of the Pacific plate over the Australian plate is accommodated through dextral-reverse movement, offsetting basement rocks laterally by ~470 km, with Quaternary horizontal displacement rates estimated at 21 – 27 mm yr^{-1} [*Norris and Cooper*, 2001; *Lamb et al.*, 2015]. Uplift across the fault is rapid, exhuming crustal rocks from depths of 20 – 30 km at a rate of ~6 – 9 mm yr^{-1} [*Little et al.*, 2002b]. Accompanying this rapid uplift is the advection of the regional geothermal gradient. Quartz fluid inclusion microthermometry places the gradient at 40 °C/km [*Toy et al.*, 2010], while titanium thermobarometry of quartz shows a gradient of 45 °C/km [*Cross et al.*, 2015] and recent shallow borehole measurements report gradients of 62.6 ± 2.1 and 125 ± 55 °C/km [*Sutherland et al.*, 2012, 2017].

Palaeoseismic evidence indicates that the Alpine Fault has had numerous geologically recent rupture episodes at, 1717 ± 25, 1630 ± 25 and 1460 ± 25 A.D., estimated to have moment magnitudes of 7.9 ± 0.3, 7.6 ± 0.3, and 7.9 ± 0.4, respectively [*Wells et al.*, 1999; *Rhoades and Van Dissen*, 2003; *Langridge et al.*, 2012]. This, coupled with recent seismicity patterns, geodetic strain records, and regional low-velocity zones indicative of high pore fluid pressures deep in the fault zone, suggests that the fault is locked above 6 – 12 km depth and is in the late stage of the earthquake cycle [*Eberhart-Phillips*, 1995; *Sutherland et al.*, 2007; *De Pascale and Langridge*, 2012; *Lamb and Smith*, 2013]. The global significance of the Alpine Fault in the study of major fault zones and crustal processes is considerable; the opportunity to study a locked continental plate boundary fault thought to be late in the earthquake cycle will yield insight into the prerupture conditions of a major fault and the nature of the interseismic physico-chemical processes that have taken place.

The Deep Fault Drilling Project (DFDP) was undertaken to better understand the processes that lead to major earthquakes by drilling into and observing a major continental fault during its build up to a large seismic event. The first phase of the Deep Fault Drilling Project (DFDP-1) comprised two pilot holes (DFDP-1A and DFDP-1B) drilled into an active thrust segment of the AFZ at Gaunt Creek, Westland in January 2011 (Figure 3.1). The boreholes reached depths of 100.6 m and 151.4 m, respectively, sampling a range of fault lithologies

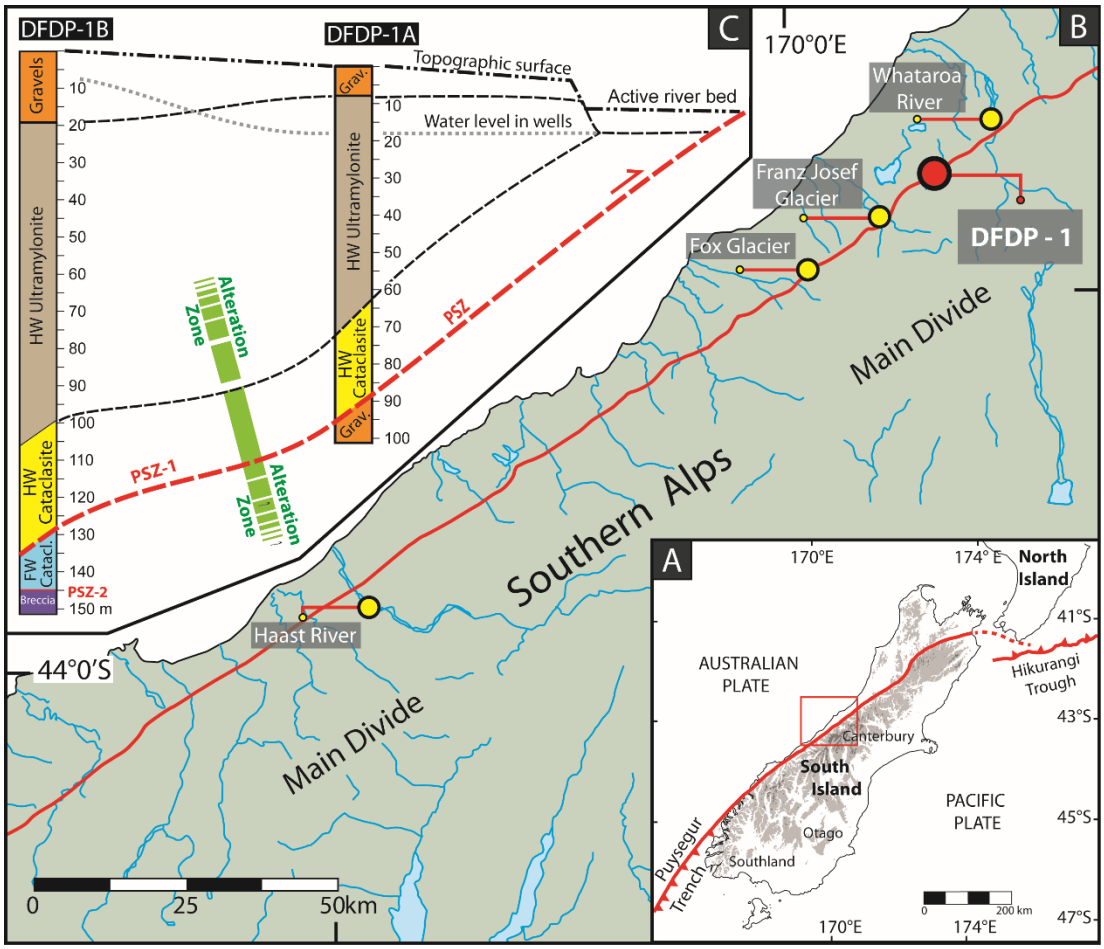

Figure 3.1 – ***[A]*** *Location of the Alpine Fault Plate Boundary across the continental New Zealand, South Island. Topography shading, light grey >800 m and dark grey >1800 m. Red box shows region of (**B**).* ***[B]*** *Central region of the Alpine Fault, location of DFDP-1 shown in red circle.* ***[C]*** *Cross-section of DFDP-1 boreholes showing schematic lithological divisions and local topography, adapted from Sutherland et al., [2012]. HW = hanging wall; FW = footwall.*

including ultramylonites, cataclasites and gouges. All samples used in this study were collected from core recovered from DFDP-1A and 1B. The principal slip zone (PSZ) of the AFZ was reached at 90.74 m depth in DFDP-1A and 128.44 m in DFDP-1B, marking the boundary between the Australian and Pacific Plates, with a second PSZ within footwall rocks recorded in DFDP-1B at 144 m. The PSZ in both boreholes is composed of clay-rich gouge (Figure 3.1) [*Sutherland et al.*, 2012].

Drilling revealed the presence of a ~30 m thick alteration zone overprinting both the fault core and damage zone. This 'alteration zone' was defined based on a distinctive light green colour in core and in outcrop produced by elevated concentrations of alteration minerals (e.g., phyllosillicates and carbonates) above regional levels [*Sutherland et al.*, 2012; *Townend et al.*, 2013; *Toy et al.*, 2015b; *Boulton et al.*, 2017a]. The degree of alteration increases with proximity to the PSZ within the fractured ultramylonites and cataclasites of the damage zone, implying that extensive fluid-rock interactions have occurred in the hanging wall of the Alpine Fault.

3.3. Methods

3.3.1. Sample selection and preparation

For this study, samples were collected from both the DFDP-1A and 1B drill cores. The drilled core diameter was 85 mm (PQ wireline bit size) and supplied for sample preparation as 200 – 300 mm-length intact core rounds and half rounds. These core sections were axially oriented to the borehole axis, however, due to core rotation during retrieval the azimuthal orientation could not be preserved [*Sutherland et al.*, 2011; *Toy et al.*, 2015]. The lithological character of the recovered core has been described in detail by *Toy et al.* [2015]. The core (and consequently the fault zone) was classified into a number of lithological units, based on the original protolith and level of damage / alteration. These unit classifications are outlined in Figure 3.2. Seven hanging wall cataclasites (Units 3 and 4), two footwall cataclasites (Units 6a and 6b) and the PSZ gouge were sampled in this study, representing a section across the plate boundary (Unit 5). For comparison, lithologies classified as potential protoliths for the Alpine Fault cataclasites were collected from the field and tested. These include an Alpine Schist, a foliated quartzofeldspathic schist, and a quartzofeldspathic ultramylonite all collected from the fault's hanging wall exposures in the

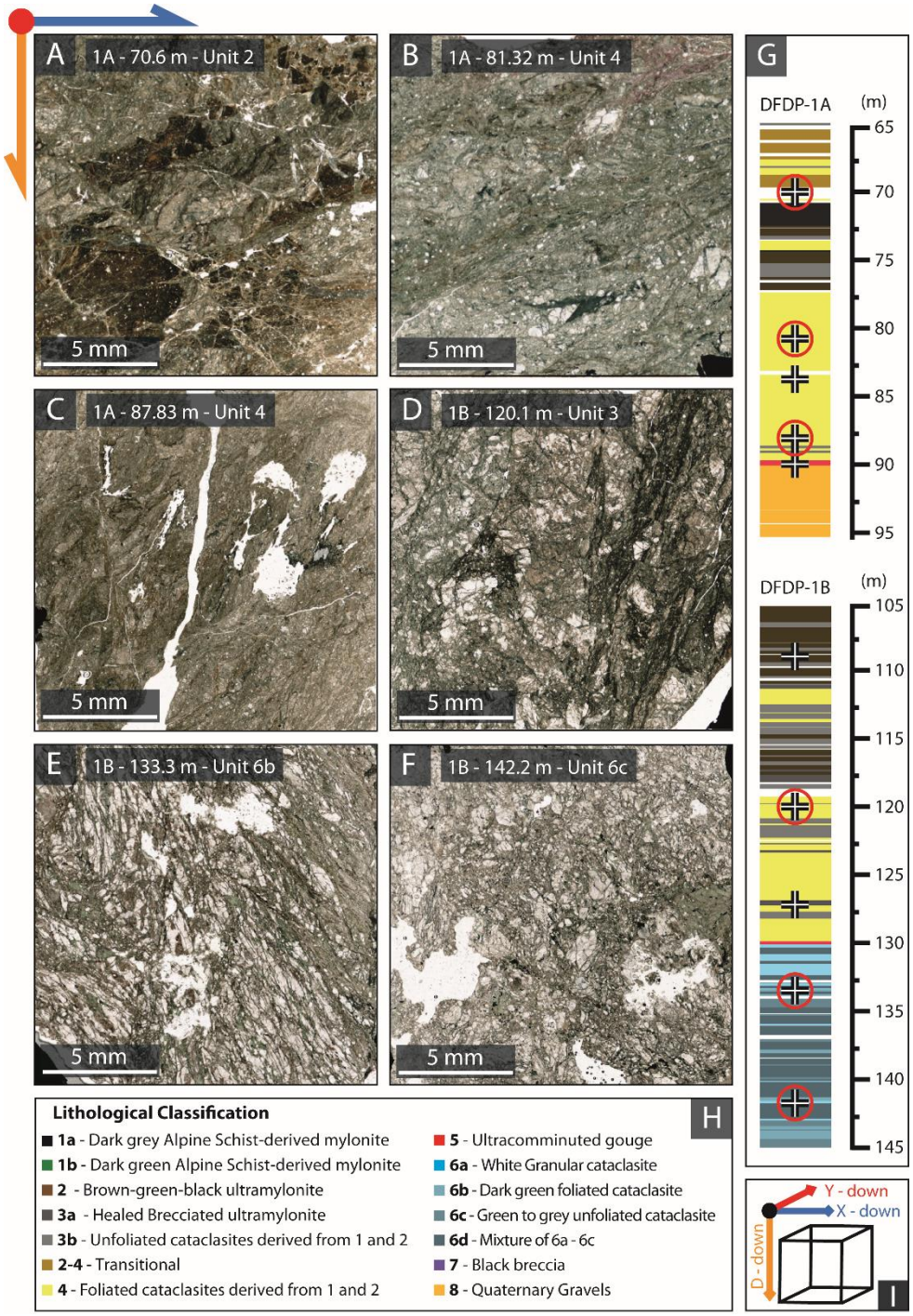

Figure 3.2 – *Photomicrographs of cataclastic microstructures from the hanging wall* ***[A – D]*** *and the footwall* ***[E and F]*** *of the Alpine Fault from both DFDP-1A and 1B drill cores. Blue / red / orange direction arrows denote the direction of measurement used in Figure 3.5 and 3.6. Crosses in (**G**) represent regions of sampling in the drill core; red circle denotes location of pictured cube micrographs (**A – F**). Classification scheme used in (**G**) and (**H**) adapted from Toy et al., [2015].*

Southern Alps foothills close to the drill site. For more details on these lithologies, see *Cooper* [1972] and *Little et al.*, [2015], respectively. Most hanging wall cataclasites used in this study were sourced from the alteration zone (see *Sutherland et al.*, 2012), a zone of heavily altered cataclasites rich in carbonate precipitation and authigenic phyllosilicates (illite / muscovite and chlorite). Figure 3.2 depicts selected optical micrographs of the tested material and a schematic outlining core sampling intervals.

Due to the friable nature of many of the test specimens, traditional methods of sample preparation such as water-lubricated coring, sawing, and grinding proved catastrophic, causing washout of the finer grain-size fractions and often total disaggregation. We therefore developed new, reliable preparation techniques to produce systematically intact samples suitable for experimental investigation. The aim was to produce cubic samples that could be used for measurements of anisotropy of both permeability and ultrasonic wave velocity.

Initially the core was wrapped in thin plastic wrap followed by the application of three to four layers of ModRoc® (gypsum plaster bandages). The original core orientation was recorded throughout the wrapping process, and once fully hardened, it was scribed onto the final plaster covering. Cutting the material was accomplished through the use of an annular saw (Revolution XT Ring Saw; Figure 3.3). The configuration of the annular blade means that only the actively cutting portion of the blade is in contact with the sample. This reduces grain plucking and disaggregation. Some cooling and lubricating fluid (water in this case) is required during cutting; this was applied by gently pressing a moist sponge to the blade edge.

After each cut, the exposed face was again covered by plastic wrap and ModRoc® following the above procedure and repeated until a ~15 × 15 × 15 mm cube was produced. The final cube is orientated to the vertical borehole axis, with two orientations orthogonal to the core cut according to any microstructural fabric if present, i.e., foliations, calcite veins and fractures. A final step, if the specimen proved sufficiently robust, involved hand grinding the cube surfaces with dry, fine emery paper to provide a smooth flat surface to maximise acoustic wave and fluid transmission from the sample assembly to the sample cube. Once preparation was complete, the specimen, porous steel spacers, and solid steel spacers were jacketed in heat-shrink polyolefin in order to secure the sample. This was then jacketed in

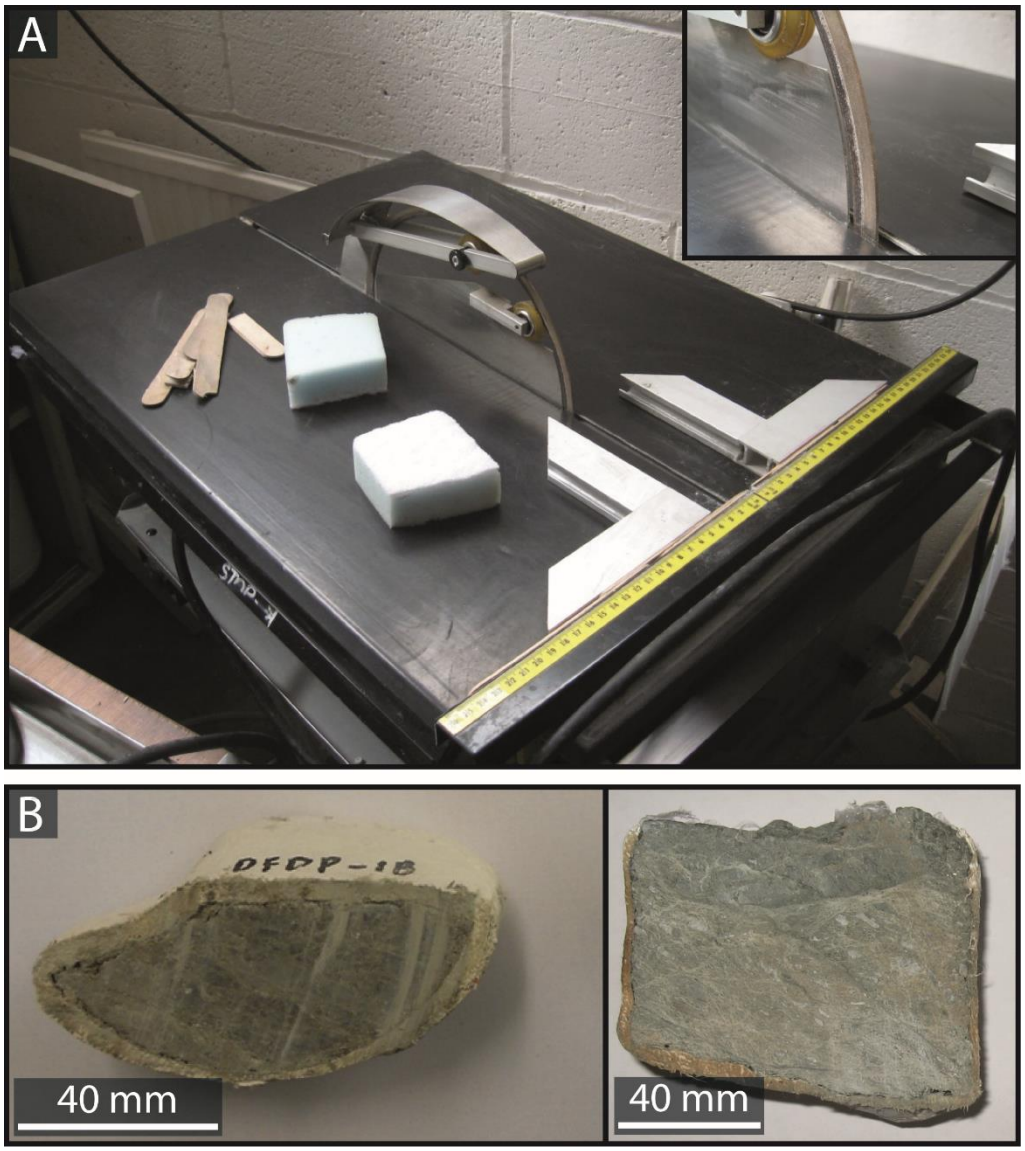

Figure 3.3 – [A] *The Revolution XT Ring Saw, developed by Gemini Saw Company, used in shaping the test specimens.* ***[B]*** *Examples of clean cut surfaces of cataclasites bound in ModRoc® bandages.*

PVC tubing, which forms a physical barrier between the sample and its pore fluid, and the silicon oil confining medium (Figure 3.4).

Once measurements were concluded, the experimental specimens were prepared for microstructural analysis, with their orientations preserved, using standard petrographic thin section techniques if the samples were sufficiently robust. Friable material was prepared by using 'water-free' polishing techniques by Paul Hands of Hand On Thin Sections Ltd. As the DFDP core is not horizontally oriented, the relative orientation of the observed microstructures cannot be conclusively related to the fault orientation.

3.3.2. Experimental procedure

The triaxial experimental apparatus used to undertake permeability and seismic velocity measurements is illustrated schematically in Figure 3.4 [*Faulkner and Armitage*, 2013]. During each experiment, the sample assembly was loaded into the pressure vessel, confining pressure (P_c) of 10 MPa was applied using a low viscosity silicon oil confining medium, and finally, the specimen was allowed to saturate with deionised water pore fluid which was allowed to equilibrate at a pore fluid pressure (P_f) of 5 MPa and an effective confining pressure (P_e) of 5 MPa, assuming a simple effective pressure law where the poroelastic constant α is equal to unity [*Rice and Cleary*, 1976]. Confining pressure and pore fluid pressure are servo-controlled to a resolution of ≤0.1 MPa.

Since each sample was recovered and tested again 3 times in three orthogonal orientations (x, y and z, see Figure 3.2I), no measurements were recorded during the first pressure cycle each sample experienced. A pressure cycle consisted of increasing the confining pressure through the range 10, 20, 35, 45, 60, 70, 85, 95 and 110 MPa, while holding the P_f at 5 MPa. These effective pressures (P_{eff} = 5, 15, 30, 40, 55, 65, 80, 90 and 105 MPa) are approximately equivalent to pressure conditions spanning the near surface to ~5 – 6 km depth. This method means that, during an experiment, the samples were overconsolidated with respect to the near-surface conditions, removing the effects of sample preparation, storage, transport, and the effect of unloading during retrieval between tests on the same sample, making comparison with borehole measurements difficult. Another consideration to be made is the evolution of the fault rocks during the exhumation of the Alpine Fault. As mentioned above, the Alpine Fault is a mature fault that has undergone extensive and

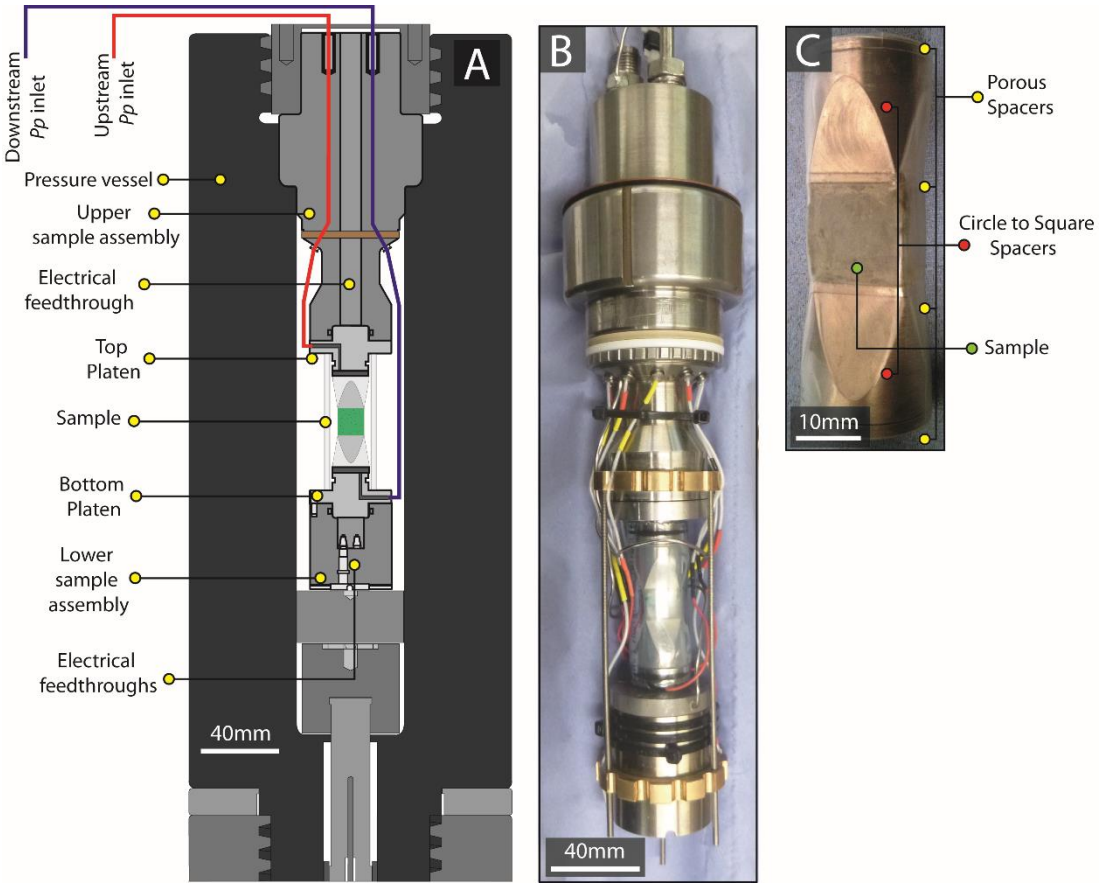

Figure 3.4 – [A] *Schematic illustration of the triaxial experimental apparatus used in the study, including the seismic sample assembly housed within the pressure vessel.* ***[B]*** *The seismic sample assembly with piezoelectric ceramics and pore fluid supply pipes set into the upstream and downstream platens.* ***[C]*** *A cube-shaped specimen set between porous steel spacers (both square and circle) and a circle to square adapter to allow coupling with the circular assembly platens.*

cyclical comminution and geochemical alteration. Consequently, the specimens tested are likely to be substantially different structurally and compositionally to fault rocks at depths of ~5 – 6 km. Nonetheless the results provide insight and an approximation of the permeability and seismic velocity of the Alpine Fault as it is exhumed from depth.

Piezoelectric ceramic transducers (Piezoelectric lead Zirconate Titanate – PZT-5H, fundamental frequency at 1.5 MHz), with P wave and orthogonal S wave polarization directions, are housed in each opposing platen and are used to produce and record ultrasonic P and S waves through the samples. The ultrasonic velocities are measured using the through-transmission method, utilizing the travel times and specimen length [*Birch*, 1960] after correction for the travel time through the loading platens. Elastic wave speeds were picked and velocities calculated over an effective pressure range of 55-105 MPa for *S-waves* (V_s) and 15 – 105 MPa for *P-waves* (V_p). Poor coupling between the loading platens and the test specimen at low effective pressures (<55 MPa for V_s and <15 MPa for V_p) made reliable picking of arrival times difficult, and so these data are not reported.

Permeability measurements were performed using the pulse transient technique [*Brace et al.*, 1968], involving the introduction of small pressure difference of <1 MPa to one end of the specimen and observing the pressure decay through the sample with time. One effective pressure cycle consisted of measuring the permeability, V_p and V_s at each effective pressure as the confining pressure is increased, with the unloading effective pressure path covering the same increments during measurement. A typical pressure cycle lasted between 3 and 7 days owing to the low permeability of some samples. Once one pressure cycle was completed for a given cube orientation, the specimen was removed from its jacket and reoriented and the above experimental procedure was repeated.

In a typical experiment, permeability and seismic velocities do not fully recover after deconfinement from the initial up-pressure leg, with upleg and downleg variations typically an order of magnitude for permeability and between 2 and 30 % for seismic velocities; see Supplementary Material Figure SM 3.1 for an illustration of this hysteresis. Subsequent variations after repeated pressure cycles become progressively smaller. Similar procedures and observations are reported by *Bernabe*, [1987], *Faulkner and Rutter*, [2000], and *Morrow et al.*, [2014]. The drying and unloading of samples at room conditions were

minimized by conducting experiments for each sample orientation in immediate succession or by sealing the sample in heat shrink or plastic film where this rapidity was not possible.

As these samples have undergone compaction and consolidation up to pressures of 105 MPa, the measurements do not correlate with borehole wireline and slug tests but rather reflect greater depths on the Alpine Fault. We refer to *Carpenter et al.*, [2014] for experimental results performed at in situ borehole conditions.

3.4. Results

3.4.1. Permeability Measurements

Permeability results are plotted as log permeability against effective pressure and show a systematic decrease with increasing P_{eff}, generally decreasing by larger increments over the lower P_{eff} range, ~5 – 40 MPa, presumably as handling / drilling-induced fractures close. This initial closure can account for a drop in permeability of up to 2 orders of magnitude (for example, the permeability trace for 1A-83.2 in Figure 3.5C); however this effect more commonly manifests itself as a drop of 1 order of magnitude. Once above ~ 30 MPa P_{eff} the rate of permeability reduction with effective pressure, in most cases, lessens with increasing pressure.

At P_{eff} 5 MPa permeabilities range from 1.49×10^{-17} m^2 in 1A-81.32 (D-down) to 1.35×10^{-20} m^2 in 1B-127.3 (X-down). At P_{eff} 105 MPa, the overall permeabilities range from 1.35×10^{-18} m^2 in 1A-81.32 (Y-down) and 1.25×10^{-21} m^2 in 1B-127.3 (X-down). In some instances, pressure sensitivity accounts for a greater variation in permeability than individual specimen variation, as shown by 1B-120.1 (D-down) and 1A-83.2 (Y-down) in Figure 3.5A and C.

Permeability variation and an indication of the permeability anisotropy throughout the boreholes are illustrated in Figure 3.6, showing the range of permeabilities of each orientation with variation in P_{eff}. With increasing proximity to the PSZ, permeability decreases. This trend is particularly noticeable in Figure 3.6A within the hanging wall alteration zone. This same feature is not as easily observed in Figure 3.6D, within the DFDP-1B core, as sparser sampling density makes it more difficult to highlight the trend,

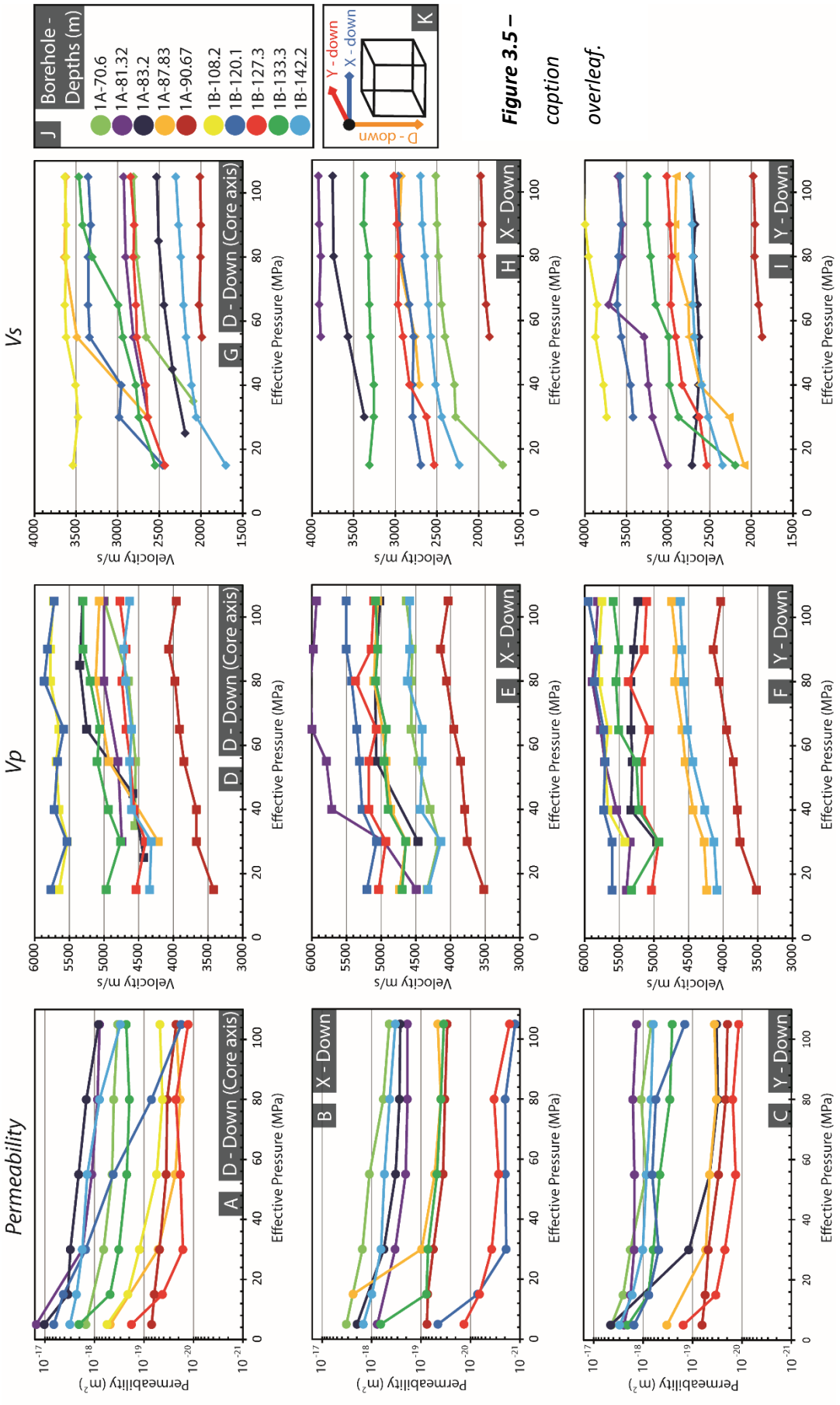

***Figure 3.5 –** caption overleaf.*

Figure 3.5 – *(above) Permeability* ***[A – C]****, P-wave velocity* ***[D – F]*** *and S-wave velocity* ***[G – I]*** *measurements as a function of effective pressure. Each row denotes the orientation of the specimen, illustrated in* ***K****. D-down is equivalent to the down core axis while X-down and Y-down represent two horizontal directions in the borehole; note the X and Y directions do not correlate between specimens due to the inability to horizontally orient samples from the drill core. Colours represent depths and are noted in the legend,* ***(J)****.*

particularly close to the PSZ. Within the DFDP-1B alteration zone, there is a decrease in permeability with depth, and the lowest permeability value of 1.25×10^{-21} m^2 was measured immediately above the PSZ. With increased distance from the PSZ, into the footwall cataclasites (e.g., 1B-142), permeability increases by up to 2 orders of magnitude from ~10^{-20} to ~10^{-18} m^2, respectively (see Figure 3.6D). Permeability measurements for the 'protolith' lithologies could not be performed as their permeability was too low for the resolution of the experimental apparatus, at ~10^{-22} m^2. At permeabilities lower than ~10^{-21} m^2, flow rates are very small and pores are inferred to be approaching molecular size. The permeability anisotropy exhibited by borehole specimens appears to have little correlation to orientation; this is conceivably due to the highly variable microstructures present in these fractured or comminuted lithologies. Direct correlation of permeability with specific microstructural causes is difficult to make, except in the case of 1A-90.67, the clay-rich PSZ gouge. This specimen exhibits the lowest permeability anisotropy at 40 %, potentially due to its finer grained and more homogenous structure in comparison to other fault core lithologies.

3.4.2. Seismic velocity measurements

Elastic wave transmission through the specimens shows a similar relation to increasing P_{eff} as permeability, with a rapid increase in velocity over initial pressure increments (e.g. 5 to 40 MPa) stabilizing once open fractures and porosity are reduced at high P_{eff} (~ 40 – 50 MPa). Both V_p and V_s show similar trends across the fault; the material exhibiting the highest V_p and V_s is on the periphery of the pervasive alteration zone, farthest from the PSZ, (1B-108.2 and 1B-120.1) with V_p of ~5700 m/s and Vs of ~4000 m/s (see Figure 3.6B-F).

Both V_p and V_s decrease with increased proximity to the PSZ with a substantial reduction in velocity within the PSZ at 1A-90.67. Across the respective pressure ranges, hanging wall V_p

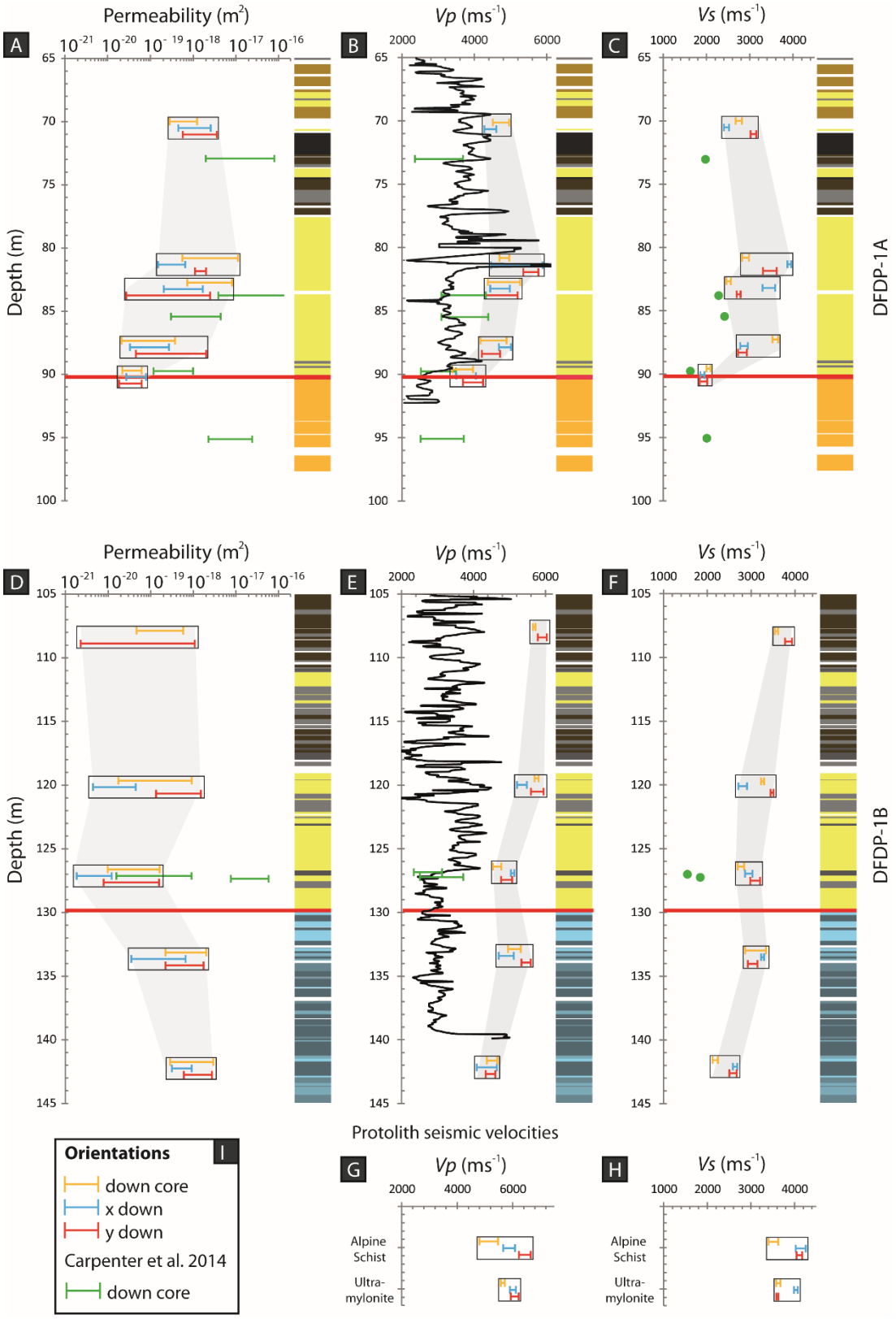

***Figure 3.6** – caption overleaf.*

Figure 3.6 – *(above)* ***[A-I]*** *Permeability and Seismic velocity ranges for material from DFDP-1A and DFDP-1B with depth, including field derived protolith lithologies* ***[G and H].*** *Each tested specimen is represented by a bar colour coded to orientation (see* ***I****); note the X and Y directions do not correlate between specimens due to the inability to horizontally orient samples from the drill core.* P_{eff} *ranges for permeability measurements are 5 – 105 MPa,* V_p *15 – 105 MPa and* V_s *55 – 105 MPa.* P_{eff} *range for measurements from Carpenter et al., [2014] at 2.5 – 65 MPa. Wireline sonic velocity logs in (****B****) and (****E****) adapted from Townend et al., [2013].*

values span 4500 to 5900 m/s with V_s values between 2400 to 4000 m/s. Material from the footwall exhibits lower velocities than the hanging wall with V_p values ranging from 4400 to 5600 m/s and V_s values from 2200 to 3500 m/s. PSZ material exhibits the lowest V_p from 3900 to 4200 m/s and V_s at 1900 to 2000 m/s. Figure 3.6G and H show seismic velocity measurements for the 'protolith' lithologies, with the Alpine Schist V_p from 4800 to 6700 m/s and V_s at 3400 to 4250 m/s while the ultramylonite had V_p of 5600 to 6170 m/s and V_s 3600 to 4030 m/s.

Performing measurements parallel to the down core axis and in two further mutually orthogonal orientations allowed the seismic velocity anisotropy present in these rocks to be investigated and approximated. As only three orientations were measured in this study and these directions are not necessarily oriented parallel to the principal axes of the dynamic elasticity tensor, the measurements presented provide only a minimum constraint on anisotropy. Figure 3.7 illustrates the magnitude of this anisotropy with depth at 105 MPa, with the anisotropy calculated using Equation 6 following *Mainprice and Humbert*, [1994],

$$\mathrm{AV_{p,s1,s2}} = \left(\frac{V_{p,s1,s2}\ \max - V_{p,s1,s2}\ \min}{\overline{V_{p,s1,s2}}}\right) \times 100 \qquad (6)$$

where $V_n max$ and $V_n min$ are the maximum and minimum seismic velocities at a given P_{eff} increment with the subscript n denoting the wave type, while $\overline{V_n}$ is the averaged velocity (0.5 ($V_n max$ + $V_n min$)) and AV_n is the value of anisotropy in percent.

The degree of anisotropy present in the test specimens appears far greater for permeability than for seismic wave velocity. Presumably, this is largely due to the maintenance of

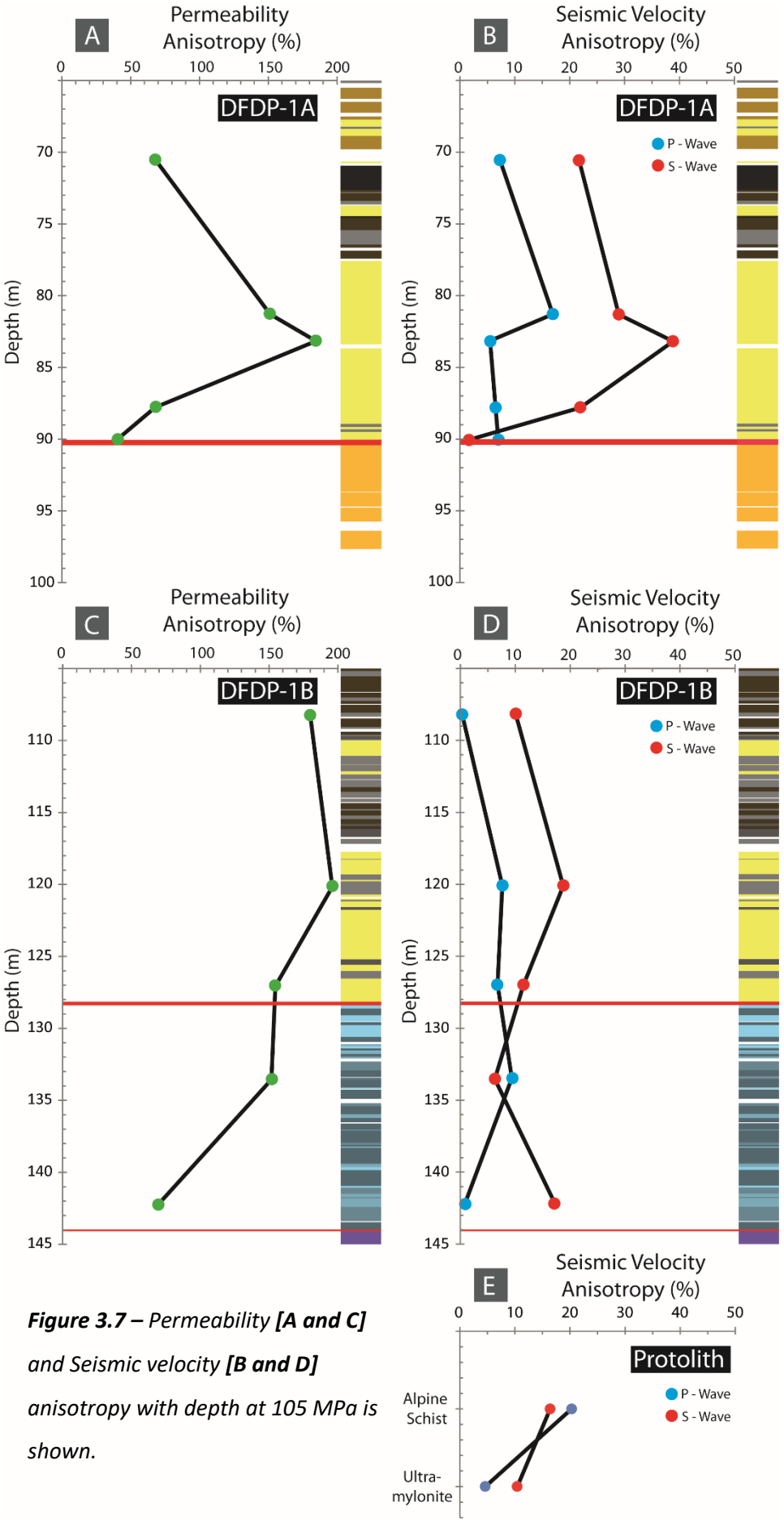

Figure 3.7 – *Permeability* ***[A and C]*** *and Seismic velocity* ***[B and D]*** *anisotropy with depth at 105 MPa is shown.*

interconnected voids and fractures for fluid mobility, which will be greatly affected by increasing P_{eff}, while the propagation of elastic waves is not limited by fracture / void connectivity in the same way. Similar observations were made by *Fortin et al.*, [2011] when hydrostatically loading fractured basalt. We must also state that the anisotropies measured in this study, due to the arbitrary horizontal directions of the test specimens, are a minimum value of transverse anisotropy.

In most specimens, most notably in 1A-83.2 and 1B-142.2, V_{s1} anisotropy is much greater than that found for V_p, potentially due to attenuation as an *S-wave* pulse will be more sensitive to scattering of wave energy via impingement on an inhomogeneity, potentially a pore, fracture, foliation or lithological interface [*Sato et al.*, 2012]. This may explain the 33 and 17 % difference in the anisotropy in 1A-83.2 and 1B-142.2, respectively. 1A-83.2 contains a penetrative foliation that may allow for easier transmission of *P-waves* while the *S-waves* are more inhibited by the aforementioned factors, particularly pores and fractures. However, 1B-142.2 has no obvious mineral or fracture alignments, implying that the heterogeneity in clast size, shape, and orientation may also result in a greater variation of V_s with orientation than with V_p. Saturation of the fractures present may also be an important influence on seismic wave velocity, particularly in regard to the anisotropy observed. In this study we can assume that the fractures are fully saturated, explaining the greater anisotropy seen in *Vs* than in *Vp;* if anisotropy was greater in *Vp,* this would imply that fractures remained dry throughout the experiments [*Guéguen and Sarout*, 2011].

3.4.3. Specimen Microstructural Variation

Figure 3.2 shows the mm to cm-scale microstructures that govern the variation of physical properties throughout the Alpine Fault damage zone in both the hanging wall and footwall. Gouge-filled fractures are common throughout the alteration zone, generally manifesting as low-displacement shears filled with unconsolidated gouge material of the same composition as adjacent wall rock with little authigenic clay, appearing as angular to subangular shaped clasts ranging from sub µm to 100 µm diameter (Figure 3.8C). Occasionally, elongated clasts show a preferred orientation parallel to the vein walls (Figure 3.8E). These fractures are typified by their lack of carbonate cementation or phyllosilicate alteration and assumingly belong to a relatively recent episode of deformation. Fracture density through the Alpine Fault's damage / alteration zone was quantified by *Williams et*

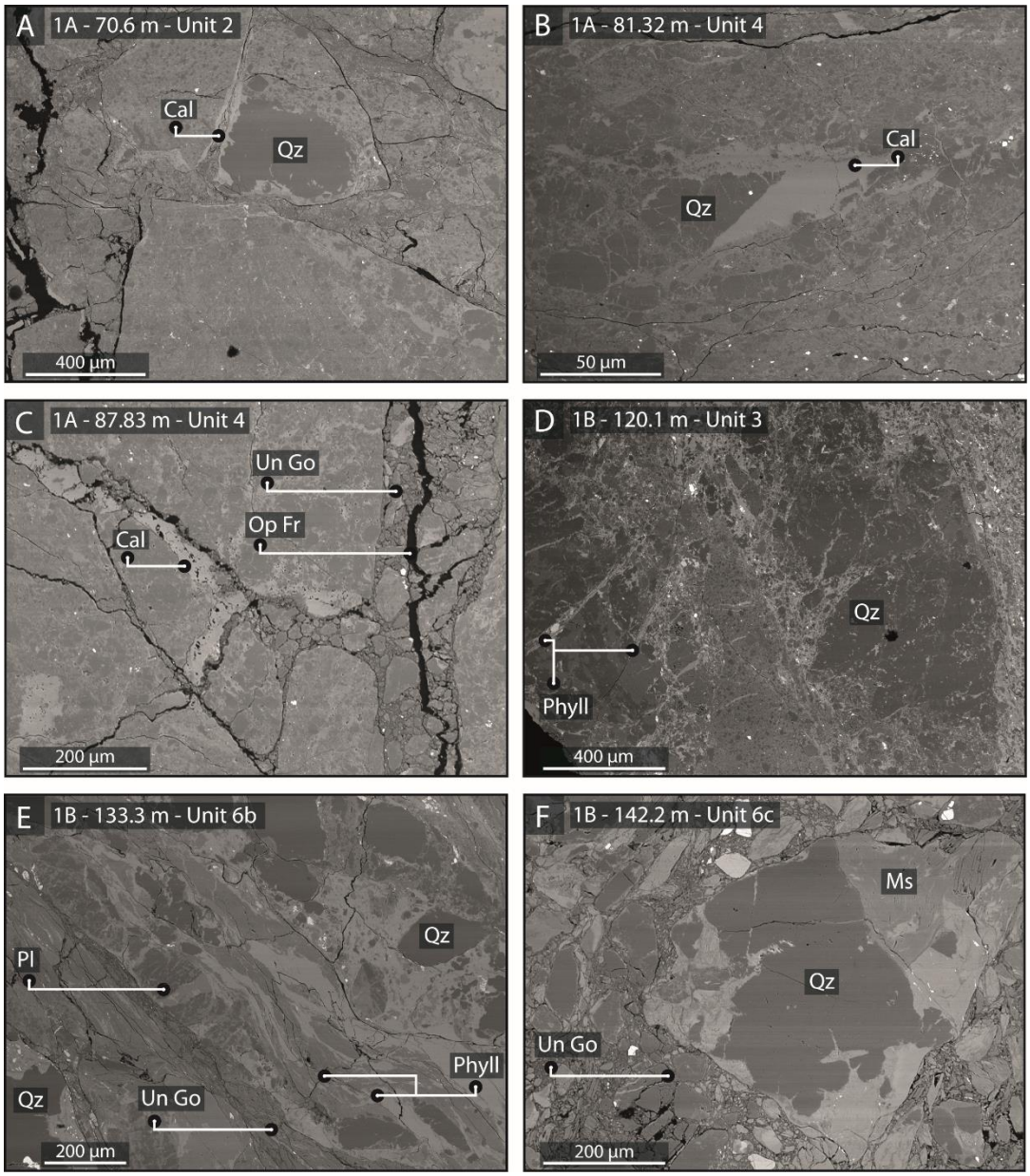

Figure 3.8 – *Backscatter Electron images of hanging wall* ***[A – D]*** *and footwall* ***[E – F]*** *cataclasites. Mineral abbreviations after Whitney and Evans, [2010]; additionally, Op Fr = open fracture, Un Go = unconsolidated gouge, Phyll = phyllosilicate. (**A**), (**B**), and (**C**) exhibit carbonate-filled veins; (**C**), (**E**), and (**F**) exhibit unconsolidated gouge-filled fractures; (**D**) contains with clay-filled fractures.*

al., [2016] using CT scans of the DFDP-1 core material, reporting that damage zone structures (including open, healed and semi healed fractures) do not increase in density with proximity to the PSZ, remaining largely uniform throughout the cored interval of the fault. The distribution of these fractures and the presence of authigenic clay minerals within them are the key controlling factors governing the permeability and seismic velocity variations of these rocks. NanoCT scans of specimens from this study are included in the Digital Supplementary Material as Videos SM 3.1 and SM 3.2; these images highlight the presence of throughgoing open fractures with little evidence of shear, particularly visible in 1B-120.1 and fractures that contain gouge material visible in 1B-133.3. Cataclasites in the hanging wall are generated from an amphibolite-facies quartzofeldspathic or metabasic mylonitic protolith and are typified by a pervasive carbonate infill, as both cement and vein precipitation, composing ~5 % of the bulk mineralogy. Veining is evidently multi-generational, exhibiting cross-cutting relationships, varying orientations (Figure 3.2), and evidence of reactivation shown by crack-seal structures. Foliation, when present, is typified by alternating phyllosilicates or opaque oxides anastomosing around sub-mm relict protolith quartz fragments.

In contrast, the footwall cataclasites contain far less carbonate veins, and as a result are far more incohesive and generally exhibit a lighter grey-white colour owing to their prehnite-pumpellyite to greenschist-facies granitic protolith [*Toy et al.*, 2015b]. Foliation is similarly variable in pervasiveness, from distinct as in 1B-133.3 (Figure 3.2E) with obvious alternating quartz / feldspar and phyllosilicate fabric, to completely absent as in 1B-142 (Figure 3.2F). Foliation is seen to be highly variable in orientation on the sub-cm scale. In contrast with both cataclasites, the PSZ ultracomminuted gouge has a finer grain size (<10 μm) and consists of two main gouge types that occur in discrete layers ~30 – 50 mm thick: a brown smectitic gouge and a blue chloritic / micaceous gouge, described in detail by *Boulton et al.*, [2014], the latter of which was tested in this study.

Overall, the mineralogy across the fault, in both the hanging wall and footwall, remains largely constant. X-ray diffraction results from *Boulton et al.*, [2017] show that calcite, precipitated as cements and veins, vary in proportion more than any other mineral phase, comprising ~5 % of the modal mineralogy in the hanging wall, decreasing sharply across the PSZ to ~1.5 % in the footwall. Phyllosilicates such as chlorite and biotite are present

throughout the fault zone, while smectite, an authigenic swelling clay, appears only within the PSZs.

3.5. Discussion

The temporal and spatial variations of permeability and seismic velocity within fault zones are thought to be largely influenced by the variation of fracture density with respect to the fault zone [*Faulkner et al.*, 2003; *Mitchell and Faulkner*, 2008, 2012]. This picture is complicated when lithological variation occurs with the fault zone [e.g., *Wibberley and Shimamoto*, 2002] and also when mineralization occurs within both the damage zone and fault core. Mineralization can occur in two ways: as authigenic mineral growth that produces clay mineral formation and as precipitation that may, respectively, heal and seal the fault [*Madariaga et al.*, 1998; *Tenthorey and Cox*, 2006]. In this section, we consider how mineralogical and microstructural characteristics influence the fault zone physical properties, how the Alpine Fault Zone compares with other mature fault zones, and finally, how mineralogy and microstructure influence earthquake processes such as thermal pressurization and the propagation of seismic waves.

3.5.1. Microstructural controls on physical properties

Other than a few discrete features such as the PSZ and pseudotachylyte veins, the bulk mineralogy remains largely consistent across the fault zone [*Toy et al.*, 2015b; *Boulton et al.*, 2017a]. Hence, the bulk mineralogy does not appear to be a major factor controlling the observed variations in physical properties. Consequently, the fracture density might be considered to be the primary influence on the physical properties at the scale of the experimental measurements. As fractures make up proportionally far less of the bulk rock than the matrix, the small variations of mineralogy associated with fractures, primarily carbonate and phyllosilicate fill, are masked by the bulk rock mineralogy in regard to seismic velocities. However, small variations in the overall mineralogy, due to fracture infill, could significantly modify the fluid transport properties of the fractures and hence those of the bulk rock.

Williams et al., [2016], using combined CT and SEM analyses of the DFDP core, to a fracture aperture resolution of >1 mm, discovered that, within the alteration zone, the majority of

the fault damage is cemented with varying carbonate, clay, and gouge materials (72 % being fully sealed and an additional 24 % remaining partially sealed). Outside of the alteration zone (<50 m away from the PSZ), fault damage may persist between periods of seismicity, as evidenced by the high in situ permeability measured during wireline slug tests and the lack of intact core recovery outside of the alteration zone due to disaggregation [*Sutherland et al.*, 2012]. Fracture porosity is likely to be the main control of fluid flow in these damage zone ultramylonites and cataclasites, as the intact protolith or cemented regions have very low permeabilities, below the capabilities of measurement of the experimental apparatus detailed above, at $<10^{-22}$ m^2 as measured in the protolith lithologies in this study. The length scales of the fractures within a rock mass have great influence on permeability and seismic wave velocities; this scale effect is detailed in *Brace et al.*, [1968] and *Nara et al.*, [2011] regarding permeability and *Budiansky and O'connell*, [1976] regarding seismic velocities. Samples prepared for this study were actively chosen away from the macroscopic fractures described by *Williams et al.*, [2016] in order to avoid sample failure during preparation. With this in mind, the measurements reported here represent the intact matrix properties of the fault lithologies, giving the minimum permeability and maximum seismic velocity values of the Alpine Fault due to the fine-scale sampling bias inherent in this study, where heterogeneity of microstructure is a key characteristic of all fault rocks analysed. In the following section, the nature of the fracture networks and their fillings present in the experimental samples are explored.

Open fractures within core material are predominantly opened along pre-existing gouge-filled or carbonate-filled fractures, as visible in Figure 3.8C and Figure 3.8E. These are presumably stress-relief fractures, opened during core retrieval, handling and resting prior to testing and microstructural analysis preparation. This is supported through the lack of displacement on the fracture or mobilisation of the fracture-fill, indicating that the fractures have opened up by dilation in 'dry' conditions. As illustrated in Section 3.1, there is a significant initial drop in permeability and increase in seismic velocity after an initial pressure interval between 5 and 40 MPa, after which trends in the data remain largely constant, marking the closure of open fractures and voids and allowing a more representative measurement for the specimen to be taken [*Nara et al.*, 2011].

Immediately after a seismic event, it is possible that the permeability within the fault damage zone is enhanced by 3 – 8 orders of magnitude [*Miller et al.*, 2004; *Mitchell and*

Faulkner, 2008; *Gomila et al.*, 2016]. This transiently enhanced fluid mobility coupled with reduced grain size via cataclasis can result in a period of heightened fluid-rock interaction. *Warr and Cox*, [2001] determined two generations of phyllosillicates on the Alpine Fault, hydrous chloritization at ~320 °C, followed by the generation of swelling clays at shallower depths and temperatures of ~120 °C. The dominant clay phases within the Alpine fault hanging wall are white mica (illite / muscovite) and chlorite [*Boulton et al.*, 2012, 2017a; *Schleicher et al.*, 2015]. *Schleicher et al.*, [2015] found enhanced levels of authigenic illite and smectite are present in the PSZ in contrast to higher levels of metamorphic illite / muscovite in surrounding cataclasites. White mica and chlorite fill a large proportion of fractures in the hanging wall while smectite is found solely in the brown PSZ fault gouges, generated from the low temperature alteration of illite / muscovite and chlorite which is further altered into kaolinite and goethite [*Craw*, 1984; *Boulton et al.*, 2012, 2017a; *Schleicher et al.*, 2015], with the combination of ultracomminuted grains and swelling clays on the PSZ reducing permeability to ~10^{-20} to 10^{-21} m^2, becoming an hydraulic seal.

The nature of carbonate precipitation is variable, occurring as veins both parallel and cross-cutting foliation, bounding gouge-filled fractures, disseminated cement in gouge-filled fractures and fragmented clasts within gouge and cataclasite. Hanging wall cataclasites contain a pervasive carbonate infill, and as a result are more cohesive than the carbonate-poor footwall cataclasites, resulting in the increase in permeability with distance from the PSZ into the footwall (Figure 3.6D).The presence of calcite networks indicates periods of damage-enhanced fluid transport focussed within the hanging wall cataclasites and ultramylonites. Mineralization effectively 'seals' the newly formed postseismic fracture networks resulting in an increase in strength and stiffness relative to its immediate post-rupture state and lowering of permeability of the fault zone lithologies [*Lund Snee et al.*, 2014]. Similar processes are inferred to take place in geothermal fields, with mineral precipitation reducing permeability potentially on the time scale of days for mm – scale fractures in high temperature settings, especially if considerable fluid pressure fluctuation occurs [*Griffiths et al.*, 2016; *McNamara et al.*, 2016].

A main control on the anisotropy of physical properties is the presence or lack thereof of a tectonic foliation [*Okaya et al.*, 1995; *Okaya and Christensen*, 2002]. For instance, the poorly developed fabric in the PSZ gouge exhibits the least anisotropy, while distinctly foliated specimens such as 1A-83.2 exhibit a strong anisotropy, with higher seismic wave

velocity and permeability parallel to foliation and slower values perpendicular to the foliation (Figures 3.6 and 3.7). However, the nature of the cataclastic fabrics within the alteration / damage zone is spatially variable, with pods of intensely foliated material (1B-133.3) located within wide swath of unfoliated material (1B-142) or vice versa (Figures 3.2E-F and 3.8E-F). With this in mind, the experimental results from this study place a lower limit on matrix permeability and an upper limit on matrix seismic wave velocity, respectively, through the Alpine Fault. Overall, both permeability and seismic velocity anisotropy show a general trend to decreasing toward the principal slip zones, in both DFDP-1A and 1B.

3.5.2. Correlation with other studies

Figure 3.6B and E show the DFDP-1 wireline logs as a black trace in comparison to the results presented here. As each test specimen was pre-compacted to 105 MPa P_{eff}, it is not possible to make a direct comparison to measurements made at pressure conditions within the DFDP-1 borehole. Furthermore, the sampling length scale for the *P-wave* velocity wireline tool (a single source, dual receiver logging sonde as documented in *Townend et al.*, [2013] used to collect V_p data is 304.8 mm, approximately 20 times the length of the experimental specimens used in this study. The selection of samples and subsequent sample preparation means that measurements were made on coherent core material that was perhaps more intact than the in situ material. Large, relative to specimen size, throughgoing fractures may not have been sampled in the experiments, and hence measurements provide a minimum value of permeability and a maximum value of seismic velocity. However, the trends of the data show a reasonable comparison, indicating that the measurements made here may be representative of the permeability and seismic velocity at greater depths, equivalent to the effective pressures used in the experiments. Slug tests performed in the distal damage zone of DFDP-1 recorded in situ permeability of 10^{-14} m^2, indicating that permeability may drop by up to 5 orders of magnitude at low effective pressures toward the fault core [*Sutherland et al.*, 2012].

Carpenter et al. [2014], illustrated in Figure 3.6B and E, presented similar laboratory measurements of DFDP-1 fault rock permeability and seismic velocity, but at a lower P_{eff} range (2.5 – 65 MPa) with no pre-consolidation. The permeability data presented in this study correlate with *Carpenter et al.'s* [2014] data, with measurement ranges overlapping at similar depths in the core. In terms of seismic velocity, the data presented here are

higher than those in *Carpenter et al.* [2014]. This is most likely due to pre-consolidation of samples in the method used here, and therefore, the values for seismic velocity are more representative of those at greater depth than the data of *Carpenter et al.* [2014]. Other factors that might produce differences are the variation in specimen dimensions, frequency, and natural specimen variation.

The overall variations in seismic velocities with depth in this study and that of *Carpenter et al.* [2014] correlate well with each other (Figure 3.6B and E). The PSZ exhibits lower velocities than the surrounding cataclasites, and the higher velocities witnessed in the hanging wall cataclasites in contrast to the footwall are indicative of a greater degree of carbonate cementation and cohesiveness and potentially asymmetrical damage imparted upon the fault zone during seismicity [*Townend et al.*, 2013].

Physical property measurements of the Alpine Fault Zone are consistent with a number of mature, geochemically altered fault zones worldwide. Similarities with studies performed on the Nojima Fault Zone [*Mizoguchi et al.*, 2008], Median Tectonic Line (MTL) [*Wibberley and Shimamoto*, 2002], the San Andreas Fault [*Morrow et al.*, 2014], and the Carboneras Fault [*Faulkner et al.*, 2003] highlight the microstructural complexity within a fault damage zone, with numerous episodes of brittle rupture damage and subsequent fluid-rock interactions. Laboratory gas permeability measurements of the MTL fault core show values between 10^{-13} and 10^{-21} m^2 (P_{eff} = 50 – 180 MPa) that are attributed to enhanced grain size reduction with increasing proximity to the PSZ [*Wibberley and Shimamoto*, 2002]. Material reclaimed from depth on the actively creeping segment of the San Andreas Fault shows a similar range of permeabilities of 10^{-18} to 10^{-23} m^2 (P_{eff} = 10 – 120 MPa), with gouge material exhibiting lower permeabilities than bounding cataclasites [*Morrow et al.*, 2014]. The gouge zones of the Carboneras Fault show permeability values in the range of 10^{-17} to 10^{-22} m^2, with permeability anisotropy of up to 3 orders of magnitude [*Faulkner and Rutter*, 2000; *Faulkner et al.*, 2003].

The permeability variations of up to 6 orders of magnitude in previous studies seem typical of major, mature fault zones and are related directly to degree of comminution and associated authigenic mineral generation and cementation. Both experimental and in situ seismic velocity measurements have revealed that faults, and their associated damage zones are regions of low seismic velocities [*Mooney and Ginzburg*, 1986; *Li et al.*, 2004;

Jeppson et al., 2010; *Jeppson and Tobin*, 2015], which concur with velocity measurements in this study.

3.5.3. Implications for fault zone properties during the seismic cycle

The hydraulic properties of fault rock have implications for transient variations in pore fluid behaviour during seismic slip. Coseismic thermal effects may promote slip propagation via processes such as thermal pressurization [*Rempel and Rice*, 2006; *Rice*, 2006]. The low permeability of the core of the Alpine Fault and alteration zone in the hanging wall may favour thermal pressurization during earthquake rupture [*Segall and Rice*, 1995; *Wibberley*, 2002; *Mizoguchi et al.*, 2008; *Leclère et al.*, 2015]. Evidence for the development of overpressures within the damage / alteration zone includes gouge-filled fractures emanating from, and propagating through, the PSZ. These features indicate that dilatancy driven pore depressurization may also stabilise slip and arrest rupture [*Segall and Rice*, 1995; *Samuelson et al.*, 2009].

Geochemical studies of vein mineralization [*Menzies et al.*, 2014] and fluids from hot springs from the Alpine Fault hanging wall [*Barnes et al.*, 1978] show that much of the fluid circulating at <2 km depth is meteorically derived. Fluid inclusion measurements indicate that water infiltration is at least 2 orders of magnitude greater than metamorphic water production [*Menzies et al.*, 2016]. In its low permeability pre-rupture state the Alpine fault appears to act as a barrier to fluid flow, isolating fluid geochemical regimes on a regional scale. Similarities can be drawn with low fluid ^{3}He / ^{4}He ratios in San Andreas Fault fluids at seismogenic depths, indicating a dominantly meteorically derived source. As the overall permeability structure across the creeping sections of the San Andreas is low, it has been suggested that the proportion of mantle derived fluids will increase within more permeable faults at distance from the active San Andreas strands within the North American Plate [*Wiersberg and Erzinger*, 2007].

The strong, penetrative tectonic and metamorphic foliations present in the protolith host-rock bounding the Alpine Fault, the hanging wall Alpine Schist and mylonite sequence lithologies, have a strong regional seismic anisotropy [*Christensen and Okaya*, 2007]. This anisotropy extends to depths of <90 km into the deep-lithosphere and is broadly distributed, according to shear wave splitting studies [*Karalliyadda and Savage*, 2013]. Fault

Zone Guided Waves (FZGWs) have been observed on the Alpine Fault, in which seismic waves are channelled and propagated along the fault zone [*Eccles et al.*, 2015]. These FZGWs occur due to material contrast between the fault zone material and the intact country rock, causing seismic waves to focus along low-velocity zones. Our observations of fault zone velocities in comparison to the intact country rock are consistent with the presence of these FZGWs. These types of seismic wave allow the fault to be imaged and some of the properties of the fault at depth, such as fault zone width, to be inferred [*Li et al.*, 1997; *Ben-Zion*, 1998]. The use of FZGWs is critically dependent on the velocity contrast between the fault and the country rock, and the orientation of any anisotropic fabric in the country rock. If the slow direction of any anisotropy is oriented perpendicular to the low velocity fault zone, seismic energy may escape the low velocity zone, making the fault difficult to recognise through FZGWs [*Kelly et al.,* 2017]. The seismic velocities and anisotropies reported in this study support previous regional observations on the behaviour of seismic waves on the Alpine Fault, where the fault core material has lower seismic velocities than the fastest direction in the country rock hosting it and the heterogeneity of microstructures within the fault zone serves to homogenize any anisotropy [*Eccles et al.*, 2015].

3.6. Conclusion

Our suite of experimental measurements shows a zone of low permeability and low seismic velocity material bounding the PSZ of the Central Alpine Fault, under conditions approximating depths of 5 – 6 km. Measurements performed on protolith lithologies show lower permeabilities and higher seismic velocities than the fault-damaged rock owing to their intact, unfractured nature. Low permeabilities at low experimental pressures are explained by the presence of fine grained alteration products and carbonate precipitation within the fracture networks of the fault hanging wall. The PSZ, being composed of ultrafine-grained alteration products, acts as a barrier to cross-fault fluid flow postseismicity. This is in agreement with other petrophysical studies on other mature faults subjected to extensive comminution and fluid-rock alteration [*Wibberley and Shimamoto*, 2002; *Faulkner et al.*, 2003; *Boulton et al.*, 2012; *Townend et al.*, 2013; *Carpenter et al.*, 2014; *Morrow et al.*, 2014].

The evolution of fault rock microstructure with seismic shear and subsequent interseismic fluid-rock interaction has a great effect on the hydraulic and elastic properties of fault zones. This evolution is complex and cyclical, potentially promoting rupture via dynamic coseismic processes such as thermal pressurization and dilatancy hardening. During interseismic periods, fluid flow is likely concentrated upon pervasive, unconsolidated gouge-filled fracture networks that are progressively mineralized / altered, reducing along-fault communication of pore fluid. With fluid focusing along these fracture networks, fault rock fabrics have little influence on permeability anisotropy. In addition, as the cataclastic microstructures are so variable on a mm – cm scale, their overall effect within the fault zone would be to homogenize seismic velocities, limiting seismic anisotropy. The main microstructural controls on fault rock physical properties are throughgoing fractures, both gouge-filled and mineralized, which have a great effect on seismic wave speeds and fluid flow at the experimental specimen scale and likely to act as preferential fluid flow paths and planes of discontinuity in the Alpine Fault Zone as a whole.

3.7. Supplementary material

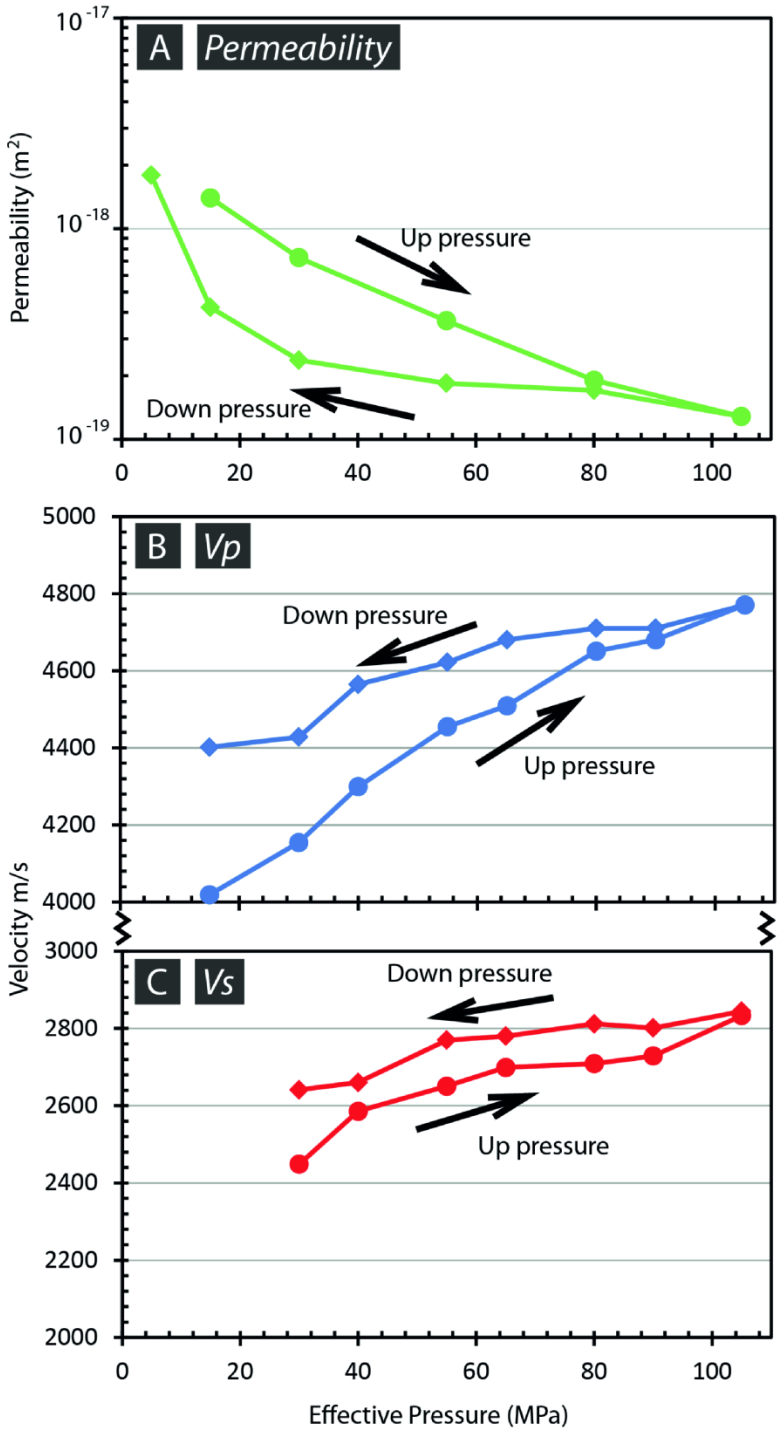

Figure SM 3.1 **–** The hysteresis effect observed in both the permeability (**A**) and seismic wave velocity (**B** and **C**) measurements during and after the initial pressurisation for specimen 1B-127.1 in the down-core orientation (d-down). Circle markers denote the up pressure portion of the cycle; diamond markers denote the down pressure portion of the cycle.

Table SM 3.1 – Experimental seismic velocity values reported in Figures 3.5 and 3.6 in the paper. See Digital Supplementary Material

Table SM 3.2 – Experimental permeability values reported in Figures 3.5 and 3.6 in the paper. See Digital Supplementary Material

Table SM 3.3 – Anisotropy values reported in Figures 3.7 in the paper. See Digital Supplementary Material

Video SM 3.1 – nanoCT tomographic reconstruction of 1B-120 parallel to the Y-down plane. See Digital Supplementary Material.

Video SM 3.2 – nanoCT tomographic reconstruction of 1B-133 parallel to the Y-down plane. See Digital Supplementary Material.

4. Cycles of fault zone sealing and restrengthening from the structure and chemistry of vein networks in the Alpine Fault, New Zealand

Key points

- The Alpine Fault hanging wall alteration zone is pervasively mineralised by carbonate precipitation, while the footwall is relatively devoid of carbonate minerals.
- Microstructural and chemical observations point to a protracted cycle of fracturing and sealing at changing ambient conditions during exhumation.
- Carbonate mineralisation reflects the transient nature of permeability on the Alpine Fault, which is currently in a low permeability interseismic state.

Abstract

The Alpine Fault, a transpressional plate boundary between the Australian and Pacific plates, is known to rupture quasi-periodically with large magnitude earthquakes (M_w ~8) and is thought to be nearing the end of its latest interseismic state. Using temporal and fine-scale spatial variations in carbonate-vein deformation microstructures and geochemistry, this study investigates the influential role of calcite in sealing and restrengthening the Alpine Fault. Phase 1 of the Deep Fault Drilling Project (DFDP-1) sampled fault lithologies from both the Alpine Fault hanging wall and footwall at Gaunt Creek, Westland. Drilling revealed a fault zone structure composed of a fault core and associated damage zone, both of which are overprinted by a zone of alteration focused in the hanging wall. This alteration was produced through enhanced fluid-rock interaction on a fault which currently has very low permeability. Carbonate is one of the primary authigenic minerals of this alteration, with mineralisation concentrated within fractures. Through electron backscatter diffraction, cathodoluminescence, and secondary ion mass spectrometry, multiple episodes of fracturing and mineralisation have been recognised.

Our observations show that the Alpine Fault alteration zone contains extensive carbonate mineralisation, occurring predominantly as vein infill. Multiple fracture and sealing events

have occurred on the fault, which provide evidence for cyclical damage generation and recovery. The lack of twinning and other signs of deformation in the most recent vein generation indicate that there has been little deformation or strain accumulation in the alteration zone since the last period of seismicity.

The trace element incorporation into the calcite during precipitation, including Mn, Mg and Fe, were sourced from fluid-rock interactions between hydrothermal fluids and cataclased rock. Mn was likely sourced from the retrogressive breakdown of Mn-rich garnet while Mg and Fe from low temperature transformations of clay minerals, i.e., biotite to chlorite to smectite and chlorite to muscovite, particularly in the principal slip zone. The variation in trace element incorporation during precipitation is due to the variation in ambient conditions and alteration reactions through fluid-rock interaction occurring in the fault core – alteration zone between periods of fracture generation. In most cases, older vein generations contain more Fe and Mg, while younger generations and recrystallised regions contain more Mn, likely due to variation in temperature and pressure during precipitation as the fault hanging wall was exhumed.

The majority of veins appear to be filled by blocky-equant calcite crystals with uniform chemistry indicating that they were rapidly sealed by a single fluid pulse. Subsequent fluid-rock interaction and deformation resulted in modification of vein microstructures and chemistry. Many of the veins were likely generated by hydrofracturing, in which a hot fluid was pulsed through the fault core / alteration zone during seismicity, rapidly propagating dilatant fractures with some shear component. The sudden pressure drop during dilation would result in rapid supersaturation of the fluid and therefore in rapid precipitation on the fracture walls, evidenced by blocky grain shapes, weak growth competition and ‘floating’ wall-rock / older calcite fragments.

The transient nature of the permeability within the fault core / alteration zone is inferred to be due to seismically-induced fractures and porosity generation, potentially from both large magnitude Alpine Fault events and moderate magnitude events elsewhere in the fault zone. Immediately postseismicity the mobilisation of fluid results in rapid mineralisation and fluid-rock interactions, which seal and restrengthen the fault until the next cycle of seismicity occurs. Outside the fault core / alteration zone, within the Alpine Fault damage zone, fractures likely remain open for longer time scales, allowing the passage of meteorically derived hydrothermal fluids above the contact of the damage zone and fault core / alteration zone, manifesting at the surface as hots springs.

4.1. Introduction

4.1.1. Fluids in fault zones and fluid-rock interactions

Fault zones, though occupying a relatively small volume of the Earth's crust, greatly influence crustal physical properties and processes, particularly fluid transport properties via grain-size reduction, dilation, fracturing, and fluid-rock interactions [*Faulkner et al.*, 2010]. Faults can variably act as conduits or barriers to fluids, or a combination of the two, depending on their tectonic setting, maturity and composition [*Chester and Logan*, 1986; *Caine et al.*, 1996; *Faulkner et al.*, 2010]. The permeability of a fault zone is therefore thought to be dynamic, evolving from highly permeable immediately post-earthquake rupture, due to seismically induced fracture damage, to becoming effectively sealed by the precipitation of minerals in pore spaces and fractures in conjunction with the compaction of ultrafine-grained fault gouges [*Blanpied et al.*, 1992; *Gratier et al.*, 2002] during the interseismic period.

During seismicity, pulses of fluid are mobilised by thermal pressurisation [*Rice*, 2006; *Viesca and Garagash*, 2015] or fluid-pressure fluctuations [*Sibson*, 1990], redistributing heat and soluble material as frictional sliding, within the shearing volume of the fault, heats up, pressurises and mobilises pore fluids. As well as initiating dramatic fault zone weakening, this results in enhanced fluid-rock interaction within the fragmented rock mass encompassing the fault core, known as the damage zone [*Evans and Chester*, 1995; *Caine et al.*, 1996; *Morton et al.*, 2012], and in the mixing of shallow, regional groundwater chemistries [*Cox et al.*, 2015]. In the shallow crust, at and above the Brittle-Viscous Transition (BVT), fluid-rock interaction is typically evidenced by the precipitation of secondary minerals, primarily calcite and quartz, as cements and veins infill [*Sibson et al.*, 1975; *Gratier et al.*, 2002; *Mittempergher et al.*, 2011] and phyllosilicate mineral precipitation, through the retrograde reaction of fine-grained, comminuted material during exhumation [*Wu et al.*, 1975; *Saffer and Marone*, 2003; *Collettini et al.*, 2009].

During brittle failure and fragmentation of rock, a number of modes of failure in the form of fracturing can occur. These modes are classified into three end members, relating the displacement of the wall rock relative to the fracture plane and edge: Mode I – extensional failure; Mode II – failure by sliding; and Mode III – failure by tear, with Mode II and III

producing shear fractures [*Griffith*, 1921; *Irwin*, 1957; *Brace*, 1960]. Cracks that exhibit both shear and extension modes of failure are classified as hybrid fractures [e.g., *Ramsey and Chester*, 2004].

Various sealing mechanisms act on fractures postseismically, reducing void space and decreasing permeability. Mechanical compression can lead to crack closure, facilitated by the readjustment of local stresses or a decrease in fluid pressure [*Brace*, 1972]. Many major, non-carbonate hosted faults contain elevated concentrations of carbonate cements and vein infill indicating that physical-chemical mechanisms contribute greatly to fault sealing [*Arai et al.*, 2003; *Mittempergher et al.*, 2011]. Fluctuations in ambient conditions (temperature, pressure, chemistry etc.) alter mineral solubility in fluids, resulting in the precipitation of secondary minerals, which can seal and strengthen fault zones over geologically short time scales [*Gratier et al.*, 2002]. The composition and mobility of the agents of sealing (fluids and their dissolved or precipitated minerals) are largely controlled by the local geothermal gradient and fluid flow paths. Calcite dominates hydrothermal vein mineralogies in the shallow crust (2 – 4 km) at temperatures of <150°C, as temperatures increase to 150 – 300°C quartz becomes increasingly prevalent down to the BVT [*Sharp*, 1965; *Renard et al.*, 2000].

A number of geochemical investigations on carbonate vein fillings from a variety of geological settings have been undertaken, including trace elements [*Möller et al.*, 1991; *Denniston et al.*, 1997; *Hickmott et al.*, 1997], stable isotopes [*Rye and Bradbury*, 1988; *Hilgers and Sindern*, 2005; *Katz et al.*, 2006] and stable oxygen / carbon isotopes together with trace elements (such as Fe, Mg, Sr, Mn) studies [*Lee et al.*, 1997; *Wogelius et al.*, 1997; *Maskenskaya et al.*, 2014]. These data-sets have constrained temporal changes in fluid sources between successive generations of calcite [*Denniston et al.*, 1997; *Hilgers and Sindern*, 2005; *Sandström and Tullborg*, 2009] and documented the evolution and characteristics of mineral-forming fluids [*Rye and Bradbury*, 1988; *Hickmott et al.*, 1997; *Lee et al.*, 1997; *Wogelius et al.*, 1997; *Barker et al.*, 2006; *Katz et al.*, 2006; *Smith et al.*, 2014]. Trace-element concentrations and stable isotope compositions within carbonate veins of a single generation can either be highly variable [*Rye and Bradbury*, 1988; *Möller et al.*, 1991; *Denniston et al.*, 1997; *Wogelius et al.*, 1997] or relatively constant [*Lee et al.*, 1997; *Hilgers and Sindern*, 2005; *Barker et al.*, 2006; *Katz et al.*, 2006; *Lund Snee et al.*, 2014]. Large variations across individual veins can be attributed to trace-element fluctuations in the

super-saturated fluid and, potentially mixing of fluids with variable chemistries [*Denniston et al.*, 1997; *Wogelius et al.*, 1997; *Barker et al.*, 2006]. Variations in ambient conditions during crystallization may impact the incorporation of trace elements [*Denniston et al.*, 1997] and fluid flow rates [*Möller et al.*, 1991]. Isotopic analyses across multiple calcite vein sets show that a (<3 ‰) variation in $\delta^{18}O$ and $\delta^{13}C$ values may indicate that: 1) the precipitating solution was buffered by bedrock [*Hilgers and Sindern*, 2005; *Smith et al.*, 2014]; 2) the solution had a stable temperature [*Lee et al.*, 1997; *Barker et al.*, 2006]; or 3) rapid mineralisation could have prevented significant isotopic water-rock exchange [*Katz et al.*, 2006]. On the other hand, large variations (<6 – 9 ‰) may indicate lesser amounts of fluid-rock interaction, so less homogenisation of the fluid with the host rock, [*Rye and Bradbury*, 1988] or that the vein infill was precipitated from a mixture of fluids from different sources.

The aim of this study is to characterise the sealing processes recorded on a major plate bounding fault zone through a fine-scale microstructural and geochemical investigation of the distinct generations of carbonate mineralisation in the pervasive vein network of the Alpine Fault. This is achieved here through the utilisation of multiple, complementary techniques including Electron Backscatter Diffraction, Optical Cathodoluminescence and spatially resolved Secondary Ion Mass Spectrometry. We focus on temporal and spatial changes in vein morphology, cement microstructures, trace element content and stable isotopic composition. We document the evolution of mineralising fluids and the fault rocks that host them throughout the seismic cycle and constrain whether advective fluid flow or local dissolution-precipitation processes control sealing behaviour within the Alpine Fault. This work will begin with establishing the geological setting of the Alpine Fault, followed by the methodology and technical aspects of the study, including a brief outline of the Deep Fault Drilling Project. The results of the microstructural and geochemical analyses are then presented and discussed. Finally, we explore how these findings elucidate fundamental fault zone processes that modulate the seismic cycle.

4.1.2. The Alpine Fault Zone, New Zealand

The Alpine Fault Zone (AFZ), bounding the western edge of the Southern Alps on New Zealand's South Island, accommodates over 70 % of the relative motion between the colliding Australian and Pacific Plate [*Norris and Cooper*, 2007; *Norris and Toy*, 2014]. The

ramping of the Pacific plate over the Australian plate is manifested through dextral-reverse movement, offsetting basement rocks laterally by over 470 km, with Quaternary horizontal displacement rates estimated at 21 – 27 mm yr-1 [Norris and Cooper, 2001; Lamb et al., 2016]. Uplift on the fault is rapid, exhuming crustal rocks from depths of 20 – 30 km at a rate of ~6 – 9 mm yr-1 [Little et al., 2002b]. Accompanying this rapid uplift is the advection of the regional geothermal gradient with fluid inclusion microthermometry placing the gradient at 40 °C/km [Toy et al., 2010] or 75 °C/km in the upper 2 km [Craw, 1997]. Recent shallow borehole measurements within the fault hanging wall report gradients of 62.6 ± 2.1 and 125 ± 55 °C/km [Sutherland et al., 2012, 2017].

Palaeoseismic evidence has indicated that the Alpine Fault has had numerous geologically recent rupture episodes at 1717 ± 25, 1630 ± 25 and 1460 ± 25 A.D., which are each estimated to have a moment magnitude of 7.9 ± 0.3, 7.6 ± 0.3, and 7.9 ± 0.4, respectively [*Wells et al.*, 1999; *Rhoades and Van Dissen*, 2003; *Langridge et al.*, 2012; *Howarth et al.*, 2016], with these ruptures propagating along nearly the entire ~600 km length of the fault. Recent seismicity patterns, geodetic strain records, and inferred high pore fluid pressures from regional seismic P- and S-wave velocity ratios and gravity surveys deep in the fault zone, suggest that the fault is locked above 13 – 18 km depth and that it is in the late stages of its earthquake cycle [*Eberhart-Phillips*, 1995; *Eberhart-Phillips and Bannister*, 2002; *Stern et al.*, 2007; *Sutherland et al.*, 2007; *Toy*, 2007; *Beavan et al.*, 2010; *Lamb and Smith*, 2013].

On the Central Alpine Fault, between the Toaroha River and Martyr River [*Barth et al.*, 2013], overprinting the fault core and transition into the damage zone, is a distinct <30 m-thick zone of hydrothermally altered rock, containing elevated concentrations of hydrous alteration minerals and cements (e.g., phyllosillicates and carbonates), as observed through field and borehole studies [*Sutherland et al.*, 2012; *Townend et al.*, 2013; *Toy et al.*, 2015b]. The extent of this alteration increases with proximity to the fault's principal slip zone (PSZ) within the hanging wall rock, with far less carbonate cementation in the footwall [*Boulton et al.*, 2017a]. This indicates a focusing of fluid in the hanging wall damage zone, with little cross-fault flow throughout the seismogenic crust [*Menzies et al.*, 2016].

Enhanced hydrothermal activity and the generation of thermal springs in the fault hanging wall, extending from 1 to 20 km south east of the Alpine Fault, gives insight into the composition and behaviour of fluids in relation to the fault [*Barnes et al.*, 1978; *Barber and*

Wenk, 1979; *Koons*, 1987; *Allis and Shi*, 1995; *Beavan et al.*, 2010]. The influence of seismicity on fluid flow across the Southern Alps appears substantial, with work by *Cox et al.*, [2015] showing that large distal earthquakes across the South Island of New Zealand, including a M_w 7.8 in south-western Fiordland, 2009 and a M_w 7.1 in eastern Canterbury, 2010, caused variation in temperature and fluid chemistry in a monitored spring in the western Southern Alps, at a distance of 350 km and 180 km from the respective earthquake epicentres.

There are a limited number of previous studies on hot spring and bulk calcite and quartz vein stable isotope signatures upon the Alpine Fault, and these have focused on the distal vein assemblages hosted in the quartzofeldspathic Alpine schists and intercalated metabasic mylonites that compose the Southern Alps, [*Jenkin et al.*, 1994; *Upton et al.*, 1995; *Menzies et al.*, 2014]. These studies suggested that fluids are dominantly of meteoric origin, indicating that the fault is a crustal-scale conduit for deep-circulating meteoric water that has undergone substantial geochemical exchange with the lithologies of the Southern Alps, down to the top of the BVT at ~6 km depth, with a small component of mantle-derived fluid [*Menzies et al.*, 2014, 2016].

The Deep Fault Drilling Project (DFDP) was undertaken to better understand the processes that lead to major earthquakes by drilling into and observing a major continental fault during its build-up to a large seismic event.

4.2. Methods

4.2.1. The Deep Fault Drilling Project

The first phase of the Deep Fault Drilling Project (DFDP-1) comprised of two pilot boreholes (DFDP-1A and DFDP-1B) drilled into an active thrust segment of the Alpine Fault at Gaunt Creek, a tributary to the Waitangitaona River, in January 2011. The boreholes reached depths of 100.6 m and 151.4 m, respectively, through percussion drilling in the upper borehole sections followed by wireline coring, collecting core for over 50 % of the borehole length [*Sutherland et al.*, 2011, 2012]. A range of fault lithologies from both the hanging wall and footwall were recovered including ultramylonites, cataclasites and fault gouges. The PSZ of the AFZ was reached at 90.74 m depth in DFDP-1A and 128.44 m in DFDP-1B,

marking the boundary between the Australian and Pacific Plates, with a second PSZ recorded in DFDP-1B at 143.85 m [*Toy et al.*, 2015b]. Both slip zones are composed of clay-rich gouge [*Sutherland et al.*, 2012; *Toy et al.*, 2015b]. A more detailed report on the drilling operations can be found in *Sutherland et al.* [2011]. The drilled core diameter was 85 mm (PQ wireline bit size) and supplied for sample preparation as 200 – 300 mm length intact core sections and half sections [*Sutherland et al.*, 2011]. These core sections were oriented with respect to the borehole vertical axis, however, due to core rotation during retrieval the horizontal orientation could not be preserved [*Sutherland et al.*, 2011; *Toy et al.*, 2015].

4.2.2. Petrology of core lithologies

Eight rock units were distinguished in the DFDP-1 boreholes and are systematically detailed in *Toy et al.*, [2015]. These include: grey and dark-green ultramylonites; brown-green-black ultramylonites; hanging wall (upper) unfoliated cataclasites; hanging wall (upper) foliated cataclasites; fault gouges; footwall (lower) cataclasites; fault breccias; and Quaternary gravels. The DFDP-1 core provided an excellent section through the AFZ, allowing a number of associated lithological units to be distinguished and classified, based on the original protolith and the level of damage and/or alteration. This classification follows the fault rock nomenclature of *Woodcock and Mort*, [2008], with units numbered sequentially as they were encountered in the recovered core, from top to bottom (Figure 4.1B).

The extent of alteration via clay and carbonate mineralisation, extending ~30 m from the PSZ, obscures the boundary between the Alpine Fault's damage zone and fault core, as well as the exhumed BVT. The hanging wall ultramylonite encountered (Unit 1 and 2) is planar-foliated with a variable quartzofeldspathic and metabasic composition. Foliations are defined by aligned phyllosillicates, graphite and opaque minerals. These ultramylonites are of midcrustal origin and have undergone extensive grain-size reduction via plastic deformation mechanisms, overprinted by successive generations of brittle cataclasis as evidenced by clay and carbonate-filled shears and fractures, with minimal quartz mineralisation evident. Ultramylonites transition to variably foliated and unfoliated cataclasites (Unit 3 and 4); composed of quartzofeldspathic and metabasic material, consisting of angular fragments of ultramylonite variably clast-supported (>10 mm diameter) and matrix-supported (<10 mm diameter) in a matrix of comminuted feldspar, quartz, chlorite, white mica, calcite and rare epidote. These cataclasites

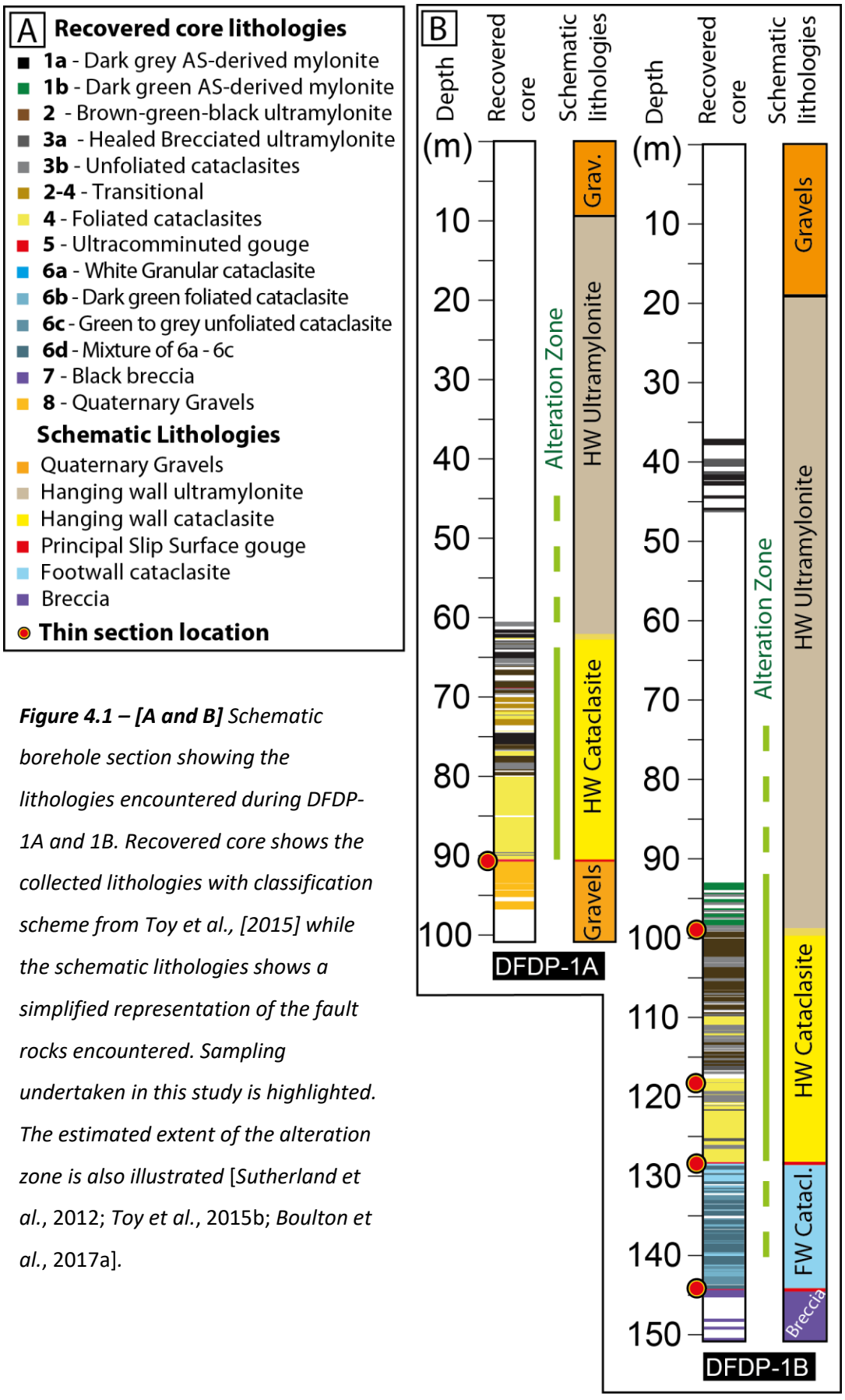

Figure 4.1 – [A and B] *Schematic borehole section showing the lithologies encountered during DFDP-1A and 1B. Recovered core shows the collected lithologies with classification scheme from Toy et al., [2015] while the schematic lithologies shows a simplified representation of the fault rocks encountered. Sampling undertaken in this study is highlighted. The estimated extent of the alteration zone is also illustrated* [*Sutherland et al.*, 2012; *Toy et al.*, 2015b; *Boulton et al.*, 2017a].

have been successively fractured and cemented as evidenced by cross-cutting relationships of mineralised (or mechanically generated gouge-filled) veins, pseudotachylytes, and clasts with cataclastic texture. The PSZ is a ~250 mm thick zone of ultracomminuted, cohesive, clay-rich gouge (Unit 5). This gouge is ultrafine-grained, variably foliated with indistinct, sub-planar layering containing fragmented clasts of smectitic-chloritic gouge and calcite. The footwall is comprised of 'lower' cataclasites (Units 6a to 6d), of granitic and gneissic origin, that are variably foliated and contain far less carbonate and less hydrothermal alteration than Units 1 to 4 of the hanging wall [*Toy et al.*, 2015b; *Boulton et al.*, 2017a].

4.2.3. Techniques

Optical cold-cathode cathodoluminescence (CL) was employed in this study, using a Nikon Eclipse Ci microscope with a CITL Mk5-2 cold stage and Nikon DS-Fi1c camera, working at conditions of 10.8 kV and 390 µA in a vacuum of 0.047-33 Torr. CL signal in calcite is strongly modified by trace element content (ppm concentrations); Fe quenches the signal while Mn enhances luminescence [*Long and Agrell*, 1965; *Marshall and Mariano*, 1988; *Waychunas*, 2014]. CL was used to obtain crucial, spatially resolved information on subtle chemical and structural variations within the carbonate vein infill and to inform further analyses with electron backscatter diffraction (EBSD) and secondary ion mass spectroscopy (SIMS).

SEM analyses were undertaken in the EBSD-SEM Laboratory at the University of Liverpool using an X500 Crystal Probe field-emission gun (FEG) SEM, designed by Obducat CamScan Ltd (for full technical specifications see *Seward et al.*, 2002). EBSD analyses were collected using an F+ Nordlys EBSD detector combined with the AZtec Oxford Instrument acquisition software. The typical operating parameters for this study were 20 kV accelerating voltage, 20 – 30 nA beam current, and 5.5 nm spot size. The raw EBSD datasets were processed and analysed using the Oxford Instruments HKL Channel5 software. Erroneous data points were carefully removed using band contrast values to sub-sample grain boundaries effectively, thus avoiding the generation of artefacts.

The EBSD data in this study are presented in All-Euler (AE), which visualises orientation through use of an Euler angle-based colour scale. Euler angles are a set of three angles ($\phi 1$, Φ, and $\phi 2$) used to describe the crystallographic orientation of crystals relative to a

reference coordinate system; defined by the primary SEM stage axes. The value of each Euler angle, reflecting the magnitude of the 3 rotations necessary to determine a rotation path from the SEM reference frame to that of the crystal analysed, is individually set to a colour scale (red, green and blue for Euler angles ϕ1, Φ, and ϕ2, respectively) which are then combined into a single RGB colour that represents the observed crystallographic orientation. However, the AE component contains a 'wraparound' effect caused by one or more of the Euler angles reaching their respective limit, causing the RGB value to vary between minimum and maximum, potentially resulting in colour speckling even when little to no orientation variation between grains exists. Crystallographic orientations are plotted in equal area upper hemisphere stereographic projections, i.e. pole figures (PF), to reveal if any crystallographic preferred orientation (CPO) exists. The data in pole figures are coloured according to their respective Euler orientation and contoured to a half width of 20° and data clustering of 5°. In order to describe the intensity of the fabric shown in a PF a statistical method is used known as the multiple of uniform density (MUD), which is quantified using the maximum intensity of a contoured PF. MUD values of 1 indicate randomly orientated grains while a MUD >1 is indicative of a fabric or CPO; these values are illustrated alongside the PFs. MUD values however are only a qualitative approximation of CPO strength because, for example in Oxford Instrument's software, they are calculated only relative to the pole figures visualised for a given mineral in a given dataset and cannot be used for direct comparison between PFs from different datasets. For more information on relevant EBSD data presentation please see *Prior et al.*, [1999, 2009] and *Bestmann and Prior*, [2003].

SIMS analyses were performed at the University of Edinburgh NERC Ion Microprobe Facility (IMF) using a Cameca IMS-4f for trace element measurements and a Cameca IMS -1270, for stable isotope measurements. For the purpose of this study, the IMS-4f used a negative mode O^- duoplasmatron ion source as oxygen implantation into the sample surface enhances ionization efficiency for electropositive elements (Al, Si and REE etc.). The IMS-1270 operated with a positive mode Cs^+ ion beam, used to enhance yields of electronegative elements (C, O and S etc.) [*Hinton*, 1995]. The settings used on the IMS-4f microprobe during the carbonate trace element analyses for collection of species ^{23}Na, ^{26}Mg, ^{27}Al, ^{30}Si, ^{44}Ca, ^{54}Fe, ^{55}Mn, ^{88}Sr, ^{138}Ba and ^{140}Ce trace elements were as follows. A primary ion beam operating with O_2^- ions with a 20 µm spot size; within the microprobe a field of view of 825 µm, 25 µm image field, 150 µm field aperture and 150 µm contrast

aperture. Measurements were collected using an offset of 75 volts with dwell times in seconds of 3 for ^{23}Na, 5 for ^{26}Mg, 2 for ^{27}Al, 2 for ^{30}Si, 2 for ^{44}Ca, 5 for ^{54}Fe, 5 for ^{55}Mn, 2 for ^{88}Sr, 5 for ^{138}Ba, 5 for ^{140}Ce and wait times in seconds of 1 for ^{23}Na, 0.2 for ^{26}Mg, 0.2 for ^{27}Al, 0.2 for ^{30}Si, 0.2 for ^{44}Ca, 0.2 for ^{54}Fe, 0.2 for ^{55}Mn, 0.2 for ^{88}Sr, 0.2 for ^{138}Ba, 0.2 for ^{140}Ce. The settings used on the IMS-1270 microprobe during the carbonate δ^{18}O analyses were as follows. A primary ion beam operating with Cs^+ ions at 10 kV with a 20 µm spot size; within the microprobe a field aperture of 3 mm, entrance slit at 60 µm, exit slit at 411 µm, energy slit of 81 µm, contrast aperture of 150 µm, transfer lens of 30 µm were used. For all analyses, the initial two measurement cycles were discarded to reduce the effects of surface contamination, with the remaining cycles averaged for the final measurement. Standards used for these analyses are reported in Table SM 2.12.

4.2.4. Sample preparation

Thin sections were prepared using standard petrographic thin section techniques to a 30 µm thickness, with final chemical-mechanical polish applied using colloidal silica of grit size 0.005 – 6 µm in an alkaline solution. This removed the amorphous layer (few nm thick) produced on the thin section surface during mechanical polishing and ensured the high quality polishing required for electron backscatter (EBSD) analyses. Samples were carbon coated to a thickness of ~10 nm and the thin section edges painted with colloidal carbon for analysis in the SEM.

For SIMS trace element analyses the traditional thin section dimensions required modification, using a standard diamond-tipped hand glass cutter and diamond grit grinder, 25 mm diameter discs containing the area of interest were created for trace element analysis. Further modification was required for SIMS stable isotope analyses with the coring of 2.5 mm diameter cores using a Gatan™ (Model 601) ultrasonic cutter using boron-carbide slurry. These cores, along with suitably chosen chemical standards were then set and pressed into an indium mount, housed within an aluminium base, using an Enerpac™ (P142) hand press, up to 200 bar axial load. These SIMS analyses required gold coating of the sample surface to avoid surface charging effects.

4.3. Results

4.3.1. An introduction to fracture and vein classification

The morphology of fractures and the minerals that precipitate within them give insight into the factors governing the brittle failure of rock as well as the processes that occur immediately following failure, particularly the behaviour of newly mobilised fluids and their interaction with rock. Therefore, before the results from this study are presented, current classifications of veins at different scales are introduced below. An effective classification, that can be useful to the broader Earth science community, requires the consideration of various factors, including: fault rock lithology, dip of planar features (bedding or foliation) relative to fault, the stress system and the composition and temperature of fluid present both during and after failure, all of which control the nature of the damage surrounding a fault [*Kim et al.*, 2004].

Previous work by *Kim et al.*, [2004] proposed a classification of fault damage zone fractures on the exposure-scale based on geometries of faults, the locations of their damage zones, and on the structures within the damage zones. *Kim et al.*, [2004] proposed three main zones according to geometries and fracture patterns: *Tip damage zones*, which are controlled by the mode of slip immediately at the fault tip and include horsetail and wing cracks; *Linking damage zones*, which occur between two sub parallel, non-coplanar fault segments and *Wall damage zones*, which form through the propagation of mode II and III fractures produced by the build-up of slip on a fault and include features such as en-échelon extension fractures, antithetic and synthetic faults.

In regard to the fracture filling the classification of tectonic veins according to the nature of their filling was reviewed by *Bons et al.*, [2012], and workers within, in which crystal morphology and growth direction were studied in relation to the fracture hosting them and the precipitating fluid. Deciphering mineral sealing processes from vein infills is complicated due to the range of factors that influence mineral precipitation, which include: degree of supersaturation, anisotropic growth kinetics, rates of local deformation and rates of fluid transport [*Hilgers et al.*, 2004; *McNamara et al.*, 2016]. Broadly, vein mineralisation, including calcite, quartz etc., can be divided into four categories, at the cm-mm scale, which form a spectrum: *syntaxial veins*, in which vein-filling minerals grow out from the fracture

wall rock into the void formed by a crack, from either both or one side, with the nucleation of new crystals inhibited due to being energetically less favourable, resulting in growth competition. As crystallography is the main control on growth competition, syntaxial veins often show [0001] c-axis CPOs perpendicular to vein walls that strengthens towards the vein centre due to elimination of unfavourably oriented crystals. *Stretching veins* occur when a fracture opens within previously precipitated vein infill (localised) or wall rock (delocalised) rather than upon the original mineral growth surface. This results in no systematic trend in location of newly precipitated material, no growth competition occurs and the void is sealed via epitaxial growth from previous vein minerals [*Bons et al.*, 2012]. *Antitaxial veins*, are distinct from other vein types due to the appearance of mineral growth originating from a median suture line towards the fracture wall in a fibrous form [*Oliver and Bons*, 2001; *Bons and Montenari*, 2005]. These veins are usually attributed to cyclical crack-seal mechanisms or diffusional mass transfer (DMT) with both processes potentially exerting enough force to open the fracture to allow further mineral growth [*Wiltschko and Morse*, 2001]. *Pressure shadows or fringes* form when a rigid object in a deforming matrix generates a low pressure zone facing the least principal stress. This results in an enrichment of soluble minerals with shadows having a diffuse edge and fringes a sharp boundary with the host matrix [*Passchier and Trouw*, 2005].

Due to the 2-dimensional nature of thin sections used in this study, accurately determining the lateral continuity and mode of fractures can be difficult. Many of the reported microstructures have been supported by hand specimen observations of the drill core samples as well as the use of multiple consecutive thin sections to act as a tomographic view to explore how structures vary within 3-dimensional space.

4.3.2. Microstructural and chemical variation with proximity to the PSZ

In this study, six calcite-filled veins, representative of the key types recognised in the AFZ damage zone up to 30 m from the PSZ, were selected as case studies for analyses using the spatially resolved research techniques described above, allowing direct correlation of microstructure and trace element chemistry. Analytical results for each key type vein are presented below, and results are organised to build a comprehensive quantitative overview of the geometry, microstructure and trace element chemistry of each type. Additional examples are included in the supplementary material at the end of this chapter.

4.3.2.1. Cataclased ultramylonite shear vein

These characteristic shear fractures are located predominantly within the ultramylonites of Unit 2 and the cataclasites of Unit 3, where the example in Figure 4.2 retrieved at 29.14 m (*1B-99.3m-A*) above the main PSZ. The vein cross-cuts the main mylonitic foliation and lithological contacts of ultramylonite-cataclasite at a high angle and exhibits shear movement, evidenced by 450 – 500 μm wide jogs, in the main vein segment and by the displacement of previous generation vein structures (*1Gen*) (Figure 4.2A). The main segment splays into smaller branches that form a "horsetail" geometry as it crosses different lithologies, with branching observed at the lithological boundaries between the ultramylonite and cataclasite and cataclasite and pseudotachylyte (Figure 4.2 A).

The *1Gen* vein (Figure 4.2 B, D and H) cross-cut by the shear vein is 400 μm wide with an irregular outline showing areas of thinning near its ends and has no lateral continuity, potentially indicating this may be a collapse structure, a phenomenon generated when a void is partially filled by mineralisation but closes through compaction of the host matrix generating an irregular shape. The shear vein (*2Gen* – see also Figures 4.2C, E, G and H) shows calcite crystals with blocky-equant grain shape and grain size of 5 – 12 μm diameter (EBSD map, Figure 4.2B), which appears to be controlled by the vein width as this is on average equal to the grain size. There is no evidence of twinning, lattice distortion or recrystallisation. Grain boundaries are oriented at a high angle (near 90°) to vein walls with the relevant pole figure (Figure 4.2G) showing a scatter of c-axis orientations. Note that due to the small number of grains that are available to measure in a constrained length of the vein, the contoured PF in Figure 4.2G is dominated by some of the biggest grains, while raw data (plotted on the right of Figure 4.2G) give an idea of the random distribution of the c-axes.

The *1Gen* vein is filled by what appears to be one single grain (green AE colouration) and has a high density of closely spaced twin lamella, manifested as two sets of e-twins (or deformation twins in calcite), the crystallographic orientations of which are highlighted in

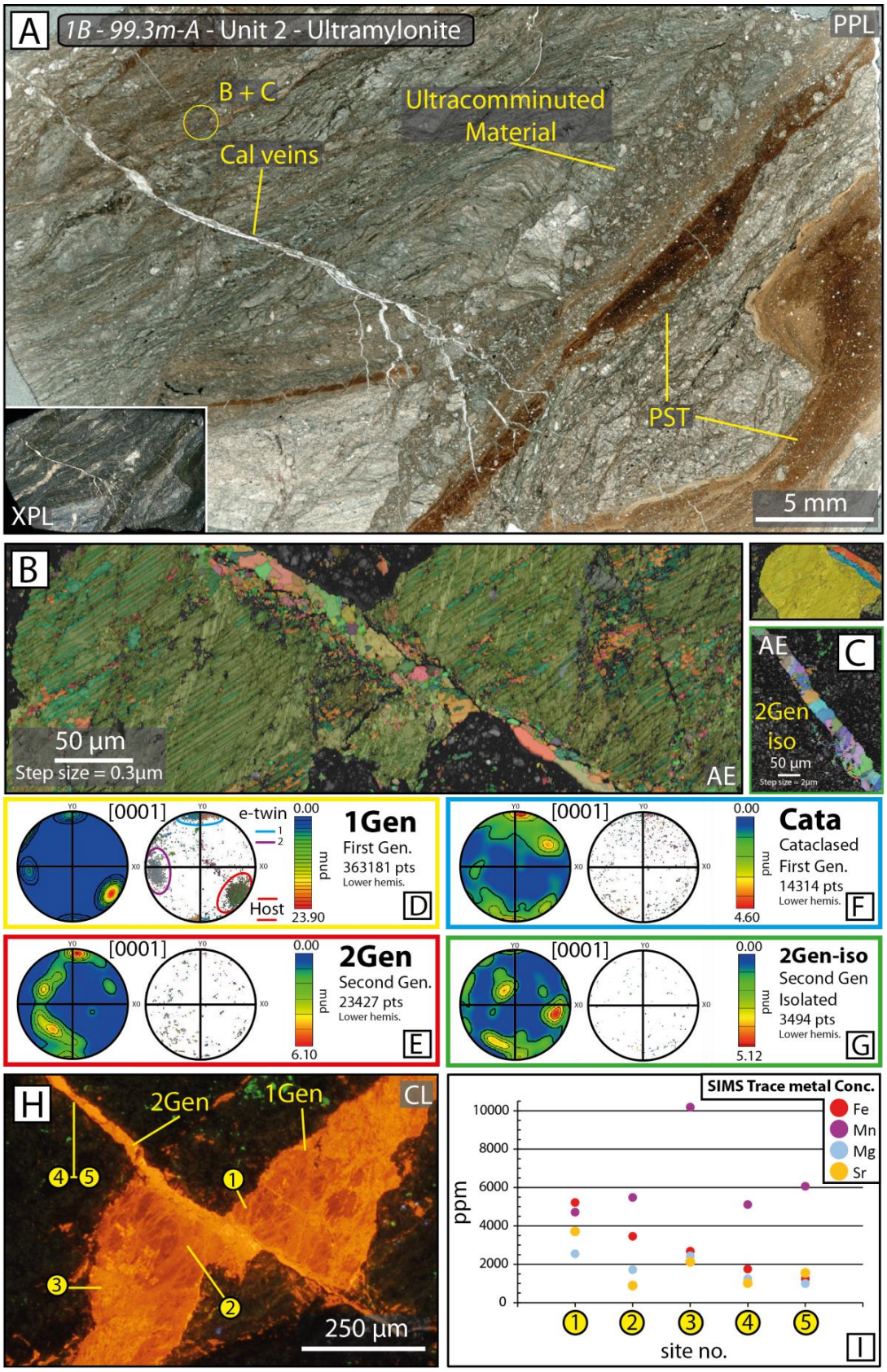

Figure 4.2 – *caption overleaf.*

Figure 4.2 – *(above)* ***[A]*** *A hanging wall ultramylonite (1B-99.3m-A – Unit 2) 29.14 m above the upper PSZ. This ultramylonite is heavily cataclased with planes of ultracomminuted material and pseudotachylyte which are cross-cut by multiple generations of calcite veins which occur both parallel to and at high angles to the original mylonitic foliation.* ***[B]*** *An AE EBSD map of a sheared calcite vein which has undergone further mineralisation. The earlier calcite (1Gen) is heavily twinned and recrystallised, the younger calcite within the shear has no evidence of deformation.* ***[C]*** *An AE EBSD map of an isolated region of 2Gen not in contact with the 1Gen.* ***[D]*** *PF for the 1Gen calcite shows the parent and e-twin orientations of the vein infill.* ***[E]*** *PF for the 2Gen calcite showing a CPO girdle similar to the 1Gen twin orientations.* ***[F]*** *PF for the cataclased / recrystallised region on the contact between 1Gen and 2Gen, it shows a CPO closely matching the orange / blue twin set of 1Gen.* ***[G]*** *PF of 2Gen calcite isolated from 1Gen, shows a weak, distributed CPO to calcite nucleated upon the previous generation.* ***[H]*** *CL image of the sheared calcite vein showing that 2Gen has a bright orange CL signal while 1Gen has highly variable CL with intensity ranging from bright orange, corresponding to fractures, twin boundaries and recrystallised regions, to dull red, corresponding to the intact 1Gen parent grain.* ***[I]*** *SIMS trace* element *concentrations for sites marked in (**H**); brighter regions are more Mn-rich while darker regions more Fe-rich.*

Figure 4.2C. The *1Gen* vein is cut by fractures and shows evidence of recrystallisation to fine grain sizes (diameters of 1 – 3 µm) along twin boundaries and at twin intersections.

Where the *2Gen* shear vein cuts across the earlier *1Gen*, *2Gen* is un-twinned, and it is characterised by elongated grains and irregular grain boundaries with orientations inherited from the *1Gen* host and twin grains upon which *2Gen* calcite has epitaxially nucleated. This is shown by the PF girdle in Figure 4.2E, where the new grains in *2Gen* inherit a spread of orientations in between those of the two dominant twin sets. At the contact with *2Gen*, *1Gen* has formed a population of fine-grained (diameters of ~0.5 – 5 µm) material, with a CPO dominated by inheritance of the main *1Gen* twin set orientation (Figure 4.2F).

From microstructural relationships, it is clear that the cataclased ultramylonite of *1B-99.3m-A* (Figure 4.2A) contains at least two distinct generations of carbonate mineralisation. However, CL analysis reveals an additional level of complexity, where four different CL signals are recognised that may be linked to chemical variations in calcite

and/or to lattice defects introduced by deformation (Figure 4.2H). The younger mineralised shear fracture (*2Gen*) has a lighter, bright orange (signal 3) and generally fairly homogeneous CL signal, with sporadic brighter yellow (signal 4) areas. The older generation (*1Gen*) consists of uniform regions of dark orange-red (signal 1) CL intersected by network of lighter orange (signal 2) CL, which in part mimics the pattern of the *1Gen* e-twin sets. Wider, irregular areas (~20 – 50 µm) of yet lighter CL, matching in colour the bright orange (signal 3) CL of *2Gen*, also exist in *1Gen*. The CL signal at the contact between *2Gen* and *1Gen* is diffuse and gradational over ~5 – 10 µm, changing from bright orange in *2Gen* to progressively darker and eventually a dark orange-red in *1Gen*. SIMS analyses show that the darker (orange-red) CL is caused by higher concentrations of Fe, accompanied by increases in Mg and Sr content as seen in Figure 4.2G and H (Point 1). The regions of *1Gen* in contact with *2Gen* show an intermediary orange CL signal and contain lower Fe, Mg and Sr and higher Mn (Point 2). Bright orange CL regions are caused by a greater proportion of Mn and are apparent in the *2Gen* vein (Point 4 and 5), and areas of *1Gen* that have been deformed and appear to have undergone recrystallisation, as evidenced by small grain sizes and lobate grain boundaries (Point 3).

4.3.2.2. Cataclased calcite vein

A heavily cataclased calcite vein runs parallel to the pseudotachylyte veins and mylonitic foliation present in the *1B-99.3m-B* ultramylonite and is cross-cut by the microstructures detailed in Section 4.3.2.1 (Figure 4.3). This vein has irregular margins indicating some shear has occurred, and it contains abundant, rounded wall rock clasts with diameters of 5 – 50 µm, frozen in place during calcite precipitation. This vein is classified as *1Gen* in this field of view. In multiple regions, 5 – 10 µm thick veins cross-cut the cataclased material and exhibit a brighter CL and enrichment in Mn; these features have been termed *2Gen*. CL and SIMS analyses show *1Gen* has a greater concentration of Fe than *2Gen* at the same depth in the core (see Section 4.3.2.1). There are four different CL signals identified at this depth interval, with dark orange-red and lighter orange CL dominating the *1Gen* vein. These two signals highlight a breccia-like texture in the vein, where older calcite (dark CL) was fragmented and the spaces in the crack network that formed were filled with newly precipitated calcite (lighter CL). Bright orange CL is typical of *2Gen* while bright yellow CL appears only in minor patches (e.g., top of Figure 4.3A).

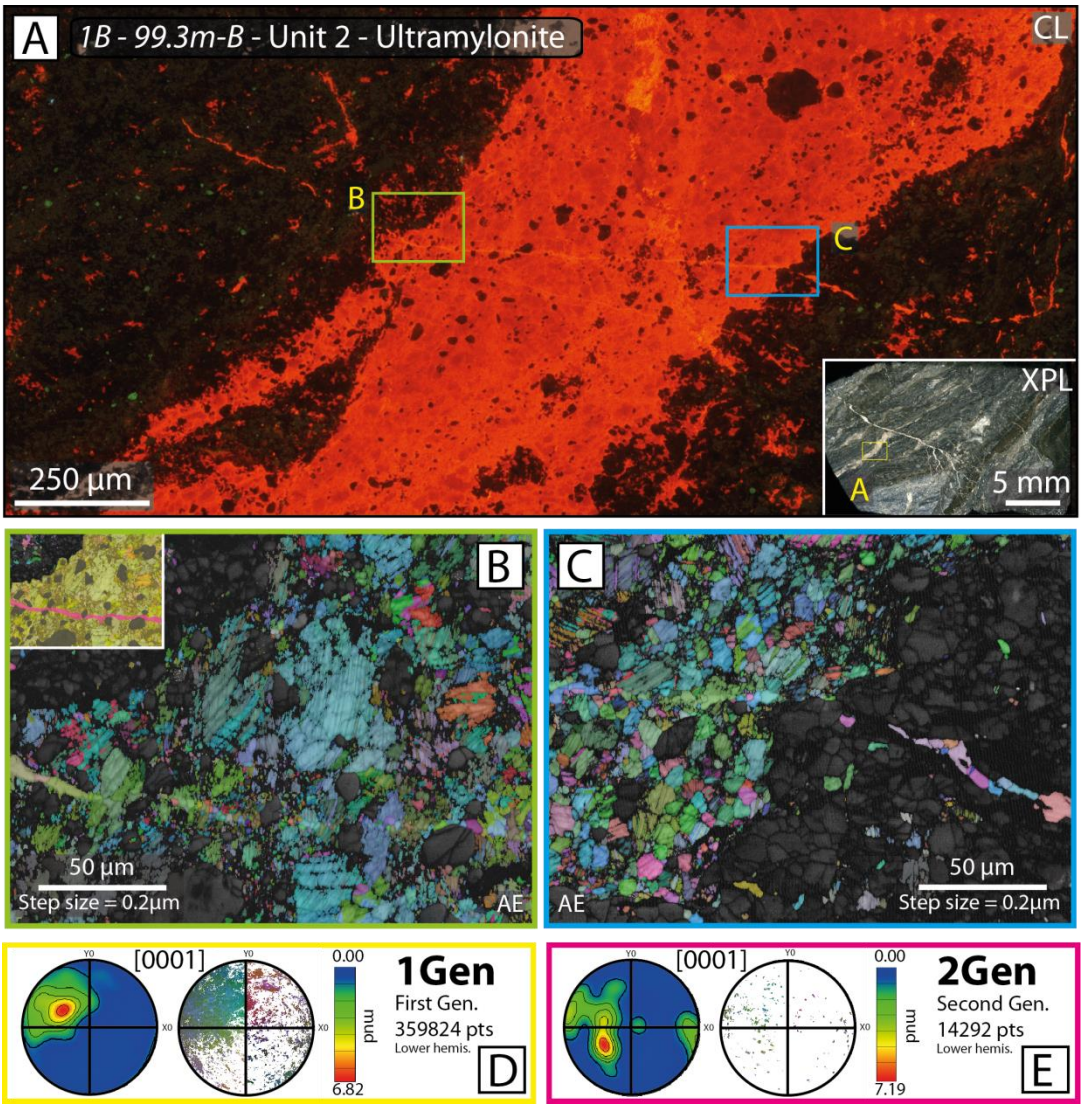

Figure 4.3 – [A] *Located within the same hanging wall ultramylonite (1B-99.3m-B – Unit 2) as Figure 4.2. The CL image shows a calcite vein with irregular margins and abundant, rounded wall rock clasts suspended in the calcite vein fill. The CL signal is predominantly dull red with fine networks of lighter CL corresponding to grain boundaries and later calcite generations.* ***[B and C]*** *The AE EBSD maps show an older generation (1Gen) of calcite composed of heavily twinned grains with angular grain shapes cross-cut by a younger generation (2Gen) that shows no evidence of deformation.* ***[D and E]*** *PFs of (**B**); show the wide spread of orientations and weak CPO present in 1Gen, the 2Gen PF shows a weak correlation with the previous generation.*

The calcite composing the *1Gen* vein is variably shaped (see EBSD maps in Figure 4.3B and 4.3C), being characterised by sub-rounded to angular grain boundaries and interlocking calcite grains with diameters of 5 – 50 μm and extensive e-twinning. Crystallographic orientation of these grains is quite variable, with [0001] c-axis orientations ranging between 230° and 040° in Figure 4.3E. However, there is a strong CPO with c-axes clustering at high angles to the trace of the vein walls. This CPO is controlled by the orientation of e-twin boundaries, the traces of which are predominantly sub-parallel to the trace of the vein walls (Figures 4.3B, C and E). *2Gen* is composed of a continuous plane of fine-grained equant calcite grains at diameters of 1 – 5 μm, which appears to deflect around wall rock clasts. These grains are largely free of any internal distortion and exhibit a similar crystallographic orientation as adjacent *1Gen* grains, indicating epitaxial growth from seeding on the earlier calcite generation (Figures 4.3B, C and F). Twin boundaries cross-cut both dark orange-red and lighter orange CL domains in *1Gen* but do not extend into *2Gen*. This suggests that e-twins formed after brecciation and further precipitation of new calcite in *1Gen*, but likely before *2Gen* veins were produced.

4.3.2.3. En-échelon void mineralisation

A foliated cataclasite (*1B-118.64m-A*) 9.8 m above the PSZ contains multiple mineralised voids that appear to be generated through en-échelon fracture development, displacing a pseudotachylyte vein by ~1 mm (Figure 4.4). The CL image highlights two distinct generations of mineralisation, the older generation (*1Gen*) exhibits a dull red-orange CL while the younger generation (*2Gen*), determined as such due to it cross-cutting and rimming of *1Gen*, exhibits an lighter orange CL. *1Gen* contains greater concentrations of Fe and Mg, while *2Gen* contains less Fe and Mg and more Mn and Sr. The brightest orange CL signal visible in Figure 4.4C are artefacts from sample preparation as there is no evidence to suggest this is caused by chemical or crystallographic variability confirmed.

Older *1Gen* is intensely twinned (EBSD maps Figures 4.4D and 4.4E), with the twins being variably tapered and bent and associated with recrystallised calcite both within and at the boundaries of the twins and host. In *1Gen* at least three e-twin sets are present, for example Figure 4.4G and H show the host calcite c-axis dip towards 270° with the two sets of e-twin c axes dipping to 000° and 180°, respectively. The later calcite cross-cutting the earlier generation, *2Gen*, has far less twinning and recrystallised material. Both the

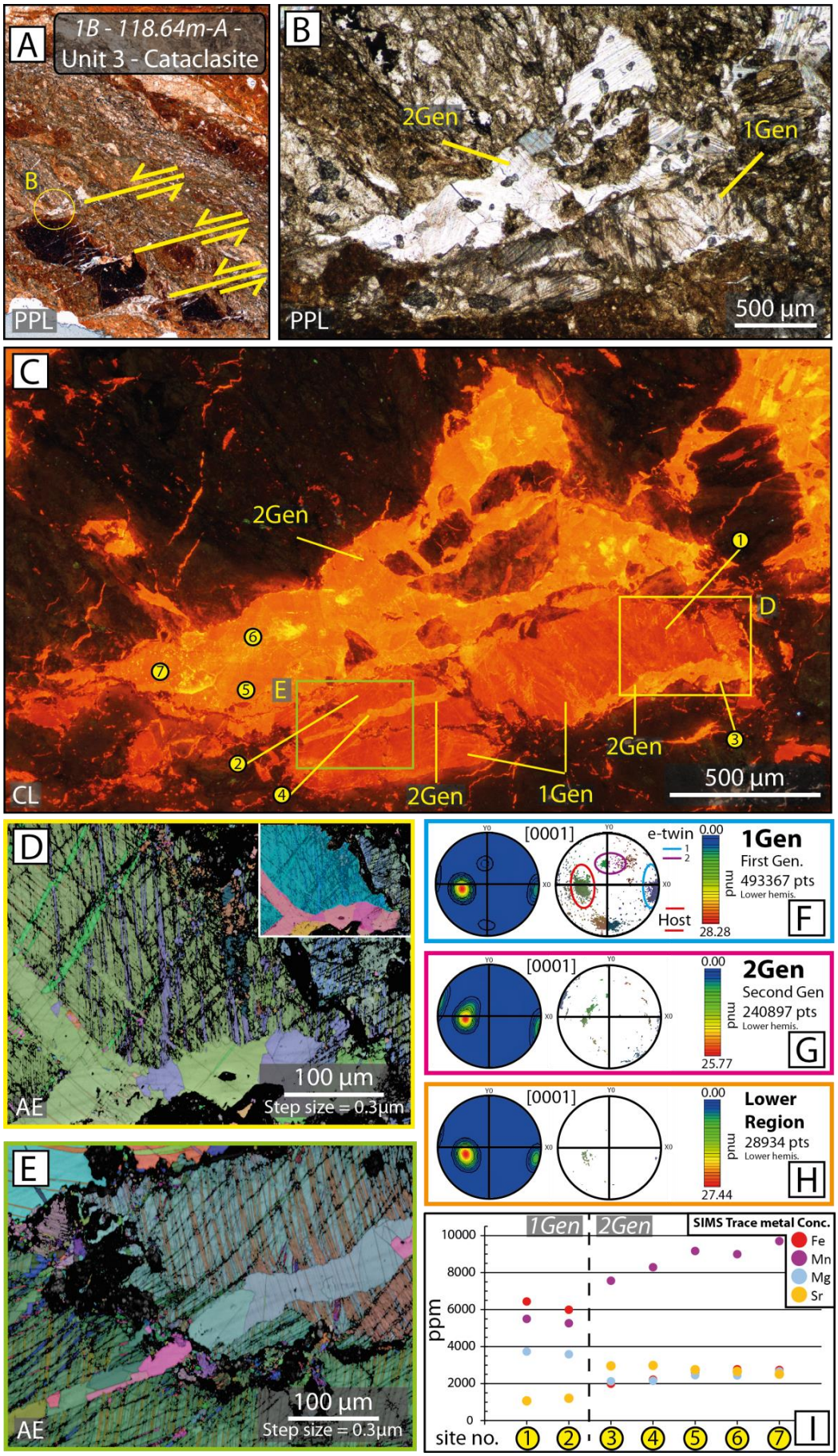

***Figure 4.4** – caption overleaf.*

Figure 4.4 – *(above)* ***[A]*** *A hanging wall cataclasite (1B-118.64m-A – Unit 3) 9.8 m above the upper PSZ. This cataclasite is heavily foliated and contains multiple en-échelon shears that cut across a pseudotachylyte vein and foliations and have been mineralised with calcite.* ***[B]*** *Site of interest in PPL at higher magnification. Two generations of calcite are evident through disparity in twinning.* ***[C]*** *CL image of (**B**); heavily twinned earlier generation (1Gen) has a dull orange CL signal with some bright traces along twin boundaries and areas of recrystallisation. Younger generation (1Gen) has bright orange CL and cross-cuts 2Gen.* ***[D and E]*** *AE EBSD maps of the sites highlighted in (**C**); shows that 1Gen is heavily twinned with abundant recrystallisation focused on twin boundaries while 2Gen has little twinning and no recrystallisation.* ***[F – H]*** *PFs of sites highlighted in (**D**); 1Gen shows the [0001] c-axis orientations for the parent and e-twins, 2Gen shows a similar CPO to the 1Gen parent and e-twin 1. Lower Region highlighted in orange showing elongate grains and separated from 2Gen by host-rock material.* ***[I]*** *SIMS trace* element *concentrations from sites marked in (**C**); 1Gen has greater Fe and Mg content, corresponding to a dull orange CL, while 2Gen has greater Mn and Sr, corresponding to a bright orange CL.*

orientation and twinning of *2Gen* calcite is inherited from those of the previous generation, with the more recently precipitated material seeding on the parent or twin terminations at the *1Gen* vein walls and growing epitaxially.

Beyond the broad identification of *1Gen* and *2Gen* in the microstructure of Figure 4.4, there are more complex aspects to be described but that prove challenging to interpret. These are: 1) on the left hand side of Figure 4.4D, the vein that branches off from the main sub-horizontal vein; and 2) on the left and bottom, the region extending down from the main vein, termed *Lower Region* and highlighted in orange. It can be noted that 1) has a CL signal equivalent to what was defined as signal 2 (lighter orange) in Section 4.3.2.1 that is strikingly darker that the bright orange of the main vein, despite the fact that from EBSD data they both look the same, more recent, generation of calcite. This may be due to local diffusion of Fe from *1Gen* calcite into some *2Gen* veins. The microstructure at 2) is separated from *2Gen* by a discontinuous boundary of wall rock material ~5 µm thick. It is characterised by boundary traces orthogonal to the vein wall and subparallel to one set of twins in *1Gen* calcite and it shows *1Gen* (and *2Gen*) orientation minus a small rotation of 20 – 30°. These features seem to suggest that 2) could be a part of *1Gen* that had drifted away when *2Gen* vein formed. However, it has a bright orange to yellow CL signal, suggesting it is relatively devoid of Fe.

4.3.2.4. Oscillatory zoned calcite in a shear vein

Associated with the en-échelon microstructure detailed in Section 4.3.2.3 at 9.8 m above the PSZ is a laterally discontinuous, ~50 μm thick and 1 mm long, micro-shear vein with ~50 μm displacement (see Figure 4.5). This fracture has been infilled with blocky calcite growth that exhibits little evidence of growth competition, with variable c-axis orientations, and has an average grain size of half the vein thickness. Most grains display one or no sets of e-twins and these are thin (<2 μm) and widely spaced (>20 μm). In contrast to other calcite vein structures observed, this vein has distinct, oscillatory zoning visible in CL (Figure 4.5A). This appears to be a largely chemically controlled feature as SIMS analyses in Figure 4.5D (traverse from blue to red dot in Figure 4.5A) show that the zoning correlates well with cyclical variations in trace metals. Peaks in Mn, Mg and Sr (and by inference troughs in Fe which could not be measured within the transect) correspond to the bright CL zones, with dramatic reductions in these ions resulting in areas of darker CL signal. The misorientation profile in Figure 4.5E, taken from the green to the red dots within the purple grain in Figure 4.5C, shows a small overall variation of ~2° in the internal orientation of this grain across the zoning. However, there appear to be some subtle variations in orientation (0.1 – 0.2°) coinciding with peaks in trace element variations. Such perturbations may be too small to influence the sealing mechanism of the vein; further nano-scale investigation would be needed to ascertain their validity.

4.3.2.5. Principal Slip Zone: reworked calcite and calcite pooling

Carbonate within the Unit 5 ultracomminuted gouges of PSZ-1 (*1A-90.74m-A*), the 25 cm thick main slip zone of the Alpine Fault, occurs as monomineralic angular clasts (diameters of 10 – 1000 μm), or as micro-veins (2 – 5 μm thick) within recycled gouge clasts (Figure 4.6) and compose ~5 % of the gouge. In Figure 4.6A and C a carbonate clast is highlighted that exhibits CL zoning with four distinct regions. SIMS analyses confirm that, as seen previously, bright CL signal corresponds to low trace Fe, while dull CL signal is caused by increasing levels of Fe (Figure 4.6A and B).

As visible in the CL and trace element analyses many clasts within the principal slip zone are composed of multiple generations of chemically distinct calcite. These variations are also marked by distinct changes in rock texture within these clasts. Figure 4.6A and C show

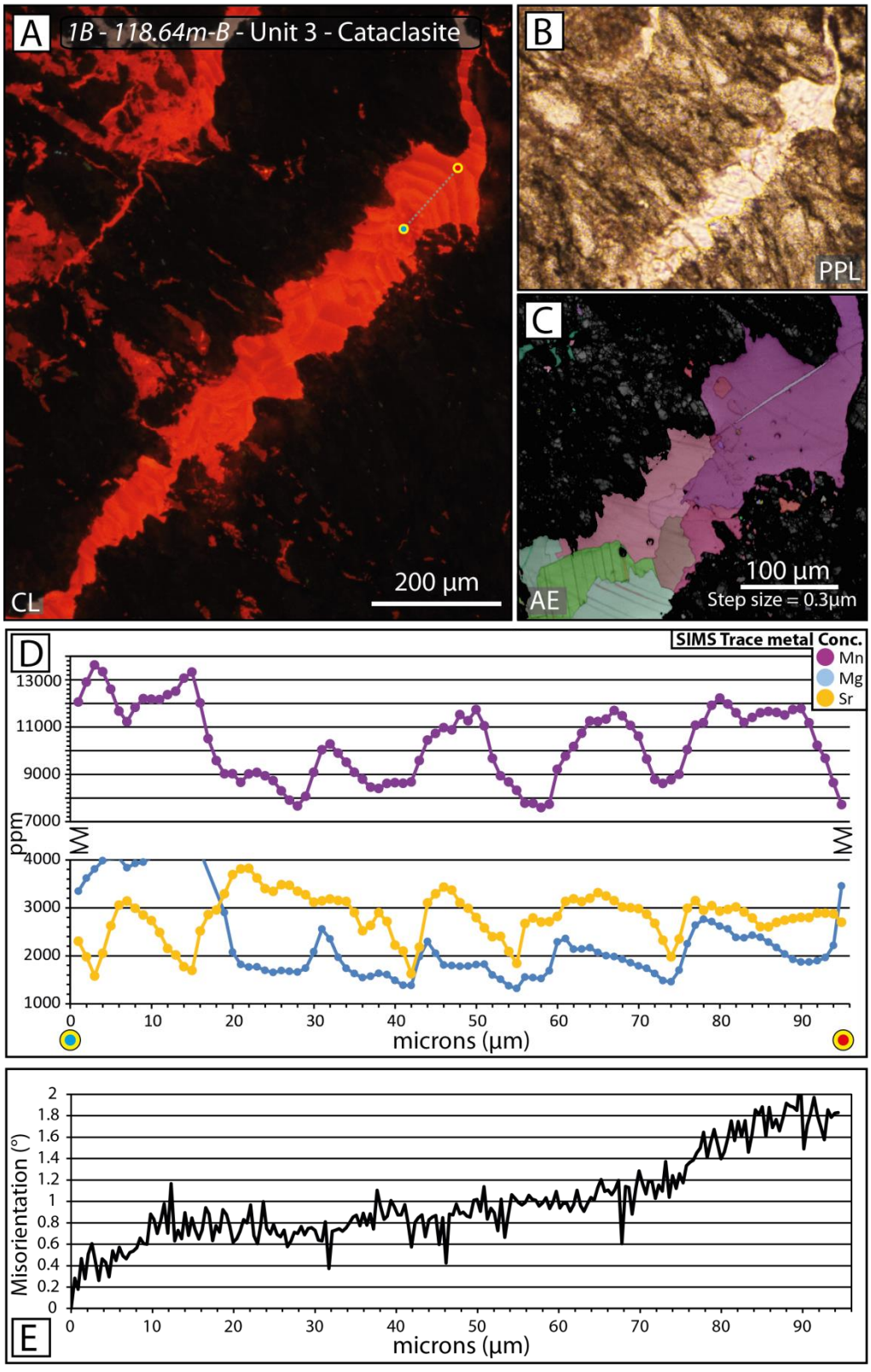

Figure 4.5 – *caption overleaf.*

Figure 4.5 – *(above)* ***[A]*** *Located within the same hanging wall cataclasite (1B-118.64m-B – Unit 3) as Figure 4.4. The CL image shows a calcite mineralised shear with regular,* oscillatory *zoning with an alternating bright – dull orange CL signal.* ***[B]*** *PPL image of (**A**).* ***[C]*** *The AE EBSD map shows that this zoning is constrained largely within a single calcite grain.* ***[D]*** *SIMS trace* element *concentration transect, location shown in (**A**);* oscillatory *zoning in CL corresponds to trace* element *variation.* ***[E]*** *The relative misorientation (in degrees) with distance along the transect detailed in (**A**); overall increase in misorientation along the calcite growth direction.*

four generations of calcite separated by 2 – 10 µm thick boundaries of finely comminuted, cataclased material. Regions 1 and 2 display yellow and bright orange CL and contain angular, interlocking grains of calcite (0 – 40 µm), which are heavily twinned into one or two sets of e-twinning lamellae. Regions 3 and 4 exhibit finer grain sizes (1 – 20 µm), lobate sometimes serrated grain boundaries and networks of subgrains. No pervasive twinning is evident.

The secondary, lower PSZ at *1B-143.85m* shown in Figure 4.7, which forms the lower boundary of the granitoid-derived footwall cataclasites, is composed of a continuous ~10 mm thick layer of cataclasite and ultracomminuted gouge, the cataclasite above this gouge layer has been cemented by calcite precipitation. The CL image reveals a fine-scale fracture mesh, localised to a layer ~1 mm thick and constrained above PSZ. Multiple shades of CL are present with larger regions of carbonate exhibiting darker CL while finer micro-veins show lighter CL.

4.3.2.6. Overall trace element variation

The most variable trace elements incorporated into calcite as it precipitated within the alteration zone are Fe, Mg, Mn and Sr. The variation of Mg and Fe concentrations within a single depth interval can be dramatic (Figure 4.8A) and some of the greatest variations can be seen in the en-échelon veins of *1B-118.64m-A* (Figure 4.4), a foliated cataclasite ~10 m above the main PSZ, with Fe spanning 300 – 6250 ppm and Mg 250 – 5900 ppm, demonstrating the variability of trace elements both between and within generations of AFZ calcite veins within a single depth interval. However, the largest variability is measured within calcite veins of the PSZ, with Fe and Mg concentrations ranging between at

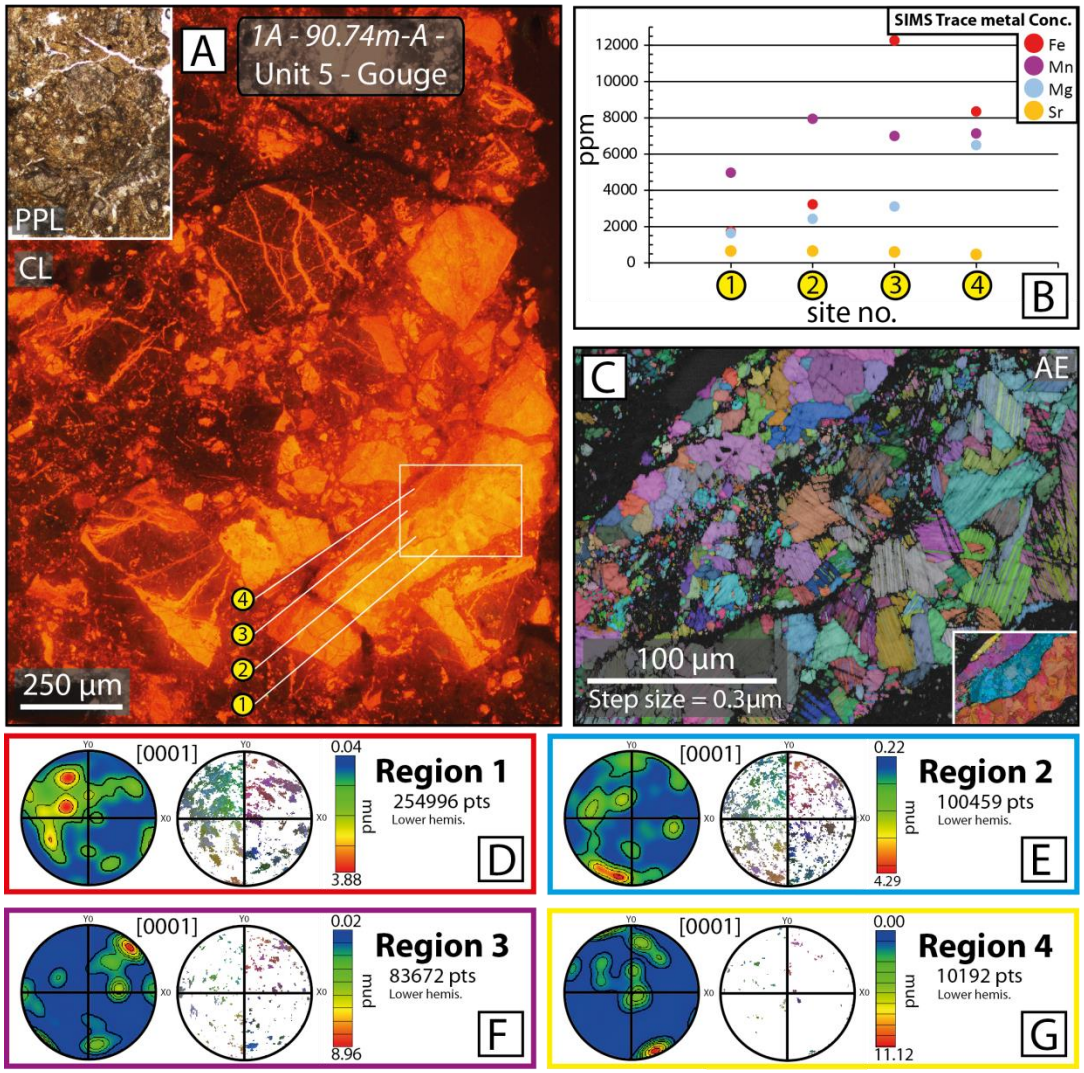

Figure 4.6 – [A] *Ultracomminuted gouge from the upper PSZ (1A-90.74m-A – Unit 5). CL image shows veined recycled gouge clasts and monomineralic calcite aggregates that variably have uniform CL signals or range from dull to bright orange.* ***[B]*** *SIMS trace* element *concentrations from sites marked in (**A**); brighter CL regions contain greater Mn content than Fe while darker CL regions more Fe than Mn, with Mg increasing with Fe.* ***[C]*** *An AE EBSD map of site highlighted in (**A**); four distinct generations of calcite can be seen differentiated by cataclastic material boundaries, degree of deformation and chemistry.* ***[D – G]*** *PFs of regions highlighted in (**C**), show that the CPO across generations is unrelated.*

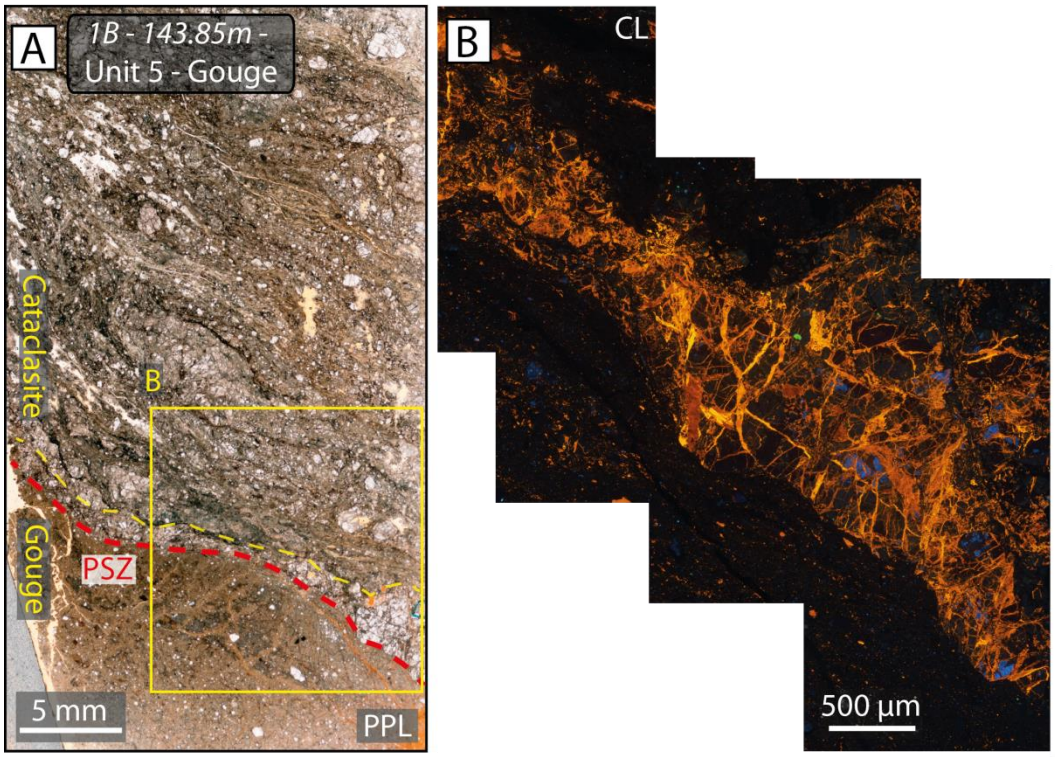

Figure 4.7 – [A] *Ultracomminuted gouge and cataclasite from the lower PSZ (1B-142.2m – Unit 5). Contact between smectite-rich gouge and cataclasite with abundant calcite veining above gouge layer (highlighted in yellow).* ***[B]*** *CL image of region marked in (**A**). Blue CL is from K-feldspar clasts and green CL is from apatite.*

1100 – 9000 ppm and between 1100 – 6450 ppm respectively, ranging higher in concentrations than all other samples (red data points in Figure 4.8A). In contrast, the concentrations of Fe and Mg in calcite veins of the AFZ footwall are low (blue data points in Figure 4.8A). The data points labelled *'Field'* in Figure 4.8B and shown in black are measurements taken from a quartz-calcite vein within an AF hanging wall metabasic mylonite acquired from field exposures at the Waikukupa River (see Figure 1.5 for sampling location) that was analysed for comparison with borehole specimens. The estimated depth of this *Field* quartz-calcite vein is ~6 km, approximately at the BVT of the Alpine Fault, based on fluid inclusion microthermometry and quartz microstructure identification by *Menzies et al.*, [2014].

4.3.2.7. Overall stable oxygen isotope variation

Just like trace element concentration analyses, stable oxygen isotope ($\delta^{18}O$) measurements were also spatially resolved, and they were taken from carbonate veins (calcite and ankerite) through the alteration zone, sampling a number of generations (based on cross-cutting relationships) at a given depth, where these were available (see Figure 4.8B). Overall $\delta^{18}O$ values range from 6.4 – 15.8 ‰ which is within the range for quartz precipitate from fluids of dominantly meteoric origin [*Menzies et al.*, 2014, 2016]. Variations between generations of calcite veins at the same depth interval are substantial, particularly in samples *1B-99.3m* and *1B-111m*. Interestingly, a close match in $\delta^{18}O$ values can be observed between *1B-118.64m* (foliated cataclasite) and *1A-90.74m* (PSZ gouge). Notably, these two samples also have the largest range of trace element concentrations, as described above. Furthermore, while recognising the large variations in the $\delta^{18}O$ values measured, a weak trend of decreasing $\delta^{18}O$ values with increasing depth within the borehole is apparent in Figure 4.8B. Bulk rock stable isotope analyses performed by *Menzies et al.*, [2014] on separated and crushed quartz-calcite, calcite and chlorite veins from field exposures, one such sample is included in these analyses as *Field*, compare well (2.5 – 15 ‰ $\delta^{18}O_{min}$ values) with our spatially resolved SIMS measurements of $\delta^{18}O_{calcite}$ in the DFDP-1 borehole samples.

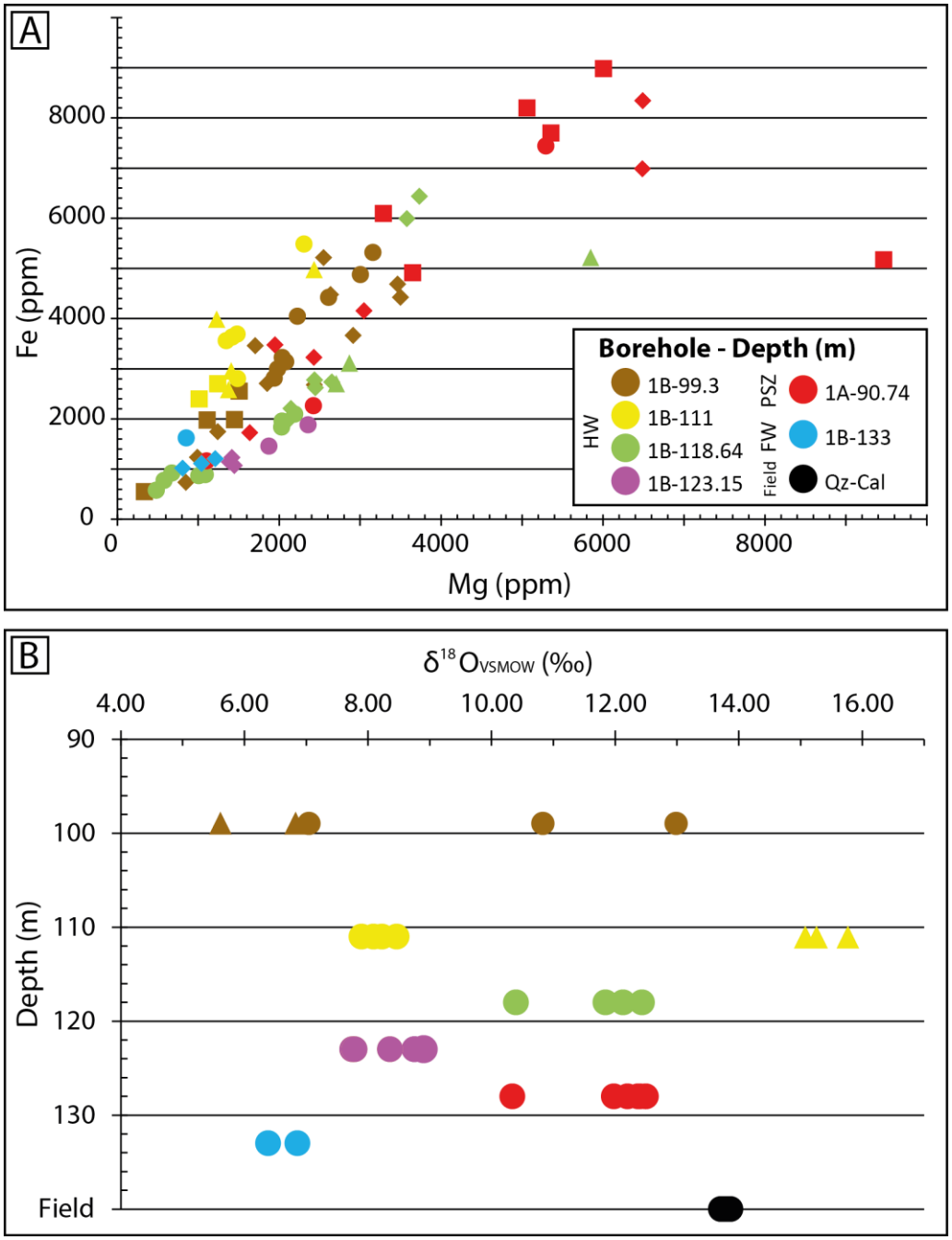

Figure 4.8 – [A] *SIMS Mg and Fe concentrations in part per million (ppm) with depth: a strong correlation of combined increase Fe and Mg content is visible; calcite within the PSZ has the greatest Fe – Mg content as well as the greatest range. Symbol variation denotes separate generations, for full key see Figure SM 4.9.* ***[B]*** *SIMS $\delta^{18}O$ measurements with depth. The quartz – calcite vein Field sample was acquired from Menzies et al., [2014]. Triangle symbols denote a separate generation measured at that depth. HW = hanging wall; PSZ = principal slip zone; FW = footwall; Field = sample retrieved from field exposure.*

4 4. Discussion

4.4.1. Classification of the Alpine Fault alteration zone carbonate veins

During an earthquake, much of the strain and thus deformation in the crust is localised in the principal slip zone of a fault. With increasing distance away from the principal slip zone, the extent of damage is progressively less [*Mitchell and Faulkner*, 2009; *Faulkner et al.*, 2010]. The length-scales of fractures within a fault damage zone can range from grain-scale micro-fractures to macro-fractures (exposure to km scale) that may in their own right be considered subsidiary fault structures [*Faulkner et al.*, 2010]. Due to the sampling limitations inherent in drilling projects, decimetres to micron scale fractures / veins are typically the only scales that can be observed in drill-core [*Williams et al.*, 2016].

In regard to the Alpine Fault fault core / alteration zone, *Kim et al.*'s [2004] *wall damage zone* classification appears most applicable in regard to the scale of fracture detailed in this study (µm – cm), while the nature of the precipitate matches most closely a *syntaxial vein* classification. However, a number of features described below may extend the range of these classifications due to the evolved, complex nature of the heavily cataclased, altered zone of rock bounding the AF. This section aims to interpret the variety of vein microstructures and chemistries that have been studied in samples from AFZ core. From interpretations a preliminary classification of AFZ calcite veins will be proposed, providing some further insight into the processes of crack sealing that may take place within a fault zone during the seismic cycle. This may have potential application to other mature, tectonic faults zones that are similarly heavily damaged and have undergone extensive geochemical alteration.

Though limited by sampling size and 2-dimensional observations, the majority of the veins and voids detailed in this study appear to be of hybrid shear-extensional (mixed mode) fracture origin [*Ramsey and Chester*, 2004]. The veins described show evidence of at least some shear, with displacements of <4 mm, and with dilation appearing to be partially shear induced but with some extensional component. These mm – cm scale microfractures concur with other studies and models on mature fault zones, with distributed deformation in the fault core cataclasites as the strain gradient reduces away from the main shearing PSZ where slip is localised.

4.4.2. The microstructure of vein calcite in the Alpine Fault

The morphology, texture and microstructure of the vein-infill can reveal much about the formation processes and conditions both before and after precipitation, however the variety of factors that influence crystal growth from a fluid and subsequent deformation means deciphering such processes and conditions can be challenging. In this section, the microstructural variation of the Alpine Fault carbonate vein-infill across generations and with proximity to the PSZ is discussed.

Crystal morphology and growth direction reveal information on the mechanisms that control the precipitation of the vein filling. Calcite, having trigonal crystal symmetry, is anisotropic and generally grows faster in the direction of the [0001] c-axis. With growth competition between grains, a CPO can develop in the vein-infill [*Nollet et al.*, 2005]. However, depending on the setting and conditions during crystal growth, different axes of the calcite crystal can preferentially grow. A number of studies report these controls on growth of calcite relative to its c-axis. *Folk*, [1974] reported that incorporation of Mg^{2+} into the calcite would sufficiently distort the crystal lattice and inhibit growth normal to the c-axis if the precipitating fluid had a high Mg/Ca ratio. Alternatively, variation in surface charges on crystal faces could lead to preferential growth of the c-axis, depending on the Ca^{2+} / HCO_3^- ratio of the precipitating fluid [*Lahann*, 1978]. Growth of particular faces would also be bound to whether the prism or basal faces of the calcite nucleates on the vein wall, with fast flowing fluid potentially forcing the prism face to nucleate on the vein wall and resulting in the subsequent growth of the c-axis basal face parallel to the vein wall, as reported by *Tulloch*, [1982] in geothermal energy pipework. In this study, all calcite crystal planes and axes were analysed. However, the strongest fabrics were observed in the [0001] c-axis PF plots, and thus these results are presented.

The majority of the veins studied in this thesis within the Alpine Fault fault core / alteration zone, whether deformed or undeformed, exhibit blocky-equant, and occasionally elongate-blocky, grains that span the entire width of the vein. These veins are characterised by little growth competition as evidenced by their weak shape preferred orientations and also, in those that show no twinning, by the weak, often inherited fabrics observed in pole figure plots. These blocky grain shapes are attributed to growth within an open cavity or rapidly opening veins that synchronously seal by mineral precipitation [*Hilgers et al.*, 2004]. Fibrous

crystals, which are usually attributed to crack-seal or progressive opening of a fracture with incremental vein precipitation, are not observed in the Alpine Fault material studied. Similar vein microstructures are observed in studies of the San Andreas Fault Zone reported by *Mittempergher et al.*, [2011] and *Hadizadeh et al.*, [2012], who attribute blocky vein-infill textures to precipitation from a free fluid in an open void. The lack of preferred orientations in calcite vein-infills have also been reported by *McNamara et al.*, [2016], who suggested that calcite crystals grow syntaxially outward from multiple orientations on a vein wall, eventually sealing the void space with a 3-dimensional interlocking set of elongated crystals.

The majority of the veins show evidence of at least partial reactivation and subsequent precipitation of calcite vein-infill indicated by: the reworking of calcite within sheared veins as in *1B-99.3m-A* and *1B-99.3m-B* (Figures 4.2 and 4.3); the incorporation of the cataclastic host-matrix as coherent boundaries as in *1B-118.64m-A*, *1A-90.74m-A* and *1B-111m-B* (Figures 4.4, 4.6 and SM 4.3), or the encompassing of older generation calcite by newer generations as in *1A-89.4m* and *1A-90.74m-B* (Figures SM 4.1 and 4.6). Reactivation predominantly occurs along vein-infill and host-wall contacts as these represent natural zones of weakness. However, in some instances fractures, especially those at high angles to pre-existing veins, propagate through the cataclasite / gouge host and calcite vein-infill as seen in *1B-99.3m-A* and *B*, *1A-90.74-A* and B, *1A-89.4m* and *1B-118.64m-C* (Figure 4.2, 4.3, 4.6 and SM 4.1, 4.4 and 4.6), resulting in clasts of the older generation calcite 'floating' within a more recent calcite cement.

The constitution of the nucleation surface has a strong influence on crystallographic orientation of vein calcite. If precipitation occurs upon pre-existing vein calcite, the CPO is inherited, as evident in *1B-99.3m-A* and *1B-118.64m-A* (Figure 4.2 and 4.4), in which the more recent generation has nucleated upon and inherited the previous generation's host or twin orientations. This is likely a result of epitaxial growth in the presence of a fluid being the most energetically favourable form of crystal growth [*Putnis and Putnis*, 2007; *Mithen and Sear*, 2014]. When a fracture or void is generated in the cataclastic wall rock and there is no pre-existing calcite, as for example in *1B-99.3m-A 2Gen-isolated* (Figure 4.2C and 4G), the calcite nucleating on the fracture wall will grow in orientations likely governed by a combination of wall rock properties such as grain size and chemistry, fracture morphology, and the stress field. The incorporation of wall rock clasts or boundaries into the vein-infill

also appears to have a considerable effect on grain shape and orientation; within *1B-118.64m-A* and *1A-90.74m-A* (Figure 4.4 and 4.6) wall-rock boundaries may serve as the nucleation surface, resulting in c-axis orientations distinct from one another in the same generation as well as subsequent generations.

The predominance of blocky grain shapes, weak growth competition and 'floating' wall-rock / old calcite fragments indicate that precipitation of the vein-infill often occurred rapidly and explosively as the fracture propagated, potentially sealing the fracture instantaneously (Figure 3 and 4). This is likely evidence of hydrofracturing, in which a fluid is pulsed through the fault core / alteration zone during seismicity, propagating Mode I – dilatant fractures through reduction of effective pressures, which undergo some shear by movement on the fault. The sudden pressure drop during dilation results in the rapid supersaturation of the fluid and therefore in rapid precipitation on the fracture walls [*Phillips*, 1972; *Sibson et al.*, 1975], which could be in the order of seconds if wall rock clasts are frozen in suspension as in Figure 4.3 and 4.4. This rapid sealing mechanism is likely most applicable to fractures that have a sub-mm width, wider fractures may only be partially filled by rapid supersaturation / precipitation, being subsequently sealed through precipitation of calcite from a constant flux of fluid over a longer, though shorter than the overall interseismic period, timescale. The common evidence of vein reactivation in the Alpine Fault may indicate the propagation of mobile hydrofractures, particularly as vein structures are sub-vertical, at high angles to the fault plane (Figure 2, 3, 5 and SM 3, and 4). These mobile hydrofractures occur when the fluid at the upper tip of a fracture is overpressured while at the bottom is underpressured. If the fluid pressure at the upper tip can overcome the rock strength and lithostatic pressure it will propagate upward while its under-pressurised lower end will close. Mobile hydrofractures preferentially ascend along planes of weakness which may explain the reactivation of many of the vein microstructures witnessed in the Alpine Fault [*Pollard*, 1976; *Bons*, 2001; *Oliver and Bons*, 2001].

Experimental and theoretical models on vein mineralisation timescales predict a time span of ~68 – 760 years for the formation of 'small' veins, with a volume of 30 mm^3, under constant room pressure and temperature, with varying fluid volume and degree of calcite saturation [*Lee and Morse*, 1999]. The typical fluid / calcite volume ratio required for the formation of these short veins ranges from 10^5 to 10^6, indicating that an 'extremely' large amount of fluid is required for their production in nature. However, the time span needed

for vein filling is highly variable depending on factors such as fluid saturation state, flow velocity, vein dimension, and precipitation kinetics. In the process of hydrofracturing on the Alpine Fault, as described above, conditions are likely to speed up mineral precipitation dramatically, with rapid fluid flow and pressure fluctuations causing supersaturation of the fluid. The high temperatures observed at the near-surface on the Alpine Fault, as well as the transiently high temperatures generated within the PSZ coseismically, also promote calcite precipitation due to its reverse solubility, which persists up to pressures of ~1100 MPa [*Caciagli and Manning*, 2003].

Deformation twinning (also termed mechanical twinning, e-twinning or deformation lamella) is the key intracrystalline deformation mechanism that takes place within calcite at low temperatures, <~400 °C, and low confining pressures [*Burkhard*, 1993; *Ferrill et al.*, 2004]. Individual e-twins are considered to be zones of perfect simple shear and, where the twin domain has a crystallographic orientation different from the host calcite grain and defined by a rotation of 75° around < $\bar{2}$021>. This shearing leads to strain incompatibilities at twin-host boundaries and twin-twin intersections resulting in strain hardening. These incompatibilities may be removed by either grain-scale pressure solution processes at low temperatures or dynamic recovery processes at higher temperatures [*Burkhard*, 1993]. Twin-twin intersections form due to multiple twin-sets occurring simultaneously, and are known as Rose-channels [*Rose*, 1868]. These can form voids within calcite due to microfracturing but can also be filled by secondary calcite precipitation.

Twin Type	Temperature (°C)	Morphology
I	<200	Thin, straight twins, up to three sets per grain.
II	150 – 300	Thick (>1 µm), straight with slight lense shape.
III	>200	Thick, curved and often themselves twinned.
IV	>250	Patchy with irregular geometries caused by recrystallisation and grain-boundary migrations.

Table 4.1 – *Classification and description of calcite twin morphology variation with increasing temperature after Vernon, [1981]; Burkhard, [1993] and Ferrill et al., [2004].*

Twin thickness is a function of the temperature at which deformation occurred (Table 4.1). This has been determined by both experimental and field observations. Type I and II twins (Table 4.1) are known as rational twins, as they reflect rigorously the crystallographic

relation with their parent grain and always post-date it. Type III and IV twins on the other hand are irrational twins, where their relation with the parent grain is often altered by high temperature processes, and they may also be twinned themselves.

Variations in orientation within a crystal lattice, within a single grain or across grain boundaries, can be investigated by misorientation analysis of EBSD data. Lattice distortions themselves may be generated by a variety of processes including: sub-grain formation, incorporation of defects or varying trace elements during growth.

Within the studied veins, twin thickness, density and morphology vary substantially, particularly between vein generations. Older generations, i.e., *1Gen 1B-99.3m-A*; *1Gen 1B-99.3m-B*; *1Gen 1B-118.64m-A* (Figures 4.2, 4.3, 4.4 and 4.6), have thick twins with irregular twin-host boundaries that are decorated at these boundaries with fine, recrystallised material, and usually contain multiple e-twin sets which are indicative of strains of more than a few percent [*Barber and Wenk*, 1979]. This indicates that older generation(s) of calcite have undergone considerable deformation and recovery processes. In the twin classification scheme, these largely fall between Type II and IV indicating formation conditions of 250 – 300 °C [*Burkhard*, 1993; *Ferrill et al.*, 2004]. Within un-twinned calcite grains in the older generation, vein misorientations in the range of 5 – 10° are observed. Younger generation veins, i.e., *2Gen 1B-99.3m-A*; *2Gen 1B-99.3m-B*; *2Gen 1B-118.64m-A*, and those regions that have undergone recovery and recrystallisation, particularly focused on twin-host boundaries and twin-twin intersections, rarely exhibit twinning and show little internal misorientation (<1°).

The presence of multiple twin-sets and internal misorientation, which are both indicative of deformation, in older generation veins (*1Gen*) indicate that the vein infill precipitated during earthquake events prior to the most recent seismicity. Twin morphology in the *1Gen* calcite indicates it has been exhumed from depths of 4 – 6 km according to local geothermal gradients stated above. The *1Gen* calcite infill may therefore have seen multiple increments of slip on the Alpine Fault and has itself accommodated some (small) amount of the deformation imparted to the fault damage zone surrounding the fault core. The lack of twinning and internal misorientation in younger generation of veins and in regions where recrystallisation has occurred within the older generations, indicates that these veins and the processes that have obliterated twinning post-date the latest episode

of deformation within the Alpine Fault Zone, as there is no evidence of seismically induced deformation.

The existence of fine-grained calcite (diameters of ~0.5 – 5 μm) decorating twin boundaries, vein – wall-rock, and vein – vein contacts is common across the range of depths of the sampled zone. In sample *1B-99.3m-A,* fine-grained regions are interpreted as areas of recrystallisation within older generations, highlighted by a typical bright-orange CL signal indicating a higher Mn content as well as showing little sign of internal lattice distortion. This indicates that temperature dependent recovery and dissolution-precipitation processes are active, especially in areas of high dislocation density such as at twin-host boundaries, twin-twin intersections and boundaries at which fracturing or shear have occurred allowing fluid ingress. For example, in the sheared vein in sample *1B-99.3m-A* (Figure 4.2), the fine-grained material is in close spatial relation with the shear plane indicating that some of the fine-grained material is a product of brittle cataclasis during shear, with some precipitation and sealing evidenced by the variation in trace element content of the cataclased region compared to the parent calcite. These cataclastic processes are also evident in the cataclased vein of sample *1B-99.3m-B* Figure 4.3, in which a calcite vein has been remobilised and sheared causing fragmentation (brecciation evidenced by CL) and grain-size reduction, with fluid infiltration and new precipitation (evidenced by lighter orange CL) cementing this calcite breccia and the incorporated rounded wall rock fragments. This process potentially happened throughout successive periods of seismicity on the Alpine Fault, indicated by the change in trace element content between the brecciated calcite and younger cementing calcite (see section 4.4.3).

The chemical and mechanical responses of carbonate material at earthquake deformation rates have been the focus of a number of experimental investigations using high velocity shear apparatus. *Smith et al.*, [2013] performed experiments on room-dry calcite gouges, with grain size <250 μm, and up to 26 MPa normal stress and found that at slip velocities ≥0.1 m/s a principal slip zone was generated within the calcite gouge that was flanked by a <300 μm-thick layer containing dynamically recrystallised grains of 1 – 10 μm diameter, with well-defined shape and CPOs. This dynamic recrystallisation was accompanied by thermal decomposition of calcite to CO_2 and CaO and fault weakening behaviour. *Smith et al.*, [2013] also report similar recrystallised material observed on a natural principal slip zone in the Garam thrust, South Korea , exhumed from <5 km depth. *Smith et al.*, [2013]

infers that frictional heating along principal slip surfaces (both experimental and natural) would produce localised dynamic recrystallisation, a feature that could be diagnostic of shallow crustal seismicity. A number of other experimental / field studies have shown similar observations. *Han et al.*, [2007] reported thermal decomposition and phase transformations during slip of room-dry siderite-calcite quartz gouges in high velocity experiments and within the Chelungpu fault zone, China. In addition *De Paola et al.*, [2011] also reported thermal decomposition of experimental room-dry calcite gouges and suggested that a variety of mechanisms, e.g., flash heating, thermal pressurization and nanoparticle lubrication, take place within a principal slip zone composed of carbonates.

Within the principal slip zone of the Alpine Fault, recrystallised regions in a number of the calcite clasts (see Regions 3 and 4 in *1A-90.74m-A*; Figure 4.6) may be an indicator of transiently high temperatures upon or in the near vicinity of the PSZ. While the Alpine Fault PSZ is not entirely composed of, or hosted within, carbonate material, as in the examples above, the presence of substantial carbonate clasts horizons within the gouge layers, as well as concentrated layers above the PSZs (see *1B-143.85m*; Figure 4.7), there is still evidence of recrystallisation that may be an indicator of coseismic heating and thus potentially weakening processes associated with carbonate decomposition. The products of calcite thermal decomposition, CO_2 and CaO, would leave no direct record in the PSZ, as CaO (lime) readily hydrates to $Ca(OH)_2$, which then forms calcite again in the presence of CO_2 [*Han et al.*, 2007b].

4.4.3. Controls on trace element variation

The Alpine Fault alteration zone has undergone extensive fluid-rock interaction, leading to the precipitation of secondary phases and to the alteration and retrogression of the fault rock protolith lithologies [*Sutherland et al.*, 2012; *Townend et al.*, 2013; *Toy et al.*, 2015b; *Boulton et al.*, 2017a]. An incomplete but informative record of these reactions exists in the trace element chemistry of the carbonate vein-infills that provides evidence on: 1) the composition of the fluids that precipitated them; 2) the composition of the rocks the fluids had interacted with; and 3) the conditions at which fluid-rock interactions occur.

The compositions of fluids in the crust are controlled by the reactions that occur between fluid and rock as well as the local geothermal gradient, due to the temperature control on

partitioning of elements between fluid and mineral phases. As a result, trace element concentrations within carbonate minerals are strongly dependent on the composition and temperature of the vein forming fluid. The influence temperature exerts on the partitioning of trace elements into calcite mineralisation has been derived both experimentally and theoretically [e.g., *Oomori et al.*, 1987; *Rimstidt et al.*, 1998]. In response to a temperature increase Mg^{2+} is more strongly partitioned into calcite, while Sr, Fe and Mn are less strongly so [*Rimstidt et al.*, 1998]. *Menzies*, [2012] showed, in studies of shallow level fluid flow on the Alpine Fault, that at higher temperatures fluid-rock interaction generates an increase in Mg, Sr and Ca concentrations in the fluid. The ratios of these trace elements would vary with incorporation or precipitation of minerals from solution, such as the precipitation of chlorite, would decrease Mg fluid concentrations, while calcite precipitation would increase Mg/Ca, Mn/Ca, Fe/Ca and Sr/Ca ratios [*Menzies*, 2012].

During calcite precipitation in the Alpine Fault alteration zone, temperature has had a measurable influence on calcite trace element incorporation. Therefore, from this, and in conjunction with microstructural observations, inferences on the location and depth of the mineralisation, and on the associated processes can be made.

CL observations and SIMS measurements in this study have revealed a number of trends in carbonate compositions. Older generation veins within the hanging wall fault core / alteration zone, such as those that show extensive deformation and are cross-cut by younger structures, generally, but not always, have dull-orange CL signals and greater Fe and Mg concentrations e.g., *1B-99.3m-A and B, 1B-118.64m-A, 1A-89.4m* (Figures 4.2, 4.3, 4.4 and SM 4.1). This is indicative of precipitation at higher temperatures, which corroborates with the twinning microstructures discussed above, with twinning temperatures estimated at 250 – 300 °C, as well as the high Mg and Fe content in the *Field* quartz-calcite veins, which are inferred to have been formed at the BVT, with estimated temperatures of 250 – 370 °C [*Menzies et al.*, 2014]. These older veins typically contain areas of bright CL, marking increased Mn and Sr, that mark regions where recrystallisation has occurred, but also marks fractures and twin boundaries e.g., *1B-99.3m-A, 1B-118.64m-A* (Figures 4.2 and 4.4). This may be evidence for fluid-rock interaction between old vein-infills and 'new' fluids in the fault zone, characterised by a composition different from that of the older vein precipitating fluid, resulting in incorporation of Mn and Sr into recrystallised material and trace element exchange at points of fluid ingress such as

fractures and twin boundaries. A similar mechanism may occur that allows the incorporation of Fe into newly precipitated calcite, which may explain the microstructure observed in *1B-118.64m-A* (Figure 4.4) wherein a *2Gen* calcite, with little twinning and lattice distortion, has an identical CL signal as *1Gen* calcite, caused by high Fe content.

Within a single generation of veins, and particularly apparent in younger generations, that show little evidence of deformation and fluid interaction, the CL signal is predominantly uniform, e.g., *1B-118.64m-A and C, 1B-111m-B, 1B-123.15m and 1B-133m* (Figures 4.3 and SM 4.4, SM 4.3, SM 4.5 and SM 4.7). Uniform CL signal in a vein suggests that pore fluid chemistry, conditions, and fluid-rock interactions remained largely constant during precipitation. This, coupled with the blocky grain morphology seen in most veins, implies that vein precipitate was substantially fluid-buffered with a constant, homogenous source of Ca and other trace elements during precipitation, which persisted at least until the fracture was entirely filled.

Distinct zoning of CL signal and thus trace element content has only been found in one example, in sample *1B-118.64m-B* (Figure 4.5), where oscillatory zoning within a vein reflects fluctuations in Mn/Ca, Sr/Ca and Mg/Ca (and by inference Fe/Ca) ratios. Along the traverse where trace element concentrations were measured (blue to red point in Figure 4.5A), within the purple grain, a gradual and progressive misorientation of up to 2° is observed, suggesting that the zoning reflects the trace of the main growth surface of the crystal. As this growth surface migrates, it incorporates trace elements and defects, and lattice rotations (distortions) develop due to such defects [*Piazolo et al.*, 2005] (Figure 4.5A and 4.5E). Trace element zoning is indicative of changing fluid composition or temperature during mineral precipitation. As observed in experimental work by *Borg et al.* [2014], this variation could be caused by rapid fluid-rock interaction during precipitation causing fluid chemistry differentiation at the calcite growth interface even in cases when the overall system is fluid-buffered. Complete sealing of the fracture hosting this zoned calcite would then limit secondary reactions or alteration by fluid in the fault zone, preserving the zoning. This may be most likely in short-lived hydrothermal activity, for example during and immediately following an earthquake [*Borg et al.* 2014]. Crystal structure and growth may also play a considerable part in preferential incorporation of trace elements. As calcite is anisotropic, different faces grow via different mechanisms, e.g., spiralling, polygonised growth or hillocks development etc. This controls the surface micro-topography, specifically

the orientation of growth steps and kink sites, resulting in differential incorporation of trace elements [*Paquette and Reeder*, 1995]. Growth rate has also been called upon to explain zoning in calcite [*Barker and Cox*, 2011], whereby decreasing precipitation rate and increasing temperature cause Fe and Mn incorporation and the ratio of Mn / Fe to increase [*Dromgoole and Walter*, 1990]. In regards to the zoning in *1B-118.64m-B* (Figure 4.5), it likely reflects slower precipitation rates within porosity that has remained open into the fault's interseismic period. If precipitation rates were slower, it would be more likely for fluctuations in temperature or trace element concentration in the fluid, or a combination of the two, to be recorded during calcite precipitation.

Of all AFZ lithologies, the calcite present in the principal slip zone shows the greatest range in Mg/Ca and Fe/Ca ratios and highest Mg/Ca and Fe/Ca ratios (Figure 4.8). An additional characteristic of veins in the PSZ is that the CL signal has a trend generally opposing that observed in the alteration zone, whereby bright CL is seen in older, deformed generations of calcite cement (samples *1A-90.74m-A* and *B,* Figure 4.6 and SM 4.6). This could be due to a number of processes and conditions unique to the PSZ gouge, such as intense grain-size reduction to <0.001 mm for the matrix and <0.01 mm clasts [*Toy et al.*, 2015b], and elevated temperatures due to frictional heating during seismicity, resulting in enhanced fluid-rock interaction and efficient mixing of trace elements and alteration [*Boulton et al.*, 2017a]. A number of reactions occurring in the alteration zone could enrich fluids with Mg and Fe, these are outlined by *Wintsch and Yeh*, [2013] and *Boulton et al.*, [2017] and include biotite to chlorite: 2phlogopite + $4H^+$ + H_2O = clinochlore + $2SiO_2$ + Mg^{2+} + $2K^+$; and chlorite to muscovite: 3clinochlore + $2K^+$ + $28H^+$ = 2muscovite + $3SiO_2$ + $15Mg^{2+}$ + $24H_2O$. Fe may be present in these reactions within clinochlore but the reactions are balanced assuming only octahedral magnesium cations. These reactions could progressively enrich the fluid in Mg and Fe, resulting in the formation of Mg and Fe-rich calcite as seen in *1A-90.74m-A and B* (Figures 4.6 and SM 4.6).

Permeabilities within the cataclasites and gouges of the fault core / alteration zone are habitually low, as shown in static experimental measurements, at ~10^{-18} to 10^{-21} m^2 [*Boulton et al.*, 2012; *Carpenter et al.*, 2014; *Allen et al.*, 2017]. Coseismically, these permeabilities are increased through fracture generation in the cataclasites, and inferred to be quickly reduced through vein sealing as evidenced by the vein microstructures detailed above. However, within the gouge layers permeability is likely only marginally increased

during seismicity, in contrast to the cataclasites, and reduced on a far shorter time-scales. This potentially occurs through coseismic thermal pressurisation within the gouges, allowing the reduction of effective stresses and fluidisation of the gouge, increasing the permeability [*Ujiie et al.*, 2011]. This permeability is then rapidly reduced through shear-induced compaction resealing the gouge layer [e.g., *Tanikawa et al.*, 2012]. This rapid reduction in gouge permeability could potentially result in the trapping of local fluids and resulting in an rock-buffered environment in which the calcite in and around the PSZ gouge layer is isolated and enriched in Mg and Fe as local fluids dominate over fluids from further afield in the fault zone.

In order to aid discussion and interpretation of trace element data as a whole, a statistical method known as Principal Component Analysis (PCA) was used. PCA may reveal simplified patterns in a complex set of variables by reducing the observed variables to a smaller number, called factors. The program used to perform PCA is XLSTAT, a data analysis and statistical application that runs through Microsoft Excel developed by Addinsoft.

PCA is a true eigenvector-based multivariate analysis. It involves the use of an orthogonal transformation that converts a set of possibly correlated variables into linearly uncorrelated variables termed principal components. The amount of principal components is less than or equal to the smaller of the number of original variables. The transformation results in the first principal component having the largest possible variance, accounting for as much of the original data's variability as possible, with each successive component having the highest variance possible under the constraint that it is orthogonal to the preceding component. This results in vectors which are an uncorrelated basis set [*Davis*, 2002; *Jolliffe*, 2002]. The spread sheet containing the calculations and original trace element datasets is included in Workbook SM 4.1 in the Digital Supplementary Materials.

After feeding the trace element concentrations of interest, comprising the Fe, Mn, Mg, Sr, Ba and Ce measurements from all the depths and veins sampled, into the PCA application, the plot illustrated in Figure 4.9 was generated. The proportion of the variance for each principal component is as follows: 1st principal component (PC), 45.88 %; 2nd PC, 21.83 %; 3rd PC, 16.16 %; 4th PC, 9.43 %; 5th PC, 6.47 %; 6th PC, 0.22 %. It is clear from the pattern of clustering in the plot that chemical variation in the veins correlates with their location in the fault. A wide cluster comprising all data from veins in the AFZ hanging wall,

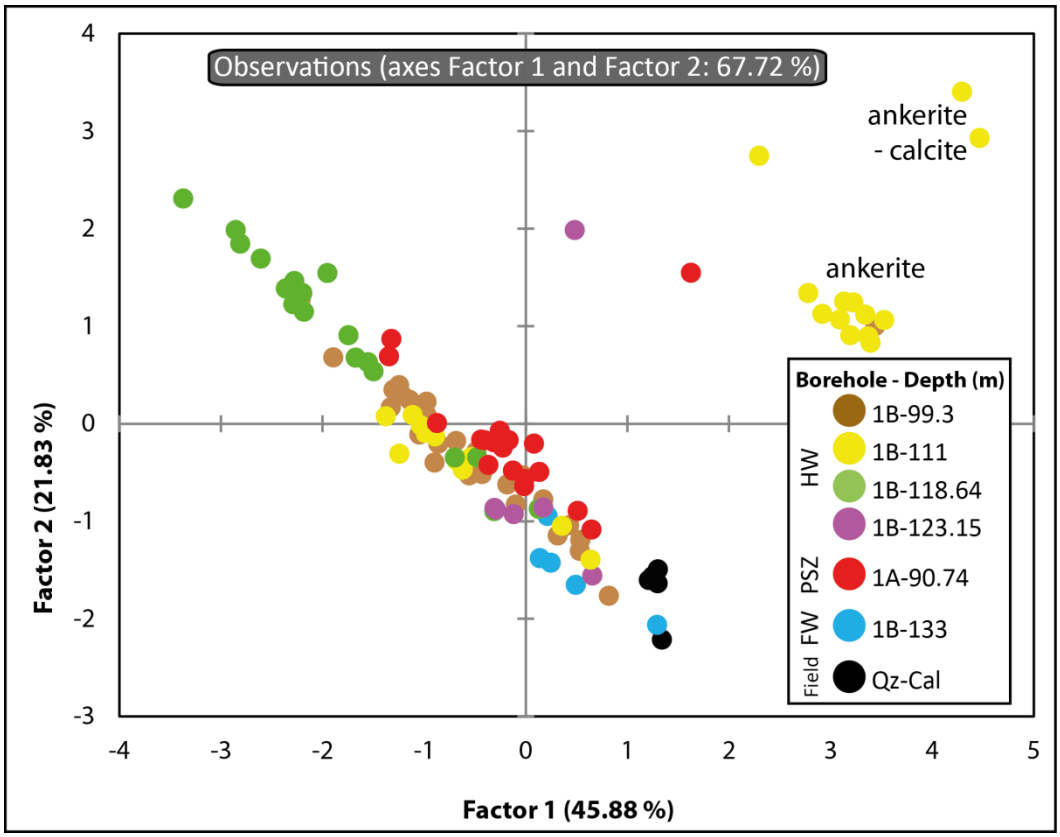

Figure 4.9 – *Principal component analysis (PCA) plot of all trace element measurements, Fe, Mn, Mg, Sr, Ba and Ce, made in this study. Clustering shows correlation between calcite composition and location on the Alpine Fault. HW = hanging wall; PSZ = principal slip zone; FW = footwall; Field = sample retrieved from field exposure.*

PSZ and footwall is clearly observed. There are clear groupings of calcite chemistries within *1B-118.64m-A* and the *PSZ 1A-90.74m*, with the remaining data highlighting the wide range of calcite chemistries present through the fault core / alteration zone calcite overlapping one another. The ankerite and mixed calcite-ankerite vein in *1B-111m-A* (Figure SM 4.2) both cluster separately from the calcite veins, due to their greater Mg, Fe and Mn content. The quartz-calcite vein *Field* sample also clusters separately, similarly due to higher Mg and Fe content, a result of higher precipitation temperatures that may be associated with a quartz-bearing vein, estimated by Menzies et al., [2014] to be between 250 – 370 °C.

Jenkin et al., [1994] speculate that the substantial Ca and CO_2 in the shallow crustal fluids of the Alpine Fault hanging wall could be explained through fluid-rock interaction with metamorphosed carbonaceous material in the fault hanging wall or dissolution of Ca from Ca-bearing minerals in the Alpine Schists (hornblende, plagioclase, garnet and epidote). As for the origin of the trace element species discussed above, the alteration, hydration and retrogressive reactions that take place within the fault likely provide substantial material for dissolution in the hot fluids of the Alpine Fault hanging wall [*Sutherland et al.*, 2012, 2017]. Mg, Fe and Sr are likely sourced from interaction with the chlorite-rich rocks within the shallow Alpine Fault, with the transformation of primary minerals, i.e., biotite, muscovite and chlorite, to kaolinite, smectite (montmorillonite), Fe- goethite and lower temperature muscovite/illite (white mica) releasing substantial Mg^{+} and Fe^{2+} into the free fluid [*Boulton et al.*, 2017a].

The abundance of Mn in the alteration zone calcite however has a less obvious source. Garnets are present throughout the Alpine Fault rock sequence, including the Alpine Schists, protomylonites and mylonites, and have been observed to have Mn-rich cores ($Alm_{19}Gr_{30}Py_{3}Sp_{48}$) and Mg-rich rims ($Alm_{61}Gr_{22}Py_{8}Sp_{9}$) [*Cooper*, 1974; *Prior*, 1988]. *Cooper*, [1974] and *Grapes and Watanabe*, [1994] found that these spessartine garnets had equilibrated at 450 – 480 °C, predominantly below the garnet zone of the amphibolite facies. Here Mn is expected to be abundant and as few other minerals form that are able to accommodate Mn at these conditions, as such it was incorporated into the garnet [*Bucher and Frey*, 2001; *Toy*, 2007]. Garnet readily retrogresses to chlorite and quartz as amphibolite facies schists and mylonites are exhumed to sub-greenschist facies conditions on the fault following the reaction (*Garnet + Mg-rich Chlorite + H_2O = Chlorite + Quartz) (*see Figure SM 4.10 for microstructural evidence). This potentially explains the lack of evidence

for garnet in the alteration zone, where no relict grains or pseudomorphs are observed. Therefore, retrogressed garnets are potentially the main source of Mn in the Alpine Fault fault core / alteration zone, as well as providing some Mg, Fe and Ca.

Ankerite, a rhombohedral carbonate Ca (Fe, Mg, Mn)$(CO_3)_2$, has been reported infrequently in the Alpine Fault, occurring as the dominant hydrothermal precipitate in the northern section of the fault, between the Whataroa River to the Taramakau River, while calcite dominates in the central section from Havelock Creek to the Whataroa River [*Campbell*, 2002; *Craw and Campbell*, 2004]. A monomineralic ankerite vein (2 – 3 mm thick) and a calcite-ankerite vein (~1 mm thick) were located in sample *1B-111m-A* (Figure SM 4.3), a finding that correlates with X-ray diffraction measurements undertaken by *Boulton et al.*, [2017] that show an ankerite peak in *1B-112.12m*. The presence of these ankeritic veins has been attributed to a precipitating fluid temperature greater than that of the host-rock, at ~200 – 300 °C [*Craw et al.*, 2009]. This may mean that ankerite precipitated from hot fluid circulating at shallow crustal depths (<5 km) and has been exhumed, with calcite then becoming the dominant hydrothermal phase at shallower depths in the alteration zone [*Craw et al.*, 2009]. The sampled ankerite is likely a relic of deeper vein mineralisation processes that preceded the calcite mineralisation documented in this study and that most ankerite has been reworked and altered during seismicity and exhumation. Alternatively, variation in the geothermal gradient along-strike of the Alpine Fault as observed within tributaries, 62.6 ± 2.1 °C/km as recorded during DFDP-1 at Gaunt Creek [*Sutherland et al.*, 2012], and valleys, 125 ± 55 °C/km as recorded during DFDP-2 at the Whataroa River Valley [*Sutherland et al.*, 2017], may result in variation in carbonate mineralisation at the same depth upon the fault.

4.4.4. Implications for fault zone processes

The observations and measurements presented in this study show that the fluids circulating in the hanging wall of the Alpine Fault carry abundant calcium and carbon dioxide, which preferentially precipitate as calcite in the alteration zone. This precipitation seals fractures and voids opened during seismicity, decreasing permeability and increasing rock strength and competency (e.g., *Boulton et al.*, 2017a). These physical properties govern many aspects of the fault through the seismic cycle.

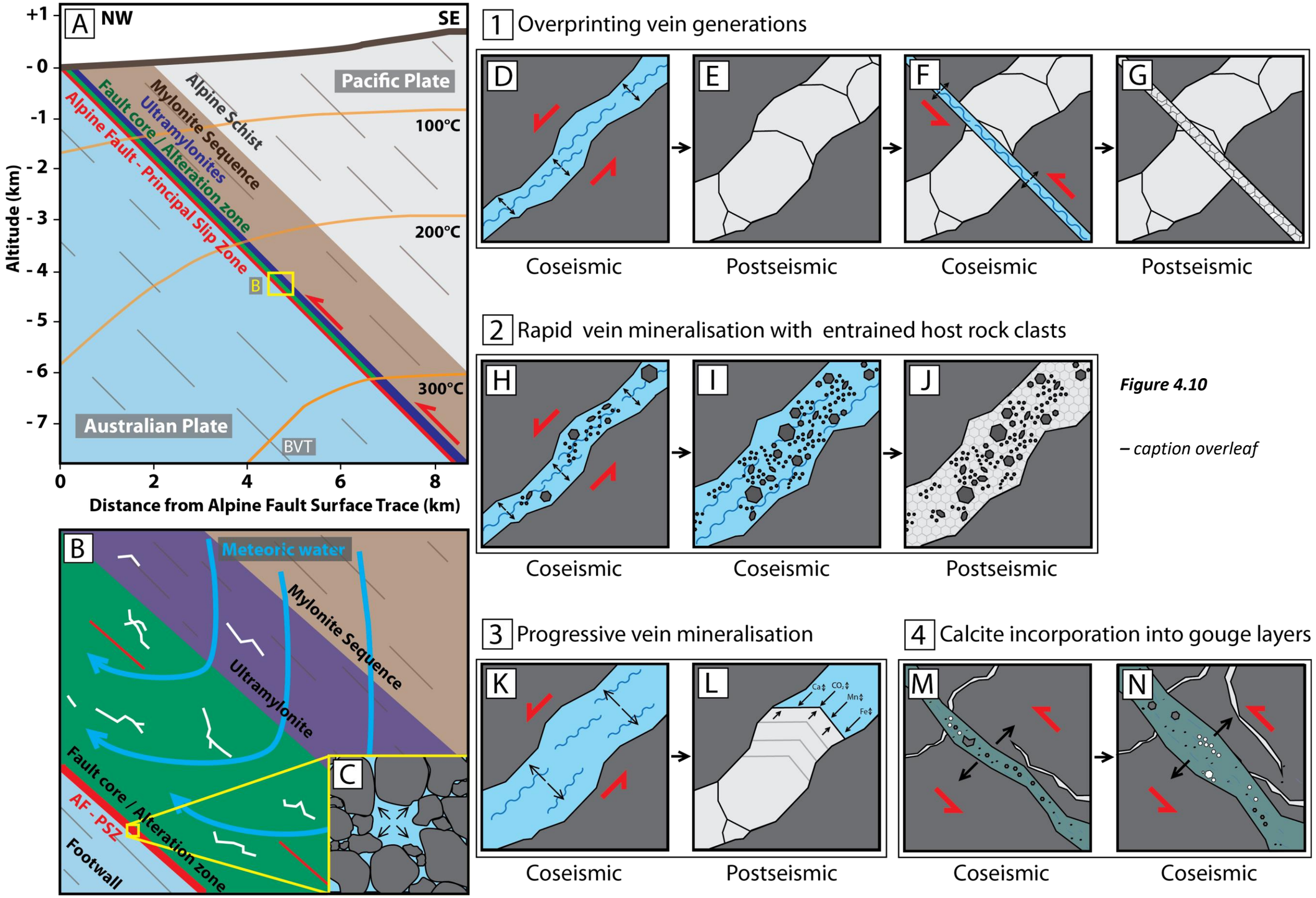

Figure 4.10

– caption overleaf

Figure 4.10 – *Schematic illustrations for the formation of the calcite vein microstructures in the Alpine Fault fault core / alteration zone.* ***[A]*** *The Alpine Fault Zone in the upper crust, showing the fault rock lithological sequence and geothermal gradient after Toy et al., [2010]. The red marker denotes the plate boundary fault between the Pacific and Australian Plate; the green marker the onset of cataclasis and alteration in the fault core above the BVT , ~30 m thick; and the purple marker denotes the ultramylonite zone, ~150 m thick, through which the fault core transitions into the fault damage zone.* ***[B]*** *Magnified view of the fault zone showing the path of meteoric fluid to and along the fault, red lines mark regions of slip and gouge generation, white lines mark calcite mineralisation.* ***[C]*** *Illustration of fluid within the pores of gouge/cataclasites within the Principal Slip Zone and fault core / alteration zone, pore fluid pressure increases due to shear heating during seismicity reducing the tensile strength of the rock inducing fracture generation.*

[1] *The formation of overprinting vein generations;* ***[D]*** *A dilatant shear fracture is generated in the fault core rock during seismicity, filled with pressurised fluid.* ***[E]*** *This fracture is sealed by calcite mineralisation immediately post-seismicity.* ***[F]*** *Subsequent seismicity generates an overprinting fracture over the previous vein generation.* ***[G]*** *The overprinting fracture is filled by calcite mineralisation.* ***[2]*** *The rapid mineralisation of a fracture entraining host rock clasts;* ***[H]*** *A dilatant shear fracture is generated in the fault core rock during seismicity, filled with pressurised fluid with wall rock clasts suspended in fluid.* ***[I]*** *Clasts are mobilised and remain suspended in the mobile fluid.* ***[J]*** *Mineralisation occurs rapidly freezing the wall rock clasts in suspension.* ***[3]*** *The formation of oscillatory zoned calcite veins;* ***[K]*** *A dilatant shear fracture is generated in the fault core rock during seismicity filled with pressurised fluid.* ***[L]*** *Fracture remains open into the interseismic period, potentially due to formation at shallow depths thus lower overburden pressures, allowing progressive mineralisation of calcite into the fracture void space. Varying amounts of trace metals is due to fluctuating ambient conditions or fluid source.* ***[4]*** *Incorporation of calcite veins into gouge layers;* ***[M]*** *As shear during seismicity is localised onto a surface gouge is generated from damaged wall rock.* ***[N]*** *Multiple subsequent slip events in the gouge zone progressively widens the slip zone resulting in incorporation of calcite veins previously generated in the more intact wall rock.*

The uniformity of vein chemistry within a single generation suggests that most veins were precipitated from a single pulse of fluid and that chemical variation within a single generation is the result of syn- and post-emplacement fluid-rock interactions and structural modification, such as fracturing and recrystallisation. This rapid generation and sealing of coseismic damage on the fault is consistent with recovery of rock strength and permeability after seismicity and brittle failure as observed in a number of crustal settings, including hydrothermal fields and fault zones [*Madariaga et al.*, 1998; *Tenthorey et al.*, 2003; *Vidale and Li*, 2003; *Tenthorey and Cox*, 2006; *Brenguier et al.*, 2008; *Cochran et al.*, 2009; *Kelly et al.*, 2013; *Griffiths et al.*, 2016; *Kitagawa and Kano*, 2016; *McNamara et al.*, 2016]. However, the presence of zoned calcite may indicate slower rates of precipitation do occur in the alteration zone, and that sealing mechanisms persist well into the interseismic period of the Alpine Fault. See Figure 4.10 for a schematic illustration of the various sealing mechanisms taking place in the Alpine Fault Zone.

The lack of thoroughgoing fractures in the PSZ gouge layers is due to the lack of cohesive strength, rapid compaction post slip and low competency at shallow crustal levels, generating an impermeable barrier which must be long-lived (e.g. *Boulton et al.*, 2012; *Sutherland et al.*, 2012; *Carpenter et al.*, 2014; *Menzies et al.*, 2016; *Allen et al.*, 2017). This interpretation is supported by the high concentration of calcite above the PSZ in the hanging wall and, in stark contrast, the lack of calcite, even reworked, in the footwall of the fault. An exception to the commonly observed calcite-free footwall is the vein network immediately above PSZ-2 (e.g., *1B-143.85m* in Figure 4.7). Here calcite is pooling between two slip zones. We propose two potential mechanisms controlling the emplacement of this horizon: 1) The percolation of a small amount of calcium carbonate-rich fluid through PSZ-1 and into the footwall during seismicity, before re-sealing, potentially as a pulse of hot fluid, reaching the secondary slip surface and pooling against the impermeable layer and precipitating; 2) the PSZ-2 is the result of a near surface thrust, generating a less mature, subsidiary slip surface. This slip surface may act as a conduit for flow at the near surface, bypassing the footwall cataclasites above it, resulting in preferential emplacement of calcite.

4.4. Conclusions

From microstructural and geochemical observations of carbonate mineralisation in the Alpine Fault alteration zone and PSZ, the following conclusions may be drawn on the behaviour of the fault and its fluids throughout the seismic cycle:

1. The Alpine Fault alteration zone shows extensive carbonate mineralisation, occurring predominantly as vein infill. Multiple fracture and sealing events have occurred on the fault, providing evidence for cyclical damage generation and recovery.
2. The lack of twinning and other signs of deformation in the most recent vein generation indicate that there has been little deformation or strain accumulation in the alteration zone since the last period of seismicity.
3. The transient nature of the permeability within the fault core / alteration zone is inferred to be due to seismically-induced fractures and porosity generation, potentially from both large magnitude Alpine Fault events and moderate magnitude events elsewhere in the fault zone. Immediately postseismically, the mobilisation of fluids results in rapid mineralisation and fluid-rock interactions, which seal and restrengthen the fault in preparation for the next cycle of seismicity occurs.
4. The trace elements incorporated into calcite during precipitation were sourced from fluid-rock interactions between hydrothermal fluids and cataclased rock. Mn was likely sourced from the retrogressive breakdown of Mn-rich garnet while Mg and Fe are derived from low temperature transformations of biotite into chlorite to smectite and muscovite alteration, particularly in the principal slip zone.
5. The variation in trace element incorporation into the carbonate veins during formation is due to the variations in ambient conditions of temperature and pressure within the fault zone and alteration reactions, through fluid-rock interaction occurring in the fault core / alteration zone between periods of fracture generation. In most cases, older vein generations contain more Fe and Mg, while younger generations and recrystallised regions contain more Mn, likely due to variation in temperature and pressure during precipitation as the fault hanging wall was exhumed. Increased Mg / Fe concentrations at the principal slip zone are

potentially caused by enhanced fluid-rock interaction within the ultracomminuted gouges, where clay-mineral alteration occurs during the exhumation of the fault.

6. Many of the veins are interpreted to be generated by hydrofracturing, where a hot fluid pulsed through the fault core / alteration zone during seismic activity, via rapidly propagating dilatant fractures with some shear component. The sudden pressure drop during dilation would result in rapid supersaturation of the fluid and therefore in rapid precipitation on the fracture walls, evidenced by blocky grain shapes, weak shape preferred orientations, uniform chemistry and 'floating' wall-rock / older calcite fragments. These features are predominantly observed in younger generation veins. Older generations may have formed via similar processes, but subsequent fluid-rock interaction and deformation has resulted in modification or sometimes obliteration of previous vein microstructures and chemistry.
7. The rare presence of oscillatory zoned vein calcite indicates that in some cases precipitation occurs over a longer time scale, with fluctuations in temperature, pressure or fluid-rock interactions, or any combination of the three, resulting in variations in calcite trace element incorporation rates. This could mean that, as well as rapid sealing occurring immediately postseismically, a fraction of void space remains open long enough to undergo slow sealing by calcite precipitation during the interseismic period.
8. Outside the fault core / alteration zone, within the AF damage zone, fractures likely remain open for far longer time scales or potentially indefinitely, allowing the passage of meteorically derived hydrothermal fluids above the contact of the damage zone and fault core / alteration zone, manifesting at the surface as hot springs.

4.5. Further work

To further understanding of fault sealing and restrengthening on the Alpine Fault a number of threads of further research could be followed. Performing calcite twin piezometry analyses, as developed by *Rowe and Rutter*, [1990] and *Yamaji*, [2015], could inform on palaeostresses on the Alpine Fault throughout periods of the seismic cycle in which calcite had been present. Another aspect to constrain better is the rate of precipitation of the calcite veins across generations, needed in order to improve understanding of the time frame for the sealing and

restrengthening of the Alpine Fault. This would require better estimates on the rate of fluid flow and the magnitude of pressure drops during seismicity on the Alpine Fault and the effect these have on oversaturation and thus precipitation rates. Undertaking a clumped isotope or fluid inclusion study on the calcite would also be useful to constrain temperature and pressure, and potentially depth, of the formation of the veins. An investigation of suspended host rock fragments within the calcite with microCT could supply more evidence for rapid depressurisation, if fragments are truly suspended in the vein precipitate.

4.6. Supplementary material

Table SM 4.1 – *Details of all the carbonate veins observed during this study, including: depth, lithology, figure number, description and techniques used during analysis. Available in the Digital Supplementary Materials included with this thesis.*

Workbook SM 4.1 – *Microsoft Excel workbook containing all carbonate trace element measurement data (Sheet SM 4.1) and workings for Principal Component Analysis (PCA) using XLSTAT® (Sheet SM 4.2). Available in the Digital Supplementary Materials included with this thesis.*

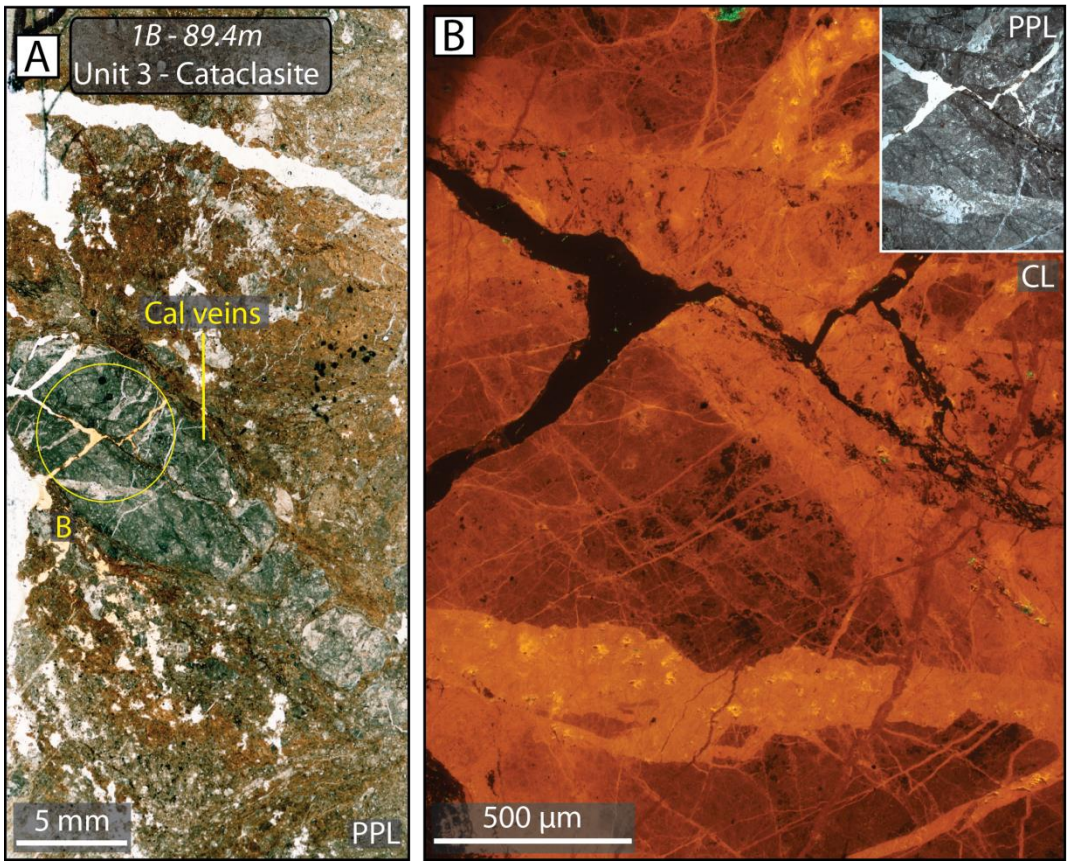

Figure SM 4.1 – [A] *A hanging wall cataclasite (1A-89.4m – Unit 3) 1.3 m above the upper PSZ. An unfoliated cataclasite containing a 5 mm thick, heavily twinned calcite vein.* ***[B]*** *CL image of location marked in (**A**); shows an older, dull-orange calcite generation cross-cut by multiple generations of brighter CL calcite.*

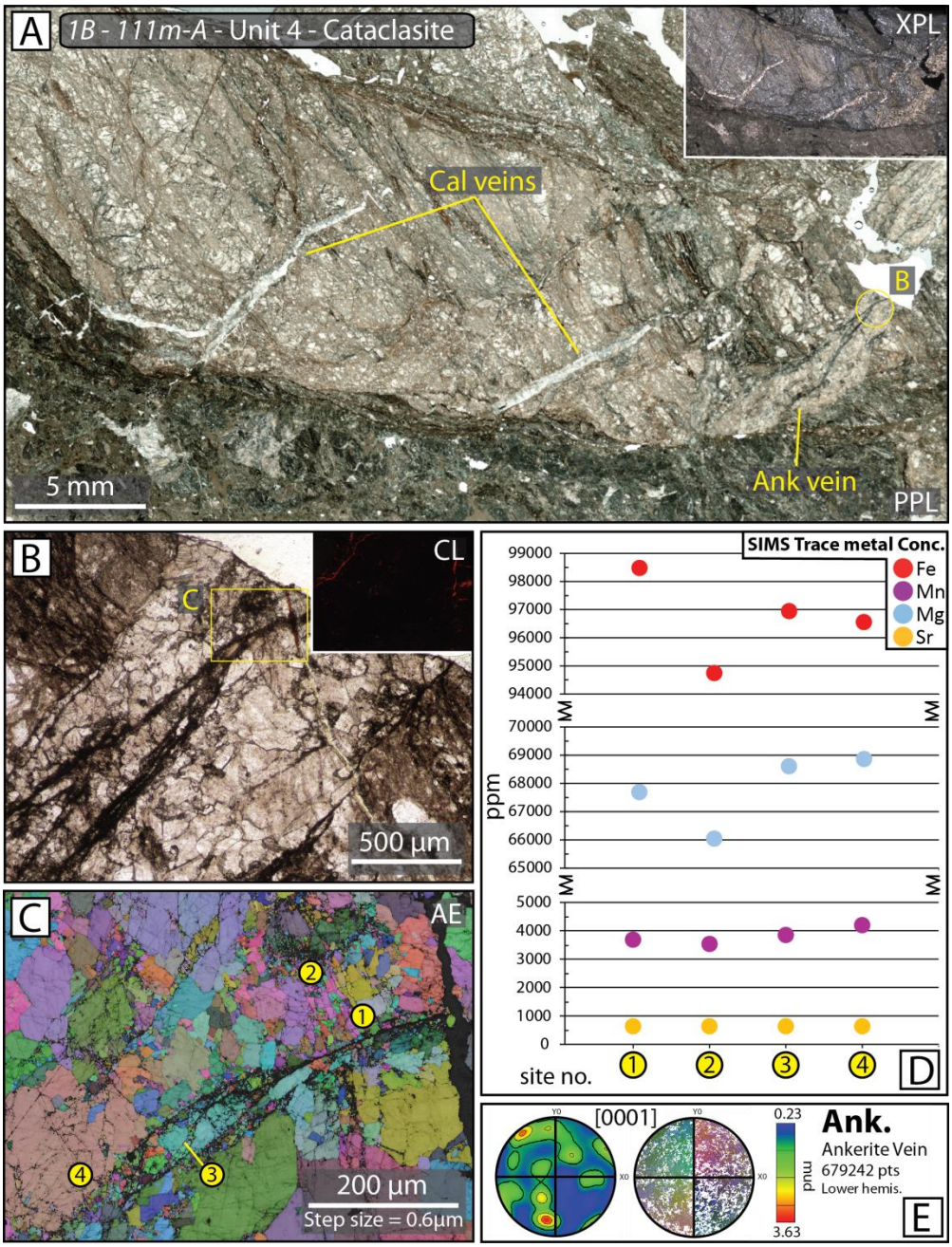

Figure SM 4.2 – [A] *A hanging wall cataclasite (1A-111m-A – Unit 4) 17.4 m above the upper PSZ. This specimen is composed of two cataclasites, black and grey. This lithological contact between the two terminating the carbonate veins in the upper grey cataclasite. These carbonates include calcite and ankerite veins.* ***[B]*** *Ankerite vein in PPL and CL at higher magnification, note the lack of luminescence.* ***[C]*** *An AE EBSD map of the ankerite vein, recrystallisation, sub grain formation and 2 – 5° misorientations within the grains is common.* ***[D]*** *SIMS trace* element *concentrations, sites marked in (**C**); show high Mg and Fe content, confirming ankerite composition.* ***[E]*** *PF of whole field of view in (**C**); note the wide spread in [0001] c-axis orientations and weak CPO.*

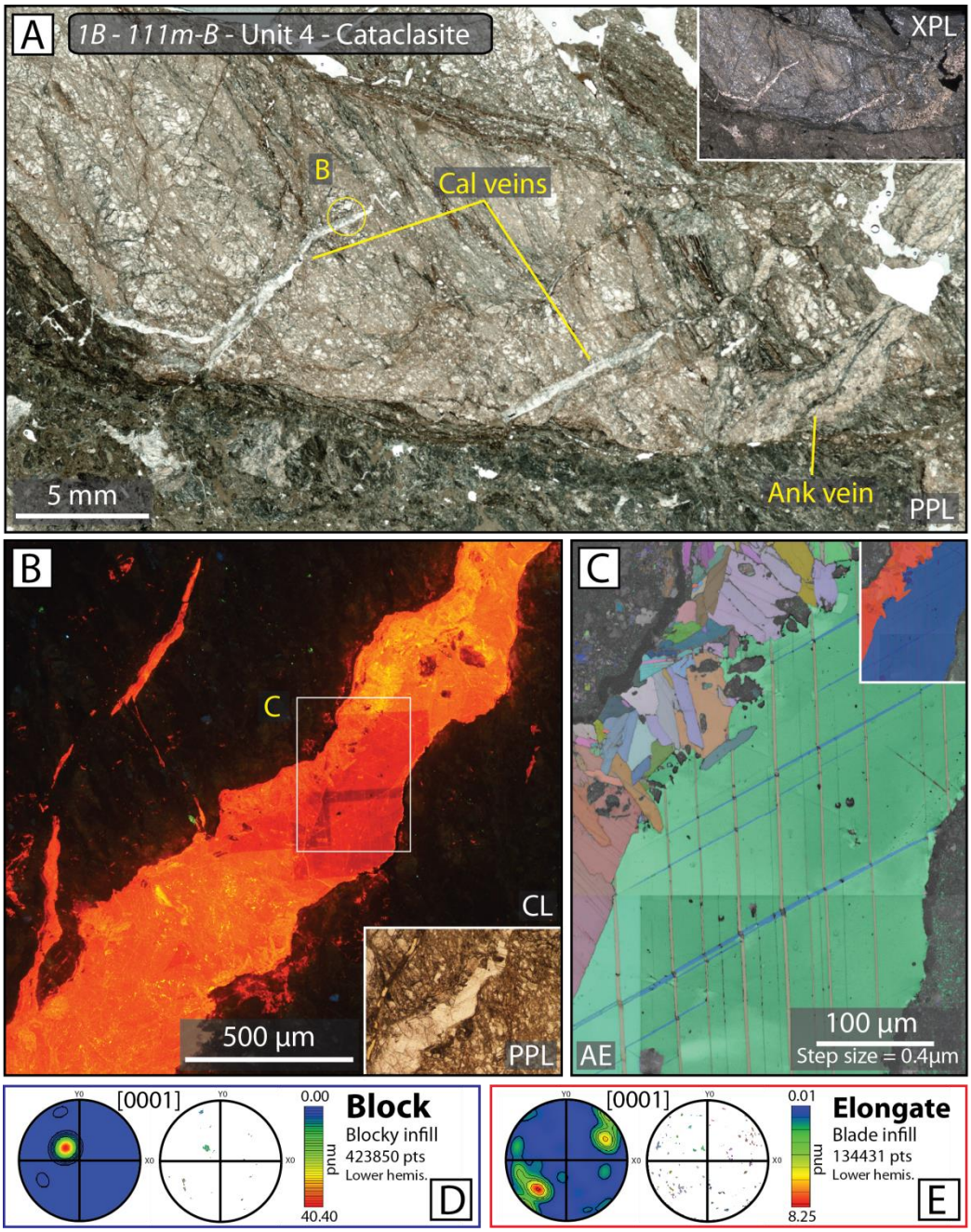

Figure SM 4.3 – [A] *Located within the same hanging wall cataclasite (1B-111m-B – Unit 4) as Figure SM 4.2. The calcite veins run perpendicular to foliation and terminate at the cataclasite lithological contact.* ***[B]*** *CL image of calcite vein showing bright orange CL signal and wall rock fragments entrained within vein fill.* ***[C]*** *An AE EBSD map showing two generations of calcite present, one of which is a large, blocky grain composing most of the vein fill and an elongate-blocky generation separated from one another by wall rock fragments.* ***[D and E]*** *PFs of the blocky and elongate-blocky infill show that they have disparate orientations.*

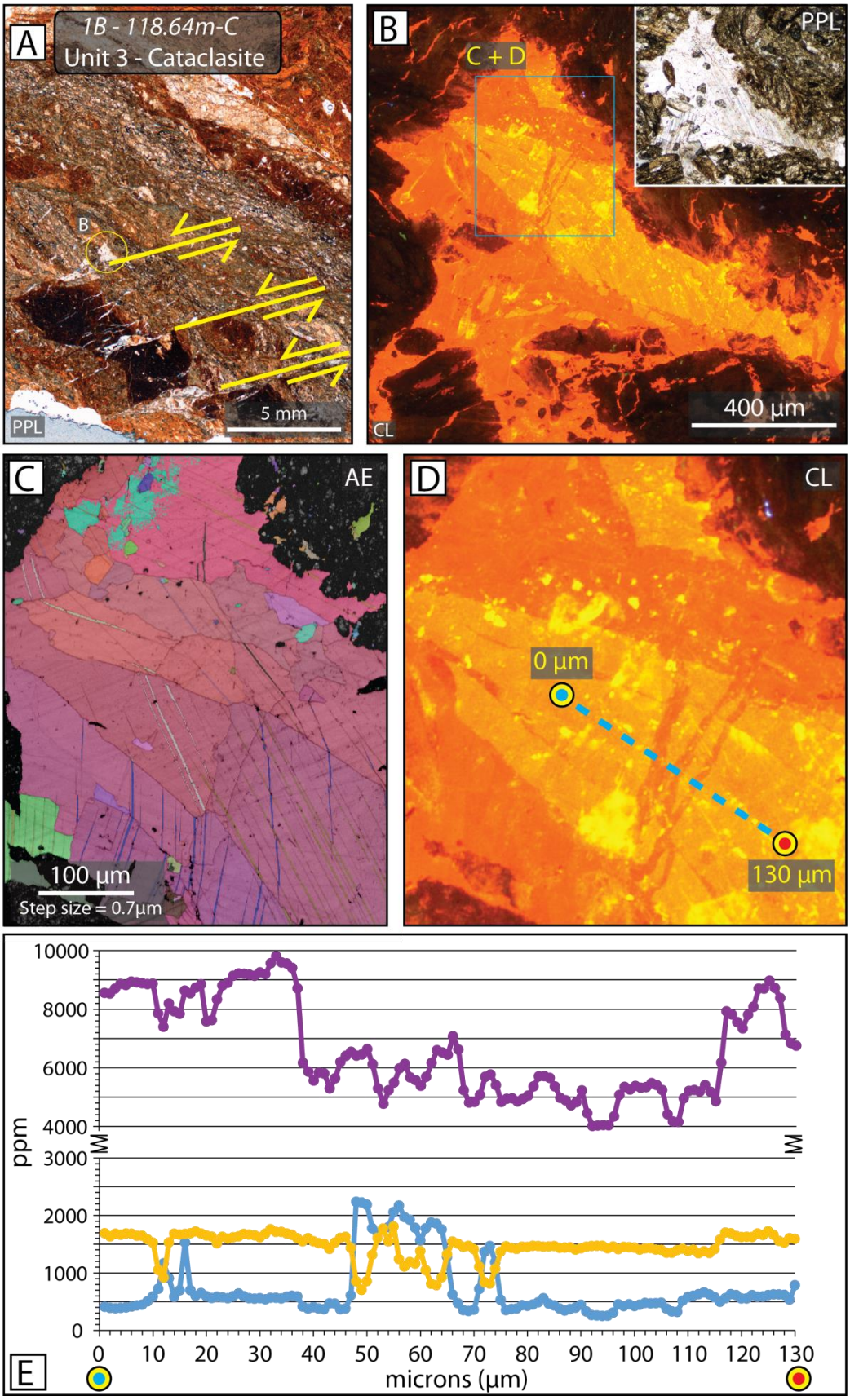

Figure SM 4.4 – *caption overleaf.*

Figure SM 4.4 – *(above)* ***[A]*** *A hanging wall cataclasite (1B-118.64m-C – Unit 3) 9.8 m above the upper PSZ. This cataclasite is heavily foliated and contains multiple en-échelon shears that cut cross a pseudotachylyte vein and foliations and have been mineralised with calcite.* ***[B]*** *CL image shows two regions distinguishable through CL, a bright orange region surrounded and cross-cut by a dull orange region.* ***[C]*** *An AE EBSD map of the region highlighted in (**B**) shows elongate-blocky crystal morphology with some twinning and fracturing in the calcite.* ***[D]*** *Site of interest in CL at higher magnification, with transect mark over fractures and accompanying CL variation.* ***[E]*** *SIMS trace elements transect, shows a decrease in Mn and Sr and increase in Mg, and likely Fe (unmeasured), over the duller CL features.*

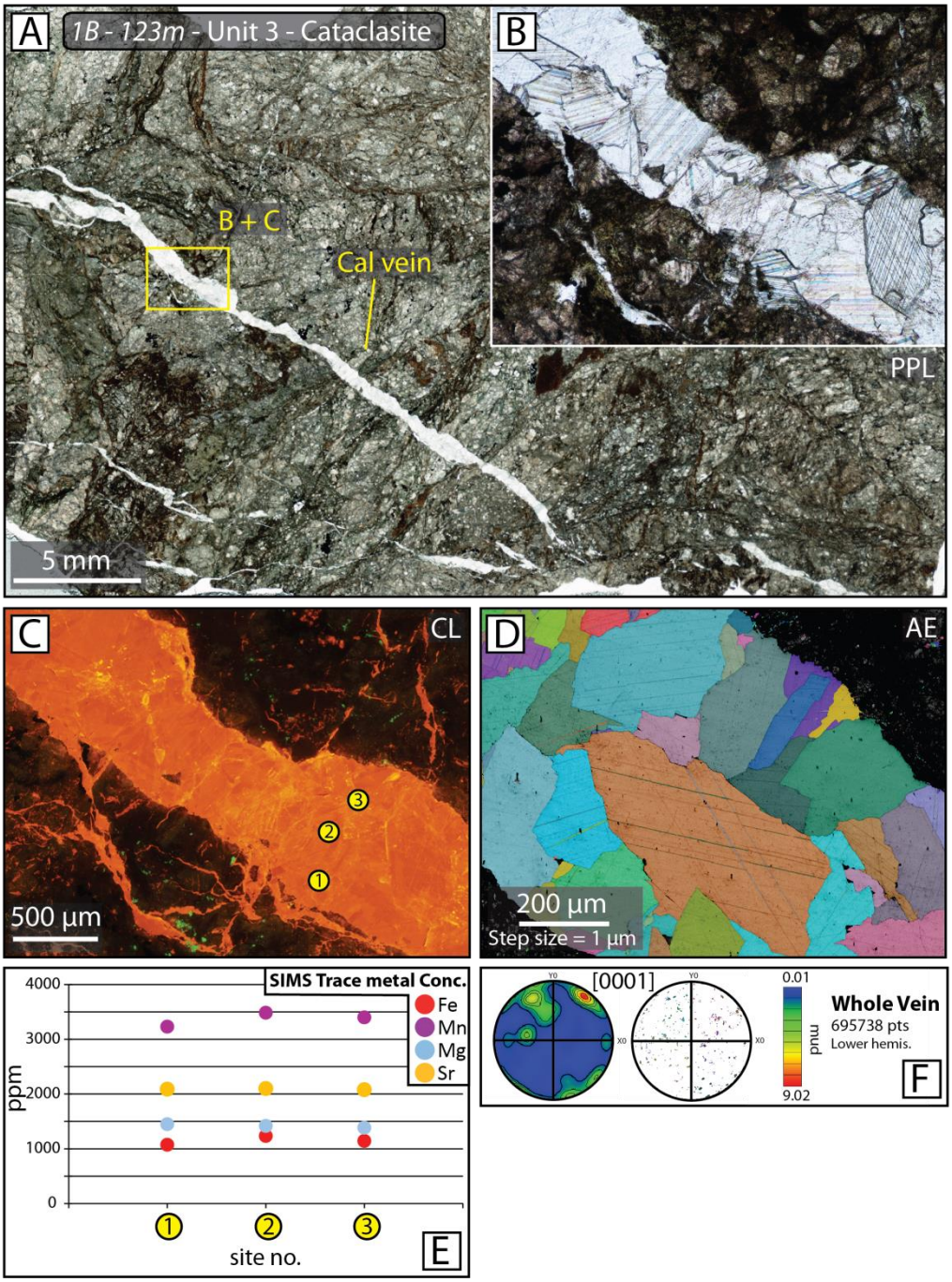

Figure SM 4.5 – [A] *A hanging wall cataclasite (1B-123.15m – Unit 3) 5.29 m above the upper PSZ, an unfoliated cataclasite with reworked pseudotachylyte material cross-cut by calcite vein.* ***[B]*** *PPL image of calcite vein showing blocky grains and twinning.* ***[C]*** *CL image showing uniform CL signal throughout the vein, grain boundaries occasionally show brighter CL signals.* ***[D]*** *An AE EBSD map showing blocky and elongate-blocky grains with some twinning.* ***[E]*** *SIMS trace* element *concentrations sites marked in (**C**); show uniform composition across vein.* ***[F]*** *PF of field of view in (**D**); shows a distributed spread of [0001] c-axis orientations of grains in vein.*

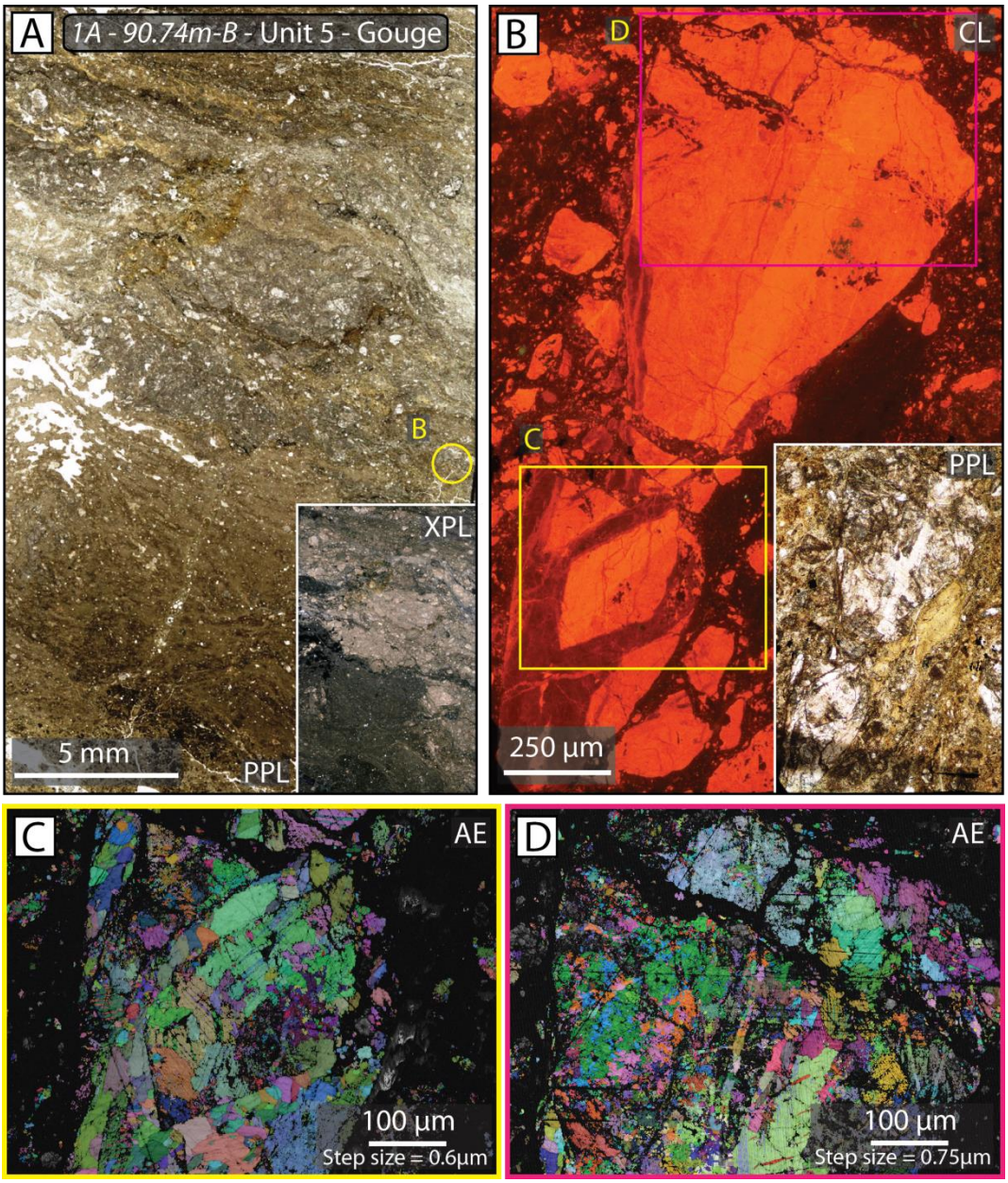

Figure SM 4.6 – [A] *Ultracomminuted gouge (1A-90.74m-B – Unit 5) within the upper PSZ-1.* ***[B]*** *A monomineralic calcite clast in a gouge and calcite clast matrix. CL shows three distinct generations of calcite, the dull-orange cut by bright-orange and both cut by a fine dull-red CL calcite.* ***[C and D]*** *EBSD AE maps of locations highlighted in (**B**); they show the varying degree of deformation in each generation.*

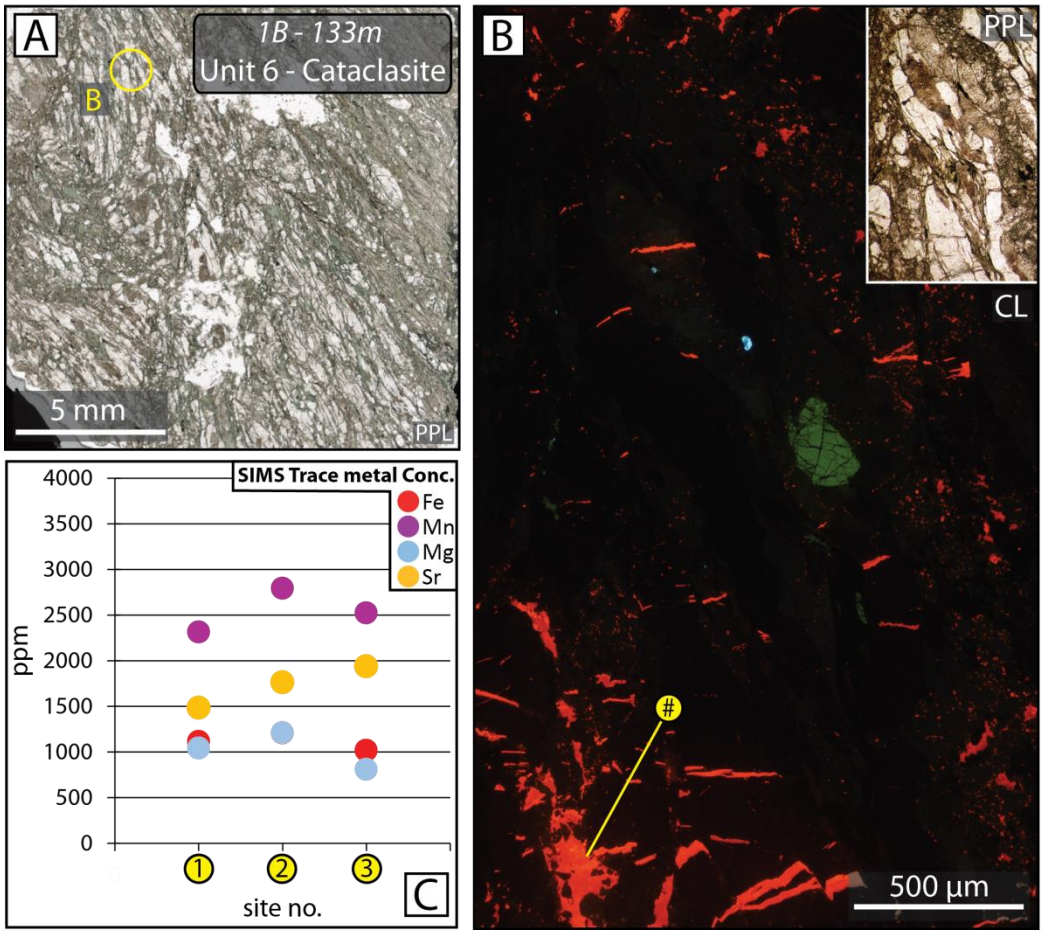

Figure SM 4.7 – [A] *A footwall cataclasite (1B-133m – Unit 6) 4.6 m below the upper PSZ, a heavily foliated cataclasite, one of the rare examples of calcite within the footwall cataclasites. Also note the green CL apatite.* ***[B]*** *CL image of calcite-filled void between foliations.* ***[C]*** *SIMS trace* element *concentrations, sites marked in (**B**), show a high Mn – low Fe content.*

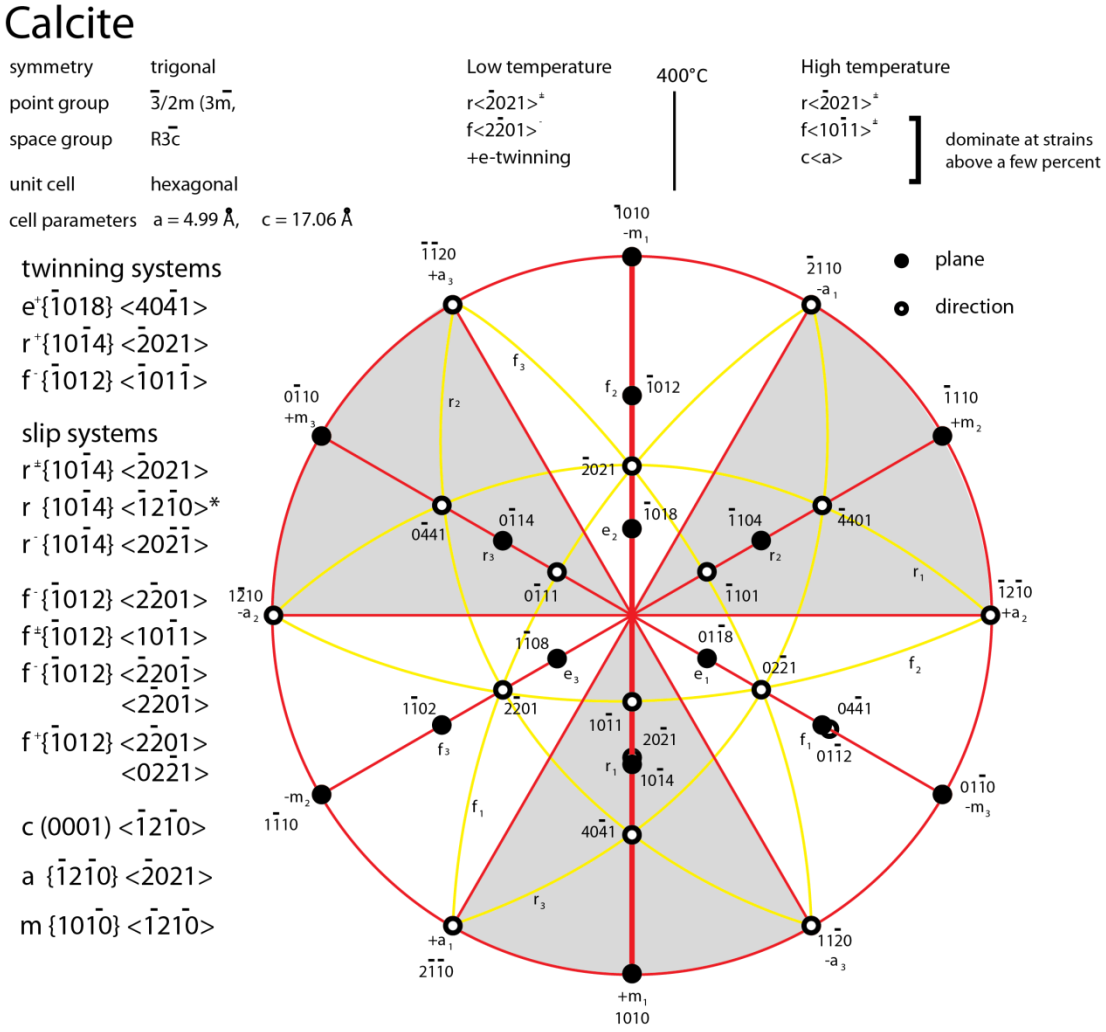

Figure SM 4.8 – *A Stereographic (upper hemisphere, equal angle) projection of calcite showing key planes and directions, adapted from [Bestmann and Prior, 2003]. These include slip systems after De Bresser and Spiers, [1997]. Shading illustrates the trigonal symmetry point group* $\bar{3}m$ *of calcite.*

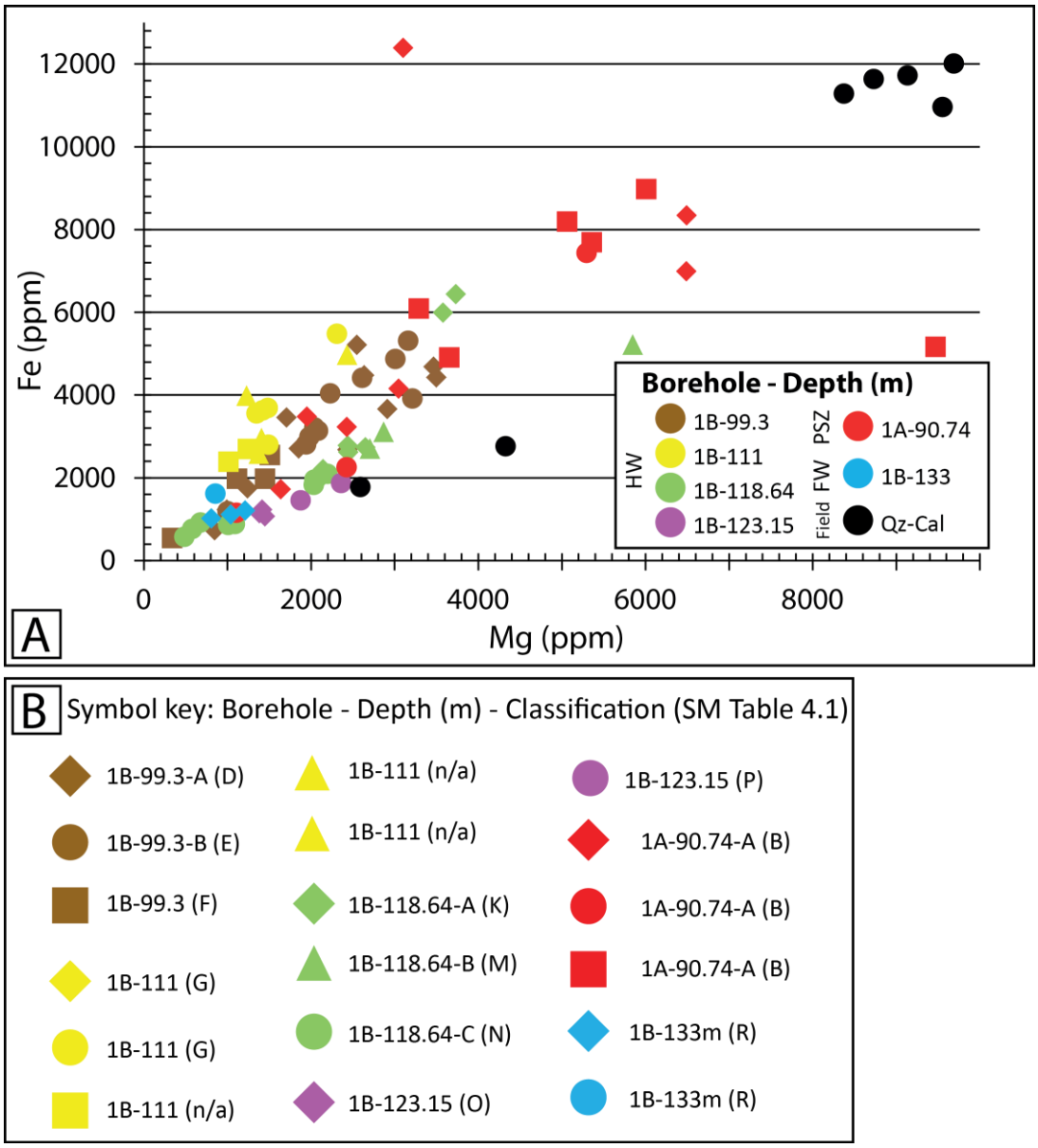

Figure SM 4.9 – [A] *SIMS Mg and Fe concentrations in part per million (ppm) with depth. Symbol variation denotes separate generations.* ***[B]*** *Key of the measurement sites in the Alpine Fault calcite veins. Bracketed letters refer to vein classification in Table SM 4.1.*

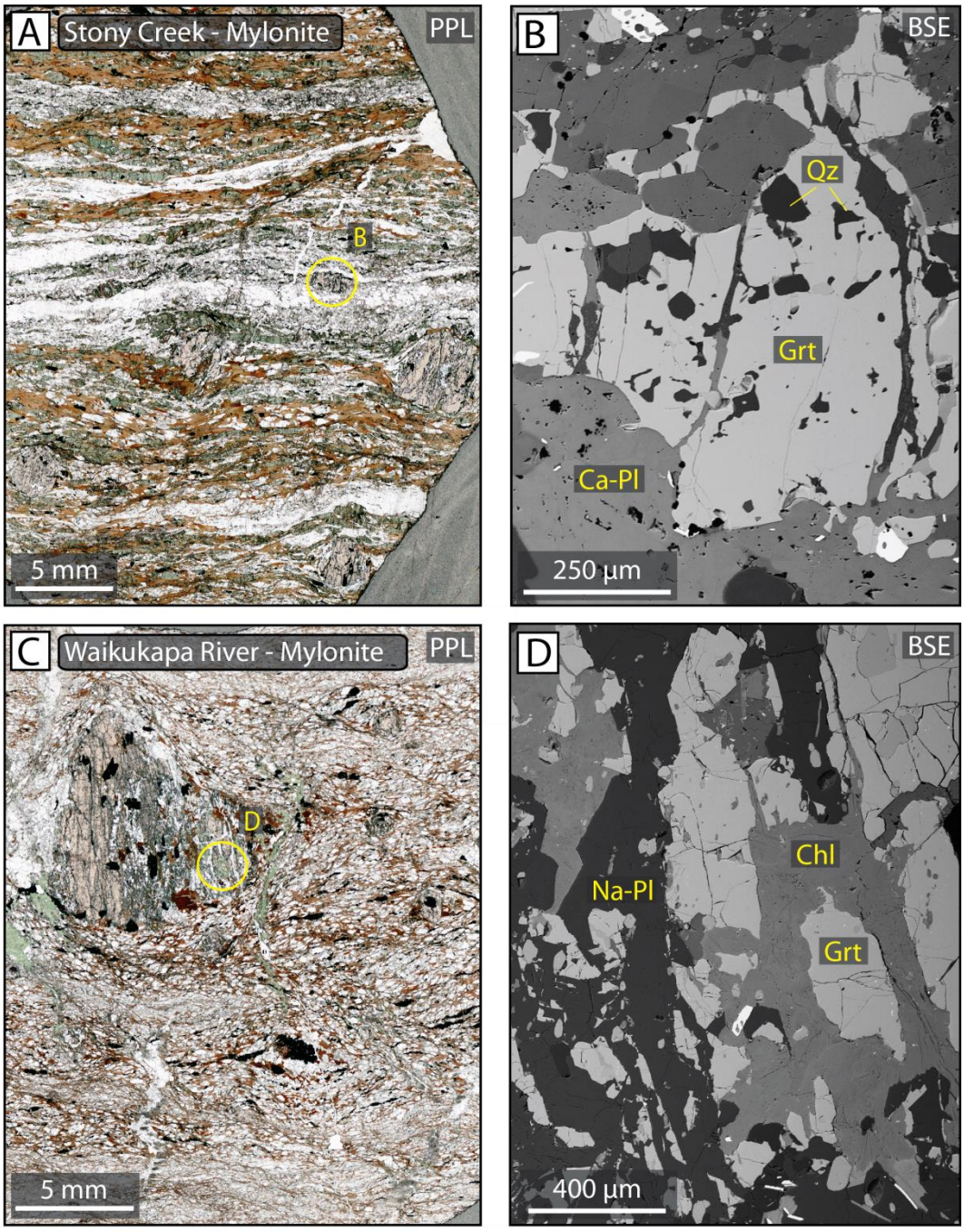

Figure SM 4.10 – [A – D] *Photomicrographs and backscatter images of a quartzofeldspathic mylonites containing Mn-bearing garnet. Garnet shows evidence for retrogressive metamorphic alteration to quartz and chlorite. Specimens acquired from Stony Creek (**A – B**) and Waikukupa River (**C – D**), West Coast, South Island, New Zealand.*

5. Occurrence and nature of pseudotachylyte and ultracomminution within the Alpine Fault, New Zealand: insight from the Deep Fault Drilling Project

Key points

- There is record of substantial pseudotachylyte generation within the Alpine Fault core, in support of *Toy et al.*, [2011].
- Frictional melt appears to be generated in the presence of fluids or in close vicinity to fluid conduits.
- Pseudotachylyte is cataclased and altered by successive seismicity and fluid input and incorporated into cataclasites and gouges.

Abstract

The Alpine Fault, a transpressional plate boundary between the Australian and Pacific plates, is known to rupture quasi-periodically with large magnitude earthquakes (M_w ~8) and is thought to be nearing the end of its latest interseismic state. Pseudotachylytes and ultracomminuted gouges, and thus nanoparticles, are both products of localised, brittle deformation within the mid to upper crust, with their respective generation dependent on the ambient conditions and concurrent processes that exist during fault slip. Using SEM-based microstructural observations and geochemical analyses, including: backscatter electron imaging; electron backscatter diffraction; and energy dispersive spectroscopy, and optical cathodoluminescence, we present a study on the occurrence of pseudotachylytes and nanoparticulates within the Alpine fault zone. We focus on the setting of these features, as well as the extent of mechanical reworking, chemical alteration and/or preservation they have undergone throughout the seismic cycle.

Phase 1 of the Deep Fault Drilling Project (DFDP-1) sampled fault lithologies from both the Alpine Fault hanging wall and footwall at Gaunt Creek, Westland. Drilling revealed a fault zone structure comprised of a fault core and associated damage zone, both of which are overprinted by a zone of alteration focused in the hanging wall. This alteration was produced through enhanced fluid-rock interaction on a fault which currently has very low

permeability. Pseudotachylytes occur throughout the Alpine Fault Zone fault core / alteration zone cataclasites, predominantly as reworked, disassociated clasts, with intact veins constrained to the fault core / damage zone transition in the fractured ultramylonites. These pseudotachylytes have an overall K-feldspathic composition but contain compositional segregations comprised of K / Si / Al-rich pseudotachylyte margins and Mg / Fe-rich and K / Si / Al-rich banding within the pseudotachylyte core. These K / Si / Al-rich bands exhibit a weak blue cathodoluminescence. Within the principal slip zone, ultracomminuted gouges contain sub – mm clasts that share similar characteristics with these pseudotachylytes. Such similarities include: a dominantly K-feldspathic composition, with minor Mg and Fe; the presence of nanoparticulates of quartz, calcite and Ti-oxides; and, in some cases, a blue cathodoluminescence. If these clasts are of pseudotachylyte origin, it can be inferred that the principal slip zone was capable of generating frictional melt at deeper crustal levels and that as it was exhumed, matured and altered, during the protracted history of seismicity, pseudotachylyte was entrained into the gouge layer, with subsequent devitrification and alteration resulting in microcrystalline clasts with entrained survivor nanoparticles. Alternatively the precipitation of K-feldspathic material within the principal slip zone from a rock-buffered alkali solution, incorporating nanoparticulates during growth, could be a viable mechanism. Further work is required to constrain the origin and nature of these materials.

The lack of intact pseudotachylyte veins within the fault core /alteration zone cataclasites and gouges suggests that frictional melt did not occur during the most recent high magnitude Alpine Fault slip event. Most pseudotachylytes observed are reworked relicts from older Alpine Fault ruptures or smaller magnitude earthquakes that have been subsequently incorporated into the widening alteration zone with exhumation. Frictional melt appears to occur in the presence of fluid, as evidenced by the cataclasis of calcite veins associated with; amygdules within; and veins overprinting the pseudotachylytes. The presence of preserved nanoparticles within K-feldspathic clasts in the principal slip zone could indicate that the Alpine Fault produced nanoparticulates during increments of slip at greater depths without the production of melt. This could indicate a transition in slip behaviour with time and exhumation; frictional melting in the more competent, dryer rock close to the Brittle – Viscous Transition, transitioning to nanoparticulate-aided slip at intermediate depths and finally with propagation of an Alpine Fault rupture occurring through steady-state slip on weak phyllosillicates at shallower crustal levels.

5.1. Occurrence of melt and ultracomminution within fault zones

During seismicity on a fault, at slip rates of 1 – 3 ms^{-1}, comminution and friction-induced melting can lead to the formation of pseudotachylyte [*McKenzie and Brune*, 1972; *Spray*, 1995; *Ray*, 1999; *Di Toro and Pennacchioni*, 2004]. The generation and accumulation of melt on a dynamically displacing surface may have implications on the seismic and mechanical behaviour of faults, particularly the lubrication of the fault plane by low viscosity melts and its subsequent sealing when melt solidifies [*Spray*, 1993; *Hirose and Shimamoto*, 2003, 2005; *Rempel and Rice*, 2006; *Rice*, 2006; *Nielsen et al.*, 2008; *Di Toro et al.*, 2011; *Mitchell et al.*, 2016]. Assuming that all frictional work is converted into heat, the production of heat, Q, during earthquake slip can be represented by the following;

$$Q \approx \mu\,(\sigma - Pp)\,V \qquad (7)$$

where μ is the friction coefficient, σ is the normal stress, Pp is the pore fluid pressure and V is the slip velocity, after *McKenzie and Brune*, [1972] and *Di Toro et al.*, [2009]. As such, the occurrence of other weakening mechanisms, particularly those that involve fluid in and around the fault, i.e. the formation of frictionally weak phyllosillicate phases or thermal pressurization, could limit frictional melting via low friction sliding of the fault on phyllosillicate-rich planes or the dissipation of heat by plumes of pressurised fluid [*Shimamoto and Logan*, 1981; *Rice*, 2006; *Ferri et al.*, 2010]. Thermal pressurization can occur when frictional heat generated during the initiation of fault slip increases temperatures within local intergranular pore-fluids generating transient increases in fluid pressure. This increase in pore-fluid pressure results in a lowering of the effective normal stress on the fault plane, with some authors proposing that this may reduce the generation of further heat during slip, limiting the generation of pseudotachylyte [*Sibson*, 1973, 1975; *Lachenbruch*, 1980]. However, if, during slip, the host-rock / fault walls become highly damaged, upon dilation fluid can escape efficiently from the heated and pressurised zone encompassing the shear zone. This would dissipate pore fluid pressures, maintain fault strength and promote melting [*Rempel and Rice*, 2006]. This damage-enhanced fluid mobility may be integral in allowing a wet fault to generate frictional melt. However, this enhanced mobility would predominantly occur within a host-rock / fault wall of low porosity, in high porosity rock the damage generated would likely produce a zone of low permeability that would limit fluid mobility [*Mitchell and Faulkner*, 2012]. The presence of

hydrous mineral phases within the host-rock may also prevent melting during fault slip, as the latent heat required to dehydrate these phases would limit temperature increase and thus melting [*Brantut et al.*, 2012].

Pseudotachylytes form from the non-equilibrium melting / preferential melting of low-melting point, volatile-rich mineral phases, such as micas and amphiboles, resulting in a pseudotachylyte matrix of a more mafic (Mg- and Fe-rich) composition relative to the host lithology. Within this mafic matrix, depending on host-rock mineralogy, refractory minerals such as quartz and feldspars survive, usually having undergone some degree of comminution and, once melting initiates, partial melting. The bulk composition (clast and matrix) of the pseudotachylyte match that of the host-rock [*Sibson*, 1975; *Bossière*, 1991; *Spray*, 1992]. However, if melt travels over sufficient distances, crystal fractionation can occur, resulting in pseudotachylytes that compositionally contrast with the host-rock [e.g. *Warr and van der Pluijm*, 2005].

Extreme comminution i.e. ultracomminution upon a shearing fault plane can occur without the initiation of frictional melt [*Wenk*, 1978; *Lin*, 1997]. A product of this shearing are nanoparticulates, materials of grain sizes <100 nm, generated through ultracomminution or chemical break down of larger clasts that may be ripped off the rock contacts at the slipping surface and subsequently undergo cataclastic flow. Such materials have recently been called upon to explain fault weakening without thermal effects as nanoparticles have contrasting physicochemical properties to their larger parent clasts, such as reduction in frictional shear resistance which could result in fault lubrication [*Goldsby and Tullis*, 2002; *Di Toro et al.*, 2011; *Han et al.*, 2011]. Although generally attributed to frictional melting, pseudotachylytes have also been speculated to be a product of ultracomminution, i.e. crush origin pseudotachylytes [*Wenk*, 1978; *Lin*, 1997]. These crush origin materials share many similarities with those of melt origin, including fluidisation, flow and injection structures. However, melt origin material can be differentiated through a number of features, including but not limited to: the presence of amygdules [*Maddock et al.*, 1987], and survivor clast-size distribution, composition and roundness [*Magloughlin*, 1992; *Shimamoto and Nagahama*, 1992; *Kirkpatrick and Rowe*, 2013].

Phase transformation and the generation of nanoparticulates have been invoked as an explanation for deep earthquakes, 30 – 70 km depth, where brittle failure is unlikely to

occur due to the increase in static frictional strength with increasing normal stress and increasing temperatures with depth [*Green and Houston*, 1995; *Kirby*, 1995; *Green II et al.*, 2015]. In experiments performed at high-pressure conditions, approaching the intermediate to deep earthquakes setting in the lower crust, high static frictional strength can be overcome in the presence of nanoparticulates, allowing shear failure at lower shear stresses than are needed for the predicted static friction [*Burnley et al.*, 1991; *Tingle et al.*, 1993]. Shear failure under deep earthquake conditions has been attributed to phase transformation, generating low-viscosity nanometric particles that are able to initiate instability and lubricate the sliding surface through grain-boundary sliding [*Green II and Burnley*, 1989; *Green II et al.*, 2015]. Nanoparticles have been produced in experiments simulating slip on faults at both seismic slip velocities at low pressures [*Di Toro et al.*, 2004; *Han et al.*, 2011; *Smith et al.*, 2013; *Green II et al.*, 2015] and slow slip velocities at high pressures [*Yund et al.*, 1990; *Pec et al.*, 2012; *Verberne et al.*, 2014; *Toy et al.*, 2015a]. Observations of nanoparticles on natural slip surfaces have also been made on exhumed faults that have accommodated several kilometres of slip [*De Paola*, 2013; *Kirkpatrick et al.*, 2013; *Green II et al.*, 2015].

As well as melt and nanoparticle lubrication a range of weakening mechanisms has been established to account for slip on faults in different settings. These include fluid-based mechanisms such as thermal pressurization, as outlined above, [*Sibson*, 1973; *Lachenbruch*, 1980; *Wibberley*, 2002; *Rempel and Rice*, 2006] and fluid film lubrication [*Brodsky and Kanamori*, 2001; *Ferri et al.*, 2011]; due to thermochemical pressurization via dehydration reactions [*Brantut et al.*, 2008, 2011; *Chen et al.*, 2013a; *Platt et al.*, 2015] or thermal runaway (thermal shear instability) in which the initiation of a highly localised zone of viscous creep generates heat and promotes slip [*Andersen et al.*, 2008; *John et al.*, 2009; *Prieto et al.*, 2013; *Thielmann et al.*, 2015].

Pseudotachylytes and ultracomminuted gouges, and thus nanoparticles, are both products of localised deformation within the mid to upper crust, with their respective generation dependent on the ambient conditions and concurrent processes that exist during fault slip. Here we aim to investigate and characterise the occurrence of frictional melting and ultracomminution, and whether they occur contemporaneously or exclusively from one another during seismicity in the Alpine Fault Zone. We present microstructural and chemical observations of pseudotachylytes throughout the Alpine Fault Zone fault core /

alteration zone (FC / AZ) and of clasts within the principal slip zone (PSZ) ultracomminuted gouges that share similar characteristics with these pseudotachylytes. This was undertaken with a variety of analytical techniques, including: optical microscopy; SEM-based backscatter electron imaging, energy dispersive spectroscopy and electron backscatter diffraction; and optical cathodoluminescence. We also explore the conditions and mechanisms allowing the coexistence of nominally 'dry' condition dependent pseudotachylytes with a fluid-rich fault and the variation of slip behaviour with time and exhumation.

5.2. Geological Setting

5.2.1. The Alpine Fault, New Zealand

The Alpine Fault Zone (AFZ), bounding the western edge of the Southern Alps on New Zealand's South Island, accommodates over 70 % of the relative motion between the colliding Australian and Pacific Plate [*Norris and Toy*, 2014]. The ramping of the Pacific plate over the Australian plate is manifested through dextral-reverse movement, offsetting basement rocks laterally by ~470 km, with Quaternary horizontal displacement rates estimated at 21 – 27 mm yr^{-1} [*Norris and Cooper*, 2001; *Lamb et al.*, 2016]. Uplift and erosion upon the fault is rapid, exhuming crustal rocks from depths of 20 – 30 km at a rate of ~6 – 9 mm yr^{-1} [*Little et al.*, 2002b]. Accompanying this rapid uplift is the advection of the regional geothermal gradient with quartz fluid inclusion microthermometry placing the gradient at 40 °C/km [*Toy et al.*, 2010], while recent shallow borehole measurements within the fault hanging wall report gradients of 62.6 ± 2.1 and 125 ± 55 °C/km [*Sutherland et al.*, 2012, 2017].

Palaeoseismic evidence has indicated that the Alpine Fault has had numerous geologically recent rupture episodes at 1717 ± 25, 1630 ± 25 and 1460 ± 25 A.D., estimated to have moment magnitudes of 7.9 ± 0.3, 7.6 ± 0.3, and 7.9 ± 0.4, respectively [*Wells et al.*, 1999; *Rhoades and Van Dissen*, 2003; *Langridge et al.*, 2012], with these ruptures propagating along nearly the entire ~600 km length of the fault. Recent seismicity patterns, geodetic strain records, and inferred high pore fluid pressures from regional seismic P- and S-wave velocity ratios and gravity surveys deep in the fault zone, suggest that the fault is locked above 6 – 12 km depth and that it is in the late stages of its earthquake cycle [*Eberhart-*

Phillips, 1995; *Eberhart-Phillips and Bannister*, 2002; *Sutherland et al.*, 2007; *De Pascale and Langridge*, 2012; *Lamb and Smith*, 2013].

Immediately upon the Central Alpine Fault, overprinting the fault core and transition into the damage zone, is a distinct <30 m thick zone of hydrothermally altered rock, containing elevated concentrations of hydrous alteration minerals and cements (e.g., phyllosillicates and carbonates), observed through field and borehole studies [*Sutherland et al.*, 2012; *Townend et al.*, 2013; *Toy et al.*, 2015b]. The extent of this alteration increases with proximity to the fault's principal slip zone (PSZ) within the hanging wall rock, with far less carbonate cementation in the footwall. This indicates a focusing of fluid in the hanging wall damage zone, with little cross-fault flow throughout the seismogenic crust [*Menzies et al.*, 2016].

5.2.2. Occurrence of pseudotachylyte in the Alpine Fault Zone

Numerous studies on Alpine Fault pseudotachylyte have been undertaken, focusing on the structural settings and age of frictional melt generation within the Alpine Fault Zone [*Wallace*, 1976; *Seward and Sibson*, 1985; *Sibson and Toy*, 2006; *Warr et al.*, 2007; *Toy et al.*, 2011]; and the petrology and compositions of pseudotachylyte, determining variations in melt composition as a function of host-rock mineralogy [*Bossière*, 1991] and crystal fractionation during melt transport [*Warr et al.*, 2003; *Warr and van der Pluijm*, 2005].

Toy et al., [2011] classified four major settings for pseudotachylyte within the Alpine Fault Zone: i) Foliated quartzofeldspathic hanging wall mylonites, containing mm – cm thick pseudotachylytes parallel to mylonitic foliations and with respect to the host-rock, deficient in Si and alkali elements and enriched in Al_2O_3 and TiO_2; ii) Lithological boundaries between hanging wall / footwall mylonites and metabasic lozenges, containing ≤ 1cm thick faults and injection veins and, with respect to the host-rock, depleted in Si, Fe and Mg and to greater extent K; iii) Footwall granitoid mylonites, containing the largest volume of pseudotachylytes occurring as chaotic, <2.5 cm thick injection structures and mm – thick pseudotachylytes; iv) Cataclasites, containing chaotic injected masses in the fault core and, with respect to the host-rock, depleted in Si and Ca and enriched in K and Na. These pseudotachylytes are estimated to have formation depths of 4 – 7 km, at host rock temperatures 170 – 300 °C [*Toy et al.*, 2011]. The settings outlined above are constrained to

depths of 4 – 10 km, below the Brittle – Viscous Transition (BVT), through distributions of current hanging wall seismicity. The greater volume of melt generation in ii) is attributed to rheological heterogeneities between lithologies and in iii) due to high stresses in anhydrous conditions.

Warr et al., [2003] and W*arr and van der Pluijm*, [2005] studied vein composition and age and found that compositional variation within pseudotachylytes, and particularly between the margin and main body of the vein, was a result of either: A) crystal fractionation during transport away from the melt-generating surface during a single seismic event, generating younger melt / glass layers enriched in Na, K and Si while being depleted in Fe, Mg and Mn, this mobile melt would become progressively less viscous due to higher melt to clast ratio with travel but also become more viscous with time due to compositional change and volatile loss; or B) successive pulses of frictional melt are generated during a single, large earthquake, generating a clast- and Si-rich vein margin and a melt-dominated main vein body.

There is abundant evidence for a sustained presence of fluid within the Alpine Fault, including: hot springs and hydrothermal activity within the fault hanging wall [*Cox et al.*, 2015; *Menzies et al.*, 2016; *Sutherland et al.*, 2017]; mineral precipitation [*Jenkin et al.*, 1994; *Craw and Campbell*, 2004; *Menzies et al.*, 2014] and extensive fluid-rock interaction witnessed in the Alpine Fault alteration zone; a zone of rock overprinting the fault core / damage zone transition of the Alpine Fault, defined by elevated concentrations of alteration minerals (e.g., phyllosillicates and carbonates) above regional levels [*Sutherland et al.*, 2012; *Townend et al.*, 2013; *Schleicher et al.*, 2015; *Toy et al.*, 2015b; *Boulton et al.*, 2017a]. As mentioned previously the presence of pore fluids in the vicinity of a fault has been speculated to limit the generation of frictional melt, through the dissipation of heat, dehydration reactions and the reduction of normal stresses on actively displacing faults.

5.3. Methods

5.3.1. The Deep Fault Drilling Project

The Deep Fault Drilling Project was undertaken to better understand the processes that lead to major earthquakes by drilling into and observing a major continental fault during its build-up to a large seismic event. The first phase of the Deep Fault Drilling Project (DFDP-1)

comprised of two pilot boreholes (DFDP-1A and DFDP-1B) drilled into an active thrust segment of the Alpine Fault at Gaunt Creek, Westland, in January 2011. The boreholes reached depths of 100.6 m and 151.4 m respectively, through percussion drilling in the upper borehole sections followed by wireline coring, collecting core for over 50 % of the borehole length. A range of fault lithologies from both the hanging wall and footwall were recovered including ultramylonites, cataclasites and fault gouges. The PSZ of the Alpine Fault Zone (AFZ) was reached at 90.74 m depth in DFDP-1A and 128.44 m in DFDP-1B, marking the boundary between the Australian and Pacific Plates, with a second PSZ recorded in DFDP-1B at 143.85 m [*Toy et al.*, 2015b]. Both slip zones are composed of clay-rich gouge [*Sutherland et al.*, 2012]. A detailed report on the drilling operations can be found in *Sutherland et al.*, [2011]. The drilled core diameter was 85 mm (PQ wireline bit size) and supplied for sample preparation as 200 – 300 mm length intact core sections and half sections. These core sections were oriented with respect to the borehole vertical axis, however due to core rotation during retrieval the horizontal orientation could not be preserved [*Sutherland et al.*, 2011; *Toy et al.*, 2015b]. One of the key aspects of the DFDP was to sample material from the Alpine Fault Zone FC / AZ, a sequence of rock that is very poorly exposed at the surface due to surface weathering and alteration. This sampling has allowed the collection of intact samples from this friable fault rock sequence, with microstructures reflecting processes that are occurring at depth on the fault away from surface effects that have previously not been observed.

5.3.2. Petrology of core lithologies

Eight rock units were distinguished in the DFDP-1 boreholes and these are systematically detailed in *Toy et al.*, 2015. These include: grey and dark-green ultramylonites; brown-green-black ultramylonites; upper unfoliated cataclasites; upper foliated cataclasites; fault gouges; lower cataclasites; fault breccias; and Quaternary gravels. The DFDP-1 core provided an excellent continuous section through the AFZ, allowing a number of associated lithological units to be distinguished and classified, based on the original protolith and the level of damage and/or alteration. This classification follows the fault rock nomenclature of *Woodcock and Mort*, [2008], with units numbered sequentially as they were encountered in the recovered core, from top to bottom, see Figure 5.1.

The hanging wall ultramylonite encountered (Unit 1 and 2) is planar-foliated, of variably quartzofeldspathic and metabasic composition. Foliations are defined by aligned phyllosillicates, graphite and opaque minerals. These ultramylonites are of midcrustal origin and have undergone extensive grain-size reduction via plastic deformation mechanisms, overprinted by successive generations of brittle cataclasis as evidenced by clay and carbonate filled shears and fractures. Ultramylonites transition to variably foliated and unfoliated cataclasites (Units 3 and 4); composed of quartzofeldspathic and metabasic material, consisting of angular fragments of ultramylonite variably clast-supported (>10 mm diameter) and matrix-supported (<10 mm diameter) in a matrix of comminuted feldspar, quartz, chlorite, white mica, calcite and (occasionally) epidote. These cataclasites have been successively fractured and cemented as evidenced by cross-cutting relationships of mineralised (or gouge filled) veins, pseudotachylytes and the presence of clasts with cataclastic texture. The PSZ is a zone of ultracomminuted, cohesive, clay-rich gouge (Unit 5). This gouge is ultrafine-grained, variably foliated with indistinct, sub-planar layering containing fragmented clasts of gouge and calcite. The footwall is comprised of 'lower' cataclasites (Units 6a to d), of granitic and gneissic origin, that are variably foliated and contain far less carbonates and less evidence of hydrothermal alteration than Units 1 to 4 of the hanging wall.

All samples used in this study were sourced from DFDP-1A and DFDP-1B core, at depths ranging from 65 m to 145 m, see Figure 5.1. The choice of samples was based on the microstructural identification of cataclasites and ultracataclasites, zones of shear and pseudotachylytes in the core during core logging, and from observations of core scans. The characteristics of these microstructures are summarised in Table SM 5.1.

5.3.3. Sample preparation

Standard 30 µm thick thin sections were prepared using standard petrographic thin section techniques. A high quality final, chemical-mechanical polish was applied using colloidal silica of grit size 0.005 – 6 µm in an alkaline solution. This removed the amorphous layer (few nm thick) produced on the thin section surface during mechanical polishing and ensured that the high quality polishing required for electron backscatter diffraction (EBSD) analyses was achieved. Thin section edges were painted with colloidal carbon paint and samples were then carbon coated to a thickness of ~10 nm for analysis in the Scanning Electron Microscope (SEM).

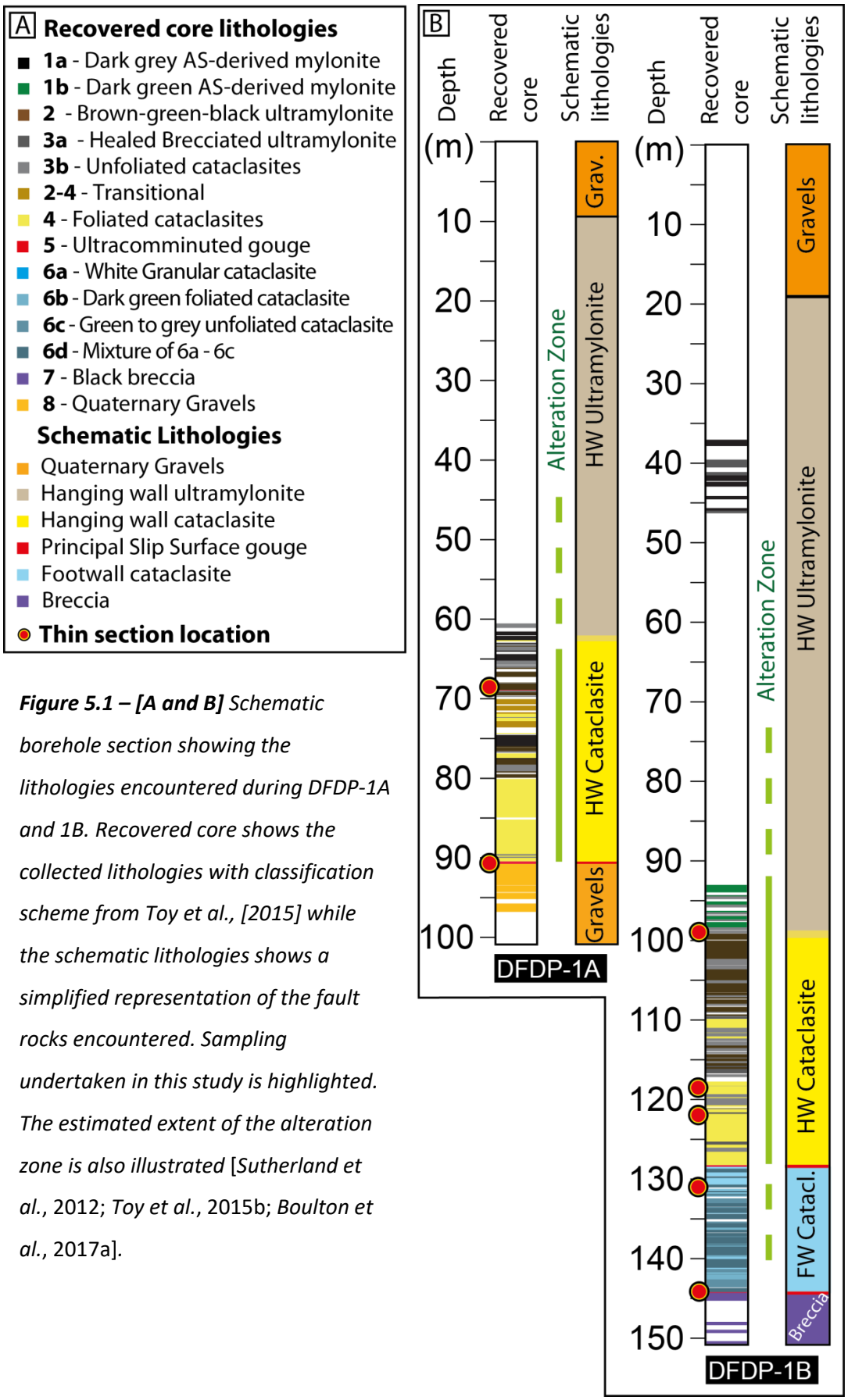

Figure 5.1 – [A and B] *Schematic borehole section showing the lithologies encountered during DFDP-1A and 1B. Recovered core shows the collected lithologies with classification scheme from Toy et al., [2015] while the schematic lithologies shows a simplified representation of the fault rocks encountered. Sampling undertaken in this study is highlighted. The estimated extent of the alteration zone is also illustrated* [*Sutherland et al.*, 2012; *Toy et al.*, 2015b; *Boulton et al.*, 2017a].

5.3.4. Techniques

SEM analyses were undertaken in the EBSD-SEM Laboratory at the University of Liverpool using an X500 Crystal Probe field-emission gun (FEG) SEM for electron backscatter diffraction (EBSD) analyses and a Philips XL30 SEM for energy dispersive spectroscopy (EDS) analyses. Cathodoluminescence (CL) observations were made using an optical cold-cathode CL apparatus and QEMSCAN analyses were performed by Alan Butcher of Intellection Pty Ltd, Milton, Australia who performed the analysis using a QEMSCAN® system. The following section outlines these techniques and the manner in which they are presented in this study.

The Philips XL30 SEM was utilised for backscatter electron (BSE) imaging and qualitative EDS analyses, operating at 20 kV accelerating voltage, 60 – 80 µA beam current and a 5 nm spot size, EDS analyses were performed using an Oxford Instruments x-act 10 mm^2 silicon drift detector; and INCA software. BSE imaging was used to visualise the compositional variation of the material within the samples. This is achieved through the use of a greyscale, which is proportional to the average atomic number of a material, with a brighter BSE intensity correlating with greater average atomic number and dark BSE intensity with lower average atomic number, allowing different mineral phases to be discerned at the micron-scale. EDS analyses, using characteristic X-ray energy emitted during electron beam interaction with the sample surface, was used to characterise the chemical variations between the various mineral and pseudotachylyte phases observed optically and in BSE imaging. EDS analyses were performed as maps in order to qualitatively visualise chemical variations.

The X500 Crystal Probe field-emission gun (FEG) SEM, designed by Obducat CamScan Ltd (for full technical specifications see *Seward et al.*, 2002) was utilised for EBSD analyses. EBSD data was collected using an F+ Nordlys EBSD detector combined with the AZtec Oxford Instrument acquisition software. The typical operating parameters for this study were 20 kV accelerating voltage, 20 – 30 nA beam current, and 5.5 nm spot size. The raw EBSD datasets were processed and analysed using the Oxford Instruments HKL Channel5 software. Erroneous data points were carefully removed using band contrast values to sub-sample grain boundaries effectively, thus avoiding the generation of artefacts.

The EBSD data in this study are presented in All-Euler (AE), which visualises orientation through use of an Euler angle-based colour scale. Euler angles are a set of three angles (ϕ1, Φ, and ϕ2) used to describe the crystallographic orientation of crystals relative to a reference coordinate system; defined by the primary SEM stage axes. The value of each Euler angle, reflecting the magnitude of the 3 rotations necessary to determine a rotation path from the SEM reference frame to that of the crystal analysed, is individually set to a colour scale (red, green and blue for Euler angles ϕ1, Φ, and ϕ2, respectively) which are then combined into a single RGB colour that represents the observed crystallographic orientation. However, the AE component contains a 'wraparound' effect caused by one or more of the Euler angles reaching their respective limit, resulting in the RGB value to vary between minimum and maximum, potentially resulting in colour speckling even when little to no orientation variation between grains exists. Crystallographic orientations are plotted in equal area upper hemisphere stereographic projections, also known as pole figures (PF), to reveal if any crystallographic preferred orientation (CPO) exists. The data in pole figures are coloured according to their respective Euler orientation and contoured to a half width of 20° and data clustering of 5°. In order to describe the intensity of the fabric shown in PF a statistical method is used known as the multiple of uniform density (MUD), which is quantified using the maximum intensity of a contoured PF. MUD values of 1 indicate randomly orientated grains while a MUD >1 is indicative of a fabric or CPO, these values are illustrated alongside the PFs. MUD values however are only a qualitative approximation of CPO strength because, for example in Oxford Instrument software, they are calculated only relative to the pole figures visualised for a given mineral in a given dataset and cannot be used for direct comparison between PFs from different datasets. For more information on relevant EBSD data presentation please see *Prior et al.*, 1999, 2009 and *Bestmann and Prior*, 2003.

Optical cold-cathode CL was employed in this study, using a Nikon Eclipse Ci microscope with a CITL Mk5-2 cold stage and Nikon DS-Fi1c camera, working at conditions of 10.8 kV and 390 μA in a vacuum of 0.047-33 Torr. CL in minerals is the result of the transformation of various energy types into visible light, through emissive transition of molecules, anions or the transition of a crystal from excited electronic states to lower energy or ground states [*Marfunin*, 1979]. In solids this is controlled by the transition of electrons between conduction and valence bands, this transition is influenced by defects in a material's crystal lattice which form luminescence centres by the addition of energy levels within the

conduction – valence band gap [*Pagel et al.*, 2000; *Götze and Kempe*, 2009]. Variation in a material's luminescence highlight subtle compositional and microstructural variations that are not visible using standard optical microscopy nor are they using other more sophisticated techniques such as the SEM-based EDS and BSE imaging. This is the case for many minerals as CL activating, sensitising or quenching trace elements are within parts per million concentrations. Specific ions incorporated into a materials structure can act as activators, sensitizers or quenchers for CL signal, depending on the mineral or material being studied.

Using similar methods as SEM EDS analyses the *quantitative evaluation of minerals by scanning electron microscopy* (QEMSCAN®) is an SEM technique developed by CSIRO to identify mineral species rapidly, automatically and non-destructively. The technique consists of the automatic acquisition of EDS spectra and BSE images of a specimen surface which are then combined with one another to identify the mineral species within it; achieved through comparison to a comprehensive mineral database incorporated into the QEMSCAN software [*Qian et al.*, 2015]. The QEMSCAN analysis in this study used a 10 µm step size and collected a total of 8,283,252 x-ray points over ~10 hours.

5.4. Results

This section describes the characteristics of the pseudotachylyte and ultracomminuted gouge microstructures observed from hand specimen to micron scale. Due to the spatial constraints of drill core sampling the lateral continuity of a number of the microstructures is difficult to determine. Pseudotachylyte is referred to as PST in figures and all mineral abbreviations are after *Whitney and Evans*, [2010].

5.4.1. Pseudotachylyte within the Alpine Fault core

Pseudotachylytes within the Alpine Fault FC / AZ appear at the hand specimen scale as blue-grey to light grey layers of flint-like, glassy material, 1 – 5 mm thick. Some pseudotachylytes show a clear shear surface (Figures 5.2, 5.3 and 5.9), but many occur in pockets and are disassociated from their generating surfaces (Figures 5.5, 5.10, 5.11 and 5.12). Segregation of the pseudotachylyte is observable in hand specimen with margins with the host-rock, 1 – 2 mm thick, appearing blue with an irregular, sharp boundary with

the pseudotachylyte main body, which appears light blue-grey with colour variations highlighting lobes and flow structures within it, see Figure 5.5A. At the drill-core scale injection veins in clear association with their parent pseudotachylyte cannot be recognised, though may not be identified due to their apparent irregular geometries on the observation surfaces and to the limited scale of the drill-core available for analyses. The pseudotachylyte hosted in the quartzofeldspathic ultramylonite at *1B-99.3m* and *1A-68.36m*, Figures 5.2 – 5.8 and 5.9, are the only laterally continuous pseudotachylyte structures at the scale of the drill-core rounds, 85 mm diameter . Within the hanging wall cataclasites, in closer proximity to the PSZ at depths of *1B-118.64m*, *1B-123.15m* and *1B-132.32m*, Figures 5.10, 5.11 and 5.12, the pseudotachylyte typically occurs as discontinuous layers, pockets or fragments 'floating' within a cataclastic matrix or irregularly shaped masses (possibly injection veins), disassociated from their generation surface.

Optically the pseudotachylyte appear predominantly light to dark brown in plane polarised light (PPL) and isotropic in crossed-polarised light (XPL), see Figures 5.2 – 5.12, many display layering and flow structures. All pseudotachylytes analysed are associated with cataclasites, either being entirely hosted within them or, when within more intact rock, i.e. fractured ultramylonite, occur adjacent to planes ultracataclasites. *1B-99.3m-A* (Figure 5.2 and 5.3) is the best example of a clear ultracataclasite to pseudotachylyte transition; from coarse, sub-rounded to sub-angular lithic clasts at 50 – 1000 µm diameter to finer monomineralic clasts at 20 – 50 µm diameter within a sub-micron clast matrix, over 3 – 5 mm with proximity to the pseudotachylyte vein. The pseudotachylytes contain extensive cross cutting veins that are mineralised by calcite, quartz and opaque minerals. Fragmentation and displacement by fracturing and shears can be observed in pseudotachylytes at the mm – scale, alongside cross-cutting mineralised veins, Figure 5.5. Within the intact veins of pseudotachylyte in samples *1B-99.3m* and *1A-68.36m* (Figure 5.2, 5.3 and 5.9), flow structures and compositional segregation of the glass is apparent. Bounding the edges of the intact veins of pseudotachylyte are pale margins (in PPL) of variable thickness, 100 – 1000 µm, see Figures 5.3, 5.4 and 5.5. The clasts in all observed pseudotachylytes are abundant and include: sub-rounded and embayed quartz clasts of 5 – 100 µm diameter; sub-rounded to angular plagioclase feldspar clasts of 5 – 50 µm diameter; lithic fragments of 50 – 200 µm diameter; and low concentrations of Fe and Ti oxides.

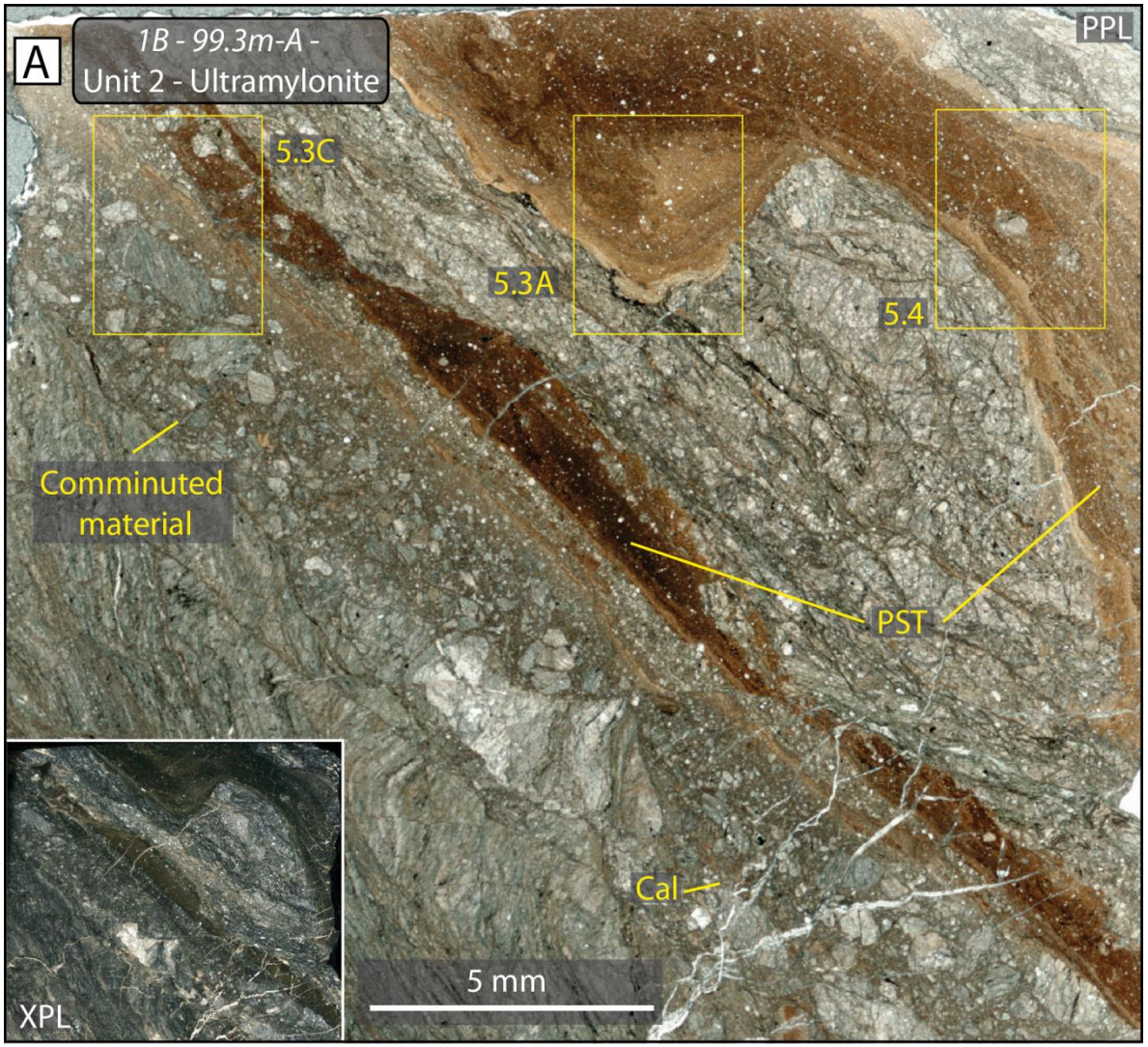

Figure 5.2 –

[A] *A hanging wall ultramylonite (1B-99.3m-A – Unit 2) 29.14 m above the upper PSZ. This ultramylonite is heavily cataclased with planes of ultracomminuted material and pseudotachylyte and calcite veins.*

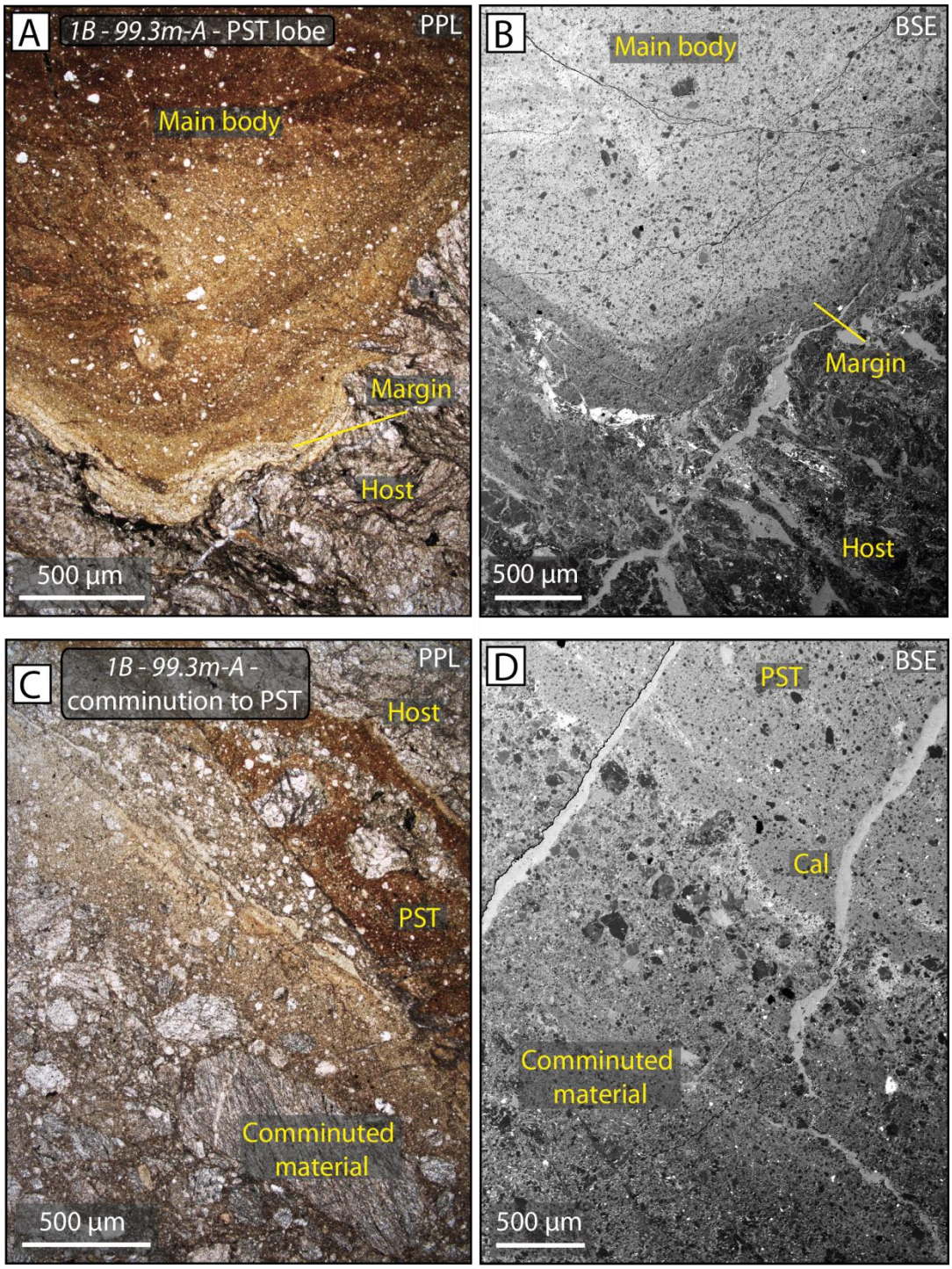

Figure 5.3 – *Photomicrographs and BSE images of areas highlighted in Figure 5.2 (1B-99.3m-A – Unit 2).* ***[A and B]*** *Lobate flow structures in pseudotachylyte matrix with compositionally segregated regions.* ***[C and D]*** *Transition of ultracomminuted material to pseudotachylyte glass with cross-cutting calcite veins.*

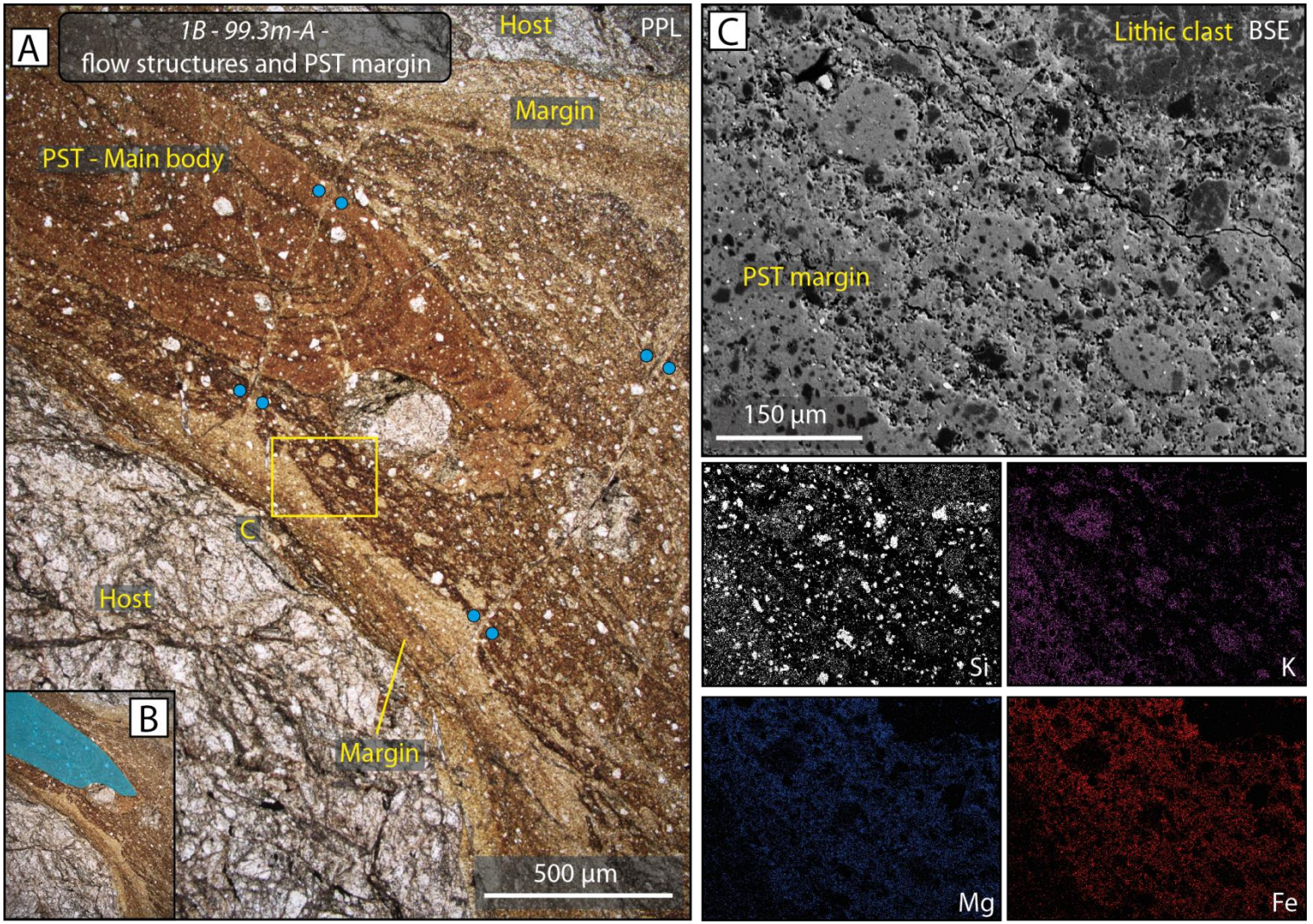

Figure 5.4 – *Photomicrographs, BSE images and EDS maps of area highlighted in Figure 5.2 (1B-99.3m-A – Unit 2).* ***[A]*** *Lobate flow structures, compositional segregation and rounded clasts are present throughout the pseudotachylyte. Blue dots denote calcite veins and associated pseudotachylyte bleaching cutting across the PST margins and main body.* ***[B]*** *Blue region highlights flow structure in (****A****).* ***[C]*** *BSE and EDS images of blebs of pseudotachylyte margin material within the main pseudotachylyte matrix. The margin and blebs are rich in K and Si and*

EDS analyses show that throughout the FC / AZ cataclasite all pseudotachylyte has elevated K content with respect to the host-rock, however flow banding highlighted by compositional segregation does occur; towards the centres of the pseudotachylyte veins these segregated regions alternate between Mg / Fe-rich and Si / K / Na-deplete regions and vice versa, see Figure 5.5, 5.8 and 5.11. EDS analyses in Figures 5.4 and 5.5 also show that the margins have increased concentrations of K and Si and are depleted in Mg and Fe in comparison with the majority of the pseudotachylyte matrix. In some instances the pale margin material blebs and fingers into the darker main body matrix with sharp contacts, Figure 5.4, shows immiscibility between the two pseudotachylyte compositions occurred to some extent. Some paler regions of the pseudotachylyte matrix flank calcite-mineralised fractures that cut across the margins and main melt bodies, as in Figure 5.4. In Figure 5.9 QEMSCAN mineral analyses attribute a K-feldspar stoichiometry to pseudotachylyte veins in sample 1A-68.36m. It has to be noted that the QEMSCAN system, designed to assign specific mineral species to EDS chemical spectra, is not calibrated to recognise specific pseudotachylyte compositions, therefore these analyses need to be considered with caution. However, the choice of mineral species was prompted by the relative quantities of K, Al, Si and O, even in the presence of Fe and Mg. All observed pseudotachylytes are deficient in Ca in their matrix, with Ca almost entirely hosted within calcite mineralisation. In Figures 5.6 and 5.7, a faint blue CL signal can be observed constrained to regions of the pseudotachylyte matrix enriched in K, Na and Si, a green CL is also visible associated with plagioclase survivor clasts.

EBSD analyses were undertaken on pseudotachylyte microstructures including survivor clasts and pseudotachylyte matrix. In Figures SM 5.5 and SM 5.6 EBSD analyses have indexed material that has strong crystallinity within the pseudotachylyte, i.e. survivor clasts and secondary mineralisation, illustrated with the grey colouration – colouration in the band contrast (BC) – All-Euler (AE) images. The lack of indexed points within the pseudotachylyte matrix indicates an absence of crystalline structure or that crystallinity of the matrix is below the resolution (~0.2 μm) of the EBSD technique. EBSD analyses of quartz survivor clasts, see Figure SM 5.6C, show little distortion of the crystalline lattice and the formation of sub-grains.

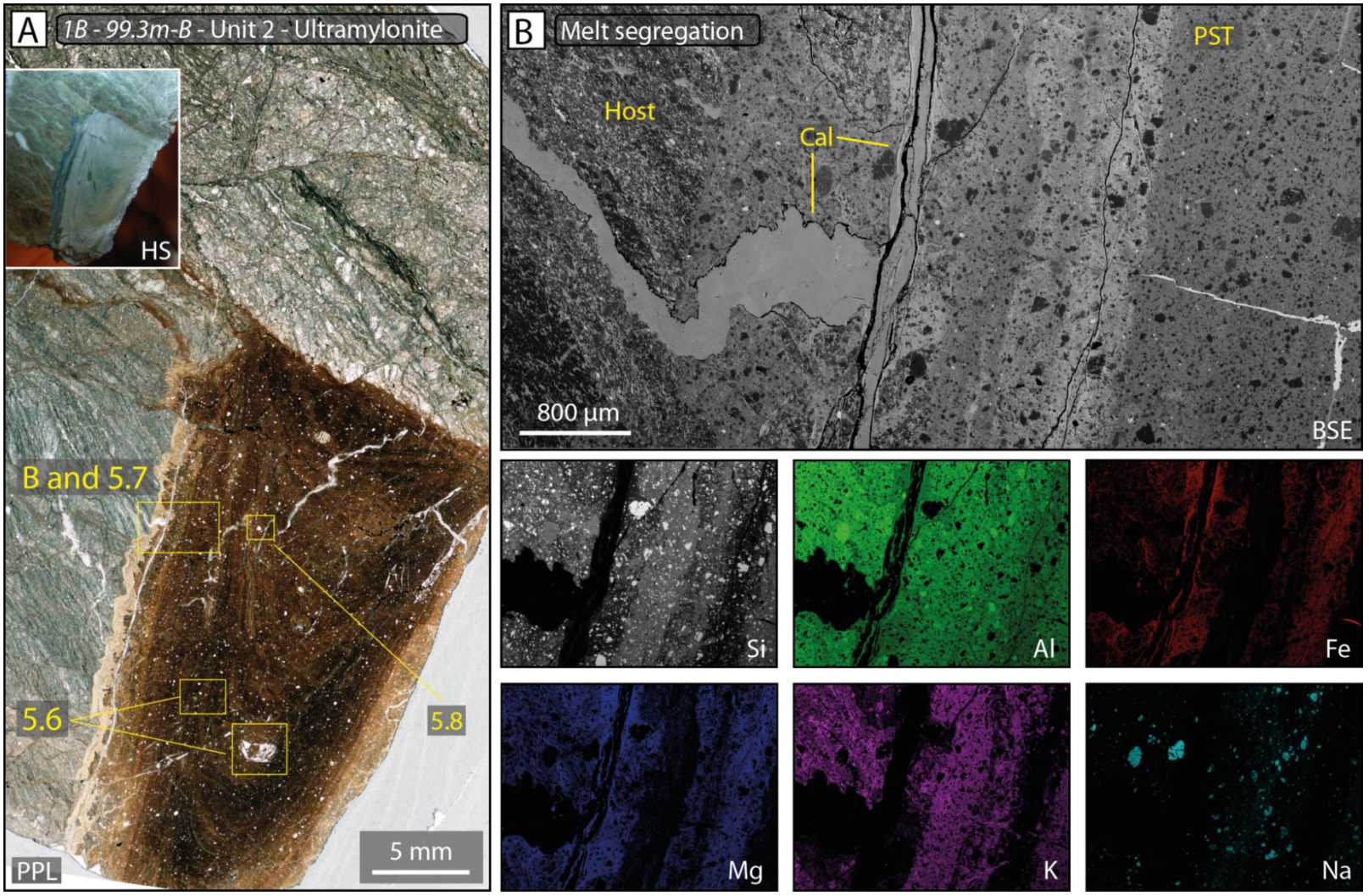

Figure 5.5 *– caption overleaf.*

Figure 5.5 – (above) [A] *A hanging wall ultramylonite (1B-99.3m-B – Unit 2) 29.14 m above the upper PSZ. This ultramylonite is heavily cataclased with planes of ultracomminuted material, pseudotachylyte and calcite veins.* ***[B and C]*** *BSE and EDS images of pseudotachylyte-host rock contact with calcite vein and Fe-oxide vein. The pseudotachylyte matrix is segregated at the vein margins into K / Si-rich layers and Mg / Fe-rich layers. EDS map step size at 1.7 µm.*

Figure 5.10 shows a fragmented pseudotachylyte within a foliated cataclasite (*1B-118.64m*), with the offset of the original vein at 2 – 5 mm. Features such as survivor clast population, a pale vein margin and brown main body (in PPL) are similar to the intact pseudotachylyte veins at greater distance from the PSZ. However, EDS analyses show that the vein material and host-rock are of near identical composition and throughout the vein matrix pitting and extensive, fine-scale calcite precipitation is present (see Figure 5.10C).

Calcite mineralisation is intimately associated with the pseudotachylytes, appearing to occur before, during and after melt solidification. In the cataclased ultramylonite at *1B-99.3m-A (Figure 5.2)*, running parallel to the tectonic foliation are both a calcite vein and an intact pseudotachylyte vein with full transition from highly comminuted host-rock to glass. The calcite vein, as reported in *Chapter 4* – Figure 4.3 of this thesis, has been extensively sheared, has irregular margins and contains abundant, rounded wall rock clasts, diameters of 5 – 50 µm, suspended in a matrix of sub-angular to angular interlocking calcite grains, diameters of 5 – 50 µm, with irregular grain boundaries and extensive e-twinning. The pseudotachylyte in *1B-99.3m-B*, Figures 5.5 – 5.8, shows abundant amygdules, mineralised vesicles, filled with variable proportions of calcite, quartz and opaque oxides. The pseudotachylyte vein itself has also been heavily fractured and mineralised with multiple, cross-cutting generations of calcite precipitation, with varying CL signal strength, see Figure 5.7. Variation in the orange – red CL signal in calcite is strongly modified by trace element content in ppm concentrations; Fe quenches the CL signal while Mn enhances it [*Long and Agrell*, 1965; *Marshall and Mariano*, 1988; *Waychunas*, 2014]. Figures 5.5B and

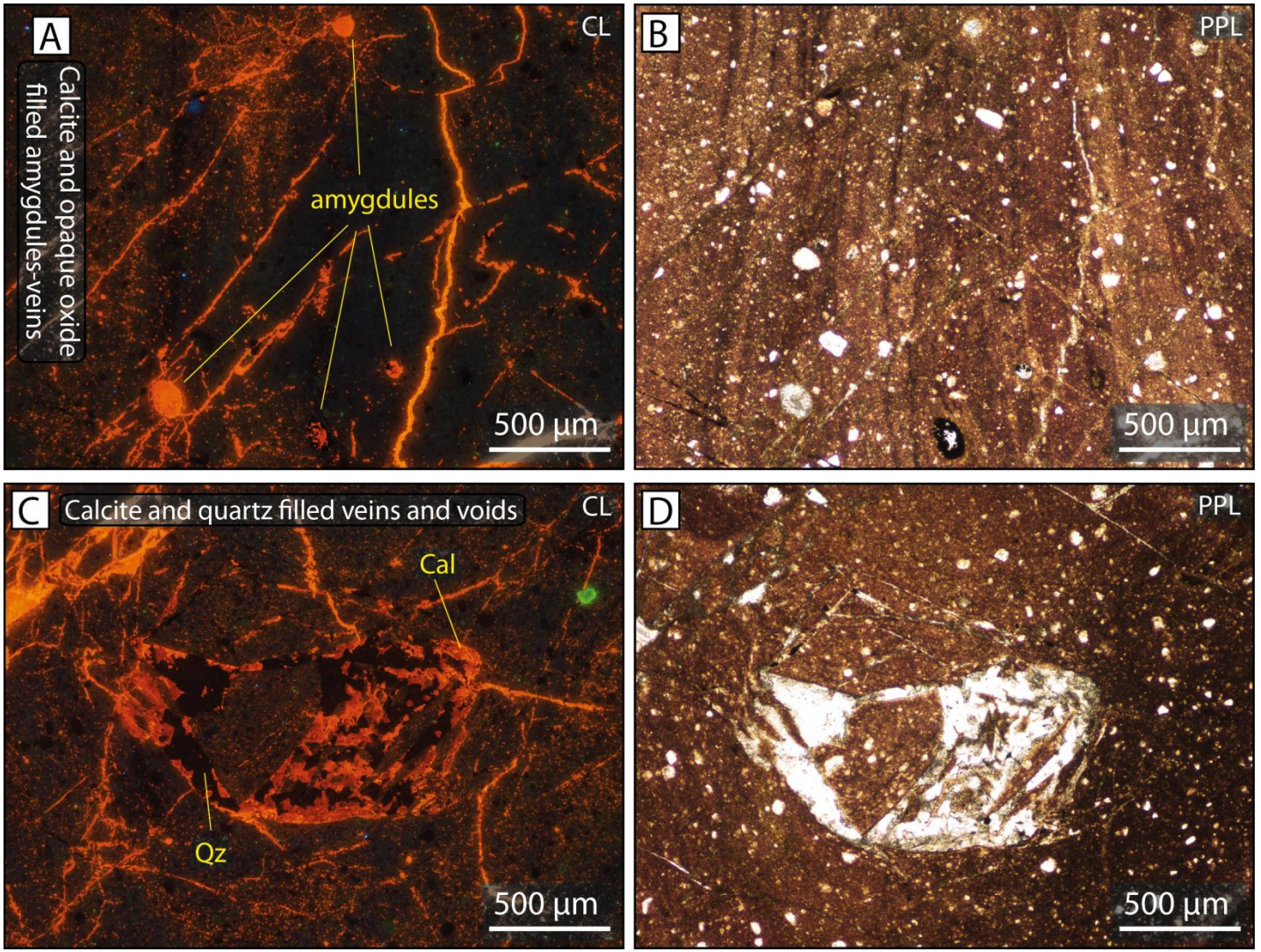

Figure 5.6 –

A hanging wall ultramylonite (1B-99.3m-B – Unit 2) 29.14 m above the upper PSZ. ***[A –D]*** *CL and micrograph images of calcite, opaque oxide and quartz-filled amygdules, veins and voids within the pseudotachylyte. A faint blue CL signal is visible in the pseudotachylyte (****A****) with distinct flow banding features visible in PPL.*

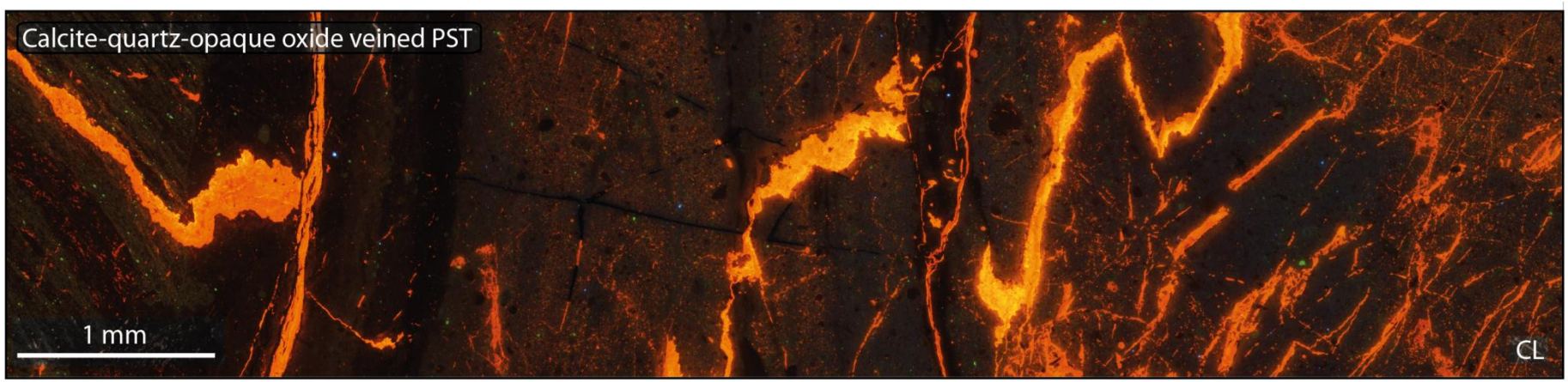

Figure 5.7 –

CL image of a heavily veined pseudotachylyte in a hanging wall ultramylonite (1B-99.3m-B – Unit 2). Multiple generations of calcite are present, differentiated by the varying light-orange to dull-orange CL signal. K-rich regions in the pseudotachylyte have a faint blue CL signal. Area highlighted in Figure 5.5.

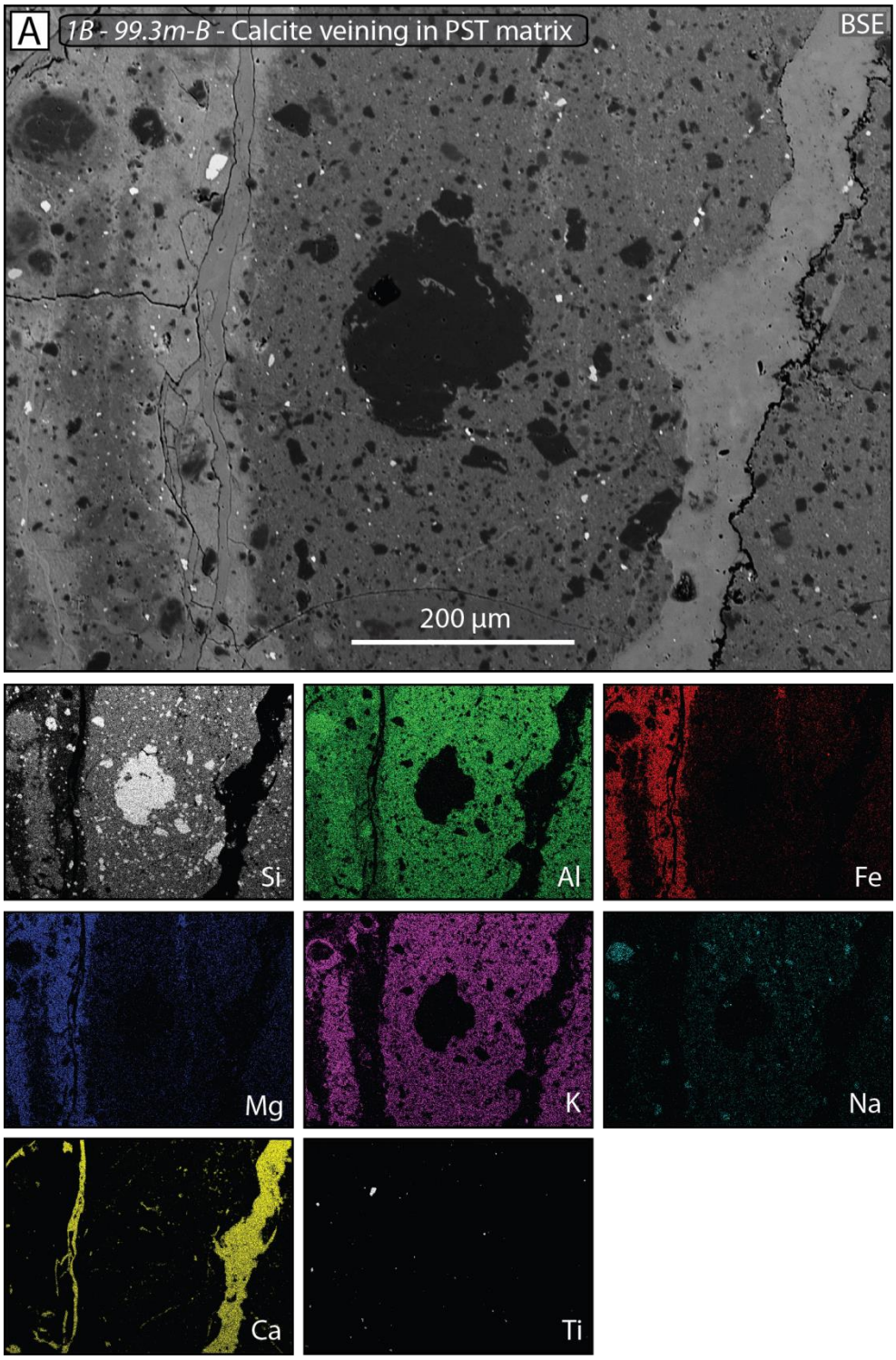

Figure 5.8 – *BSE and EDS maps of veined pseudotachylyte in a hanging wall ultramylonite (1B-99.3m-B – Unit 2). Note the variation in pseudotachylyte composition in immediate vicinity to calcite vein. Area highlighted in Figure 5.5. EDS map step size at 1.6 µm.*

SM 5.5 show a calcite vein cutting across the contact between the host-rock and pseudotachylyte with irregular, lobate margins. EBSD analyses of this vein, reported in Figure SM 5.5, shows that the portion of the vein within the pseudotachylyte (Figure SM 5.5B) contains 50 – 100 µm diameter grains, showing little twinning and crystal lattice distortion; the same vein within the host-rock (Figure 5.5C) runs parallel to the host tectonic foliation, and similarly contains calcite grains with little twinning and crystal lattice distortion though with a finer grain size at 10 – 50 µm. Two separate generations of calcite vein are reported in Figure SM 5.6 within the pseudotachylyte of *1B-99.3m-B.* Both exhibit little twinning and crystal lattice distortion but differ in regards to vein-infill morphology. For example in Figure 5.6B the grains are blocky and span the entire vein width while in Figure 5.6D the calcite occurs as fine-grained, 10 – 40 µm equant fill, with little preferred orientation of the calcite axis, see Figure 5.6G.

The setting of the pseudotachylytes in the Alpine Fault influences the morphology and chemistry of the pseudotachylytes, as outlined in Toy et al., [2011]. For comparison with the FC / AZ pseudotachylytes in this study a pseudotachylyte from hanging wall mylonites was analysed. This pseudotachylyte (Figure SM 5.3 and SM 5.4), hosted within a metabasic mylonite, was acquired from the field in float at Cataclasite Creek / Little Man River, see Figure 1.5B for location. Due to the limited size of the hand specimen the extent and morphology of the pseudotachylyte is difficult to constrain. The pseudotachylyte is 5 – 15 mm thick and appears black and aphanitic in hand specimen. Optically, in PPL, again it appears homogenously black with an indistinguishable matrix while appearing isotropic in XPL, with lithic clasts and survivor clasts present throughout the matrix, no flow banding is apparent. The pseudotachylyte is cross-cut and edged by secondary mineralisation, including chlorite and calcite, with pseudotachylyte fragments floating in the vein-infill within the pseudotachylyte main body, see Figures SM 5.4A. BSE and EDS analyses show homogenous matrix chemistry with high concentrations of Na, Si and Al, with lesser amounts of Ca, Fe, Mg and K, see Figure SM 5.3. The clast population in this pseudotachylyte comprises a large proportion of the material ,~80 %, comprised of: sub-rounded, embayed quartz clasts at 5 – 30 µm diameter; sub-rounded plagioclase clasts at 5 – 20 µm diameter; sub-rounded host lithic fragments at 20 – 100 µm diameter; and Fe and Ti oxides, which compose ~20 % of the pseudotachylyte, at 1 – 20 µm diameter.

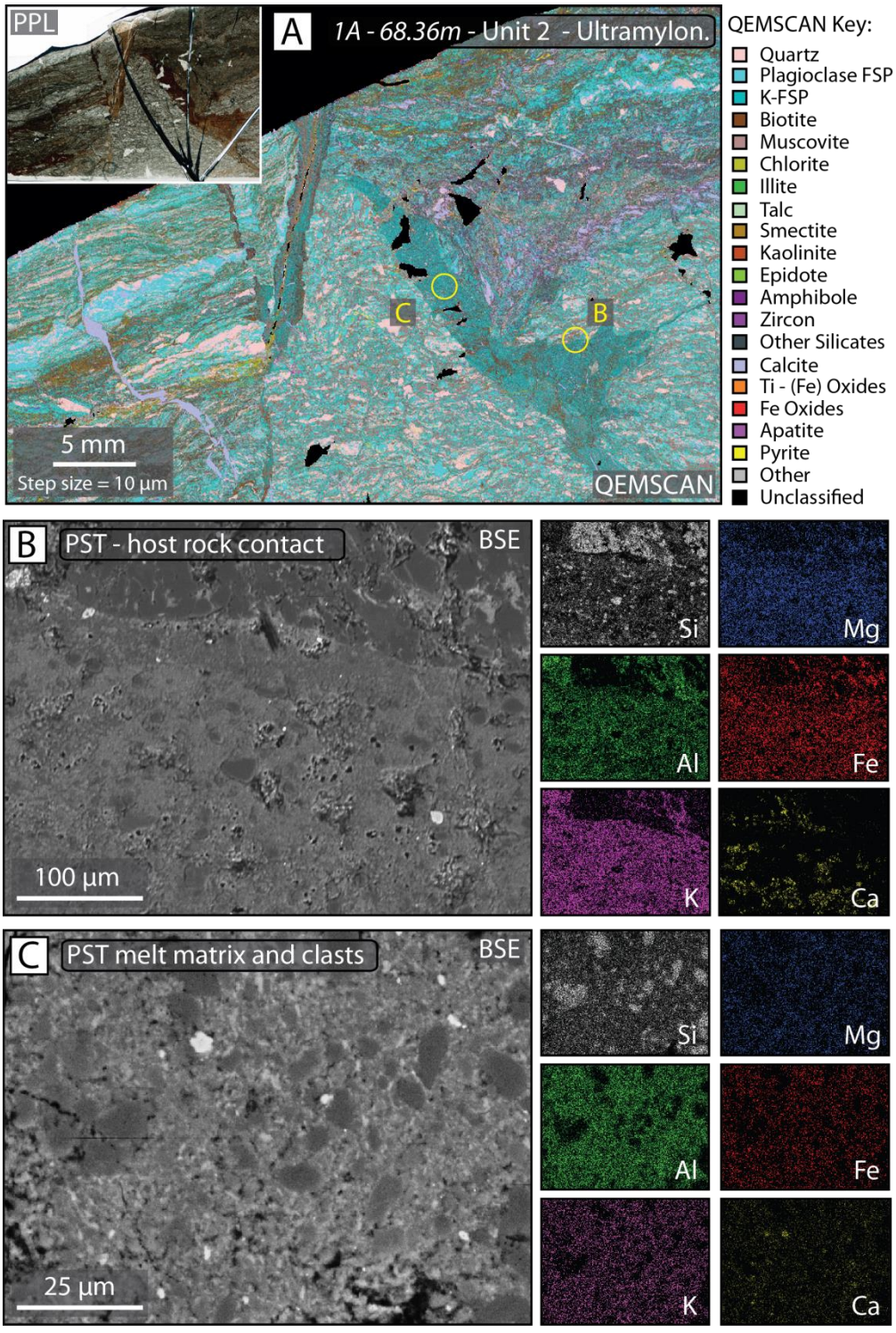

Figure 5.9 – [A] *A hanging wall ultramylonite (1A-68.36m – Unit 2) 22.38 m above the upper PSZ. The QEMSCAN map shows that the pseudotachylyte material is indexed as K-feldspar.* ***[B and C]*** *BSE images and EDS maps of the pseudotachylyte matrix in (**A**), note the significant proportion of Mg and Fe with some Ca, indicating QEMSCAN indexing is inaccurate when dealing with melt origin material. EDS map step size at 1.6 µm.*

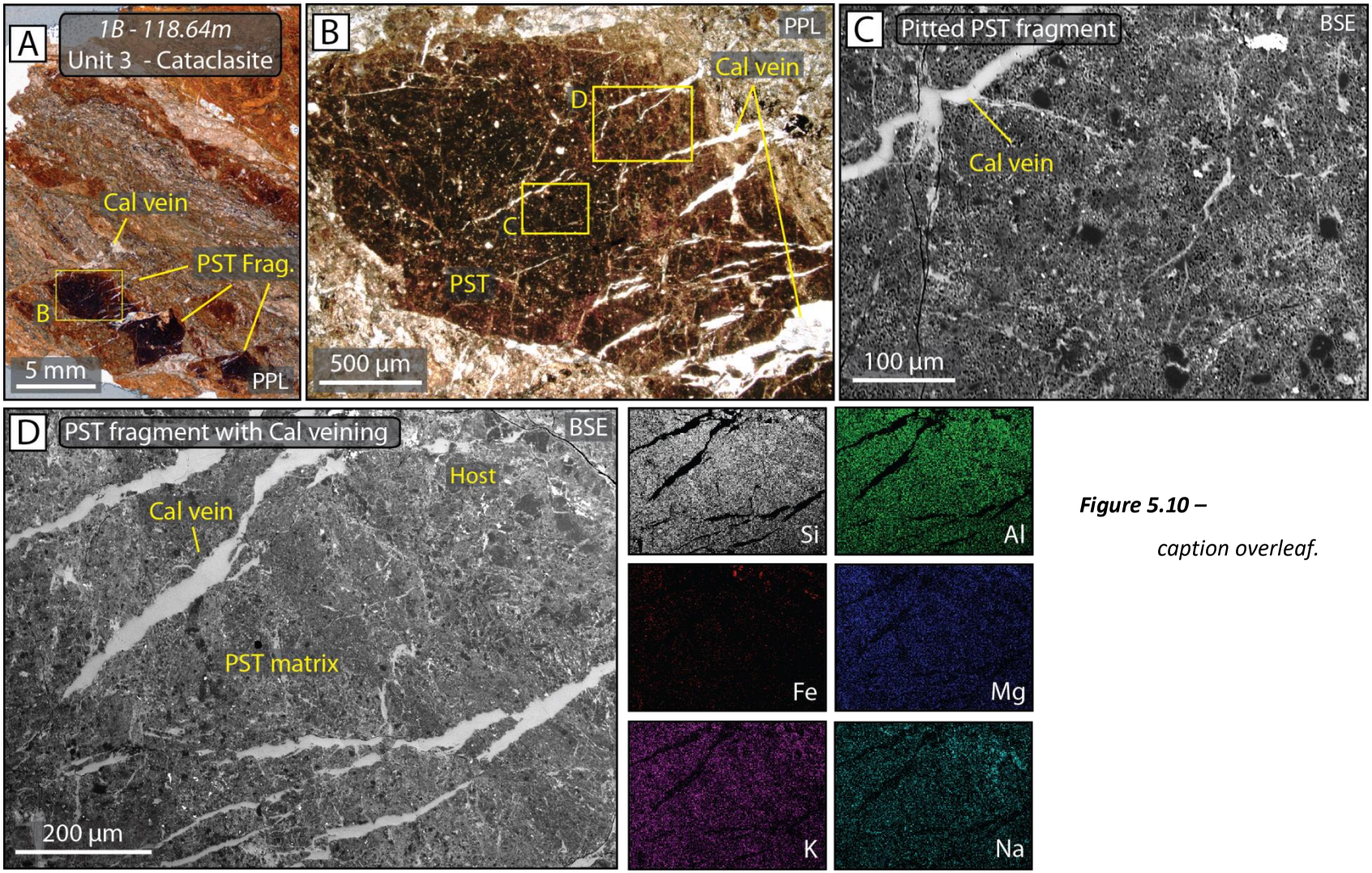

Figure 5.10 –

caption overleaf.

Figure 5 .10 – *(above)* ***[A]*** *A hanging wall cataclasite (1B-118.64m – Unit 3) 9.8 m above the upper PSZ. This cataclasite is heavily foliated and contains multiple en-échelon shears that cut cross a pseudotachylyte vein and foliations.* ***[B]*** *Higher magnification micrograph of region highlighted in (A); showing a pseudotachylyte fragment with extensive calcite mineralisation.* ***[C]*** *BSE image of pseudotachylyte fragment matrix with calcite vein, note the heavily pitted and altered matrix material.* ***[D]*** *BSE images and EDS of maps of the contact between the host cataclasite and pseudotachylyte fragment both cross-cut with calcite veining. Compositionally the host and pseudotachylyte appear similar; however the pseudotachylyte clasts are far finer grain-sizes (10 - 20 µm, as opposed to the host fragments 50 – 100 µm) and appear rounded and embayed. EDS map step size at 3.5 µm.*

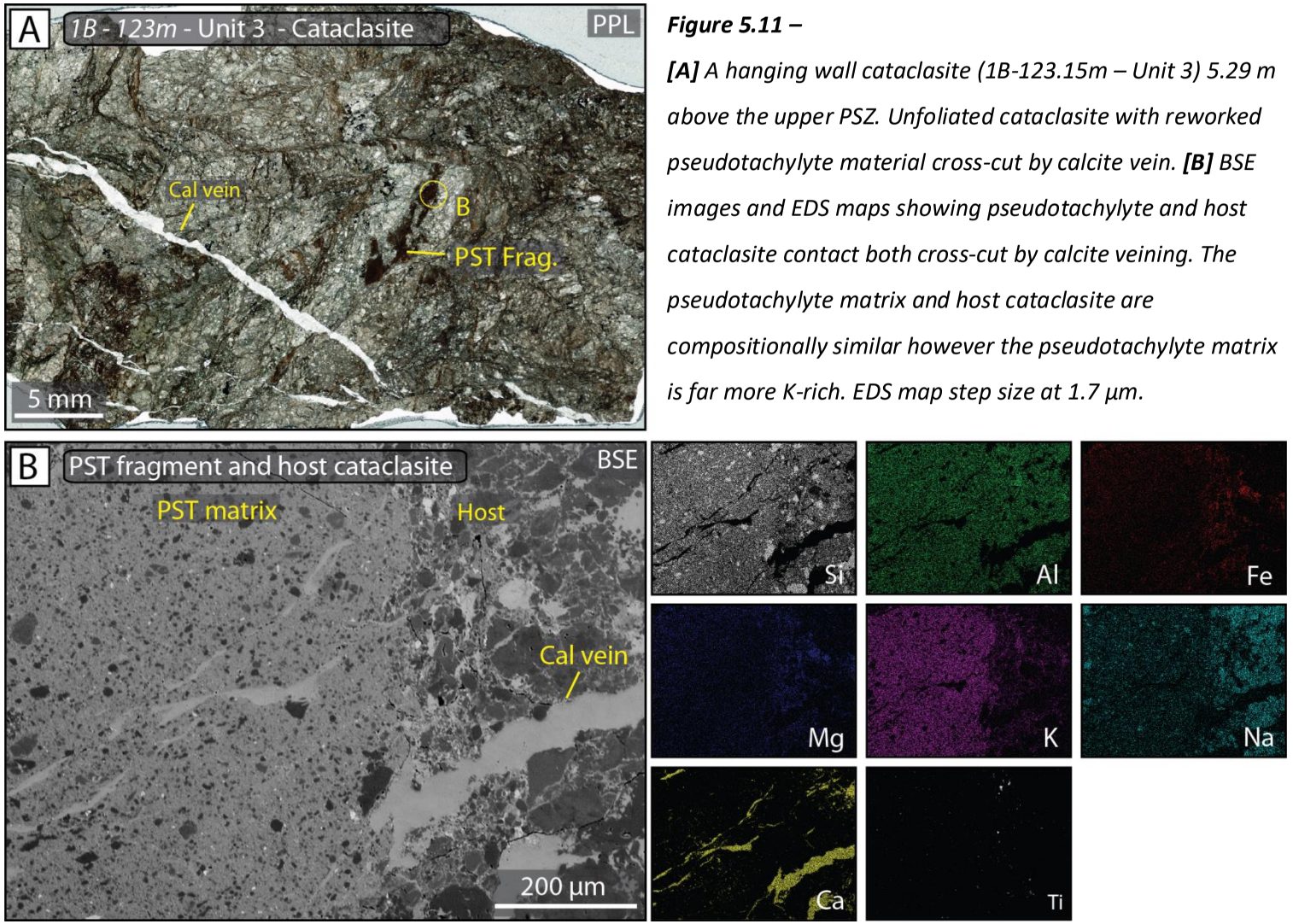

Figure 5.11 –

[A] *A hanging wall cataclasite (1B-123.15m – Unit 3) 5.29 m above the upper PSZ. Unfoliated cataclasite with reworked pseudotachylyte material cross-cut by calcite vein.* ***[B]*** *BSE images and EDS maps showing pseudotachylyte and host cataclasite contact both cross-cut by calcite veining. The pseudotachylyte matrix and host cataclasite are compositionally similar however the pseudotachylyte matrix is far more K-rich. EDS map step size at 1.7 µm.*

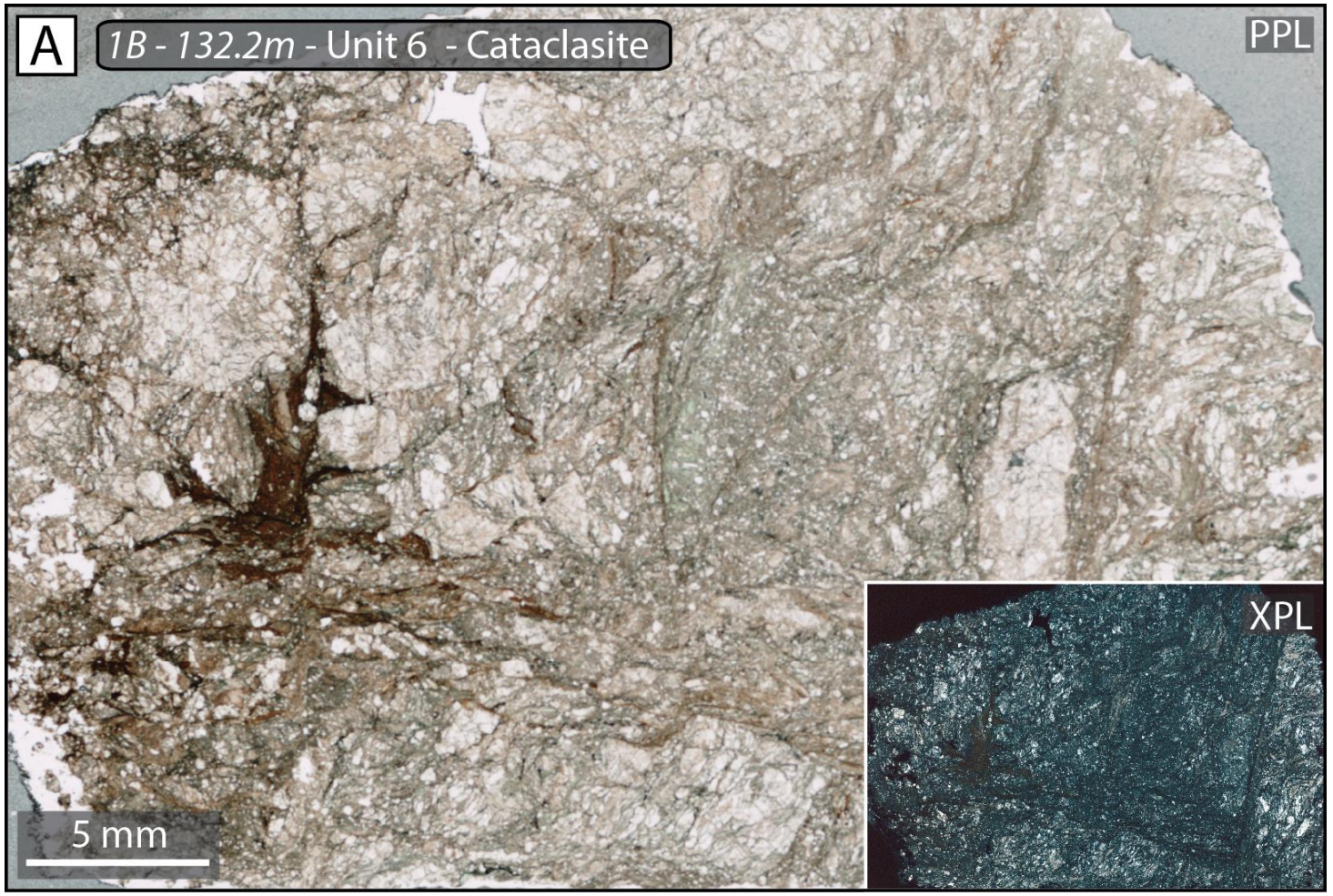

Figure 5.12 –

[A] *A footwall cataclasite (1B-132.m – Unit 6) 3.8 m below the upper PSZ. Contains a non-planar pseudotachylyte, likely an injection structure.*

5.4.2. Principal Slip Zone ultracomminuted gouges of the Alpine Fault

A continuous sequence of Alpine Fault's cataclastic fault rocks was acquired during the DFDP-1; from the heavily fractured ultramylonites in the damage zone, transitioning to the FC / AZ cataclasites. Hosted within the FC / AZ cataclasites are discrete zones of ultracataclasis, where slip has been localised over successive cycles of seismicity generating ultracomminuted gouges known as the principal slip zones (PSZ). The Alpine Fault cataclastic rocks, have been described by numerous workers at field exposures [*Reed*, 1964; *Sibson et al.*, 1981; *White and White*, 1983; *Cooper and Norris*, 1994; *Boulton et al.*, 2012] as well as in the DFDP drill-core [*Toy et al.*, 2015b; *Williams et al.*, 2016]. These localised occurrences of ultracataclasis also occur along the same planes in which pseudotachylytes occur, present within *1B-99.3m-A* of the drill-core in Figure 5.2 and 5.3 and described in Section 5.1.1.

The upper PSZ of the Alpine Fault (PSZ-1), encountered at *1A-90.74m* and *1B-128.3m*, is composed of a ~25 cm-thick zone of ultracomminuted gouge that marks the oblique thrust contact (055 / 29°SE, lineation 23 / 109) between the Alpine Fault hanging wall and footwall lithologies [*Boulton et al.*, 2015]. A secondary slip surface (PSZ-2) was also encountered at *1B-143.85m* marking the boundary between the footwall cataclasites and breccias. Each of these PSZs can be delineated into separate gouge lithologies, based on mineralogy and morphology. These lithological classifications are illustrated in Figure 5.13 after *Boulton et al.*, [2015] and are as follows:

- *Smectitic brown gouges*, an incohesive gouge composed of a smectite, white mica and goethite matrix with quartzofeldspathic and recycled gouge clasts with diameters of 20 – 100 µm.
- *Blue gouge*, a poorly cohesive gouge composed of a chloritic and white mica matrix with quartzofeldspathic and calcite clasts with diameters of 20 – 1000 µm.
- *Calcite fragments*, composed of boudinaged lenses and sub-rounded clasts within the blue gouge.
- *Cataclasites,* a cohesive unit with 10 – 80 % chloritic matrix with regions of chaotic breccia composed of calcite and quartz clasts.

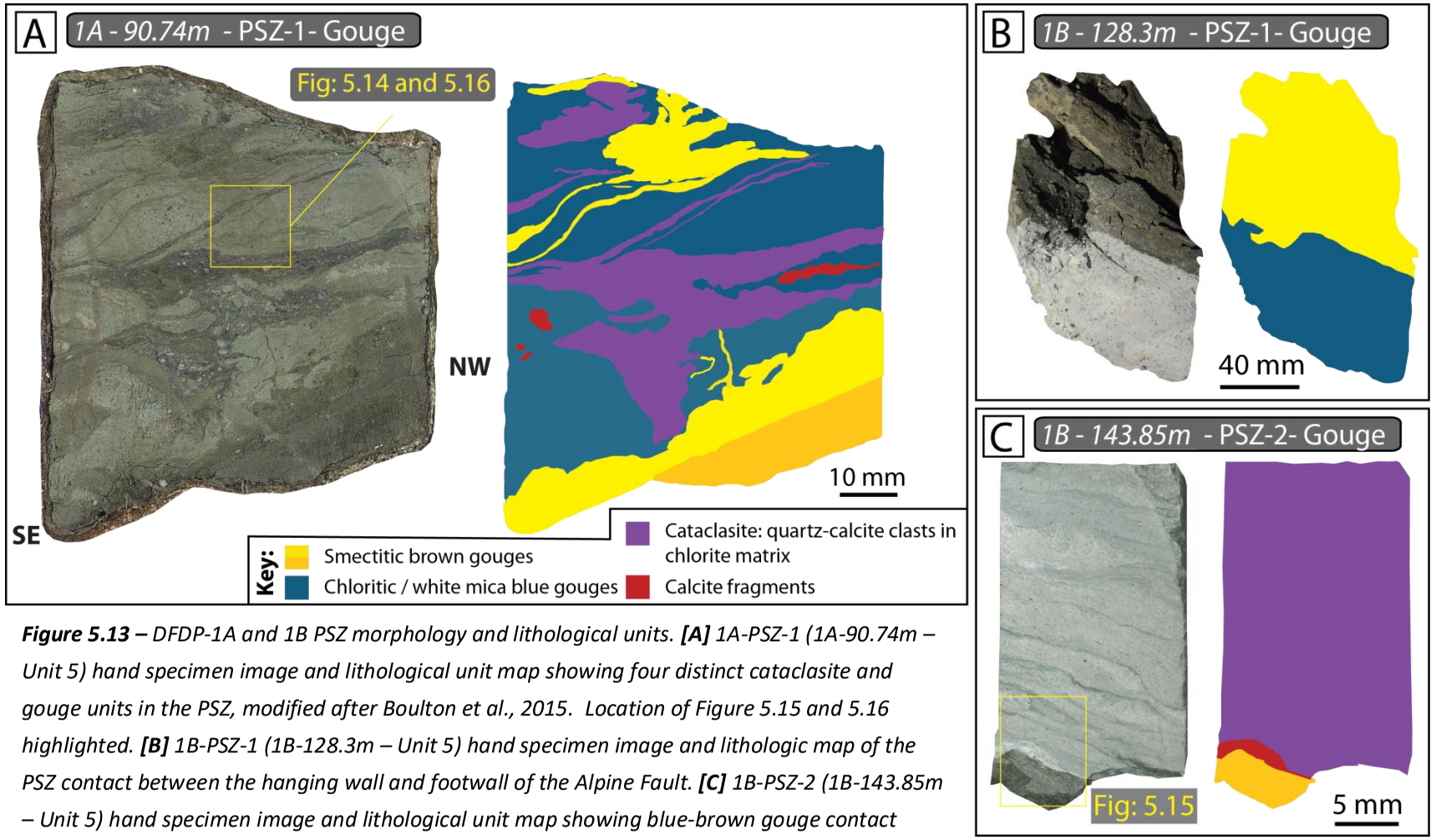

Figure 5.13 – *DFDP-1A and 1B PSZ morphology and lithological units.* ***[A]*** *1A-PSZ-1 (1A-90.74m – Unit 5) hand specimen image and lithological unit map showing four distinct cataclasite and gouge units in the PSZ, modified after Boulton et al., 2015. Location of Figure 5.15 and 5.16 highlighted.* ***[B]*** *1B-PSZ-1 (1B-128.3m – Unit 5) hand specimen image and lithologic map of the PSZ contact between the hanging wall and footwall of the Alpine Fault.* ***[C]*** *1B-PSZ-2 (1B-143.85m – Unit 5) hand specimen image and lithological unit map showing blue-brown gouge contact within the footwall of the fault with calcite layer above the brown gouge.*

All of the above gouge types appear in the PSZ-1 of 1A-90.74m, Figure 5.13A. The brown gouges inject and bifurcate into the more cohesive units and are reworked into recycled gouge clasts. The blue gouges encompass all other PSZ lithologies and are cross-cut by the brown gouge structures; contacts between the blue and brown gouges are sharp and undulating and the cataclasites contain fault-parallel Y-shears. XRD results show that calcite comprises ~10 % of the blue gouge with clast diameters of up to 200 µm while the brown gouge contains ~4 % calcite at finer grain sizes [*Boulton et al.*, 2015]. Considerable variation in calcite CL signal exists within PSZ-1 (see Chapter 4) indicating that the calcite was precipitated in fluctuating pressure – temperature conditions with the precipitating fluid containing variable trace elements in solution, due to varying fluid-rock interactions during exhumation and the seismic cycle. It is likely this calcite was derived from many, separate increments of mineral precipitation evidenced by the many cross-cutting veins.

PSZ-1 was also sampled within *1B-128.3m,* Figure 5.13B, and is comprised of all four of the gouge materials as described in *1A-90.74m* above. However, both the brown and blue gouge layers are thicker and with a more homogenous internal structure. The PSZ-2 brown gouge shows microstructures and chemistry near identical to that in *1A-90.74m.* The secondary PSZ-2 of *1B-143.85m,* Figure 5.13C, includes an upper Unit 6 footwall cataclasite in sharp contact with a smectitic brown gouge layer. Above the contact a layer of calcite-cemented clasts sits; this feature is discussed in more detail in Section 4.3.2.5 of this thesis.

Within the brown gouges of both PSZ-1 and PSZ-2 four distinctive types of K-feldspathic composition clasts were observed. *Type 1 clasts in 1A-90.74m*, detailed in Figures 5.14, occur as angular clasts with diameters of 50 – 200 µm, appearing homogenously dirty-brown in PPL and isotropic in XPL. In CL they exhibit a blue CL signal that varies in strength between individual clasts. They have a K-feldspathic composition, with minor Mg, Fe, Na and Ti, containing inclusions of quartz (<5 µm), calcite (<5 µm) and Ti-Oxides (~1 µm) that comprise a combined ~5 % of the clast; see Figure SM 5.1 for EDS analyses. EBSD analyses reveal that these clasts are composed of cryptocrystalline, <5 µm, feldspar grains (indexed as orthoclase) visible in Figures 5.14C and D, that comprise ~40 % of the clast. When plotted in a PF the crystallographic orientations of the feldspathic cryptocrystalline material exhibits a very weak CPO.

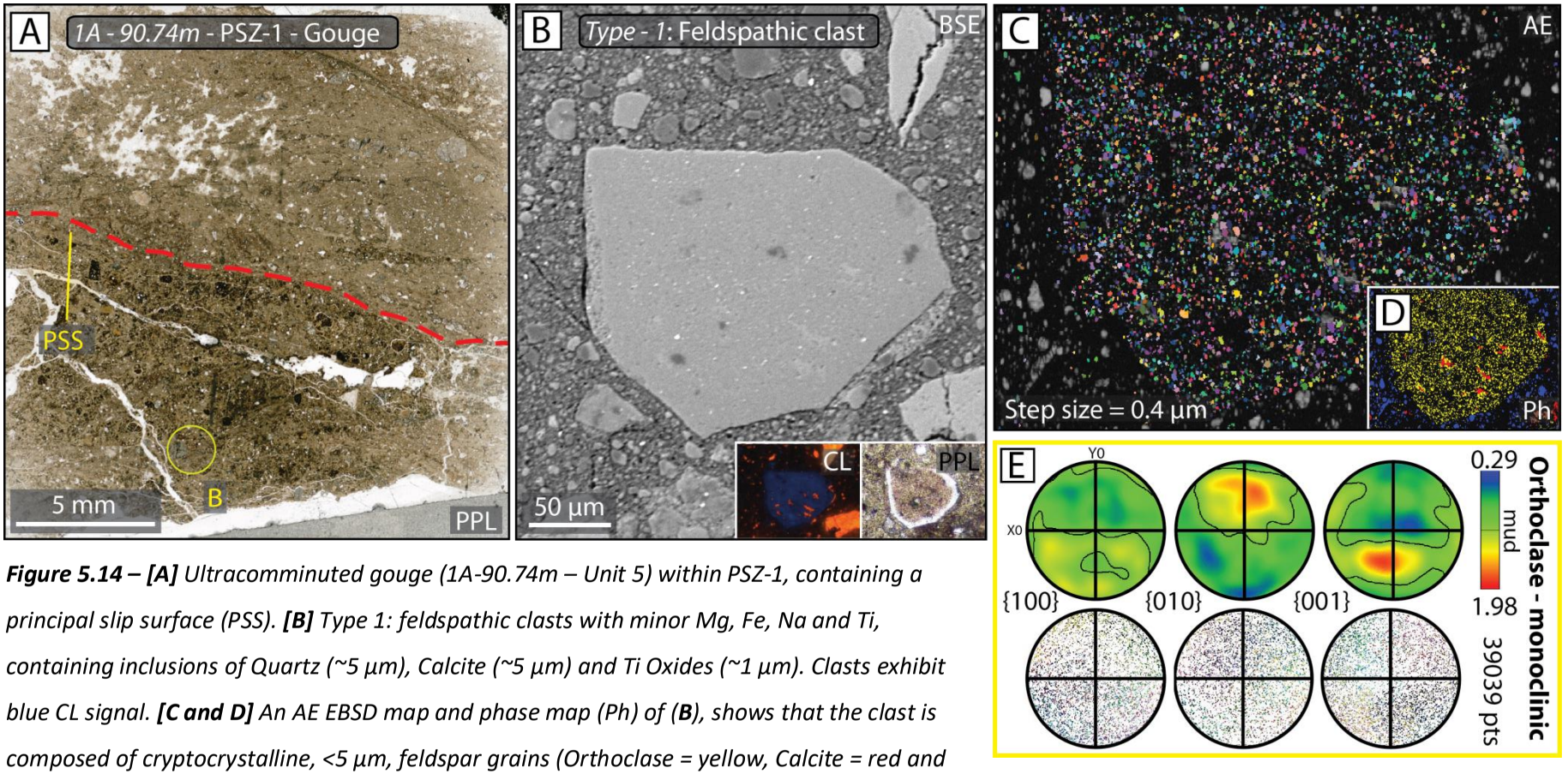

Figure 5.14 – [A] *Ultracomminuted gouge (1A-90.74m – Unit 5) within PSZ-1, containing a principal slip surface (PSS).* ***[B]*** *Type 1: feldspathic clasts with minor Mg, Fe, Na and Ti, containing inclusions of Quartz (~5 µm), Calcite (~5 µm) and Ti Oxides (~1 µm). Clasts exhibit blue CL signal.* ***[C and D]*** *An AE EBSD map and phase map (Ph) of (**B**), shows that the clast is composed of cryptocrystalline, <5 µm, feldspar grains (Orthoclase = yellow, Calcite = red and Quartz = blue).* ***[E]*** *PF of the feldspathic clast (Orthoclase only) showing it exhibits a weak CPO (<2 MUD).*

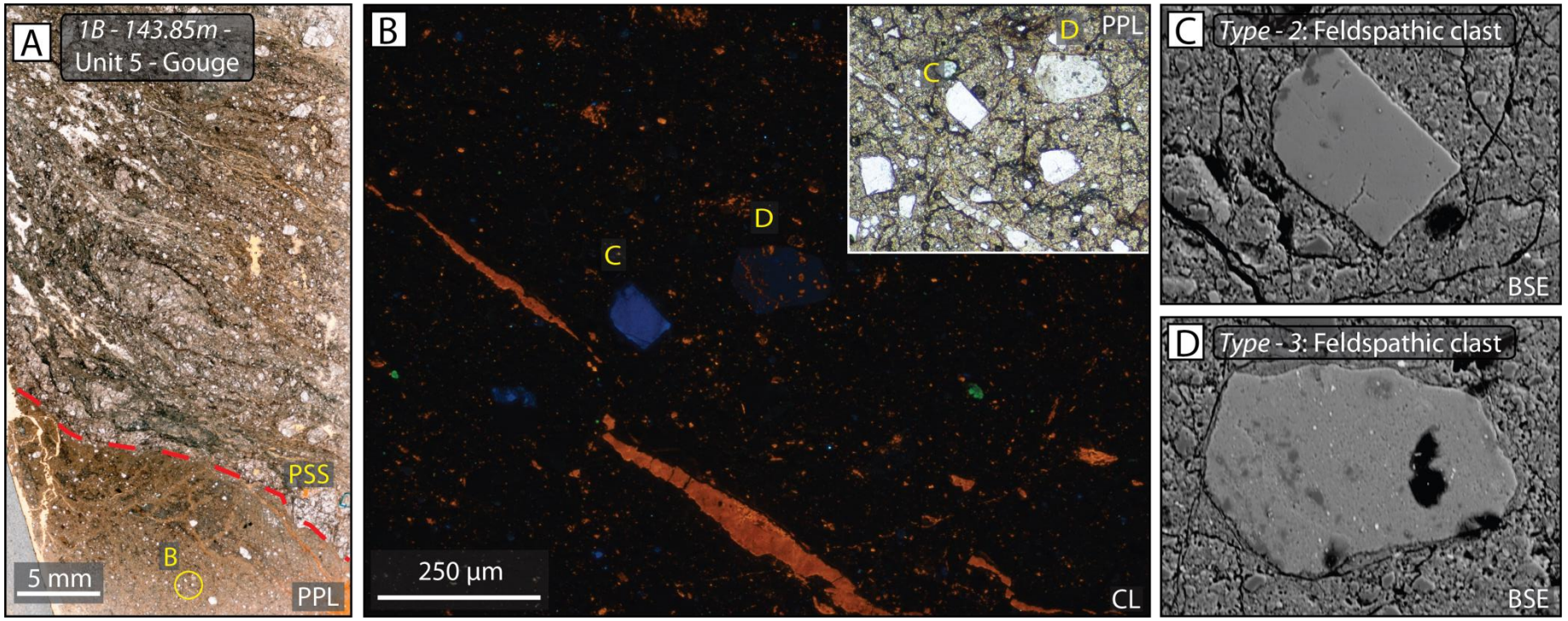

Figure 5.15 – [A] *Ultracomminuted gouge (1B-143.85m – Unit 5) within PSZ-2, containing a principal slip surface (PSS).* ***[B]*** *CL image of Type 2 and 3: feldspathic clasts and fragmented calcite vein, feldspathic clasts exhibit a blue CL signal and occasionally contain isolated calcite fragments.* ***[C and D]*** *BSE images of Type 2 and 3: feldspathic clasts highlighted in (**B**); both containing embayed quartz and Ti oxide grains with a matrix of K-feldspathic composition.*

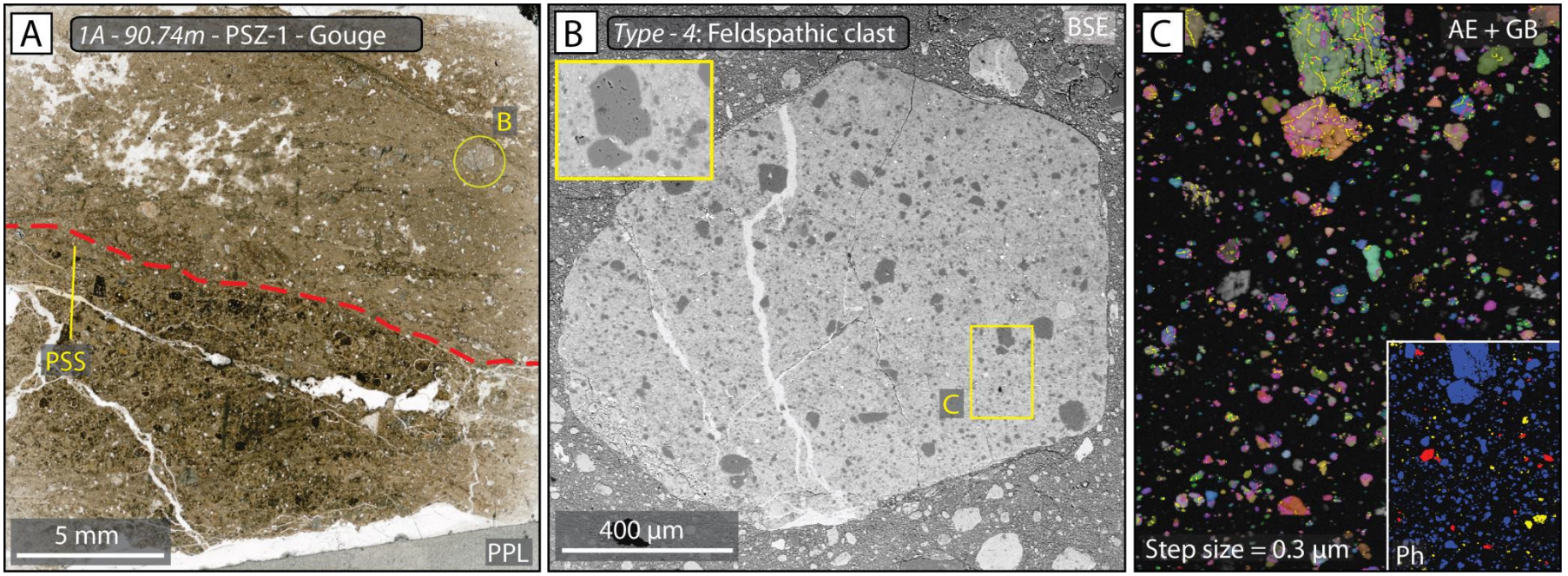

Figure 5.16 – [A] *Ultracomminuted gouge (1A-90.74m – Unit 5) within PSZ-1, containing a principal slip surface (PSS).* ***[B]*** *Type 4: feldspathic clast containing embayed quartz grains (5 – 50 µm) and Ti oxide (1 – 5 µm) set in a matrix of feldspathic composition, with calcite mineralising thoroughgoing joints and clast edges. The clast matrix appears isotropic in XPL and exhibits no CL emissions.* ***[C]*** *An AE EBSD map with grain boundaries (GB) and phase map (Ph) (Orthoclase = yellow, Calcite = red and Quartz = blue) showing lack crystalline material of clast matrix, resulting in no EBSD indexing) and heavily deformed and embayed quartz grains which exhibit sub-grain formation with grain boundaries of <10 ° (Grain Boundaries: >2° = yellow, >5° = green, >10° = blue and >15° = purple).*

Clasts Type 2 and Type 3 are present in the secondary PSZ-2 at 1B-143.85m, Figure 5.15. Type 2 occur as angular clasts, ~30 – 50 µm diameter, appearing colourless in PPL, with first-order grey or white birefringence in XPL and have a bright blue CL. Type 3 occur as sub-rounded clasts, ~30 – 50 µm, appearing cloudy-brown in PPL, isotropic in XPL and have a dull blue CL. Both clasts contain inclusions of quartz (<5 µm), calcite (<5 µm) and Ti-Oxides (~1 µm) within a K-feldspathic matrix with minor amounts of Mg and Fe. *Type 1* and *3* clasts may be the same clast type; further analyses are required to confirm this.

Clast *Type 4*, detailed in Figure 5.16, occur as polygonal clasts with diameters of 100 – 800 µm, containing embayed quartz grains (5 – 50 µm) and Ti oxide (1 – 5 µm) set in a matrix of K-feldspathic composition, see Figure SM 5.2 for EDS analyses, with calcite mineralising thoroughgoing joints and the clast edges. The matrix in these clasts appears isotropic in XPL and exhibits no CL emissions. The matrix material could not be indexed using EBSD. Quartz grains >40 µm exhibit sub-grain boundaries (<10° misorientation), indicating that crystal-plastic deformation prior to entrainment in the gouge affected these grains (Figure 5.16C). A small fraction of the grains hosted in the clast were indexed as feldspars.

5.5. Discussion

In this section we present a number of potential mechanisms for the generation of the microstructures detailed above and infer what these features may tell us about seismicity on the Alpine Fault and the processes that take place within the fault during the seismic cycle.

5.5.1. Melt behaviour and subsequent alteration and reworking of pseudotachylytes

The features termed pseudotachylytes in this study are demonstrably of frictional melt origin, as evidenced by a variety of features determined by previous workers, including: mineralised vesicles (amygdules) [*Maddock et al.*, 1987] and evidence of melting and assimilation of survivor clasts into the vein matrix [*Magloughlin*, 1992] as well as the survivor clasts being predominantly rounded [*Lin*, 1999]. The observed association of the pseudotachylyte veins with ultracomminuted material (Figure 5.2) could represent further indication of a frictional melt origin, as cataclasis is generally accepted as being a precursor

to the generation of pseudotachylyte during seismic slip [*Magloughlin*, 1992; *Bjornerud and Magloughlin*, 2004]. Additionally, multiple studies show the genetic relation between cataclasites and solidified melt within fault zones [*Otsuki*, 2003; *Rowe et al.*, 2005; *Sibson and Toy*, 2006; *Toy et al.*, 2011]. A clear transition from a pseudotachylyte vein margin to ultracataclasites is not always observed, as in injection features and cataclastically reworked pseudotachylyte, this may be due to poor mobility of ultracataclasites along the generation surface into injection structures or their mechanical assimilation into the host cataclasite during subsequent reworking.

The only observed occurrence of intact vein of pseudotachylyte occurs at 1A-68.36m (Figure 5.9) and 1B-99.3m (Figure 5.2 – 5.5), within the fractured ultramylonites that mark the boundary between the damage zone and fault core / alteration. With increasing proximity to the PSZ the lack of intact veins of pseudotachylyte could be due to the extensive fragmentation and comminution during periods of seismicity within the fault core.

As pseudotachylyte melt is so transiently mobile and occupy such small volumes, gravitational and convectional fractionation is unlikely to occur. The nature of melt segregation observed in the pseudotachylyte veins of this study (Figure 5.2 – 5.4), particularly between the vein margins and the main body of the melt, is likely due to processes outlined by *Warr et al.*, [2003] and *Warr and van der Pluijm*, [2005] where two related mechanisms are used to explain sequential formation of pseudotachylyte of different compositions. The first involves successive and rapid injections of frictionally generated material in the form of melt pulses. The first pulse, preserved on the vein margins is proximally derived, has a Si-rich composition and high concentration of survivor clasts, the second pulse is comprised of a distally derived melt with lesser clast content. This behaviour is attributed to a single, large earthquake that has undergone stick-slip generating potentially multiple pulses of melt at asperity contacts along the rupture plane [*Warr et al.*, 2003]. The second mechanism is rapid crystal fractionation during transport of the melt, in which an initial mobile, low viscosity, melt-clast mixture migrates along fractures and coats the vein margin, followed by a more viscous melt that has undergone more fractionation and volatile loss which fills the vein centre. Though not identical in regard to clast population in the segregations described by *Warr et al.*, [2003] and *Warr and van der Pluijm*, [2005], a combination of these mechanisms may be at work in

pseudotachylyte observed within the Alpine Fault core, with enrichment of K / Si and Mg / Fe in segregated melt layers caused by preferential comminution and melting of biotite and muscovite, both of which are present in the host-rock but not in the pseudotachylyte. In this study, where the immiscibility of two melts in the same pseudotachylyte is observed (Figure 5.4), segregation is interpreted as being encouraged by viscosity contrasts [*Spray*, 1993]. These variations in composition and inferred viscosity contrasts between the margin and main body melt indicate that these margins are not a result of rapid quenching, relative to the inner main body melt, but are due to initial contrasting melt compositions. Due to limited scale of sampling it is unclear whether this immiscibility occurred via unmixing of one melt or the mingling of two separate melts.

Amorphous materials, i.e. melt glasses, do not produce CL emissions themselves but rather strongly absorb them. Any CL signal observed in a glass is due to the presence of chemical and structural defects, potentially products of devitrification, which manifest as CL signals of variable colouration. If these CL signals are weak, with emission wavelengths of <350 nm, they can be obscured by the glassy medium, making observations difficult [*MacRae and Wilson*, 2008]. Blue CL emissions have been observed in the Alpine Fault FC / AZ pseudotachylytes, as shown in Figures 5.4 and 5.5. This blue CL has also been observed in other compositionally related materials, in moldavites, glass derived from meteoric impacts [*Fritzke et al.*, 2017], or in synthetically derived material such as amorphous quartz [*Stevens-Kalceff*, 2013]. Blue CL has been attributed to the presence of various crystallographic lattice defects and include: nonbridging oxygen-hole centres (NBOHC), where an electron hole in the 2pπ – orbital of a single, nonbridging oxygen is bound to a threefold coordinated silicon (O_3 = Si - O·); the generation of lattice defects during interactions with an electron beam are known as self-trapped excitions, where an electron-hole pair is formed which can coexist with other defects such as electron centres with an interstitial oxygen or NBOHC; and oxygen deficiency centres [*Pacchioni et al.*, 2000; *Stevens-Kalceff*, 2009, 2013; *Fritzke et al.*, 2017]. Green CL emissions are attributed to defects related to a strong local disorder, which can indicate local amorphisation, as well as Al - O^- - Al defects [*Fritzke et al.*, 2017]. As both blue and green CL emissions are observed in the studied pseudotachylytes it can be inferred that the original glass has undergone alteration and devitrification with differing products according to its original chemistry. In the K, Al and Si-rich matrix regions a blue or green CL could be attributed to any number of

the above causes. Further analysis using transmission electron microscopy (TEM) to distinguish the crystallinity of the pseudotachylyte matrix is required.

All pseudotachylytes observed in this study are pervasively associated with secondary mineralisation of calcite, quartz and Fe-oxides. Calcite mineralisation is interpreted to predate, occur synchronously and postdate pseudotachylytes. As described in the result section, evidence for this is provided by: (pre-) disrupted and cataclased calcite veins; (syn-) the presence of amygdules; (post-) multiple generations of calcite mineralisation cutting across the solidified melt. In the instances where calcite veins within the pseudotachylytes are encompassed by regions of pale material, as in *1B-99.3m-B*; Figure 5.4, localised fluid-rock interaction along fracture planes may be indicated, as these regions are enriched in Mg and Fe. This interaction is likely short-lived due to the rapid sealing by blocky-equant calcite [*Hilgers et al.*, 2004], see Figure SM 5.6. The presence of amygdules in pseudotachylyte is likely further evidence for the presence of fluids during frictional melting. Calculations by *Dixon and Dixon*, [1989] suggest that, in order to generate vesicles, melt must first entrain available volatiles (H_2O and CO_2) from the surrounding rock mass as there is insufficient time to nucleate bubbles via degassing before melt quenching. Fluid flux through the damaged region, encompassing the pseudotachylyte, would then cause mineralisation of the vesicles with its dissolved load. This evidence would appear to counter the previous schools of thought that the presence of fluid in the vicinity of a shearing plane would buffer temperature and/or cause thermal pressurisation thus lowering normal stresses on the fault and inhibiting frictional melting [*Sibson*, 1973; *Lachenbruch*, 1980]. Recent experiments on the reactivation of slip surfaces at room temperature under high normal stresses using axial load or fluid pressure fluctuations, by *Hayward and Cox*, [2017], showed that at normal stresses of >500 MPa melting and frictional welding occurred at asperity contacts while the rock was fully saturated. *Violay et al.*, [2014] also generated frictional melting in experiments on saturated, cohesive rock at lower effective stresses, 20 MPa, at displacements of 8 - 12 m. This gives credence to models by *Rempel and Rice*, [2006] claiming that damage-enhanced fluid mobility would allow a saturated rock to generate frictional melt, as fluid would migrate away from the slip surface and allow frictional heating to take place. This may be a coseismic mechanism commonly taking place within the Alpine Fault core.

The susceptibility of pseudotachylytes to hydration and chemical alteration and cataclastic reworking has been invoked to explain the dearth of frictional melt observed in the rock record, leading to the underrepresentation of episodes of seismicity [*Kirkpatrick and Rowe*, 2013]. This is likely the case in the Alpine Fault core. Candidate melt-origin microstructures are common in the alteration zone. However, due to reworking and alteration processes, definite recognition of pseudotachylytes is difficult. With this in mind, pseudotachylyte may play a larger part in the accommodation of off-fault damage in the fault during seismicity than previously thought, with subsidiary fault planes localising displacement within the fault damage zone as opposed to exclusively on the PSZ.

In comparison to the field pseudotachylyte sampled from Cataclasite Creek / Little Man River within a metabasic ultramylonite, the FC / AZ pseudotachylytes have a lower clast / matrix ratio, have far more secondary minerals disseminated within them, and appear blue-grey rather than the typical black colouration of pseudotachylytes. The comparatively small clast population in the FC / AZ pseudotachylytes is potentially due to the cataclased nature of its host / protolith, with finer starting grain sizes being assimilated into melt more easily than fragments generated during shear in intact rock. In regard to the greater amount of secondary mineralisation and colouration, this is likely due to a greater degree of fracturing and fluid ingress into the pseudotachylytes within the FC / AZ compared to within the distal fault damage zone mylonite sequence, altering the pseudotachylyte matrix and subsequently followed by mineralisation of the fractures.

5.5.2. The nature and behaviour of the principal slip zone

The progressive localisation of slip in a fault zone results in the generation of fine-grained gouge layers as displacement increases and exhumation to the upper crust occurs. During periods of gouge generation material is entrained and reworked in a principal slip zone, where deformation is highly localised [*Faulkner et al.*, 2010; *Boulton et al.*, 2012]. Fault gouges can potentially serve as indicators of the conditions and mechanisms of coseismic slip on the principal slip zone [*Han and Hirose*, 2012; *Janssen et al.*, 2014]. They are formed of material with fine grain-sizes down to nanoparticles, which are known to be characterised by physical properties, and therefore mechanical behaviour, different from that of the coarser materials throughout the rest of the fault. This is particularly true for nanoparticulates which have been found to reduce frictional shear resistance of a slipping

plane [*Goldsby and Tullis*, 2002; *Reches and Lockner*, 2010; *Chen et al.*, 2013b]. Therefore, processes in PSZs are likely to be unique to these highly localised zones in fault systems.

This section outlines the inferred evolution of the Alpine Fault principal slip zone over many cycles of seismicity, with particular focus on the entrainment and reworking of pseudotachylytes and nanoparticulates generated throughout successive seismic cycles.

The principal slip zone is a lithologically and mechanically distinct unit within the fault rock sequence of the Alpine Fault zone. The presence of reworked gouge clasts, reworked multigenerational calcite veins and sheared injection structures indicate a long-lived structure that has undergone many increments of high magnitude slip events and has potentially accommodated up to 460 km of cumulative displacement in the past 25 Myr [*Wellman*, 1953; *Sutherland et al.*, 2000]. AFZ fault gouges are unique in the fault zone as they contain abundant low temperature (<120 °C) phyllosillicates kaolinite, smectite and montmorillonite, the presence of which suggests that the PSZs exclusively host reactions not seen elsewhere on the fault, and have undergone the most extensive alteration [*Inoue and Utada*, 1991; *Schleicher et al.*, 2015; *Boulton et al.*, 2017a]. Experimental measurement have shown that the presence of these weak, strongly anisotropic minerals, results in a slip surface with intermediate frictional strengths with coefficients of friction of 0.36 – 0.61 at sub-seismic velocities between 0.1 – 10 μm/s at 30 MPa [*Boulton et al.*, 2015]. The gouges show velocity strengthening behaviour, have low static and dynamic permeabilities of 10^{-20} – 10^{-21} m^2 and have been predicted to slip in a stable manner at the near surface [*Boulton et al.*, 2015, 2017b; *Allen et al.*, 2017]. The mechanical and physical properties outlined result in long fluid diffusion times within the gouge layers. This, coupled with shear-enhanced compaction, favours the generation of pore fluid overpressures, which may limit the generation of frictional melt and nanoparticles, as normal stresses and dynamic friction on the slipping surface is reduced thus limiting frictional sliding and cataclasis, but would still facilitate seismic rupture [*Lachenbruch*, 1980].

The presence of material with K-feldspathic composition, as observed in the pseudotachylytes and gouge clasts detailed above, is anomalous in the Alpine Fault rock sequence. K-feldspar is not present in the hanging wall mylonitic protolith lithologies, the Alpine schists, nor in its mylonitic sequence. However, quantitative XRD analyses performed by *Boulton et al.*, [2017] throughout the Alpine Fault alteration zone found that K-feldspar

was only present within the hanging wall, 5 m above the PSZ in DFDP-1A and in the footwall sampled in DFDP-1B. These occurrences have been attributed to incorporation of footwall material derived from granitic protoliths just above the PSZ-1 into the hanging wall, while within the PSZ layers it is speculated by *Boulton et al.*, [2017] that elevated K_2O is caused by a combination of footwall K-feldspar, adularia and/or potassic pseudotachylyte.

Blue CL in feldspars can be attributed to the alteration of feldspars inducing local disorder and amorphisation, and the presence of Al – O^- – Al defects [*Krbetschek et al.*, 1997; *Götze et al.*, 2000; *Wendler et al.*, 2012]. However, these Al - O^- - Al defect centres can be eliminated by fluid-feldspar interaction below ~450 °C via ordering of the Si – Al bonds [*Finch and Klein*, 1999]. K-feldspars also exhibit blue CL emissions when Ti^{4+} is substituted into the feldspar lattice (Al – O – Ti) [*Lee et al.*, 2007; *Parsons et al.*, 2008; *Kayama et al.*, 2010].

A potential origin for the enrichment of K_2O and K-feldspathic clasts are localised, deformation induced, alteration reactions within the PSZs. During seismicity, biotite and muscovite undergo comminution; due to their affinity for H^+ over K^+ they release K^+ into the local system [*Eisenman*, 1962]. This K^+ creates ultrafine-grained particles with high surface energy and generates local disequilibrium conditions. In order to return to equilibrium chlorite and/or K-feldspar are precipitated. This metasomatic 'cataclastically catalysed' dissolution-precipitation reaction mechanism has been outlined both theoretically and experimentally by *Wintsch*, [1975] and *Wintsch et al.*, [1995]. The reaction of muscovite + 6 quartz + 2K+ = 3 K-feldspar + 2 H^+ while classically occurring at ~600 °C and 200 MPa, conditions far higher than is found in the brittle field of the Alpine Fault, may occur at lower temperatures and pressures by chemical disequilibrium, increased surface area by cataclasis and the activity of key ions in the solution, allowing K-feldspar precipitation to occur at temperatures as low as ~250 °C. A similar reaction can occur with biotite in the place of muscovite. However, biotite only occurs in significant quantities within the Alpine Fault schists and mylonite sequence with most replaced through shallow alteration to chlorite in the FC / AZ [*Toy et al.*, 2015b; *Boulton et al.*, 2017a]. The 'feldspathization' reaction outlined above would not be able to take place in the schist / mylonite sequence due to the inability to maintain dis-equilibrium conditions over sufficient time scales that are possible in the PSZ ultracomminuted, low permeability, clay-rich gouges. The fluid-rock interactions of materials, particularly pseudotachylyte post-emplacement, may result in the

leaching/depletion of Fe, Mg, etc. and the subsequent enrichment of K. Observations of pseudotachylytes hosted in granitoid rocks by *Di Toro and Pennacchioni*, [2004] show K-rich coronas rimming 'spherulites', a feature attributed to fluid-rock interaction.

The above 'cataclastically catalysed' dissolution-precipitation reaction holds some similarities to field observations undertaken by *Green II et al.*, [2015]. On the principal slip surface of the Punchbowl Fault, California, USA, where ~15 µm diameter, porous, K-feldspar crystals containing nanoparticulates of quartz, albite, sphene and pyroxene were discovered. *Green II et al.*, [2015] speculate that K-feldspathic material grew authigenically, engulfing the gouge nanoparticles that were generated in the most recent slip event, protecting them from subsequent interseismic fluid-rock interaction.

An alternative hypothesis for the origin of the *Blue-CL clasts* implicates the K-enriched pseudotachylytes observed throughout the alteration zone. This is as follows: the initiation of coseismic slip within the fault zone causes rupture on a heterogeneous plane, on which high normal stresses at asperity contacts can generate frictional heating. During slip the host-rock is damaged while melt is generated and mobilised along the shearing surface and surrounding damage zone, forming injection veins. This melt is rapidly quenched once slip ceases, with the enhanced permeability of the host-rock, due to coseismic fracture damage, allowing the mobilisation of fluids around the solidified pseudotachylyte. Due to the rapid quenching, polygonal joints may be generated and represent preferential zones of weakness along which solidified melt fails brittely during successive deformation. These newly formed clasts are reworked into the cataclasite and gouge, and represent survivor clasts from a pseudotachylyte generated during seismic slip, and are variably altered by fluid-rock interactions and devitrification over time. Figure 5.17 is a schematic block diagram illustrating this process. Undeformed pseudotachylytes have not been observed within and in the immediate vicinity of the PSZ, perhaps indicating that melting is unlikely to occur along this slip zone. The energy required to dehydrate hydrous phyllosillicates within the PSZ and the preference for clays to undergo thermal pressurisation [*Faulkner et al.*, 2011], evidenced within the AF PSZ by gouge fluidisation and injection structures [*Boulton et al.*, 2015], would severely limit melt production. As such, pseudotachylyte clasts may be entrained in the PSZ gouge at greater depths on the fault where melting is more likely on a less mature, less altered, more competent and wider PSZ, with the clasts being repeatedly reworked within the developing gouge layer during exhumation of the fault.

The origin of clast *Types 1, 3* and *4* could be explained by the processes outlined above. *Types 1* and *3* have the most similarities with pseudotachylytes within the FC / AZ, including: a matrix of dominantly K-feldspathic composition with minor Mg and Fe content; inclusions of quartz, calcite and Ti-Oxides; and weak blue CL emissions. However, the FC / AZ pseudotachylyte matrices lack any observable crystallinity, as evidenced by the lack of indexed material through EBSD, in marked contrast to the *Type 1* clast. *Type 4* clasts, lacking the blue CL signal of *Types 1* and *3*, could have the potential for being a candidate for the 'cataclastically catalysed' dissolution-precipitation reaction. The presence of quartz clasts with subgrains and crystal lattice distortion in the *Type 4* clast also indicates that no annealing during entrainment in a frictional induced melt took place, which appears to have occurred in other quartz survivor clasts within definite pseudotachylytes, Figure SM 5.6.

Figure 5.17 –

caption overleaf.

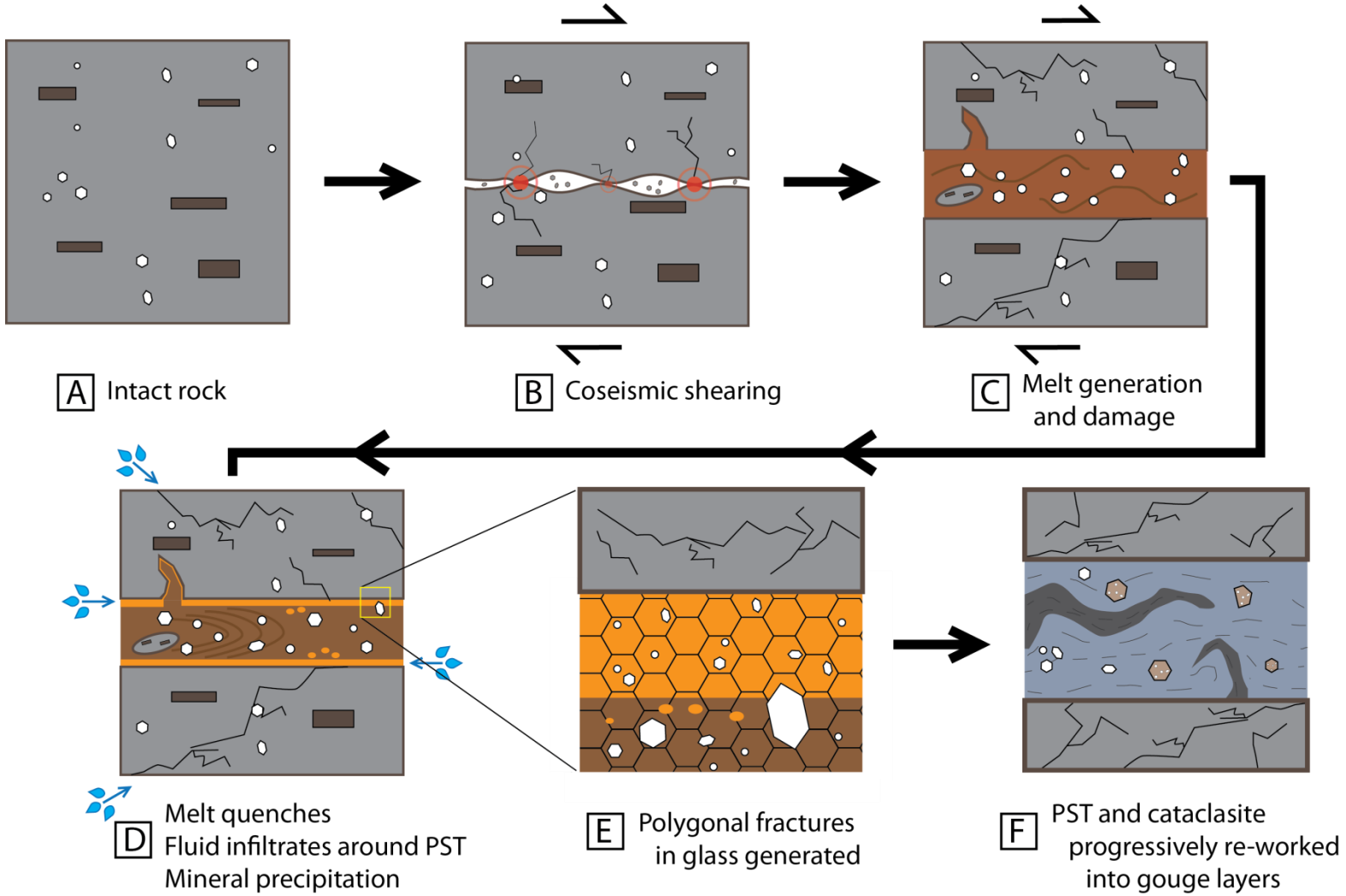

Figure 5.17 – (above) *Schematic block illustration of the stages involved in the generation of microstructures detailed in Figures 5.15 and 5.16.* ***[A]*** *The intact rock (ultramylonite, cataclasite, gouge etc.)* ***[B]*** *Coseismic shearing initiates causing a rupture on a heterogeneous plane upon which asperities contact and generate frictional heating.* ***[C]*** *The host rock is damaged during rupture and melt is generated from volatile minerals and mobilised incorporating host-rock fragments and more refractory mineral clasts.* ***[D]*** *The melt is rapidly quenched once slip ceases, by dissipation of heat into the host-rock. Fracturing in the host rock increases permeability and fluids are mobilised around the site of the pseudotachylyte, allowing precipitation of secondary minerals and alteration of the glass.* ***[E]*** *Due to this rapid quenching of the melt polygonal joints are generated upon which the glass preferentially breaks upon during subsequent deformation.* ***[F]*** *These clasts are reworked into cataclasite and gouge material and are variably altered by fluid-rock interactions and devitrification over time.*

This annealing of quartz in association with pseudotachylyte generation has been observed in natural specimens by *Bestmann et al.*, [2012]. *Type 2*, appears mostly likely to be a K-feldspar incorporated into PSZ gouges from the footwall granitoids, its optical properties matching that of K-feldspar, with its blue CL likely due to any number of the CL activators described above.

5.5.3. Implications for fault processes

As previously mentioned, the generation of frictional melt and nanoparticulates on a fault surface could potentially act as lubricant. However, it has also been proposed that the solidification of melt within fault zones could be a mechanism in which faults recover strength postseismicity**.** A number of studies speculate that once melt is transported and distributed across a sliding surface and solidifies, the surfaces will be locally welded together [*Di Toro et al.*, 2005; *Rice*, 2006; *Mitchell et al.*, 2016], hindering reactivation of the slip surface or encouraging the migration of slip surfaces in subsequent slip events [*Chester and Chester*, 1998]. This restrengthening hypothesis is supported by experimental work performed by *Mitchell et al.*, [2016] in which triaxial deformation strength tests were performed on intact rock, saw-cut samples, and pseudotachylyte bearing rock. These experiments showed that pseudotachylyte welded rock and intact rock had comparable cohesive strength. There is also experimental evidence suggesting that the initiation of

melting at asperity contacts is accompanied by an abrupt increase in frictional strength, potentially arresting slip before the transition to macroscopic melting occurs [*Tsutsumi and Shimamoto*, 1997; *Hirose and Shimamoto*, 2005]. However, this may only be true for cohesive rocks at low normal stresses, <10 MPa, at higher normal stresses, >25 MPa, the increase in frictional strength with asperity melting may no longer occur as evidenced in experiments by *Violay et al.*, [2014a, 2014b].

The length-scale over which natural pseudotachylytes form is an important factor when considering the above. Rupture surfaces may locally weld together but if the remainder of the fault remains free these sites of increased strength will likely be overcome by the rupture and associated weakening mechanisms. In regards to the Alpine Fault pseudotachylyte, they occur distributed throughout the fault core, indicating that zones of rupture migrate within it, or are active simultaneously, each accommodating increments of displacement, perhaps indicating that solidified melt locally welds material until broad cataclasis of the rock mass results in the reworking of the pseudotachylyte into the cataclastic matrix.

A transitioning of weakening mechanisms and the manner in which slip was accommodated within the principal slip zone with exhumation likely took place: frictional melting in the more competent, dryer rock below and about the Brittle – Viscous transition; transitioning to cataclastic flow, generating gouges and nanoparticulates, and thermal pressurisation at intermediary depths (4 – 7 km); and finally with propagation of an Alpine Fault rupture occurring through steady-state slip on weak phyllosillicates at shallower crustal levels (0 – 4 km). Pseudotachylytes both within the PSZ and in the encompassing ultramylonites are entrained into the increasingly widening FC / AZ with exhumation, being either destroyed / altered into the cataclastic material, becoming unrecognisable or more rarely preserved as fragmented survivor clasts as observed in the microstructures detailed above; see Figure 5.18 for an illustration and explanation of this process.

Both *Warr et al.*, [2003] and *Toy et al.*, [2011] infer from field and microstructural studies that pseudotachylytes in the Alpine Fault are not voluminous enough to account for all the increments of slip on the Alpine Fault and that the observed pseudotachylytes preserve moderate magnitude events ($3 < M_w < 6$), which include foreshock and aftershock events of larger earthquakes. *Toy et al.*, [2011] concluded that thermal pressurisation and granular fluidisation are more important dynamic weakening mechanisms than frictional melt during large magnitude Alpine Fault events.

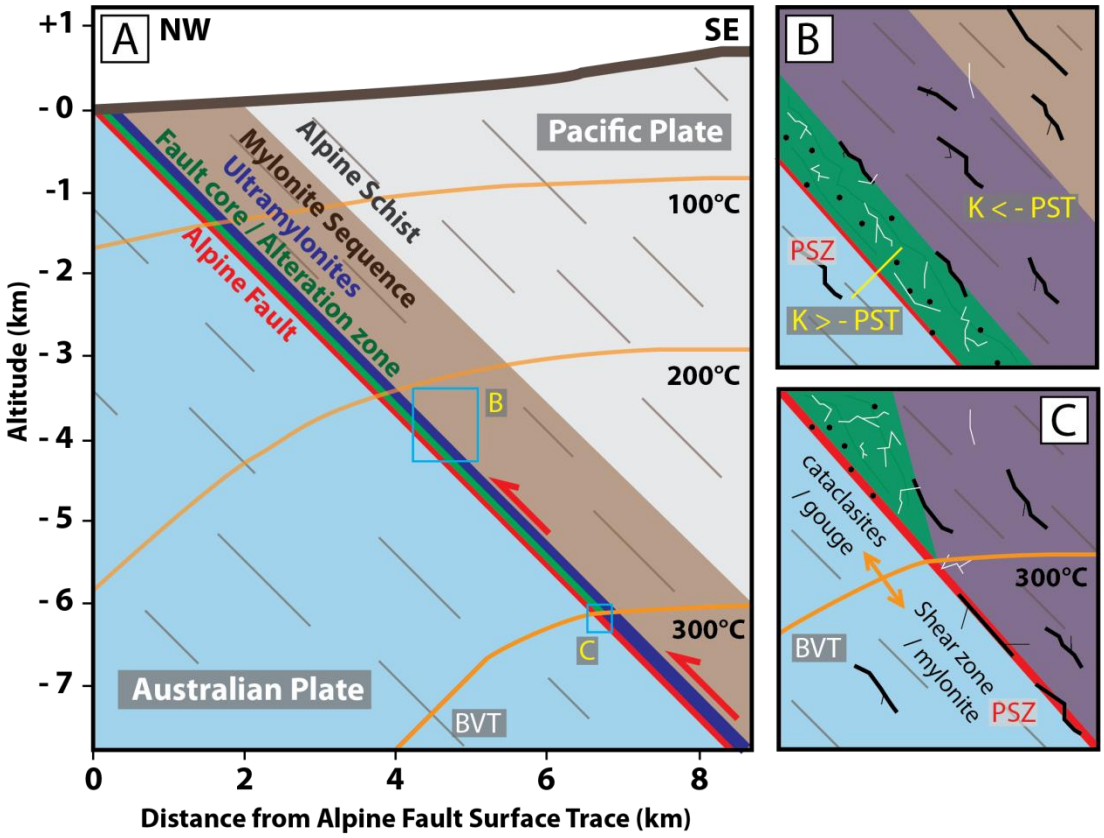

Figure 5.18 – [A] *Schematic illustration of the Alpine Fault Zone in the upper crust, showing the fault rock lithological sequence and geothermal gradient after Toy et al.*, [2010]**.** *The red marker denotes the plate boundary fault between the Pacific and Australian Plate; the green marker the onset of cataclasis and alteration in the fault core above the BVT , ~30 m thick; and the purple marker denotes the ultramylonite zone, ~150 m thick, through which the fault core transitions into the fault damage zone.* ***[C]*** *Magnified view of the fault zone at the BVT, highlighted in (**A**). The Black marks represent areas of PST generation and preservation; the black dots represent reworked PST within the FC / AZ; and the white marks represent mineralised fractures, predominantly filled with calcite and quartz. It is inferred that PST was generated upon the PSZ below the BVT within the localised, viscous shear zone. As gouge generation on the PSZ initiated around the BVT, PST generation on the PSZ was restricted by other dynamic weakening processes, such as thermal pressurisation. The PST on the PSZ is progressively reworked in the PSZ gouge and appears now as fragmented clasts.* ***[B]*** *Magnified view of the fault zone at the cut off depth of PST generation as estimated by Toy et al.*, [2011]*, highlighted in (**A**).PST are progressively reworked in the FC / AZ cataclasites and overprinted by mineralised fractures and shears. Within the FC / AZ the PST is enriched in K in comparison to PST within the mylonite sequence rocks, likely due to localised alteration reactions.*

5.6. Conclusions

1. Frictional melt appears to occur in the presence of fluid on the Alpine Fault, as evidenced by the cataclasis of calcite veins associated with pseudotachylyte, as well as the postseismic mineralisation of vesicles showing fluid-rock / melt interaction during and immediately prior to melt solidification and the overprinting of pseudotachylyte and surrounding host-rock by multiple generations of calcite veins.
2. As there is a lack of intact pseudotachylyte veins within and in the immediate vicinity of the PSZ it can be inferred that frictional melt did not occur during the most recent high magnitude Alpine Fault slip event. It is more likely that observed pseudotachylytes are reworked relicts from older Alpine Fault ruptures below the Brittle – Viscous transition, or rather aftershocks and smaller earthquakes off the principal slip zone that have produced pseudotachylytes, which have been subsequently incorporated into the widening alteration zone with exhumation.
3. The origin of the K-feldspathic clasts within the principal slip surfaces is currently uncertain. If these clasts are of pseudotachylyte origin, it can be inferred that the PSZ was capable of generating frictional melt at deeper crustal levels and that as the PSZ exhumed, matured and altered during the protracted history of seismicity, pseudotachylyte was entrained into the gouge layer. After entrainment subsequent devitrification and alteration results in microcrystalline clasts with entrained survivor nanoparticles. Alternatively the K-feldspathic material precipitated within the PSZ from a rock-buffered alkali solution, incorporating nanoparticulates during growth, could be a viable mechanism.
4. The presence of preserved nanoparticles within K-feldspathic clasts in the principal slip zone could indicate that the Alpine Fault produced nanoparticulates during increments of slip at greater depths without the production of melt. This could indicate a transition in weakening mechanisms with exhumation; frictional melting may occur in the more competent rock close to the Brittle – Viscous Transition, nanoparticulate-aided slip may be important at intermediate depths aided by thermal pressurisation, while cataclasis dominates at shallower crustal levels.

5.7. Further work

This study requires further work, particularly focused on the nature of the K-feldspathic PSZ clasts. TEM and /or XRD analyses, utilising characteristic Laue diffraction techniques, would be necessary in order to determine whether any amorphous material can be found in the K-feldspathic clasts, potentially clarifying whether they are of frictional melt origin or precipitated from isolated fluids in the PSZ. EBSD analyses are to be extended to the various PSZ clasts outlined above as well as the pseudotachylyte matrix throughout the FC / AZ. This will better our understanding of the ultracataclasis – pseudotachylyte transition and whether alteration and devitrification of amorphous pseudotachylyte material correlates with the cryptocrystalline PSZ clasts identified through EBSD. Image analyses, using ImageJ or similar software, are to performed on the pseudotachylyte and ultracomminuted survivor clasts populations; this is intended to give quantitative observations on grain sizes, clast : matrix ratio and clast roundness in order to inform on the behaviour of the material entraining these clasts, i.e. whether these clasts are a product of melt or comminution. This work has undergone some preliminary steps with pseudotachylyte survivor clast grain shape analyses; see Section SM 5.8.2 for a summary of this preliminary work. Fully quantitative chemistry could also performed, likely microprobe analyses, in order to fully understand the chemical make-up of the melts and clasts.

5.8. Supplementary material

5.8.1. Additional tables and figures

Table SM 5.1 – *Details of all the pseudotachylyte and related structures observed during this study, including: depth, lithology, description and techniques used during analysis. Available in the Digital Supplementary Materials included with this thesis.*

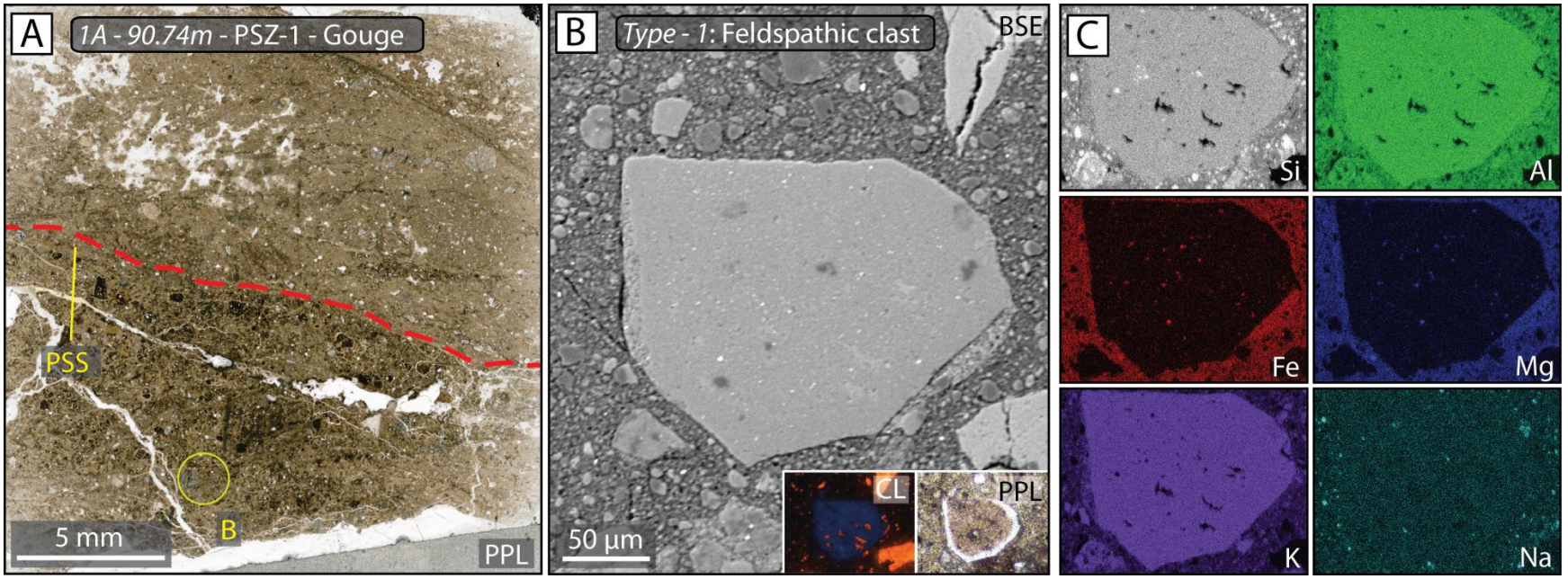

Figure SM 5.1 – [A] *Ultracomminuted gouge (1A-90.74m – Unit 5) within PSZ-1, containing a principal slip surface (PSS).* ***[B]*** *Type 1: feldspathic clast exhibiting blue CL signal.* ***[C]*** *EDS maps of Type 1: feldspathic clast showing high Si, Al, K, low Mg and Fe and similar Na content relative to gouge hosting the clast. EDS map step size at 0.4 µm.*

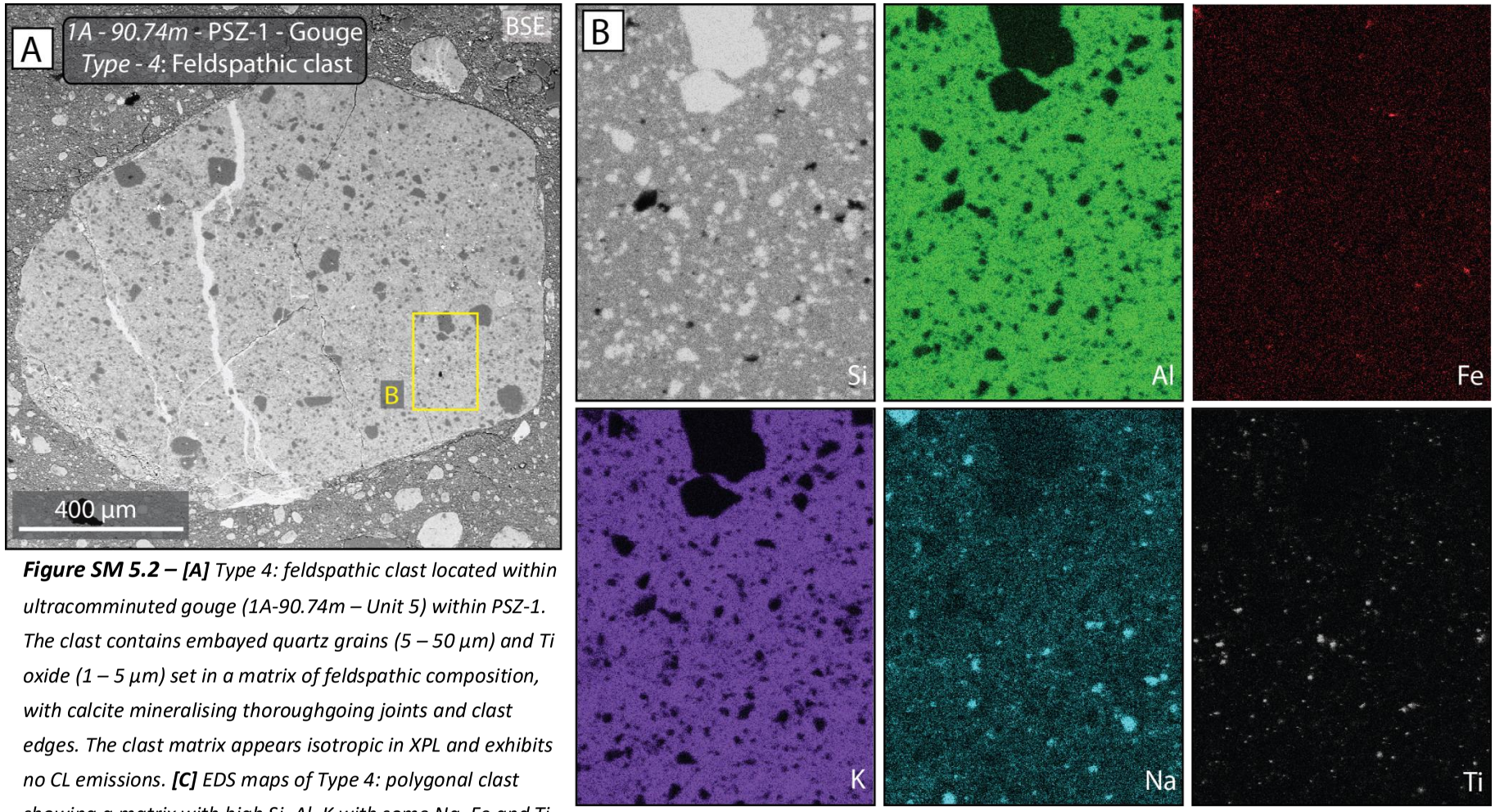

Figure SM 5.2 – [A] *Type 4: feldspathic clast located within ultracomminuted gouge (1A-90.74m – Unit 5) within PSZ-1. The clast contains embayed quartz grains (5 – 50 µm) and Ti oxide (1 – 5 µm) set in a matrix of feldspathic composition, with calcite mineralising thoroughgoing joints and clast edges. The clast matrix appears isotropic in XPL and exhibits no CL emissions.* ***[C]*** *EDS maps of Type 4: polygonal clast showing a matrix with high Si, Al, K with some Na, Fe and Ti. EDS map step size at 0.3 µm.*

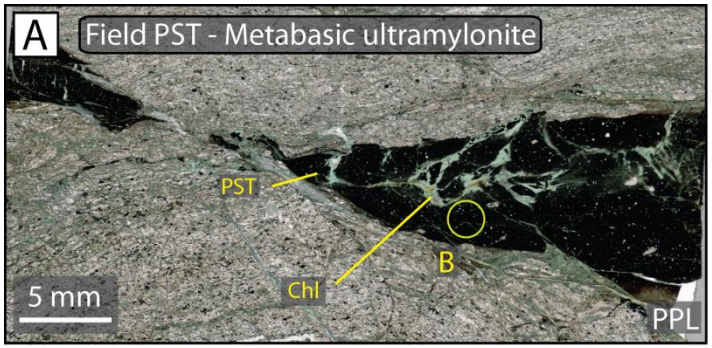

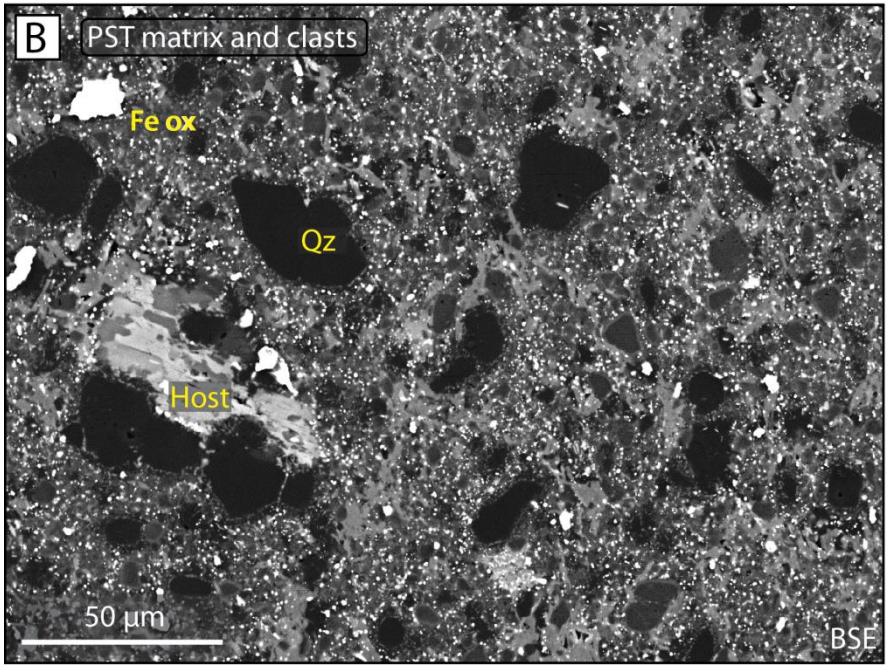

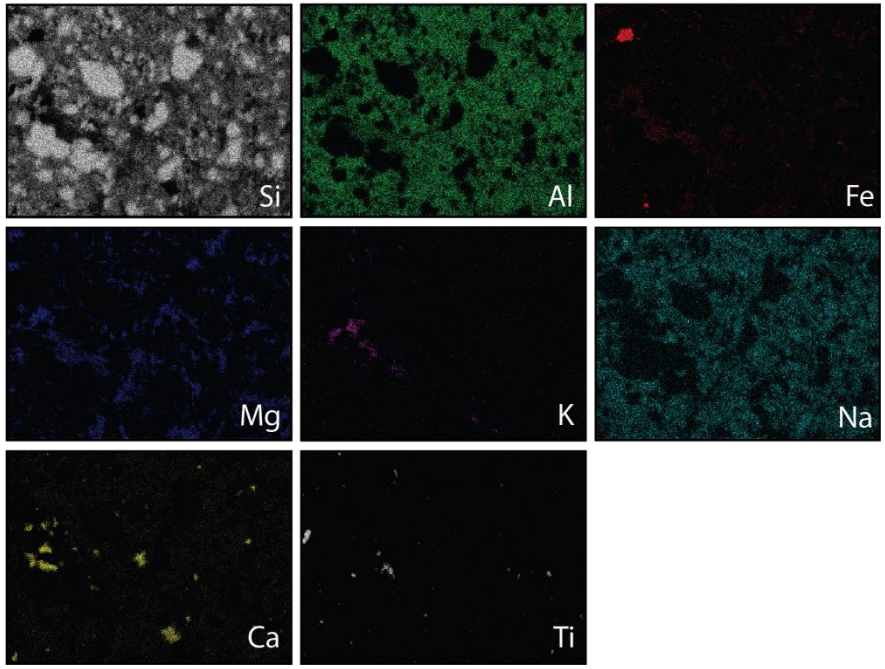

Figure SM 5.3 – [A] *A hanging wall metabasic ultramylonite acquired from float at Cataclasite Creek / Little Man River. Pseudotachylyte is a bounded and cross-cut by chlorite veins.* ***[B]*** *BSE images and EDS images show Al / Na-rich melt with abundant Fe oxides and Ti droplets. EDS map step size at 0.4 µm. (**B**) has been rotated 90° from (**A**).*

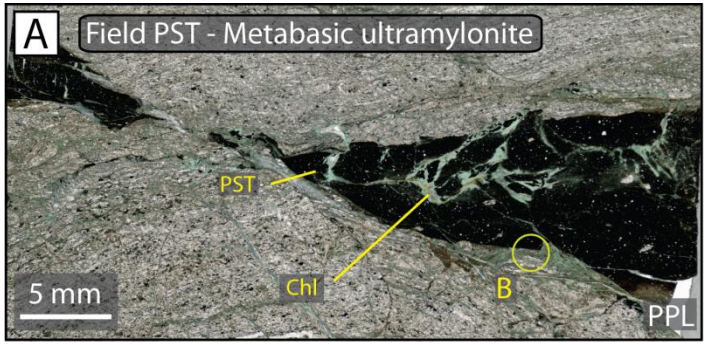

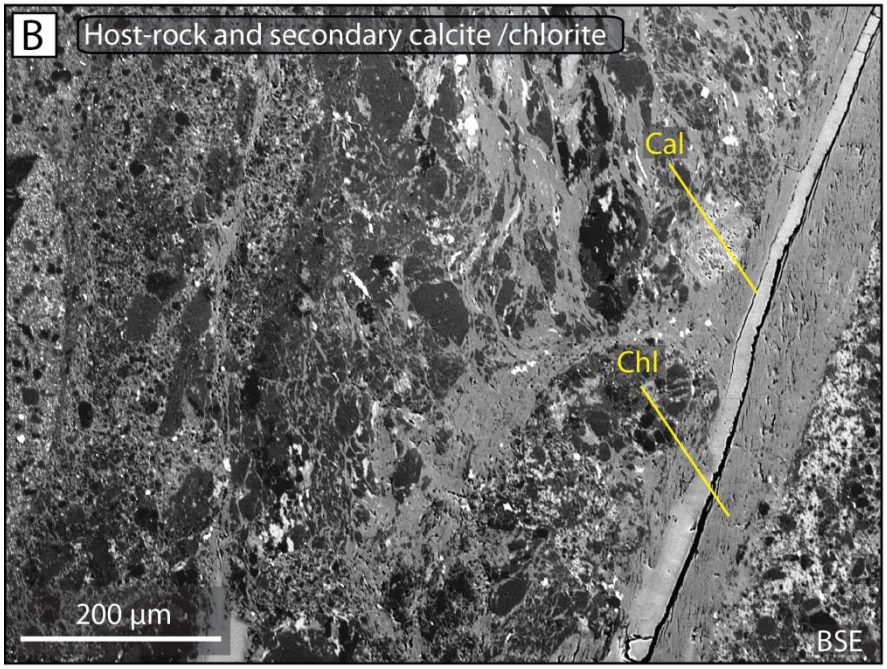

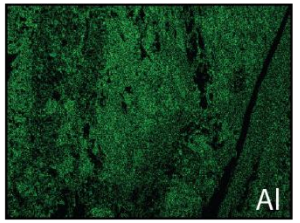

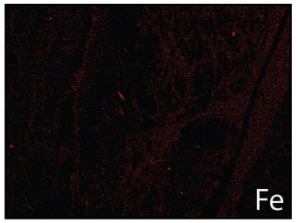

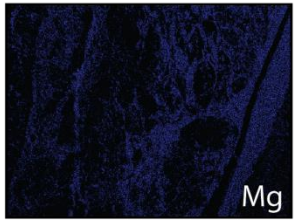

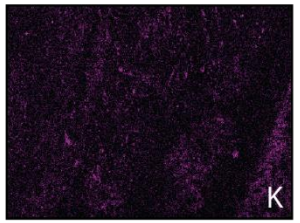

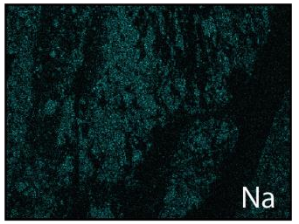

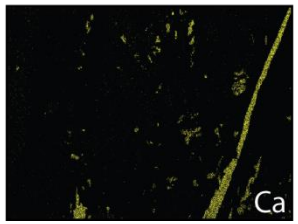

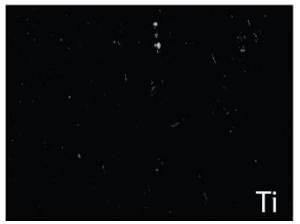

Figure SM 5.4 – [A] *A hanging wall metabasic ultramylonite acquired from float at Cataclasite Creek / Little Man River. Pseudotachylyte is a bounded and cross-cut by chlorite veins.* ***[B]*** *BSE images and EDS images show a chlorite-calcite vein bounding the edge of the pseudotachylyte. EDS map step size at 1.7 µm. (**B**) has been rotated 90° from (**A**).*

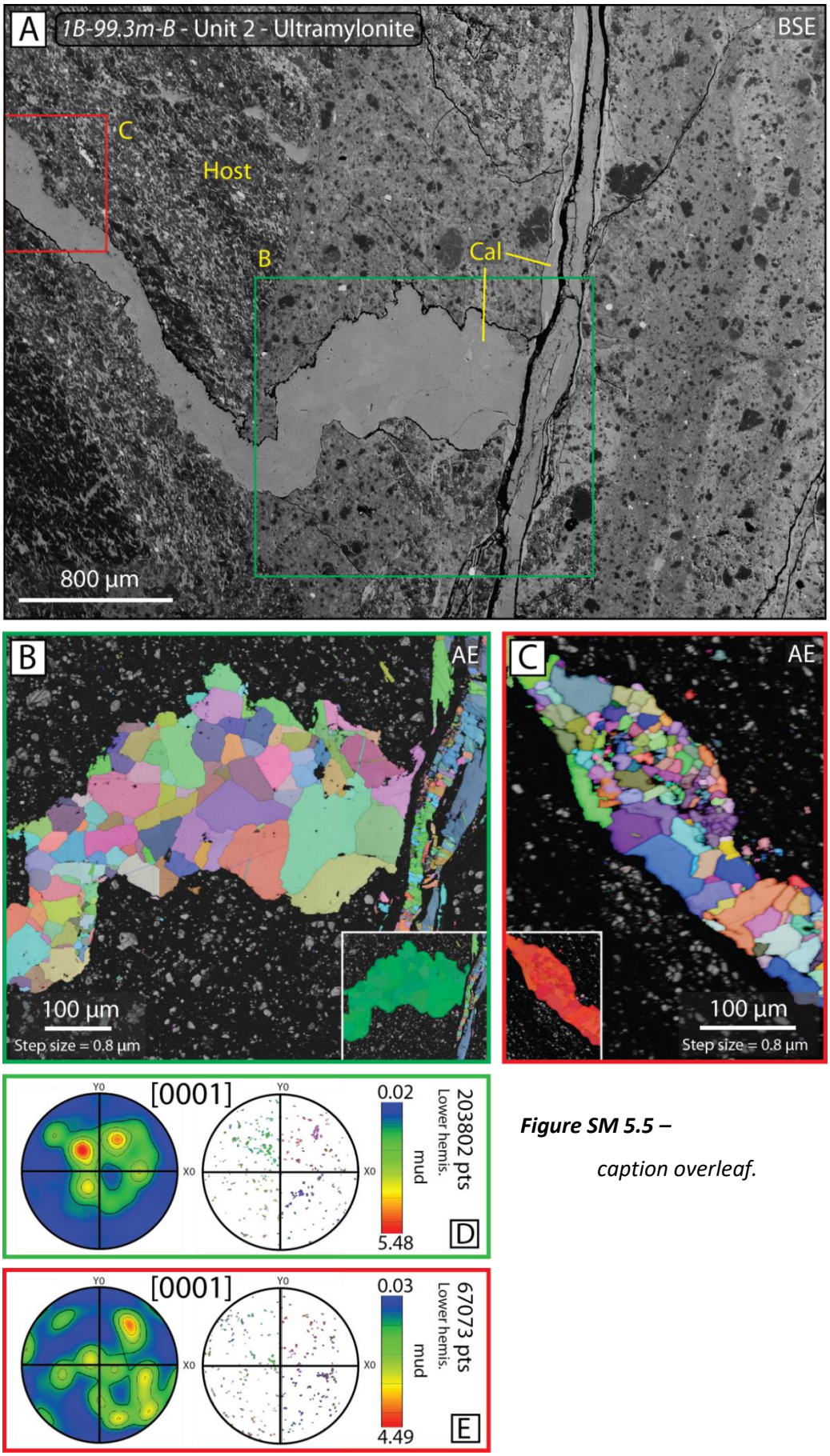

Figure SM 5.5 –

caption overleaf.

Figure SM 5.5 – *(above)* ***[A]*** *BSE image of a pseudotachylyte margin and calcite vein from a hanging wall ultramylonite (1B-99.3m-B – Unit 2) 29.14 m above the upper PSZ. This ultramylonite is heavily cataclased with planes of ultracomminuted material, pseudotachylyte and calcite veins.* ***[B]*** *An AE EBSD map of a calcite vein cutting through the host-rock and pseudotachylyte margin, the region is highlighted in (**A**). The calcite vein-infill has blocky-equant grains with very little twinning and no crystal lattice distortion, indicating little deformation.* ***[B]*** *An AE EBSD map of a calcite vein cutting through the host-rock and pseudotachylyte margin, the region is highlighted in (**A**). The portion of the calcite vein within the host-rock is similarly blocky-equant, has little twinning and no crystal lattice distortion, with the only difference being a smaller grain size.* ***[D and E]*** *PFs of areas highlighted in (**B**) and (**C**), respectively, show a large spread in crystallographic orientations in the calcite vein-infill.*

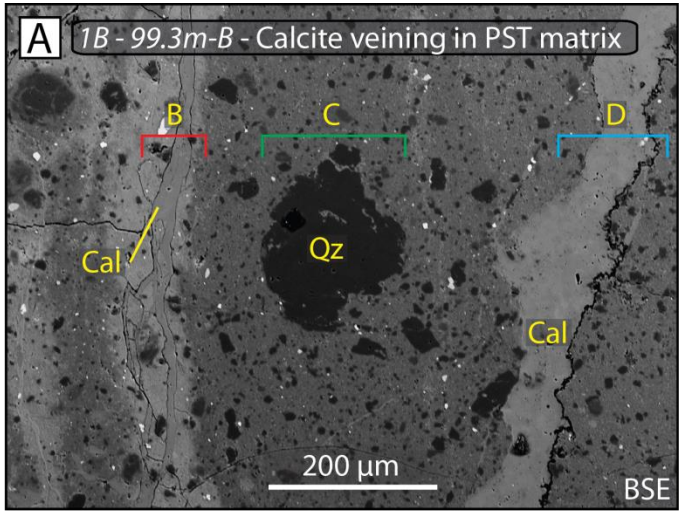

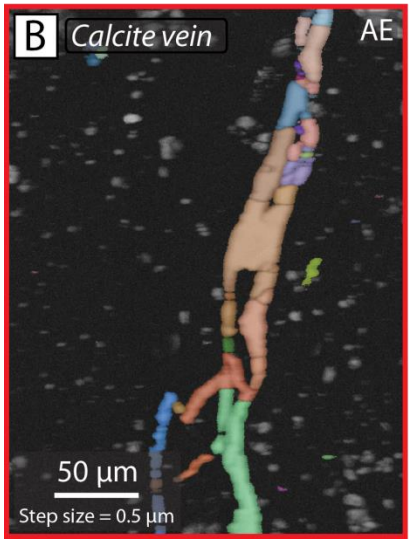

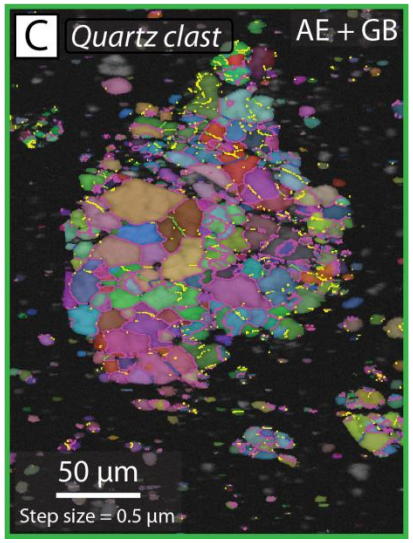

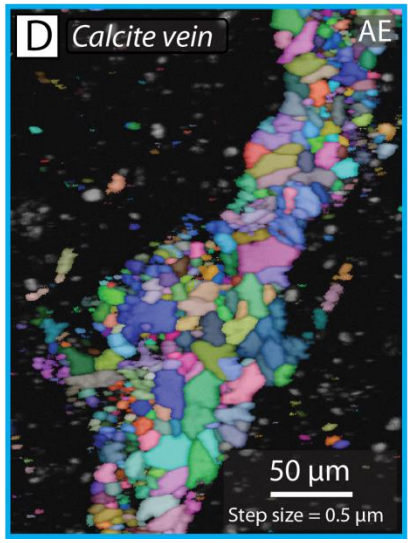

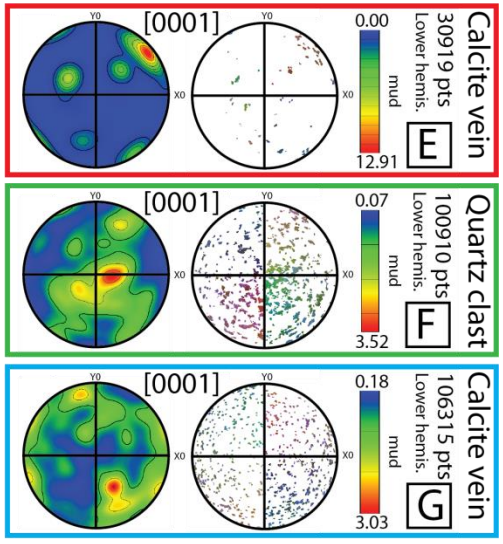

Figure SM 5.6 – [A] *BSE image of a pseudotachylyte matrix and calcite veins from a hanging wall ultramylonite (1B-99.3m-B – Unit 2) 29.14 m above the upper PSZ. This ultramylonite is heavily cataclased with planes of ultracomminuted material, pseudotachylyte and calcite veins.* ***[B]*** *An AE EBSD map of a calcite vein associated with a Fe- / Mg-rich band in the pseudotachylyte matrix, see Figure 5.8 for EDS maps.* ***[D]*** *An AE EBSD map of a calcite vein associated with a K- / Si-rich band in the pseudotachylyte matrix. Both calcite veins in (**B**) and (**D**) show no evidence of twinning or crystal lattice distortion and show blocky-equant grain shapes.* ***[C]*** *An AE EBSD map of a quartz survivor clast showing equant grains with no crystal lattice distortion and no evidence of recrystallisation or subgrains, potentially indicating annealing in a high temperature melt. (Grain Boundaries: >2° = yellow, >5° = green, >10° = blue and >15° = purple).* ***[E – G]*** *PFs of the microstructures shown in (**B**), (**C**), (**D**); colours correspond to respective image.*

5.8.2. Grain shape analyses

Preliminary grain shape analyses were undertaken on pseudotachylyte survivor clasts, predominantly quartz with minor plagioclase, using backscatter electron (BSE) images and ImageJ image analysis software. BSE images visualise the compositional variation of a sample through the use of a greyscale, proportional to the atomic number of a sample with a brighter BSE intensity correlating with greater average atomic number and dark BSE intensity with lower average atomic number. Survivor clasts are dominantly quartz and plagioclase feldspars their BSE intensity is dark in comparison to the pseudotachylyte matrix, secondary calcite mineralisation and Fe – Ti oxides. The colour thresholding tool in ImageJ was then used to separate regions of the image based on intensity variation between pixels, in this case greyscale. A pixel intensity threshold range was then chosen, allowing the rejection of all pixels that did not correspond with a survivor clast, generating a monochrome image highlighting the survivor clasts, see Figures SM 5.7B and SM 5.8B. This monochrome image is then analysed using the ImageJ grain shape analysis tool allowing the calculation of the grain area and circularity. Circularity is a measure of how circular a grain is according to the following; circularity = 4π (area / perimeter^2), with a value of 1 indicating a perfect circle and a value approaching 0 being an increasingly elongate polygon. The results of these analyses are presented in Table SM 5.2., with results suggesting the survivor grains are largely circular. Further analyses using the Image software will be undertaken to calculate roundness of survivor clasts and how this relates to melt behaviour in the Alpine Fault.

Table SM 5.2 – *Table showing the results of preliminary grain shape analyses of pseudotachylyte survivor clasts shown in Figures SM 5.7 and 5.8. Available in the Digital Supplementary Materials included with this thesis.*

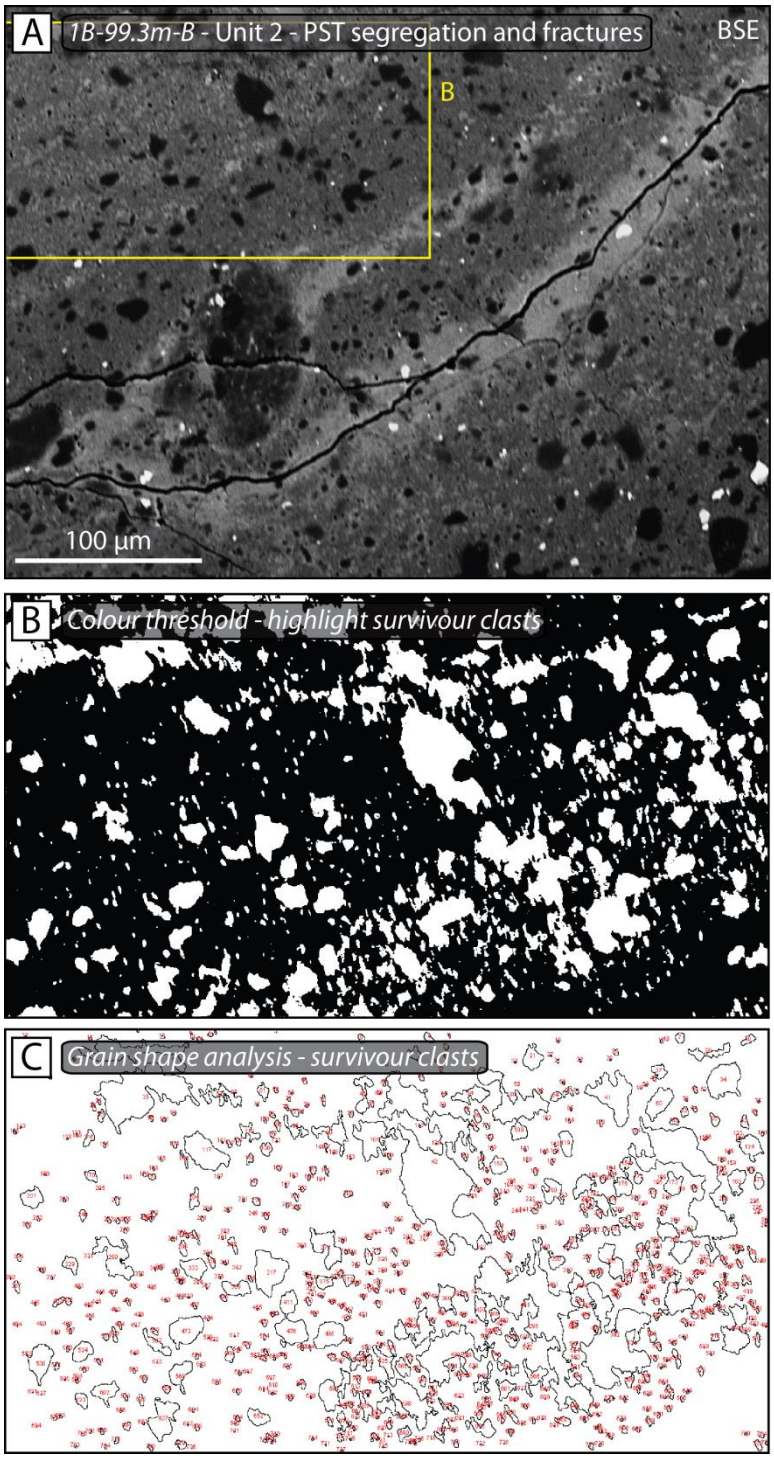

Figure SM 5.7 – [A] *BSE image of a region in the pseudotachylyte from 1B-99.3m-B, chosen as a preliminary site for survivor clast grain shape analysis.* ***[B]*** *Region of pseudotachylyte highlighted in (**A**). Colour thresholding in ImageJ allows the differentiation of material of different compositions using the BSE greyscale image. Here the quartz survivor clasts, darkest grey in BSE, have been highlighted.* ***[C]*** *Image showing the grain shapes determined by the ImageJ software, numbering refers to clast number in Table SM 5.2.*

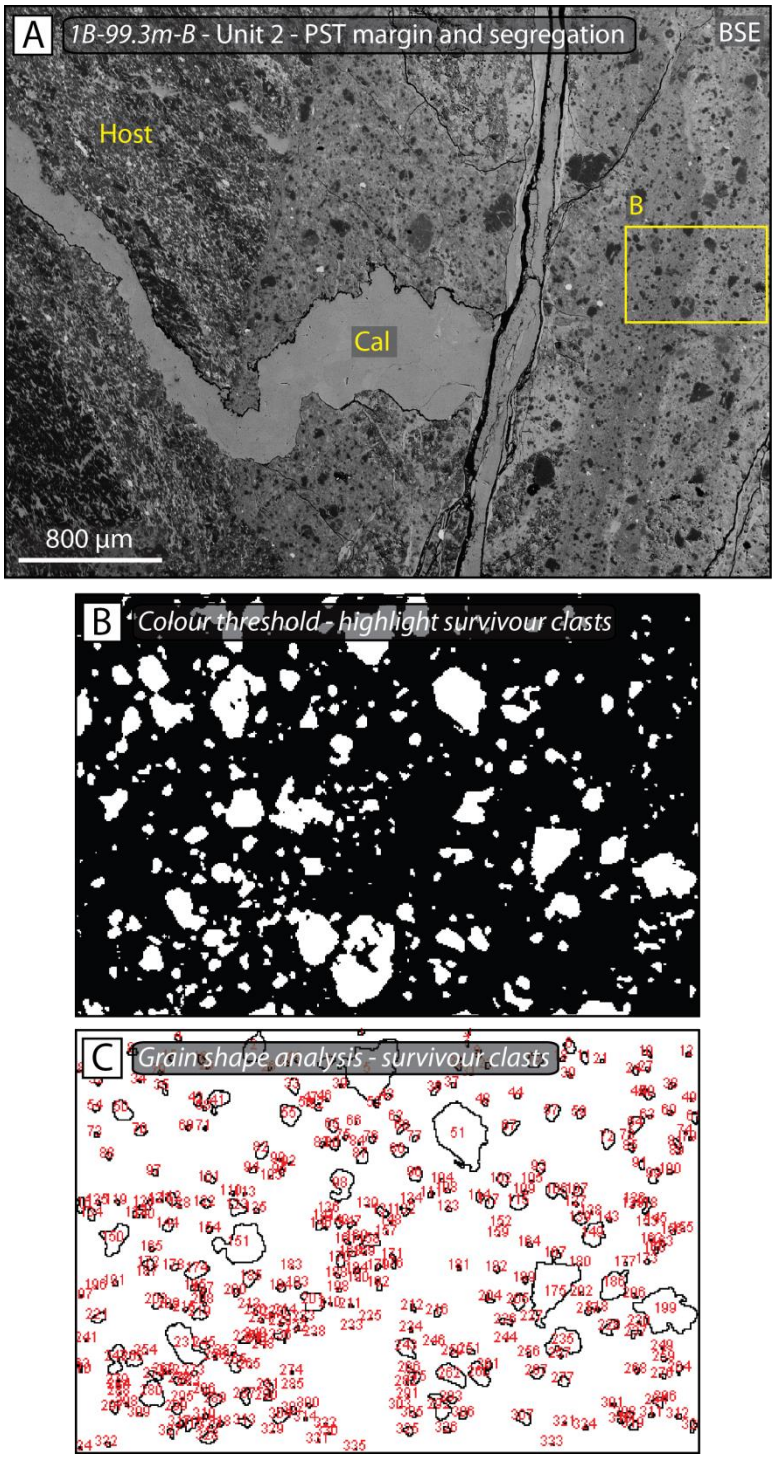

Figure SM 5.8 – [A] *BSE image of a region in the pseudotachylyte from 1B-99.3m-B, chosen as a preliminary site for survivor clast grain shape analysis.* ***[B]*** *Region of pseudotachylyte highlighted in (**A**). Colour thresholding in ImageJ allows the differentiation of material of different compositions using the BSE greyscale image. Here the quartz survivor clasts, darkest grey in BSE, have been highlighted.* ***[C]*** *Image showing the grain shapes determined by the ImageJ software, numbering refers to clast number in Table SM 5.2.*

6. Conclusions

The following chapter summarises the main conclusions presented in *Chapters 3*, *4* and *5*, and their implications on processes occurring within the Alpine Fault Zone throughout its seismic cycle.

The suite of experimental measurements, presented in *Chapter 3,* shows that a zone of low permeability and low seismic velocity material bounds the PSZ of the Central Alpine Fault, i.e. fault core / alteration zone (FC / AZ), under conditions approximating depths of 5 – 6 km. Measurements performed on protolith lithologies show lower permeabilities and higher seismic velocities than the fault-damaged rock, owing to their intact, unfractured nature. Low permeabilities at low experimental pressures are explained by the presence of fine grained alteration products and carbonate precipitation within the fracture networks of the fault hanging wall, that seal porosities in the fault core up to 2 – 10 %, estimate based on modal proportion filled fractures. The PSZ is predominantly composed of ultrafine-grained gouges and alteration products, and therefore acts as a barrier to cross-fault fluid flow postseismicity.

During interseismic periods fluid flow is likely concentrated outside the FC / AZ, within the damage zone. The damage zone fractures are likely to remain open for long time scales or potentially indefinitely, allowing the flow of meteorically derived hydrothermal fluids above the contact of the damage zone and FC / AZ, manifesting at the surface as hot springs. Within the FC / AZ, pervasive, unconsolidated gouge-filled fracture networks are progressively mineralized and altered, reducing along-fault communication of pore fluid. With fluid focusing along these fracture networks, fault rock fabrics have little influence on permeability anisotropy. In addition, as the cataclastic microstructures are so variable on a mm – cm scale, their overall effect within the fault zone is to homogenize seismic velocities, limiting seismic anisotropy. The main microstructural controls on fault rock physical properties are throughgoing fractures, both gouge-filled and mineralized, which have a great effect on seismic wave speeds and fluid flow at the experimental specimen scale and likely to act as preferential fluid flow paths and planes of discontinuity in the Alpine Fault Zone as a whole.

From microstructural and geochemical observations on carbonate mineralisation in the Alpine Fault FC / AZ, as presented in *Chapter 4*, it is shown that the Alpine Fault FC / AZ is pervasively mineralised with carbonate precipitation, occurring predominantly as vein infill. Multiple fracture and sealing events have occurred on the fault, evidence for cyclical damage generation and recovery. The evidence of extensive fluid-rock interaction and the current low permeability state of the FC / AZ indicates that permeability of this rock volume is transient. This is inferred to be due to seismically-induced fractures and porosity generation, potentially from both large magnitude Alpine Fault earthquake events and moderate magnitude events elsewhere in the wider fault zone. Immediately postseismicity the mobilisation of fluid results in rapid mineralisation and fluid-rock interactions, which seal and restrengthen the fault until the next cycle of seismicity occurs.

The trace elements incorporated into calcite during precipitation were sourced from fluid-rock interactions between hydrothermal fluids and cataclased rock. The variation in trace element incorporation into the carbonate veins during formation is due to the variation in ambient conditions and alteration reactions, through fluid-rock interaction occurring in the FC / AZ between periods of fracture generation. In most cases, older vein generations contain more Fe and Mg, while younger generations and recrystallised regions contain more Mn, likely due to variation in temperature and pressure during precipitation as the fault hanging wall was exhumed. Increased Mg / Fe concentrations at the PSZ are potentially caused by enhanced fluid-rock interaction within the ultracomminuted gouges, where alteration to clay minerals during the exhumation of the fault occurs. Mn was likely sourced from the retrogressive breakdown of Mn-rich garnet while Mg and Fe are derived from low temperature transformations of biotite into chlorite to smectite and muscovite alteration, particularly in the PSZ.

Many of the FC / AZ veins are interpreted to be generated by hydrofracturing, where a hot fluid was pulsed through the FC / AZ during seismicity, via rapidly propagating dilatant fractures with some shear component. The sudden pressure drop during dilation would result in rapid supersaturation of the fluid and therefore in rapid precipitation, in the order of seconds, onto the fracture walls, evidenced by blocky grain shapes, weak shape preferred orientations, uniform chemistry of the calcite vein-infill and ‘floating’ wall-rock / older calcite fragments within it. These features are predominantly observed in younger generation veins. The lack of twinning, localised microshears in the most recent vein

generations indicate that there has been little deformation or strain accumulation in the alteration zone since the last period of seismicity. Older generations may have been similarly formed. However subsequent fluid-rock interaction and deformation has resulted in modification or sometimes obliteration of previous vein microstructures and chemistry.

The rare presence of oscillatory zoned vein calcite indicates that in some cases precipitation occurs over a longer time scale, with fluctuations in temperature, pressure or fluid-rock interactions, or any combination of the three, resulting in variations in calcite trace element incorporation rates. This could mean that, as well as rapid sealing occurring immediately after seismicity, there is a fraction of void space remaining open long enough to undergo slow sealing by calcite precipitation during the interseismic period. This sealing potentially over a period on the order of months to years, as inferred from in situ borehole studies on permeability evolution [*Xue et al.*, 2013], and the recovery of seismic wave velocities around recently active fault zones [*Peng and Ben-Zion*, 2006].

The evolution of fault rock microstructure with seismic shear and subsequent interseismic fluid-rock interaction has a great effect on the hydraulic and elastic properties of fault zones. This evolution is complex and cyclical, and potentially promotes rupture via dynamic coseismic processes such as thermal pressurization.

The study in *Chapter 5* details the occurrence of pseudotachylytes throughout the Alpine Fault FC / AZ cataclasites, predominantly as reworked, disassociated clasts, with intact pseudotachylyte veins constrained to the fault core / damage zone contact in the fractured ultramylonites. It has been previously theorised that the presence of fluid in the vicinity of a shearing plane would buffer temperature and/or cause thermal pressurisation, thus lowering normal stresses on the fault and inhibiting frictional melting [e.g. Sibson, 1973; Lachenbruch, 1980]. However, frictional melting is observed to occur in the presence of fluid on the Alpine Fault, evidenced by the cataclasis of calcite veins associated with pseudotachylyte, the mineralisation of vesicles showing fluid-rock / melt interaction during and immediately prior to melt solidification and the overprinting of pseudotachylyte and surrounding host-rock by multiple generations of calcite veins. Examples of natural pseudotachylytes potentially produced in fluid-rich environments have been reported by multiple workers, including; *Rowe et al.*, 2005; *Meneghini et al.*, 2010; *Ujiie et al.*, 2011.

As there is a lack of intact pseudotachylyte veins within and in the immediate vicinity of the PSZ it can be inferred that frictional melt did not occur during the most recent high magnitude Alpine Fault slip event. It is more likely that pseudotachylytes observed are reworked relicts from older Alpine Fault ruptures below the Brittle – Viscous Transition or rather aftershocks and smaller earthquakes off of the principal slip zone that have produced pseudotachylytes that have been subsequently incorporated into the widening alteration zone with exhumation.

The pseudotachylytes observed have an overall K-feldspathic composition but contain compositional segregations comprised of K / Si / Al-rich pseudotachylyte margins and Mg / Fe-rich and K / Si / Al-rich banding within the pseudotachylyte core. These K / Si / Al-rich bands exhibit a weak blue CL. Within the PSZ, ultracomminuted gouges containing sub – mm clasts that share similar characteristics with these pseudotachylytes exist. Such similarities include: a dominantly K-feldspathic composition with minor Mg and Fe content; the presence of nanoparticulates of quartz, calcite and Ti-oxides; and, in some cases, a blue CL. If these clasts are of pseudotachylyte origin, it can be inferred that the PSZ was capable of generating frictional melt at deeper crustal levels and that as the PSZ exhumed, matured and altered during the protracted history of seismicity pseudotachylyte was entrained into the gouge layer, with subsequent devitrification and alteration resulting in microcrystalline clasts with entrained survivor nanoparticles. Alternatively the precipitation K-feldspathic material within the PSZ from a rock-buffered alkali solution, incorporating nanoparticulates during growth, could be a viable mechanism. Further work is required to constrain the origin and nature of these materials.

The presence of preserved nanoparticles within K-feldspathic clasts in the PSZ could indicate that the Alpine Fault produced nanoparticulates during increments of slip at greater depths without the production of melt. This could indicate a transition in weakening mechanisms with exhumation; frictional melting may occur in the more competent rock close to the Brittle – Viscous Transition, nanoparticulate-aided slip may be important at intermediate depths and aided by thermal pressurisation, while cataclasis dominates at shallower crustal levels.

7. Future work

The studies presented in this thesis have allowed us to advance our understanding of the mechanics of the Alpine Fault Zone and the nature of the seismic cycle in mature plate boundary faults. However, it has also highlighted the scientific challenges that await us in future research of these topics. This section outlines potential avenues for future work for the thesis author and the Deep Fault Drilling Project (DFDP) as a whole.

Further constraints on the conditions and time scales of fracture mineralisation

The study presented in Chapter 4 of this thesis has shown the microstructural and geochemical character of carbonate mineralisation associated with seismic and interseismic processes on a major plate boundary fault. To truly understand the processes during which these features are formed, processes which vary considerably as evidenced by the wide range of structures and chemistries described, further constraints must be made on the ambient conditions during their formation. These key aspects include, but are not limited to: stress states; temperature; and the rate of precipitation. Estimation of the stresses imparted upon the calcite veins could be achieved through calcite twin paleo piezometry, allowing the comparison of the transient stresses imposed upon the calcite-bearing veins during successive periods of seismicity as well as with the modern regional stresses as determined from borehole and geophysical techniques. Temperature is another key factor, as it controls the fluid solubility of the carbonate as well as the partitioning of the trace elements into the precipitating carbonates. Temperatures could be constrained through the use the of chemical ratios of Ca and the trace metals within the calcite, specifically Sr/Ca and Mg/Ca. Using these ratios and estimated temperatures it is possible to calculate back to fluid chemistry, giving us a better understanding of fluid and temperature fluctuations during and between periods of seismicity. The rate of precipitation of calcite in conditions during and immediately post seismicity is key in improving our understanding of the time frame for the sealing and restrengthening of a fault and how this influences earthquake recurrence intervals. This would require better estimates on the rate of fluid flow and the magnitude of pressure drops during seismicity on the Alpine Fault and the effect these have on oversaturation and thus precipitation rates.

The occurrence and alteration of frictional melt in a mature plate boundary fault core

The study presented in Chapter 5 of this thesis described and highlighted the microstructural and chemical variations of cataclastically and frictionally derived structures within the Alpine Fault core. The aim of the study was to characterise the occurrence of frictional melt and provide evidence for frictional melt at shallow crustal conditions in the presence of fluid in highly pulverised rock. In order to strengthen this study a number of further lines of evidences need to be collected and presented, these include: undertaking TEM analyses on features where their formation is ambiguous, i.e. ultracataclasis or frictional melting, allowing the analysis of amorphous material and devitrification or alteration products; further microstructural evidence for coexistence of pseudotachylytes and calcite mineralisation is to be collected. Bolstered by these lines of evidence a better contribution could be made to the understanding of the formation and destruction of pseudotachylytes, their role in seismic faulting and their abundance in nature.

Future of the Alpine Fault and the Deep Fault Drilling Program

The material retrieved from shallow depths in the first phase of the Deep Fault Drilling Project has yielded a partial view on the shallow behaviour of the fault. In order to better understand this behaviour, particularly in the deeper locked sections of the fault where strain accumulation and seismic slip occurs, further phases, at greater depths, of the DFDP must be undertaken. If drilling operations were to reach their final objectives of reaching the Alpine Fault at depths of ~3 km the evolution of the mechanical properties and microstructure with exhumation could be better understood, particularly if an oriented suite of fault rock core could be retrieved. This coupled with determination of the magnitude and orientation of the principal stresses, pore fluid pressure, fluid chemistry and geophysical properties via wireline logging, through analyses undertaken during drilling, will further advance our understanding of the fault at depth.

8. References

Agarwal, B. K. (1991), *X-Ray Spectroscopy*, Springer Series in Optical Sciences, 2nd ed., Springer Berlin Heidelberg, Berlin, Heidelberg.

Ague, J. J. (2003), Fluid Flow in the Deep Crust, in *Treatise on Geochemistry*, pp. 195–228, Elsevier.

Allen, M. J., D. J. Tatham, D. R. Faulkner, E. Mariani, and C. Boulton (2017), Permeability and seismic velocity and their anisotropy across the Alpine Fault, New Zealand: an insight from laboratory measurements on core from the Deep Fault Drilling Project phase 1 (DFDP-1), *J. Geophys. Res. Solid Earth*, doi:10.1002/2017JB014355.

Allis, R. G., and Y. Shi (1995), New insights to temperature and pressure beneath the central Southern Alps, New Zealand, *New Zeal. J. Geol. Geophys.*, *38*(August), 585–592, doi:10.1080/00288306.1995.9514687.

Allis, R. G., R. . Henley, and A. F. Carman (1979), The thermal regime beneath the Southern Alps, in *The origin of the Southern Alps. Bulletin of the Royal Society of New Zealand*, edited by R. I. Walcott and M. M. Cresswell, pp. 79–85, Royal Society of New Zealand, Wellington, N.Z.

Anders, M. H., and D. V. Wiltschko (1994), Microfracturing, paleostress and the growth of faults, *J. Struct. Geol.*, *16*(6), 795–815, doi:10.1016/0191-8141(94)90146-5.

Andersen, T. B., K. Mair, H. Austrheim, Y. Y. Podladchikov, and J. C. Vrijmoed (2008), Stress release in exhumed intermediate and deep earthquakes determined from ultramafic pseudotachylyte, *Geology*, *36*(12), 995–998.

Arai, T., H. Tsukahara, and T. Morikiyo (2003), Sealing Process with Calcite in the Nojima Active Fault Zone Revealed from Isotope Analysis of Calcite, *J. Geogr. (Chigaku Zasshi)*, *112*(6), 915–925, doi:10.5026/jgeography.112.6_915.

Barber, D. J., and H.-R. Wenk (1979), Deformation twinning in calcite, dolomite, and other rhombohedral carbonates, *Phys. Chem. Miner.*, *5*(2), 141–165, doi:10.1007/BF00307550.

Barker, S. L. L., and S. F. Cox (2011), Oscillatory zoning and trace element incorporation in hydrothermal minerals: Insights from calcite growth experiments, *Geofluids*, *11*(1), 48–56, doi:10.1111/j.1468-8123.2010.00305.x.

Barker, S. L. L., S. F. Cox, S. M. Eggins, and M. K. Gagan (2006), Microchemical evidence for episodic growth of antitaxial veins during fracture-controlled fluid flow, *Earth Planet. Sci. Lett.*, *250*(1–2), 331–344, doi:10.1016/j.epsl.2006.07.051.

Barnes, I., C. J. Downes, and J. R. Hulston (1978), Warm springs, South Island, New Zealand, and their potentials to yield laumontite, *Am. J. Sci.*, *278*(10), 1412–1427, doi:10.2475/ajs.278.10.1412.

Barth, N. C., V. G. Toy, R. M. Langridge, and R. J. Norris (2012), Scale dependence of oblique plate-boundary partitioning: New insights from LiDAR, central Alpine fault, New Zealand, *Lithosphere*, *4*(5), 435–448, doi:10.1130/L201.1.

Barth, N. C., C. Boulton, B. M. Carpenter, G. E. Batt, and V. G. Toy (2013), Slip localization on the southern Alpine Fault, New Zealand, *Tectonics*, *32*(3), 620–640, doi:10.1002/tect.20041.

Bear, J. (1972), Dynamics of Fluids in Porous Media, *Soil Sci.*, *120*(2), 162–163, doi:10.1097/00010694-197508000-00022.

Beavan, J., P. Denys, M. Denham, B. Hager, T. Herring, and P. Molnar (2010), Distribution of present-day vertical deformation across the Southern Alps, New Zealand, from 10 years of GPS data, *Geophys. Res. Lett.*, *37*(16), n/a-n/a, doi:10.1029/2010GL044165.

Bedford, J. D. (2017), The kinetics and mechanics of a dehydrating system and the deformation of porous rock, University of Liverpool.

Ben-Zion, Y. (1998), Properties of seismic fault zone waves and their utility for imaging low-velocity structures, *J. Geophys. Res. Earth*, *103*(B6), 12567–12585, doi:10.1029/98JB00768.

Benninghoven, A., F. G. Rudenauer, and H. W. Werner (1987), *Secondary ion mass spectrometry: basic concepts, instrumental aspects, applications and trends*, John Wiley and Sons,New York, NY, United States.

Bernabe, Y. (1987), The effective pressure law for permeability during pore pressure and confining pressure cycling of several crystalline rocks, *J. Geophys. Res.*, *92*(B1), 649, doi:10.1029/JB092iB01p00649.

Bestmann, M., and D. J. Prior (2003), Intragranular dynamic recrystallization in naturally deformed calcite marble: Diffusion accommodated grain boundary sliding as a result of subgrain rotation recrystallization, *J. Struct. Geol.*, *25*(10), 1597–1613, doi:10.1016/S0191-8141(03)00006-3.

Bestmann, M., G. Pennacchioni, S. Nielsen, M. Göken, and H. de Wall (2012), Deformation and ultrafine dynamic recrystallization of quartz in pseudotachylyte-bearing brittle faults: A matter of a few seconds, *J. Struct. Geol.*, *38*(May 2012), 21–38, doi:10.1016/j.jsg.2011.10.001.

Birch, F. (1960), The velocity of compressional waves in rocks to 10 kilobars: 1., *J. Geophys. Res.*, *65*(4), 1083–1102, doi:10.1029/JZ065i004p01083.

Bjornerud, M., and J. F. Magloughlin (2004), Pressure-related feedback processes in the generation of pseudotachylytes, *J. Struct. Geol.*, *26*(12), 2317–2323, doi:10.1016/j.jsg.2002.08.001.

Blake, O. (2011), Seismic Transport Properties of Fractured Rocks, University of Liverpool.

Blanpied, M. L., D. A. Lockner, and J. D. Byerlee (1992), An earthquake mechanism based on rapid sealing of faults, *Nature*, *358*(6387), 574–576, doi:10.1038/358574a0.

Blenkinsopp, T. (2000), *Deformation Microstructures and Mechanisms in Minerals and Rocks*, Kluwer Academic Publishers, New York, Boston, Dordrecht, London, Moscow.

Bons, P. D. (2001), The formation of large quartz veins by rapid ascent of fluids in mobile hydrofractures, *Tectonophysics*, *336*(1), 1–17, doi:10.1016/S0040-1951(01)00090-7.

Bons, P. D., and M. Montenari (2005), The formation of antitaxial calcite veins with well-developed fibres, Oppaminda Creek, South Australia, *J. Struct. Geol.*, *27*(2), 231–248, doi:10.1016/j.jsg.2004.08.009.

Bons, P. D., M. A. Elburg, and E. Gomez-Rivas (2012), A review of the formation of tectonic veins and their microstructures, *J. Struct. Geol.*, *43*, 33–62, doi:10.1016/j.jsg.2012.07.005.

Borg, S., W. Liu, M. Pearce, J. Cleverley, and C. MacRae (2014), Complex mineral zoning patterns caused by ultra-local equilibrium at reaction, *Geology*, *42*(5), 415–418, doi:10.1130/G35287.1.

Bossière, G. (1991), Petrology of pseudotachylytes from the Alpine Fault of New Zealand, *Tectonophysics*, *196*(1–2), 173–193, doi:10.1016/0040-1951(91)90295-4.

Boulton, C., B. M. Carpenter, V. Toy, and C. Marone (2012), Physical properties of surface outcrop cataclastic fault rocks, Alpine Fault, New Zealand, *Geochemistry, Geophys. Geosystems*, *13*(1), 1–13, doi:10.1029/2011GC003872.

Boulton, C., C. D. Menzies, M. J. Allen, D. R. Faulkner, and E. Mariani (2015), Observations and implications of cyclical slip in DFDP-1 principal slip zone gouges, Alpine Fault, New Zealand, *EOS Trans. AGU Fall Meet. Suppl. Abstr.*, *T23D–66079*.

Boulton, C., C. D. Menzies, V. G. Toy, J. Townend, and R. Sutherland (2017a), Geochemical and microstructural evidence for interseismic changes in fault zone permeability and strength, Alpine Fault, New Zealand, *Geochemistry, Geophys. Geosystems*, *18*(1), 238–265, doi:10.1002/2016GC006588.

Boulton, C., L. Yao, D. R. Faulkner, J. Townend, V. G. Toy, R. Sutherland, S. Ma, and T. Shimamoto (2017b), High-velocity frictional properties of Alpine Fault rocks: Mechanical data, microstructural analysis, and implications for rupture propagation, *J. Struct. Geol.*, *97*, 71–92, doi:10.1016/j.jsg.2017.02.003.

Boulton, C. J., D. E. Moore, D. A. Lockner, V. G. Toy, J. Townend, and R. Sutherland (2014), Frictional properties of exhumed fault gouges in DFDP-1 cores, Alpine Fault, New Zealand, *Geophys. Res. Lett.*, *41*(2), 356–362, doi:10.1002/2013GL058236.

Brace, W. F. (1960), An extension of the Griffith theory of fracture to rocks, *J. Geophys. Res.*, *65*(10), 3477–3480, doi:10.1029/JZ065i010p03477.

Brace, W. F. (1972), Pore Pressure in Geophysics, *Flow Fract. Rocks; Geophys. Monogr. Ser. Vol. 16*, *16*, 265–273, doi:10.1029/GM016p0265.

Brace, W. F., J. B. Walsh, and W. T. Frangos (1968), Permeability of granite under high pressure, *J. Geophys. Res.*, *73*(6), 2225–2236, doi:10.1029/JB073i006p02225.

Brantut, N., A. Schubnel, J.-N. Rouzaud, F. Brunet, and T. Shimamoto (2008), High-velocity frictional properties of a clay-bearing fault gouge and implications for earthquake mechanics, *J. Geophys. Res. Solid Earth*, *113*(B10), n/a-n/a, doi:10.1029/2007JB005551.

Brantut, N., R. Han, T. Shimamoto, N. Findling, and A. Schubnel (2011), Fast slip with inhibited temperature rise due to mineral dehydration: Evidence from experiments on gypsum, *Geology*, *39*(1), 59–62, doi:10.1130/G31424.1.

Brantut, N., A. Schubnel, E. C. David, E. Héripré, Y. Guéguen, and A. Dimanov (2012), Dehydration-induced damage and deformation in gypsum and implications for subduction zone processes, *J. Geophys. Res. Solid Earth*, *117*(B3), n/a-n/a, doi:10.1029/2011JB008730.

Brenguier, F., M. Campillo, C. Hadziioannou, N. M. Shapiro, R. M. Nadeau, and E. Larose

(2008), Postseismic Relaxation Along the San Andreas Fault at Parkfield from Continuous Seismological Observations, *Science (80-.).*, *321*(5895), 1478–1481.

Britton, T. B., J. Jiang, Y. Guo, A. Vilalta-Clemente, D. Wallis, L. N. Hansen, A. Winkelmann, and A. J. Wilkinson (2016), Tutorial: Crystal orientations and EBSD — Or which way is up?, *Mater. Charact.*, *117*, 113–126, doi:10.1016/j.matchar.2016.04.008.

Brodsky, E. E., and H. Kanamori (2001), Elastohydrodynamic lubrication of faults, *J. Geophys. Res. Solid Earth*, *106*(B8), 16357–16374, doi:10.1029/2001JB000430.

Bucher, K., and M. Frey (2001), *Petrogenesis of Metamorphic Rocks*, 7th ed., Springer, Heidelberg.

Budiansky, B., and R. J. O'connell (1976), Elastic moduli of a cracked solid, *Int. J. Solids Struct.*, *12*(2), 81–97, doi:10.1016/0020-7683(76)90044-5.

Burkhard, M. (1993), Calcite twins, their geometry, appearance and significance as stress-strain markers and indicators of tectonic regime: a review, *J. Struct. Geol.*, *15*(3–5), 351–368, doi:10.1016/0191-8141(93)90132-T.

Burnley, P. C., H. W. Green, and D. J. Prior (1991), Faulting associated with the olivine to spinel transformation in Mg2GeO4 and its implications for deep-focus earthquakes, *J. Geophys. Res. Solid Earth*, *96*(B1), 425–443, doi:10.1029/90JB01937.

Caciagli, N. C., and C. E. Manning (2003), The solubility of calcite in water at 6–16 kbar and 500–800 °C, *Contrib. to Mineral. Petrol.*, *146*(3), 275–285, doi:10.1007/s00410-003-0501-y.

Caine, J. S., J. P. Evans, and C. B. Forster (1996), Fault zone architecture and permeability structure, *Geol.* , *24*(11), 1025–1028, doi:10.1130/0091-7613(1996)024<1025:FZAAPS>2.3.CO;2.

Campbell, J. R. (2002), Hydrothermal Alteration within the Alpine Fault Zone, University of

Otago.

Cande, S. C., and J. M. Stock (2004), Pacific—Antarctic—Australia motion and the formation of the Macquarie Plate, *Geophys. J. Int.*, *157*(1), 399–414.

Carpenter, B. M., H. Kitajima, R. Sutherland, J. Townend, V. G. Toy, and D. M. Saffer (2014), *Hydraulic and acoustic properties of the active Alpine Fault, New Zealand: Laboratory measurements on DFDP-1 drill core*.

Carter, N. L., A. K. Kronenberg, J. V Ross, and D. V Wiltschko (1990), Control of fluids on deformation of rocks, *Geol. Soc. London, Spec. Publ.*, *54*(1), 1–13.

Carter, R. M., and R. J. Norris (1976), Cainozoic history of southern New Zealand: An accord between geological observations and plate-tectonic predictions, *Earth Planet. Sci. Lett.*, *31*(1), 85–94, doi:10.1016/0012-821X(76)90099-6.

Chamberlain, C. ., M. . Poage, D. Craw, and R. . Reynolds (1999), Topographic development of the Southern Alps recorded by the isotopic composition of authigenic clay minerals, South Island, New Zealand, *Chem. Geol.*, *155*(3–4), 279–294, doi:10.1016/S0009-2541(98)00165-X.

Chen, J., X. Yang, Q. Duan, T. Shimamoto, and C. J. Spiers (2013a), Importance of thermochemical pressurization in the dynamic weakening of the Longmenshan Fault during the 2008 Wenchuan earthquake: Inferences from experiments and modeling, *J. Geophys. Res. Solid Earth*, *118*(8), 4145–4169, doi:10.1002/jgrb.50260.

Chen, X., A. S. Madden, B. R. Bickmore, and Z. Reches (2013b), Dynamic weakening by nanoscale smoothing during high-velocity fault slip, *Geology*, *41*(7), 739–742.

Chester, F. M., and J. S. Chester (1998), Ultracataclasite structure and friction processes of the Punchbowl fault, San Andreas system, California, *Tectonophysics*, *295*(1), 199–221, doi:10.1016/S0040-1951(98)00121-8.

Chester, F. M., and J. M. Logan (1986), Implications for mechanical properties of brittle faults from observations of the Punchbowl fault zone, California, *pure Appl. Geophys.*, *124*(1), 79–106, doi:10.1007/BF00875720.

Chester, F. M., J. P. Evans, and R. L. Biegel (1993), Internal structure and weakening mechanisms of the San Andreas Fault, *J. Geophys. Res.*, *98*(B1), 771, doi:10.1029/92JB01866.

Childs, C. (1986), The Measurement of Low Temperatures.pdf, University of London.

Christensen, N. I., and D. A. Okaya (2007), Compressional and Shear Wave Velocities in South Island, New Zealand Rocks and their Application to the Interpretation of Seismological Models of the New Zealand Crust, in *A Continental Plate Boundary: Tectonics at South Island, New Zealand*, pp. 123–155, American Geophysical Union.

Cnudde, V., and M. N. Boone (2013), High-resolution X-ray computed tomography in geosciences: A review of the current technology and applications, *Earth-Science Rev.*, *123*, 1–17, doi:10.1016/j.earscirev.2013.04.003.

Cochran, E. S., Y.-G. Li, P. M. Shearer, S. Barbot, Y. Fialko, and J. E. Vidale (2009), Seismic and geodetic evidence for extensive, long-lived fault damage zones, *Geology*, *37*(4), 315–318.

Collettini, C., C. Viti, S. A. F. Smith, and R. E. Holdsworth (2009), Development of interconnected talc networks and weakening of continental low-angle normal faults, *Geol.* , *37*(6), 567–570, doi:10.1130/G25645A.1.

Company, H. P. E. (2014), High Pressure Valves, Fittings and Tubing, *High Press. Equip.* Available from: www.HighPressure.com (Accessed 20 April 2004)

Cooper, A. F. (1970), Metamorphism, structure and postmetamorphic intrusives of the Haast River area, south Westland, New Zealand, University of Otago.

Cooper, A. F. (1972), Progressive metamorphism of metabasic rocks from the haast schist group of Southern New Zealand, *J. Petrol.*, *13*(3), 457–492, doi:10.1093/petrology/13.3.457.

Cooper, A. F. (1974), Multiphase deformation and its relationship to metamorphic crystallisation at Haast River, South Westland, New Zealand, *New Zeal. J. Geol. Geophys.*, *17*(4), 855–880, doi:10.1080/00288306.1974.10418230.

Cooper, A. F., and R. J. Norris (1994), Anatomy, structural evolution, and slip rate of a plate-boundary thrust: The Alpine fault at Gaunt Creek, Westland, New Zealand, *GSA Bull.*, *106*(5), 627–633.

Cooper, A. F., B. A. Barreiro, D. L. Kimbrough, and J. M. Mattinson (1987), Lamprophyre dike intrusion and the age of the Alpine fault, New Zealand, *Geol.* , *15*(10), 941–944, doi:10.1130/0091-7613(1987)15<941:LDIATA>2.0.CO;2.

Cox, S. C., C. D. Menzies, R. Sutherland, P. H. Denys, C. Chamberlain, and D. A. H. Teagle (2015), Changes in hot spring temperature and hydrogeology of the Alpine Fault hanging wall, New Zealand, induced by distal South Island earthquakes, *Geofluids*, *15*(1–2), 216–239, doi:10.1111/gfl.12093.

Craw, D. (1984), Ferrous-iron-bearing vermiculite-smectite series formed during alteration of chlorite to kaolinite, Otago Schist, New Zealand, *Clay Miner.*, *19*(4), 509–520.

Craw, D. (1997), Fluid inclusion evidence for geothermal structure beneath the Southern Alps, New Zealand, *New Zeal. J. Geol. Geophys.*, *40*(August), 43–52, doi:10.1080/00288306.1997.9514739.

Craw, D., and J. R. Campbell (2004), Tectonic and structural setting for active mesothermal gold vein systems, Southern Alps, New Zealand, *J. Struct. Geol.*, *26*(6–7), 995–1005, doi:10.1016/j.jsg.2003.11.012.

Craw, D., P. Upton, and D. J. Mackenzie (2009), Hydrothermal alteration styles in ancient

and modern orogenic gold deposits, New Zealand, *New Zeal. J. Geol. Geophys.*, *52*(1), 11–26, doi:10.1080/00288300909509874.

Cross, A. J., S. Kidder, and D. J. Prior (2015), Using microstructures and TitaniQ thermobarometry of quartz sheared around garnet porphyroclasts to evaluate microstructural evolution and constrain an Alpine Fault Zone geotherm, *J. Struct. Geol.*, *75*, 17–31, doi:10.1016/j.jsg.2015.02.012.

Davis, J. C. (2002), *Statistics and Data Analysis in Geology*.

De Bresser, J. H. P., and C. J. Spiers (1997), Strength characteristics of the r, f, and c slip systems in calcite, *Tectonophysics*, *272*(1), 1–23, doi:10.1016/S0040-1951(96)00273-9.

DeMets, C., R. G. Gordon, D. F. Argus, and S. Stein (1994), Effect of recent revisions to the geomagnetic reversal time scale on estimates of current plate motions, *Geophys. Res. Lett.*, *21*(20), 2191–2194, doi:10.1029/94GL02118.

Dempsey, E. D., D. J. Prior, E. Mariani, V. G. Toy, and D. J. Tatham (2011), Mica-controlled anisotropy within mid-to-upper crustal mylonites: an EBSD study of mica fabrics in the Alpine Fault Zone, New Zealand, *Geol. Soc. London, Spec. Publ.*, *360*(1), 33–47, doi:10.1144/SP360.3.

Denniston, R. F., C. K. Shearer, G. D. Layne, and D. T. Vaniman (1997), SIMS analyses of minor and trace element distributions in fracture calcite from Yucca Mountain, Nevada, USA, *Geochim. Cosmochim. Acta*, *61*(9), 1803–1818, doi:10.1016/S0016-7037(97)00049-5.

De Pascale, G. P., and R. M. Langridge (2012), New on-fault evidence for a great earthquake in A.D. 1717, central alpine fault, New Zealand, *Geology*, *40*(9), 791–794, doi:10.1130/G33363.1.

De Paola, N. (2013), Nano-powder coating can make fault surfaces smooth and shiny: implications for fault mechanics?, *Geology*, *41*(6), 719–720.

De Paola, N., T. Hirose, T. Mitchell, G. Di Toro, C. Viti, and T. Shimamoto (2011), Fault lubrication and earthquake propagation in thermally unstable rocks, *Geology*, *39*(1), 35–38, doi:10.1130/G31398.1.

Dieterich, J. H. (1978), Time-dependent friction and the mechanics of stick-slip, *pure Appl. Geophys.*, *116*(4), 790–806, doi:10.1007/BF00876539.

Dieterich, J. H. (1979), Modeling of rock friction: 1. Experimental results and constitutive equations, *J. Geophys. Res. Solid Earth*, *84*(B5), 2161–2168, doi:10.1029/JB084iB05p02161.

Di Toro, G., and G. Pennacchioni (2004), Superheated friction-induced melts in zoned pseudotachylytes within the Adamello tonalites (Italian Southern Alps), *J. Struct. Geol.*, *26*(10), 1783–1801, doi:10.1016/j.jsg.2004.03.001.

Di Toro, G., D. L. Goldsby, and T. E. Tullis (2004), Friction falls towards zero in quartz rock as slip velocity approaches seismic rates, *Nature*, *427*(6973), 436–439.

Di Toro, G., G. Pennacchioni, and G. Teza (2005), Can pseudotachylytes be used to infer earthquake source parameters? An example of limitations in the study of exhumed faults, *Tectonophysics*, *402*(1–4 SPEC. ISS), 3–20, doi:10.1016/j.tecto.2004.10.014.

Di Toro, G., G. Pennacchioni, and S. Nielsen (2009), *Pseudotachylytes and earthquake source mechanics*, 1st ed., Elsevier Inc.

Di Toro, G., R. Han, T. Hirose, N. De Paola, S. Nielsen, K. Mizoguchi, F. Ferri, M. Cocco, and T. Shimamoto (2011), Fault lubrication during earthquakes, *Nature*, *471*(7339), 494–498, doi:10.1038/nature09838.

Dixon, J. E., and T. H. Dixon (1989), Vesicles, amygdales and similar structures in fault-generated pseudotachylites - comment, *Lithos*, *23*(3), 225–227, doi:10.1016/0024-4937(89)90007-8.

Dromgoole, E. L., and L. M. Walter (1990), Iron and manganese incorporation into calcite: Effects of growth kinetics, temperature and solution chemistry, *Chem. Geol.*, *81*(4), 311–336, doi:10.1016/0009-2541(90)90053-A.

Eberhart-Phillips, D., and S. Bannister (2002), Three-dimensional crustal structure in the Southern Alps region of New Zealand from inversion of local earthquake and active source data, *J. Geophys. Res. Solid Earth*, *107*(B10), ESE 15-1-ESE 15-20, doi:10.1029/2001JB000567.

Eberhart-Phillips, D. (1995), Examination of seismicity in the central Alpine Fault region, South Island, New Zealand, *New Zeal. J. Geol. Geophys.*, *38*(4), 571–578, doi:10.1080/00288306.1995.9514685.

Eccles, J. D., A. K. Gulley, P. E. Malin, C. M. Boese, J. Townend, and R. Sutherland (2015), Fault Zone Guided Wave generation on the locked, late interseismic Alpine Fault, New Zealand, *Geophys. Res. Lett.*, *42*(14), 5736–5743, doi:10.1002/2015GL064208.

Eisenman, G. (1962), Cation Selective Glass Electrodes and their Mode of Operation, *Biophys. J.*, *2*(2), 259–323, doi:10.1016/S0006-3495(62)86959-8.

Evans, J. P., and F. M. Chester (1995), Fluid-rock interaction in faults of the San Andreas system: Inferences from San Gabriel fault rock geochemistry and microstructures, *J. Geophys. Res. Solid Earth*, *100*(B7), 13007–13020, doi:10.1029/94JB02625.

Evans, J. P., C. B. Forster, and J. V Goddard (1997), Permeability of fault-related rocks, and implications for hydraulic structure of fault zones, *J. Struct. Geol.*, *19*(11), 1393–1404, doi:10.1016/S0191-8141(97)00057-6.

Farrell, N. J. C., D. Healy, and C. W. Taylor (2014), Anisotropy of permeability in faulted

porous sandstones, *J. Struct. Geol.*, *63*, 50–67, doi:10.1016/j.jsg.2014.02.008.

Faulkner, D. R., and P. J. Armitage (2013), *The effect of tectonic environment on permeability development around faults and in the brittle crust*.

Faulkner, D. R., and E. H. Rutter (1998), The gas permeability of clay-bearing fault gouge at 20°C, *Geol. Soc. London, Spec. Publ.* , *147*(1), 147–156, doi:10.1144/GSL.SP.1998.147.01.10.

Faulkner, D. R., and E. H. Rutter (2000), Comparisons of water and argon permeability in natural clay-bearing fault gouge under high pressure at 20°C, *J. Geophys. Res. Solid Earth*, *105*(B7), 16415–16426, doi:10.1029/2000JB900134.

Faulkner, D. R., A. Lewis, and E. H. Rutter (2003), On the internal structure and mechanics of large strike-slip fault zones: field observations of the Carboneras fault in southeastern Spain, *Tectonophysics*, *367*(3), 235–251, doi:10.1016/S0040-1951(03)00134-3.

Faulkner, D. R., T. M. Mitchell, E. H. Rutter, and J. Cembrano (2008), On the structure and mechanical properties of large strike-slip faults, *Geol. Soc. London, Spec. Publ.* , *299*(1), 139–150, doi:10.1144/SP299.9.

Faulkner, D. R., C. A. L. Jackson, R. J. Lunn, R. W. Schlische, Z. K. Shipton, C. A. J. Wibberley, and M. O. Withjack (2010), A review of recent developments concerning the structure, mechanics and fluid flow properties of fault zones, *J. Struct. Geol.*, *32*(11), 1557–1575, doi:10.1016/j.jsg.2010.06.009.

Faulkner, D. R., T. M. Mitchell, J. Behnsen, T. Hirose, and T. Shimamoto (2011), Stuck in the mud? Earthquake nucleation and propagation through accretionary forearcs, *Geophys. Res. Lett.*, *38*(18), n/a-n/a, doi:10.1029/2011GL048552.

Faulkner D.R. (1997), The role of clay-bearing fault gouges in controlling fluid pressures in fault zones: implications for fault mechanics, University of Manchester.

Ferri, F., G. Di Toro, T. Hirose, and T. Shimamoto (2010), Evidence of thermal pressurization in high-velocity friction experiments on smectite-rich gouges, *Terra Nov.*, *22*(5), 347–353, doi:10.1111/j.1365-3121.2010.00955.x.

Ferri, F., G. Di Toro, T. Hirose, R. Han, H. Noda, T. Shimamoto, M. Quaresimin, and N. de Rossi (2011), Low- to high-velocity frictional properties of the clay-rich gouges from the slipping zone of the 1963 Vaiont slide, northern Italy, *J. Geophys. Res. Solid Earth*, *116*(B9), n/a-n/a, doi:10.1029/2011JB008338.

Ferrill, D. A., A. P. Morris, M. A. Evans, M. Burkhard, R. H. Groshong, and C. M. Onasch (2004), Calcite twin morphology: A low-temperature deformation geothermometer, *J. Struct. Geol.*, *26*(8), 1521–1529, doi:10.1016/j.jsg.2003.11.028.

Finch, A. A., and J. Klein (1999), The causes and petrological significance of cathodoluminescence emissions from alkali feldspars, *Contrib. to Mineral. Petrol.*, *135*(2), 234–243, doi:10.1007/s004100050509.

Folk, R. L. (1974), The natural history of crystalline calcium carbonate; effect of magnesium content and salinity, *J. Sediment. Res.*, *44*(1), 40–53.

Fortin, J., S. Stanchits, S. Vinciguerra, and Y. Guéguen (2011), Influence of thermal and mechanical cracks on permeability and elastic wave velocities in a basalt from Mt. Etna volcano subjected to elevated pressure, *Tectonophysics*, *503*(1–2), 60–74, doi:10.1016/j.tecto.2010.09.028.

Fritzke, B., J. Götze, and J.-M. Lange (2017), Cathodoluminescence of moldavites, *Meteorit. Planet. Sci.*, *52*(7), 1428–1436, doi:10.1111/maps.12852.

Fulton, P., E. Brodsky, Y. Kano, J. Mori, F. Chester, T. Ishikawa, R. Harris, W. Lin, N. Eguchi, and S. Toczko (2013), Low Coseismic Friction on the, *Science (80-.).*, (December), 1214–1217, doi:10.1126/science.1243641.

Fulton, P. M., D. M. Saffer, R. N. Harris, and B. A. Bekins (2004), Re-evaluation of heat flow

data near Parkfield, CA: Evidence for a weak San Andreas Fault, *Geophys. Res. Lett.*, *31*(15), n/a-n/a, doi:10.1029/2003GL019378.

Goldsby, D. L., and T. E. Tullis (2002), Low frictional strength of quartz rocks at subseismic slip rates, *Geophys. Res. Lett.*, *29*(17), 25-1-25–4, doi:10.1029/2002GL015240.

Goldstein, J. I., D. E. Newbury, P. Echlin, D. C. Joy, C. E. Lyman, E. Lifshin, L. Sawyer, and J. R. Michael (2003), *Scanning Electron Microscopy and X-ray Microanalysis*, Springer US, Boston, MA.

Gomila, R., G. Arancibia, T. M. Mitchell, J. M. Cembrano, and D. R. Faulkner (2016), Palaeopermeability structure within fault-damage zones: A snap-shot from microfracture analyses in a strike-slip system, *J. Struct. Geol.*, *83*, 103–120, doi:10.1016/j.jsg.2015.12.002.

Götze, J., and U. Kempe (2009), Physical Principles of Cathodoluminescence (CL) and its Applications in Geosciences, in *Cathodoluminescence and its Application in the Planetary Sciences*, edited by A. Gucsik, pp. 1–22, Springer Berlin Heidelberg, Berlin, Heidelberg.

Götze, J., M. R. Krbetschek, D. Habermann, and D. Wolf (2000), High-Resolution Cathodoluminescence Studies of Feldspar Minerals, in *Cathodoluminescence in Geosciences*, edited by M. Pagel, V. Barbin, P. Blanc, and D. Ohnenstetter, pp. 245–270, Springer Berlin Heidelberg, Berlin, Heidelberg.

Graham, C. M., J. W. Valley, J. M. Eiler, and H. Wada (1998), Timescales and mechanisms of fluid infiltration in a marble: an ion microprobe study, *Contrib. to Mineral. Petrol.*, *132*(4), 371–389, doi:10.1007/s004100050430.

Grapes, R., and T. Watanabe (1992), Metamorphism and uplift of Alpine schist in the Franz Josef–Fox Glacier area of the Southern Alps, New Zealand, *J. Metamorph. Geol.*, *10*(2), 171–180, doi:10.1111/j.1525-1314.1992.tb00077.x.

Grapes, R., and T. Watanabe (1994), Mineral composition variation in Alpine Schist, Southern Alps, New Zealand: Implications for recrystallization and exhumation, *Isl. Arc*, *3*(3), 163–181, doi:10.1111/j.1440-1738.1994.tb00105.x.

Gratier, J. P., P. Favreau, F. Renard, and E. Pili (2002), Fluid pressure evolution during the earthquake cycle controlled by fluid flow and pressure solution crack sealing, *Earth, Planets Sp.*, *54*(11), 1139–1146, doi:10.1186/BF03353315.

Green, H. W., and H. Houston (1995), The Mechanics of Deep Earthquakes, *Annu. Rev. Earth Planet. Sci.*, *23*(1), 169–213, doi:doi:10.1146/annurev.ea.23.050195.001125.

Green II, H. W., and P. C. Burnley (1989), A new self-organizing mechanism for deep-focus earthquakes, *Nature*, *341*(6244), 733–737.

Green II, H. W., F. Shi, K. Bozhilov, G. Xia, and Z. Reches (2015), Phase transformation and nanometric flow cause extreme weakening during fault slip, *Nat. Geosci.*, *8*(6), 484–489, doi:10.1038/ngeo2436.

Griffith, A. A. (1921), The Phenomena of Rupture and Flow in Solids, *Philos. Trans. R. Soc. A Math. Phys. Eng. Sci.*, *221*(582–593), 163–198, doi:10.1098/rsta.1921.0006.

Griffiths, L., M. J. Heap, F. Wang, D. Daval, H. A. Gilg, P. Baud, J. Schmittbuhl, and A. Genter (2016), Geothermal implications for fracture-filling hydrothermal precipitation, *Geothermics*, *64*, 235–245, doi:10.1016/j.geothermics.2016.06.006.

Guéguen, Y., and J. Sarout (2011), Characteristics of anisotropy and dispersion in cracked medium, *Tectonophysics*, *503*(1), 165–172, doi:10.1016/j.tecto.2010.09.021.

Hadizadeh, J., S. Mittempergher, J. P. Gratier, F. Renard, G. Di Toro, J. Richard, and H. A. Babaie (2012), A microstructural study of fault rocks from the SAFOD: Implications for the deformation mechanisms and strength of the creeping segment of the San Andreas Fault, *J. Struct. Geol.*, *42*, 246–260, doi:10.1016/j.jsg.2012.04.011.

Han, R., and T. Hirose (2012), Clay–clast aggregates in fault gouge: An unequivocal indicator of seismic faulting at shallow depths?, *J. Struct. Geol.*, *43*, 92–99, doi:10.1016/j.jsg.2012.07.008.

Han, R., T. Shimamoto, J. Ando, and J.-H. Ree (2007a), Seismic slip record in carbonate-bearing fault zones: An insight from high-velocity friction experiments on siderite gouge, *Geology*, *35*(12), 1131–1134.

Han, R., T. Shimamoto, T. Hirose, J.-H. Ree, and J. Ando (2007b), Ultralow Friction of Carbonate Faults Caused by Thermal Decomposition, *Science (80-.).*, *316*(5826), 878–881.

Han, R., T. Hirose, T. Shimamoto, Y. Lee, and J. Ando (2011), Granular nanoparticles lubricate faults during seismic slip, *Geology*, *39*(6), 599–602.

Hayward, K. S., and S. F. Cox (2017), Stress-driven versus fluid-driven slip: using experiments to explore differences in modes of earthquake rupture, in *Deformation Mechanisms, Rheology and Tectonics - DRT 2017*, p. 63, Inverness, Scotland.

Hickmott, D. D., B. E. Treves, G. T. Roselle, and L. P. Baumgartner (1997), Micro-PIXE analysis of carbonates and silicates: Tracking fluid flow in crustal environments, *Nucl. Instruments Methods Phys. Res. Sect. B Beam Interact. with Mater. Atoms*, *130*(1), 660–665, doi:10.1016/S0168-583X(97)00262-0.

Hilgers, C., and S. Sindern (2005), Textural and isotopic evidence on the fluid source and transport mechanism of antitaxial fibrous microstructures from the Alps and the Appalachians, *Geofluids*, *5*(4), 239–250, doi:10.1111/j.1468-8123.2005.00114.x.

Hilgers, C., K. Dilg-Gruschinski, and J. L. Urai (2004), Microstructural evolution of syntaxial veins formed by advective flow, *Geol.* , *32*(3), 261–264, doi:10.1130/G20024.1.

Hinton, R. W. (1995), Microprobe Techniques in the Earth Sciences, edited by P. J. Potts, J. F. W. Bowles, S. J. B. Reed, and M. R. Cave, pp. 235–289, Springer US, Boston, MA.

Hirose, T., and T. Shimamoto (2003), Fractal dimension of molten surfaces as a possible parameter to infer the slip-weakening distance of faults from natural pseudotachylytes, *J. Struct. Geol.*, *25*(10), 1569–1574, doi:10.1016/S0191-8141(03)00009-9.

Hirose, T., and T. Shimamoto (2005), Growth of molten zone as a mechanism of slip weakening of simulated faults in gabbro during frictional melting, *J. Geophys. Res. Solid Earth*, *110*(B5), n/a-n/a, doi:10.1029/2004JB003207.

Hoffmann-Rothe, A., O. Ritter, and C. Janssen (2004), Correlation of electrical conductivity and structural damage at a major strike-slip fault in northern Chile, *J. Geophys. Res. B Solid Earth*, *109*(10), doi:10.1029/2004JB003030.

Holdsworth, R. E. (2004), Weak Faults-Rotten Cores, *Science (80-.).*, *303*(5655), 181–182, doi:10.1126/science.1092491.

Holm, D. K., R. J. Norris, and D. Craw (1989), Brittle and ductile deformation in a zone of rapid uplift: Central Southern Alps, New Zealand, *Tectonics*, *8*(2), 153–168, doi:10.1029/TC008i002p00153.

Howarth, J. D., S. J. Fitzsimons, R. J. Norris, R. Langridge, and M. J. Vandergoes (2016), A 2000 yr rupture history for the Alpine fault derived from Lake Ellery, South Island, New Zealand, *Bull. Geol. Soc. Am.*, *128*(3–4), 627–643, doi:10.1130/B31300.1.

Imber, J., R. E. Holdsworth, C. A. Butler, and R. A. Strachan (2001), A reappraisal of the Sibson-Scholz fault zone model: The nature of the frictional to viscous ("brittle-ductile") transition along a long-lived, crustal-scale fault, Outer Hebrides, Scotland, *Tectonics*, *20*(5), 601–624, doi:10.1029/2000TC001250.

Inoue, A., and M. Utada (1991), Smectite-to-chlorite transformation in thermally metamorphosed volcanoclastic rocks in the Kamikita area, northern Honshu, Japan, *Am. Mineral.*, *76*(3–4), 628–640.

Irwin, G. R. (1957), Analysis of Stresses and Strains Near the End of a Crack Traversing a Plate, *J. Appl. Mech.*

Jaeger, J. C., N. G. W. Cook, and R. Zimmerman (2007), *Fundamentals of rock mechanics*, fourth edi., Wiley-Blackwell, London.

Janssen, C., R. Wirth, H. R. Wenk, L. Morales, R. Naumann, M. Kienast, S. R. Song, and G. Dresen (2014), Faulting processes in active faults - Evidences from TCDP and SAFOD drill core samples, *J. Struct. Geol.*, *65*, 100–116, doi:10.1016/j.jsg.2014.04.004.

Jenkin, G. R. T., D. Craw, and A. E. Fallick (1994), Stable isotopic and fluid inclusion evidence for meteoric fluid penetration into an active mountain belt; Alpine Schist, New Zealand, *J. Metamorph. Geol.*, *12*(4), 429–444, doi:10.1111/j.1525-1314.1994.tb00033.x.

Jeppson, T. N., and H. J. Tobin (2015), San Andreas fault zone velocity structure at SAFOD at core, log, and seismic scales, *J. Geophys. Res. Solid Earth*, *120*(7), 4983–4997, doi:10.1002/2015JB012043.

Jeppson, T. N., K. K. Bradbury, and J. P. Evans (2010), Geophysical properties within the San Andreas Fault Zone at the San Andreas Fault Observatory at Depth and their relationships to rock properties and fault zone structure, *J. Geophys. Res. Solid Earth*, *115*(12), 1–20, doi:10.1029/2010JB007563.

John, T., S. Medvedev, L. H. Rüpke, T. B. Andersen, Y. Y. Podladchikov, and H. Austrheim (2009), Generation of intermediate-depth earthquakes by self-localizing thermal runaway, *Nat. Geosci.*, *2*, 137.

Jolliffe, I. T. (2002), *Principal Component Analysis*, Springer Series in Statistics, 2nd ed., Springer-Verlag, New York.

Karalliyadda, S. C., and M. K. Savage (2013), Seismic anisotropy and lithospheric deformation of the plate-boundary zone in South Island, New Zealand: inferences

from local S-wave splitting, *Geophys. J. Int.*, *193*(2), 507–530, doi:10.1093/gji/ggt022.

Karner, S. L., and C. Marone (2000), Effects of Loading Rate and Normal Stress on Stress Drop and Stick-Slip Recurrence Interval, in *Geocomplexity and the Physics of Earthquakes*, pp. 187–198, American Geophysical Union.

Kasemann, S. A., D. N. Schmidt, J. Bijma, and G. L. Foster (2009), In situ boron isotope analysis in marine carbonates and its application for foraminifera and palaeo-pH, *Chem. Geol.*, *260*(1–2), 138–147, doi:10.1016/j.chemgeo.2008.12.015.

Katz, D. A., G. P. Eberli, P. K. Swart, and L. B. Smith (2006), Tectonic-hydrothermal brecciation associated with calcite precipitation and permeability destruction in Mississippian carbonate reservoirs, Montana and Wyoming, *Am. Assoc. Pet. Geol. Bull.*, *90*(11), 1803–1841, doi:10.1306/03200605072.

Kayama, M., S. Nakano, and H. Nishido (2010), Characteristics of emission centers in alkali feldspar: A new approach by using cathodoluminescence spectral deconvolution, *Am. Mineral.*, *95*(11–12), 1783–1795.

Kelly, C. M., A. Rietbrock, D. R. Faulkner, and R. M. Nadeau (2013), Temporal changes in attenuation associated with the 2004 M6.0 Parkfield earthquake, *J. Geophys. Res. Solid Earth*, *118*(2), 630–645, doi:10.1002/jgrb.50088.

Kelly, C. M., D. R. Faulkner, and A. Rietbrock (2017), Seismically invisible fault zones: Laboratory insights into imaging faults in anisotropic rocks, *Geophys. Res. Lett.*, n/a-n/a, doi:10.1002/2017GL073726.

Ketcham, R. A., and W. D. Carlson (2001), Acquisition, optimization and interpretation of X-ray computed tomographic imagery: applications to the geosciences, *Comput. Geosci.*, *27*(4), 381–400, doi:10.1016/S0098-3004(00)00116-3.

Kilian, R., M. Bestmann, and R. Heilbronner (2016), Absolute orientations from EBSD measurements - as easy as it seems ?, , *18*, 8221.

Kim, Y. S., D. C. P. Peacock, and D. J. Sanderson (2004), Fault damage zones, *J. Struct. Geol.*, *26*(3), 503–517, doi:10.1016/j.jsg.2003.08.002.

Kirby, S. (1995), Interslab earthquakes and phase changes in subducting lithosphere, *Rev. Geophys.*, *33*(S1), 287–297, doi:10.1029/95RG00353.

Kirkpatrick, J. D., and C. D. Rowe (2013), Disappearing ink: How pseudotachylytes are lost from the rock record, *J. Struct. Geol.*, *52*(1), 183–198, doi:10.1016/j.jsg.2013.03.003.

Kirkpatrick, J. D., C. D. Rowe, J. C. White, and E. E. Brodsky (2013), Silica gel formation during fault slip: Evidence from the rock record, *Geology*, *41*(9), 1015–1018.

Kitagawa, Y., and Y. Kano (2016), Changes in permeability of the Nojima fault damage zone inferred from repeated water injection experiments, *Earth, Planets Sp.*, *68*(1), 185.

Kitagawa, Y., K. Fujimori, and N. Koizumi (2007), Temporal change in permeability of the Nojima fault zone by repeated water injection experiments, *Tectonophysics*, *443*(3–4), 183–192, doi:10.1016/j.tecto.2007.01.012.

Kohlstedt, D. L., B. Evans, and S. J. Mackwell (1995), Strength of the lithosphere: Constraints imposed by laboratory experiments, *J. Geophys. Res. Solid Earth*, *100*(B9), 17587–17602, doi:10.1029/95JB01460.

Koons, P. O. (1987), Some thermal and mechanical consequences of rapid uplift: an example from the Southern Alps, New Zealand, *Earth Planet. Sci. Lett.*, *86*(2), 307–319, doi:10.1016/0012-821X(87)90228-7.

Koons, P. O., and D. Craw (1991), Evolution of fluid driving forces and composition within collisional orogens, *Geophys. Res. Lett.*, *18*(5), 935–938, doi:10.1029/91GL00910.

Koons, P. O., D. Craw, S. C. Cox, P. Upton, A. S. Templeton, and C. P. Chamberlain (1998), Fluid flow during active oblique convergence: A Southern Alps model from mechanical and geochemical observations, *Geology*, *26*(2), 159–162.

Krbetschek, M. R., J. Götze, A. Dietrich, and T. Trautmann (1997), Spectral information from minerals relevant for luminescence dating, *Radiat. Meas.*, *27*(5), 695–748, doi:10.1016/S1350-4487(97)00223-0.

Kronenberg, A. K., and J. Tullis (1984), Flow strengths of quartz aggregates: Grain size and pressure effects due to hydrolytic weakening, *J. Geophys. Res. Solid Earth*, *89*(B6), 4281–4297, doi:10.1029/JB089iB06p04281.

Lachenbruch, A. H. (1980), Frictional heating, fluid pressure, and the resistance to fault motion, *J. Geophys. Res.*, *85*(B11), 6097, doi:10.1029/JB085iB11p06097.

Lahann, R. W. (1978), A chemical model for calcite crystal growth and morphology control, *J. Sediment. Res.*, *48*(1), 337–347.

Lamb, S., and E. Smith (2013), The nature of the plate interface and driving force of interseismic deformation in the New Zealand plate-boundary zone, revealed by the continuous GPS velocity field, *J. Geophys. Res. Solid Earth*, *118*(6), 3160–3189, doi:10.1002/jgrb.50221.

Lamb, S., E. Smith, T. Stern, and E. Warren-Smith (2015), Continent-scale strike-slip on a low-angle fault beneath New Zealand's Southern Alps: Implications for crustal thickening in oblique collision zones, *Geochemistry, Geophys. Geosystems*, *16*(9), 3076–3096, doi:10.1002/2015GC005990.

Lamb, S., N. Mortimer, E. Smith, and G. Turner (2016), Focusing of relative plate motion at a continental transform fault: Cenozoic dextral displacement >700 km on New Zealand's Alpine Fault, reversing >225 km of Late Cretaceous sinistral motion, *Geochemistry, Geophys. Geosystems*, *17*(3), 1197–1213, doi:10.1002/2015GC006225.

Langridge, R. M., R. Basili, L. Basher, and A. P. Wells (2012), Late Holocene landscape change history related to the Alpine Fault determined from drowned forests in Lake Poerua, Westland, New Zealand, *Nat. Hazards Earth Syst. Sci.*, *12*(6), 2051–2064, doi:10.5194/nhess-12-2051-2012.

Langridge, R. M., W. F. Ries, T. Farrier, N. C. Barth, N. Khajavi, and G. P. De Pascale (2014), Developing sub 5-m LiDAR DEMs for forested sections of the Alpine and Hope faults, South Island, New Zealand: Implications for structural interpretations, *J. Struct. Geol.*, *64*, 53–66, doi:10.1016/j.jsg.2013.11.007.

Lay, V., S. Buske, A. Lukács, A. R. Gorman, S. Bannister, and D. R. Schmitt (2016), Advanced seismic imaging techniques characterize the Alpine Fault at Whataroa (New Zealand), *J. Geophys. Res. Solid Earth*, *121*(12), 8792–8812, doi:10.1002/2016JB013534.

Leclère, H., F. Cappa, D. Faulkner, O. Fabbri, P. Armitage, and O. Blake (2015), Development and maintenance of fluid overpressures in crustal fault zones by elastic compaction and implications for earthquake swarms, *J. Geophys. Res. Solid Earth*, *120*, 4450–4473, doi:10.1002/2014JB011759.

Lee, M. R., I. Parsons, P. R. Edwards, and R. W. Martin (2007), Identification of cathodoluminescence activators in zoned alkali feldspars by hyperspectral imaging and electron-probe microanalysis, *Am. Mineral.*, *92*(2–3), 243–253.

Lee, Y.-J., D. V. Wiltschko, E. L. Grossman, J. W. Morse, and W. M. Lamb (1997), Sequential vein growth with fault displacement: An example from the Austin Chalk Formation, Texas, *J. Geophys. Res. Solid Earth*, *102*(B10), 22611–22628, doi:10.1029/97JB01945.

Lee, Y. J., and J. W. Morse (1999), Calcite precipitation in synthetic veins: Implications for the time and fluid volume necessary for vein filling, *Chem. Geol.*, *156*(1–4), 151–170, doi:10.1016/S0009-2541(98)00183-1.

Leeman, J., M. M. Scuderi, C. Marone, and D. Saffer (2015), Stiffness evolution of granular layers and the origin of repetitive, slow, stick-slip frictional sliding, *Granul. Matter*, *17*(4), 447–457, doi:10.1007/s10035-015-0565-1.

Li, Y. G., W. L. Ellsworth, C. H. Thurber, P. E. Malin, and K. Aki (1997), Fault-zone guided waves from explosions in the San Andreas fault at Parkfield and Cienega Valley, California, *Bull. Seismol. Soc. Am.*, *87*(1), 210–221.

Li, Y. G., J. E. Vidale, and E. S. Cochran (2004), Low-velocity damaged structure of the San Andreas Fault at Parkfield from fault zone trapped waves, *Geophys. Res. Lett.*, *31*(12), doi:10.1029/2003GL019044.

Lin, A. (1997), Injection veins of crushing-originated pseudotachylyte and fault gouge formed during seismic faulting, in *Developments in Geotechnical Engineering*, vol. 81, pp. 163–179.

Lin, A. (1999), Roundness of clasts in pseudotachylytes and cataclastic rocks as an indicator of frictional melting, *J. Struct. Geol.*, *21*(5), 473–478, doi:10.1016/S0191-8141(99)00030-9.

Little, T. A., and N. Mortimer (2001), Rotation of ductile fabrics across the Alpine Fault and Cenozoic bending of the New Zealand orocline, *J. Geol. Soc. London.*, *158*(5), 745–756, doi:10.1144/jgs.158.5.745.

Little, T. A., R. J. Holcombe, and B. R. Ilg (2002a), Ductile fabrics in the zone of active oblique convergence near the Alpine Fault, New Zealand: identifying the neotectonic overprint, *J. Struct. Geol.*, *24*(1), 193–217, doi:10.1016/S0191-8141(01)00059-1.

Little, T. A., R. J. Holcombe, and B. R. Ilg (2002b), Kinematics of oblique collision and ramping inferred from microstructures and strain in middle crustal rocks, Central Southern Alps, New Zealand, *J. Struct. Geol.*, *24*(1), 219–239, doi:10.1016/S0191-8141(01)00060-8.

Little, T. A., D. J. Prior, V. G. Toy, and Z. R. Lindroos (2015), The link between strength of lattice preferred orientation, second phase content and grain boundary migration: A case study from the Alpine Fault zone, New Zealand, *J. Struct. Geol.*, *81*, 59–77, doi:10.1016/j.jsg.2015.09.004.

Little, T. A., D. J. Prior, and V. G. Toy (2016), Are quartz LPOs predictably oriented with respect to the shear zone boundary?: A test from the Alpine Fault mylonites, New Zealand, *Geochemistry, Geophys. Geosystems*, *17*(3), 981–999,

doi:10.1002/2015GC006145.

Long, J. V. P., and S. O. Agrell (1965), The cathodoluminescence of minerals in thin section., *Mineral. Mag.*, *34*, 318–326.

Lund Snee, J.-E., V. G. Toy, and K. Gessner (2014), Significance of brittle deformation in the footwall of the Alpine Fault, New Zealand: Smithy Creek Fault zone, *J. Struct. Geol.*, *64*, 79–98, doi:10.1016/j.jsg.2013.06.002.

Ma, K.-F. et al. (2006), Slip zone and energetics of a large earthquake from the Taiwan Chelungpu-fault Drilling Project, *Nature*, *444*(7118), 473–476.

MacRae, C. M., and N. C. Wilson (2008), Luminescence database I - Minerals and materials, *Microsc. Microanal.*, *14*(2), 184–204, doi:10.1017/S143192760808029X.

Madariaga, R., K. Olsen, and R. Archuleta (1998), Modeling dynamic rupture in a 3D earthquake fault model, *Bull. Seismol. Soc. Am.*, *88*(5), 1182–1197.

Maddock, R. H., J. Grocott, and M. Van Nes (1987), Vesicles, amygdales and similar structures in fault-generated pseudotachylytes, *Lithos*, *20*(5), 419–432, doi:10.1016/0024-4937(87)90019-3.

Magloughlin, J. F. (1992), Microstructural and chemical changes associated with cataclasis and frictional melting at shallow crustal levels: the cataclasite-pseudotachylyte connection, *Tectonophysics*, *204*(3–4), 243–260, doi:10.1016/0040-1951(92)90310-3.

Magloughlin, J. F., and J. G. Spray (1992), Frictional melting processes and products in geological materials: introduction and discussion, *Tectonophysics*, *204*(3–4), 197–204, doi:10.1016/0040-1951(92)90307-R.

Mainprice, D., and M. Humbert (1994), Methods of calculating petrophysical properties from lattice preferred orientation data, *Surv. Geophys.*, *15*(5), 575–592, doi:10.1007/BF00690175.

Marfunin, A. S. (1979), Luminescence, in *Spectroscopy, Luminescence and Radiation Centers in Minerals*, pp. 141–222, Springer-Verlag, Berlin.

Mariani, E., and E. Ghassemieh (2010), Microstructure evolution of 6061 O Al alloy during ultrasonic consolidation: An insight from electron backscatter diffraction, *Acta Mater.*, *58*(7), 2492–2503, doi:10.1016/j.actamat.2009.12.035.

Marone, C. (1998), Laboratory-derived friction laws and their application to seismic faulting, *Annu. Rev. Earth Planet. Sci.*, *26*(1), 643–696, doi:10.1146/annurev.earth.26.1.643.

Marshall, D. J. (Donald J. ., and A. N. Mariano (1988), *Cathodoluminescence of geological materials*, Unwin Hyman.

Marshall, J. D. (1991), Cathodoluminescence of geological materials, *Geol. J.*, *26*(4), 351–351, doi:10.1002/gj.3350260409.

Maskenskaya, O. M., H. Drake, C. Broman, J. K. Hogmalm, G. Czuppon, and M. E. Åström (2014), Source and character of syntaxial hydrothermal calcite veins in Paleoproterozoic crystalline rocks revealed by fine-scale investigations, *Geofluids*, *14*(4), 495–511, doi:10.1111/gfl.12092.

McKenzie, D. P., and J. Brune (1972), Melting on fault planes during large earthquakes, *Geophys. J. R. A .S.*, *29*, 65–78.

McNamara, D. D., A. Lister, and D. J. Prior (2016), Calcite sealing in a fractured geothermal reservoir: Insights from combined EBSD and chemistry mapping, *J. Volcanol. Geotherm. Res.*, *323*, 38–52, doi:10.1016/j.jvolgeores.2016.04.042.

Meneghini, F., G. Di Toro, C. D. Rowe, J. C. Moore, A. Tsutsumi, and A. Yamaguchi (2010), Record of mega-earthquakes in subduction thrusts: The black fault rocks of Pasagshak Point (Kodiak Island, Alaska), *GSA Bull.*, *122*(7–8), 1280–1297.

Menzies, C. D. (2012), Fluid Flow Associated with the Alpine Fault, South Island, New

Zealand, University of Southampton.

Menzies, C. D., D. A. H. Teagle, D. Craw, S. C. Cox, A. J. Boyce, C. D. Barrie, and S. Roberts (2014), Incursion of meteoric waters into the ductile regime in an active orogen, *Earth Planet. Sci. Lett.*, *399*, 1–13, doi:10.1016/j.epsl.2014.04.046.

Menzies, C. D., D. A. H. Teagle, S. Niedermann, S. C. Cox, D. Craw, M. Zimmer, M. J. Cooper, and J. Erzinger (2016), The fluid budget of a continental plate boundary fault: Quantification from the Alpine Fault, New Zealand, *Earth Planet. Sci. Lett.*, *445*, 125–135, doi:10.1016/j.epsl.2016.03.046.

Miller, S. A., C. Collettini, L. Chiaraluce, M. Cocco, M. Barchi, and B. J. P. Kaus (2004), Aftershocks driven by a high-pressure CO2 source at depth, *Nature*, *427*(6976), 724–727.

Mitchell, T. M., and D. R. Faulkner (2008), Experimental measurements of permeability evolution during triaxial compression of initially intact crystalline rocks and implications for fluid flow in fault zones, *J. Geophys. Res. Solid Earth*, *113*(11), 1–16, doi:10.1029/2008JB005588.

Mitchell, T. M., and D. R. Faulkner (2009), The nature and origin of off-fault damage surrounding strike-slip fault zones with a wide range of displacements: A field study from the Atacama fault system, northern Chile, *J. Struct. Geol.*, *31*(8), 802–816, doi:10.1016/j.jsg.2009.05.002.

Mitchell, T. M., and D. R. Faulkner (2012), Towards quantifying the matrix permeability of fault damage zones in low porosity rocks, *Earth Planet. Sci. Lett.*, *339–340*, 24–31, doi:10.1016/j.epsl.2012.05.014.

Mitchell, T. M., V. Toy, G. Di Toro, J. Renner, and R. H. Sibson (2016), Fault welding by pseudotachylyte formation, *Geology*, (12), G38373.1, doi:10.1130/G38373.1.

Mithen, J. P., and R. P. Sear (2014), Computer simulation of epitaxial nucleation of a crystal

on a crystalline surface, *J. Chem. Phys.*, *140*(8), 1–6, doi:10.1063/1.4866035.

Mittempergher, S., G. Di Toro, J. P. Gratier, J. Hadizadeh, S. A. F. Smith, and R. Spiess (2011), Evidence of transient increases of fluid pressure in SAFOD phase III cores, *Geophys. Res. Lett.*, *38*(3), doi:10.1029/2010GL046129.

Mizoguchi, K., T. Hirose, T. Shimamoto, and E. Fukuyama (2008), Internal structure and permeability of the Nojima fault, southwest Japan, *J. Struct. Geol.*, *30*(4), 513–524, doi:10.1016/j.jsg.2007.12.002.

Möller, P., V. Lüders, J. Schröder, and J. Luck (1991), Element partitioning in calcite as a function of solution flow rate: a study on vein calcites from the Harz Mountains, *Miner. Depos.*, *26*(3), 175–179, doi:10.1007/BF00209255.

Mooney, W. D., Beroza, G. C., and Kind, R. (2009), Fault zones from top to bottom: a geophysical perspective, in *Tectonic Faults: Agents of Change on a Dynamic Earth*, vol. 95, edited by H. M.R, H. G., and H. N., pp. 131–133, Routledge.

Mooney, W. D., and A. Ginzburg (1986), Seismic measurements of the internal properties of fault zones, *Pure Appl. Geophys. PAGEOPH*, *124*(1–2), 141–157, doi:10.1007/BF00875723.

Morrow, C. A., D. A. Lockner, D. E. Moore, and S. Hickman (2014), Deep permeability of the San Andreas Fault from San Andreas Fault Observatory at Depth (SAFOD) core samples, *J. Struct. Geol.*, *64*, 99–114, doi:10.1016/j.jsg.2013.09.009.

Mortimer, N. (2000), Metamorphic discontinuities in orogenic belts: example of the garnet–biotite–albite zone in the Otago Schist, New Zealand, *Int. J. Earth Sci.*, *89*(2), 295–306, doi:10.1007/s005310000086.

Mortimer, N., and B. P. Roser (1992), Geochemical evidence for the position of the Caples–Torlesse boundary in the Otago Schist, New Zealand, *J. Geol. Soc. London.*, *149*(6), 967–977.

Morton, N., G. H. Girty, and T. K. Rockwell (2012), Fault zone architecture of the San Jacinto fault zone in Horse Canyon, southern California: A model for focused post-seismic fluid flow and heat transfer in the shallow crust, *Earth Planet. Sci. Lett.*, *329–330*, 71–83, doi:10.1016/j.epsl.2012.02.013.

Muir, R. J., T. R. Ireland, S. D. Weaver, J. D. Bradshaw, J. A. Evans, G. N. Eby, and D. Shelley (1998), Geochronology and geochemistry of a Mesozoic magmatic arc system, Fiordland, New Zealand, *J. Geol. Soc. London.*, *155*(6), 1037–1053.

Murrell, S. A. F. (1963), A criterion for brittle fracture of rocks and concrete under triaxial stress and the effect of pore pressure on the criterion, *Rock Mech.*, 563–577.

Nara, Y., P. G. Meredith, T. Yoneda, and K. Kaneko (2011), Influence of macro-fractures and micro-fractures on permeability and elastic wave velocities in basalt at elevated pressure, *Tectonophysics*, *503*(1–2), 52–59, doi:10.1016/j.tecto.2010.09.027.

Nielsen, S., G. Di Toro, T. Hirose, and T. Shimamoto (2008), Frictional melt and seismic slip, *J. Geophys. Res. Solid Earth*, *113*(1), 1–20, doi:10.1029/2007JB005122.

Nishikawa, S., and S. Kikuchi (1928), Diffraction of Cathode Rays by Mica, *Nature*, *121*(3061), 1019–1020, doi:10.1038/1211019a0.

Nollet, S., J. L. Urai, P. D. Bons, and C. Hilgers (2005), Numerical simulations of polycrystal growth in veins, *J. Struct. Geol.*, *27*(2), 217–230, doi:10.1016/j.jsg.2004.10.003.

Norris, R. J., and A. F. Cooper (2001), Late Quaternary slip rates and slip partitioning on the Alpine Fault, New Zealand, *J. Struct. Geol.*, *23*(2–3), 507–520, doi:10.1016/S0191-8141(00)00122-X.

Norris, R. J., and A. F. Cooper (2003), Very high strains recorded in mylonites along the Alpine Fault, New Zealand: Implications for the deep structure of plate boundary faults, *J. Struct. Geol.*, *25*(12), 2141–2157, doi:10.1016/S0191-8141(03)00045-2.

Norris, R. J., and A. F. Cooper (2007), The Alpine Fault, New Zealand: Surface Geology and Field Relationships, in *A Continental Plate Boundary: Tectonics at South Island, New Zealand*, edited by D. Okaya, T. A. Stern, and F. Davey, pp. 157–175, American Geophysical Union.

Norris, R. J., and V. G. Toy (2014), Continental transforms: A view from the Alpine Fault, *J. Struct. Geol.*, *64*, 3–31, doi:10.1016/j.jsg.2014.03.003.

Okaya, D., N. Christensen, D. Stanley, T. Stern, South Island Geophysical Transect (, and S. I. G. T. (SIGHT) W. Group (1995), Crustal anisotropy in the vicinity of the Alpine Fault Zone, South Island, New Zealand, *New Zeal. J. Geol. Geophys.*, *38*(4), 579–583, doi:10.1080/00288306.1995.9514686.

Okaya, D. A., and N. I. Christensen (2002), Anisotropic effects of non-axial seismic wave propagation in foliated crustal rocks, *Geophys. Res. Lett.*, *29*(11), 1507, doi:10.1029/2001GL014285.

Oliver, N. H. S. (1996), Review and classification of structural controls on fluid flow during regional metamorphism, *J. Metamorph. Geol.*, *14*(4), 477–492, doi:10.1046/j.1525-1314.1996.00347.x.

Oliver, N. H. S., and P. D. Bons (2001), Mechanisms of fluid flow and fluid–rock interaction in fossil metamorphic hydrothermal systems inferred from vein–wallrock patterns, geometry and microstructure, *Geofluids*, *1*(2), 137–162, doi:10.1046/j.1468-8123.2001.00013.x.

Oomori, T., H. Kaneshima, Y. Maezato, and Y. Kitano (1987), Distribution coefficient of Mg2+ ions between calcite and solution at 10–50°C, *Mar. Chem.*, *20*(4), 327–336, doi:10.1016/0304-4203(87)90066-1.

Otsuki, K. (2003), Fluidization and melting of fault gouge during seismic slip: Identification in the Nojima fault zone and implications for focal earthquake mechanisms, *J. Geophys. Res.*, *108*(B4), 2192, doi:10.1029/2001JB001711.

Pacchioni, G., L. Skuja, and D. . Griscom (2000), Defects in SiO2 and related dielectrics: Science and chemistry, in *Defects in SiO2 and related dielectrics: Science and chemistry*, p. 624, Kluwer Academic Publishers, Dordrecht.

Pagel, M., V. Barbin, P. Blanc, and D. Ohnenstetter (2000), Cathodoluminescence in Geosciences: An Introduction, in *Cathodoluminescence in Geosciences*, edited by M. Pagel, V. Barbin, P. Blanc, and D. Ohnenstetter, pp. 1–21, Springer Berlin Heidelberg, Berlin, Heidelberg.

Paquette, J., and R. J. Reeder (1995), Relationship between surface structure, growth mechanism, and trace element incorporation in calcite, *Geochim. Cosmochim. Acta*, *59*(4), 735–749, doi:10.1016/0016-7037(95)00004-J.

Parsons, I., D. A. Steele, M. R. Lee, and C. W. Magee (2008), Titanium as a cathodoluminescence activator in alkali feldspars, *Am. Mineral.*, *93*(5–6), 875–879.

Passchier, C. W., and R. R. A. J. Trouw (2005), *Microtectonics*.

Pec, M., H. Stünitz, R. Heilbronner, M. Drury, and C. de Capitani (2012), Origin of pseudotachylites in slow creep experiments, *Earth Planet. Sci. Lett.*, *355*, 299–310, doi:10.1016/j.epsl.2012.09.004.

Peng, Z., and Y. Ben-Zion (2006), Temporal changes of shallow seismic velocity around the Karadere-Düzce branch of the north Anatolian fault and strong ground motion, *Pure Appl. Geophys.*, *163*(2–3), 567–600, doi:10.1007/s00024-005-0034-6.

Phillips, W. J. (1972), Hydraulic fracturing and mineralization, *J. Geol. Soc. London.*, *128*(4), 337–359.

Piazolo, S., D. J. Prior, and M. D. Holness (2005), The use of combined cathodoluminescence and EBSD analysis: a case study investigating grain boundary migration mechanisms in quartz, *J. Microsc.*, *217*(2), 152–161, doi:10.1111/j.1365-2818.2005.01423.x.

Platt, J. D., R. C. Viesca, and D. I. Garagash (2015), Steadily propagating slip pulses driven by thermal decomposition, *J. Geophys. Res. Solid Earth*, *120*(9), 6558–6591, doi:10.1002/2015JB012200.

Poirier, J. P. (1985), *Creep of crystals: High-temperature deformation processes in metals, ceramics and minerals*, Cambridge University Press, Cambridge and New York.

Pollard, D. D. (1976), On the form and stability of open hydraulic fractures in the Earth's crust, *Geophys. Res. Lett.*, *3*(9), 513–516, doi:10.1029/GL003i009p00513.

Price, N. J., and J. W. Cosgrove (1990), *Analysis of Geological Structures*.

Prieto, G. A., M. Florez, S. A. Barrett, G. C. Beroza, P. Pedraza, J. F. Blanco, and E. Poveda (2013), Seismic evidence for thermal runaway during intermediate-depth earthquake rupture, *Geophys. Res. Lett.*, *40*(23), 6064–6068, doi:10.1002/2013GL058109.

Prior, D. J. (1988), Deformation processes in the Alpine Fault Mylonites, South Island, New Zealand, University of Leeds.

Prior, D. J. et al. (1999), The application of electron backscatter diffraction and orientation contrast imaging in the SEM to textural problems in rocks, *Am. Mineral.*, *84*, 1741–1759.

Prior, D. J., E. Mariani, and J. Wheeler (2009), EBSD in the Earth Sciences: Applications, Common Practice, and Challenges, edited by A. J. Schwartz, M. Kumar, B. L. Adams, and D. P. Field, pp. 345–360, Springer US, Boston, MA.

Putnis, A., and C. V. Putnis (2007), The mechanism of reequilibration of solids in the presence of a fluid phase, *J. Solid State Chem.*, *180*(5), 1783–1786, doi:10.1016/j.jssc.2007.03.023.

Qian, G., Y. Li, and A. R. Gerson (2015), Applications of surface analytical techniques in Earth Sciences, *Surf. Sci. Rep.*, *70*(1), 83–133, doi:10.1016/j.surfrep.2015.02.001.

Ramsey, J., and M. Chester (2004), Hybrid fracture and the transition from extension fracture to shear fracture, *Nature*, *428*, 63–66, doi:10.1029/2001GL014320.

Randle, V. (1992), Microtexture determination and its applications, *Inst. Mater. 1992,*, 174.

Ray, S. K. (1999), Transformation of cataclastically deformed rocks to pseudotachylyte by pervasion of frictional melt: inferences from clast-size analysis, *Tectonophysics*, *301*(3), 283–304, doi:10.1016/S0040-1951(98)00229-7.

Reches, Z., and D. A. Lockner (2010), Fault weakening and earthquake instability by powder lubrication, *Nature*, *467*(7314), 452–455.

Reed, J. J. (1964), Mylonites, cataclasites, and associated rocks along the Alpine fault, South Island, New Zealand, *New Zeal. J. Geol. Geophys.*, *7*(4), 645–684, doi:10.1080/00288306.1964.10428124.

Rempel, A. W., and J. R. Rice (2006), Thermal pressurization and onset of melting in fault zones, *J. Geophys. Res.*, *111*(B9), B09314, doi:10.1029/2006JB004314.

Renard, F., J. P. Gratier, and B. Jamtveit (2000), Kinetics of crack-sealing, intergranular pressure solution, and compaction around active faults, *J. Struct. Geol.*, *22*(10), 1395–1407, doi:10.1016/S0191-8141(00)00064-X.

Rhoades, D. A., and R. J. Van Dissen (2003), Estimates of the time-varying hazard of rupture of the Alpine Fault, New Zealand, allowing for uncertainties, *New Zeal. J. Geol. Geophys.*, *46*(4), 479–488, doi:10.1080/00288306.2003.9515023.

Rice, J. R. (2006), Heating and weakening of faults during earthquake slip, *J. Geophys. Res. Solid Earth*, *111*(5), doi:10.1029/2005JB004006.

Rice, J. R., and M. P. Cleary (1976), Some basic stress diffusion solutions for fluid-saturated elastic porous media with compressible constituents, *Rev. Geophys.*, *14*(2), 227–241, doi:10.1029/RG014i002p00227.

Rietbrock, A. (2001), P wave attenuation structure in the fault area of the 1995 Kobe earthquake, *J. Geophys. Res. Solid Earth*, *106*(B3), 4141–4154, doi:10.1029/2000JB900234.

Rimstidt, J. D., A. Balog, and J. Webb (1998), Distribution of trace elements between carbonate minerals and aqueous solutions, *Geochim. Cosmochim. Acta*, *62*(11), 1851–1863, doi:10.1016/S0016-7037(98)00125-2.

Rose, G. (1868), Ueber die im Kalkspath vorkommenden hohlen Canale., *Abh. konigl. Akad. Wiss*, *23*, 57–79.

Rowe, C. D., J. C. Moore, F. Meneghini, and A. W. McKeirnan (2005), Large-scale pseudotachylytes and fluidized cataclasites from an ancient subduction thrust fault, *Geology*, *33*(12), 937–940, doi:10.1130/G21856.1.

Rowe, K. J., and E. H. Rutter (1990), Palaeostress estimation using calcite twinning: experimental calibration and application to nature, *J. Struct. Geol.*, *12*(1), 1–17, doi:10.1016/0191-8141(90)90044-Y.

Ruina, A. (1983), Slip instability and state variable friction laws, *J. Geophys. Res. Solid Earth*, *88*(B12), 10359–10370, doi:10.1029/JB088iB12p10359.

Rutter, E. H. (1983), Pressure solution in nature, theory and experiment, *J. Geol. Soc. London.*, *140*(5), 725 LP-740.

Rye, D. M., and H. J. Bradbury (1988), Fluid flow in the crust; an example from a Pyrenean thrust ramp, *Am. J. Sci.* , *288*(3), 197–235, doi:10.2475/ajs.288.3.197.

Saffer, D. M., and C. Marone (2003), Comparison of smectite- and illite-rich gouge frictional properties: application to the updip limit of the seismogenic zone along subduction megathrusts, *Earth Planet. Sci. Lett.*, *215*(1–2), 219–235, doi:10.1016/S0012-821X(03)00424-2.

Samuelson, J., D. Elsworth, and C. Marone (2009), Shear-induced dilatancy of fluid-saturated faults: Experiment and theory, *J. Geophys. Res. Solid Earth*, *114*(12), doi:10.1029/2008JB006273.

Sandström, B., and E. L. Tullborg (2009), Episodic fluid migration in the Fennoscandian Shield recorded by stable isotopes, rare earth elements and fluid inclusions in fracture minerals at Forsmark, Sweden, *Chem. Geol.*, *266*(3–4), 135–151, doi:10.1016/j.chemgeo.2009.04.019.

Sato, H., M. C. Fehler, and T. Maeda (2012), *Seismic Wave Propagation and Scattering in the Heterogeneous Earth : Second Edition*, Springer-Verlag, Berlin, Heidelberg.

Scambelluri, M., G. Pennacchioni, and P. Philippot (1998), Salt-rich aqueous fluids formed during eclogitization of metabasites in the Alpine continental crust (Austroalpine Mt. Emilius unit, Italian western Alps), *Lithos*, *43*(3), 151–167, doi:https://doi.org/10.1016/S0024-4937(98)00011-5.

Schleicher, A. M., R. Sutherland, J. Townend, V. G. Toy, and B. van der Pluijm (2015), Clay mineral formation and fabric development in the DFDP-1B borehole, central Alpine Fault, New Zealand, *New Zeal. J. Geol. Geop.*, *58*(1), 13–21, doi:10.1080/00288306.2014.979841.

Schmid, S., and M. Handy (1991), Towards a genetic classification of fault rocks: geological usage and tectonophysical implications, in *Controversies in Modern Geology: Evolution of Geological Theories in Sedimentology, Earth History and Tectonics*, edited by D. Müller, J. McKenzie, and H. Weissert, pp. 339–361, London.

Scholz, C. H. (1988), The brittle-plastic transition and the depth of seismic faulting, *Geol. Rundschau*, *77*(1), 319–328, doi:10.1007/BF01848693.

Scholz, C. H. (2002), *The Mechanics of Earthquakes and Faulting*, second edi., University press, Cambridge.

Segall, P., and J. R. Rice (1995), Dilatancy, compaction, and slip instability of a fluid-infiltrated fault, *J. Geophys. Res. Earth*, *100*(B11), 22155–22171, doi:10.1029/95JB02403.

Seward, D., and R. H. Sibson (1985), Fission-track age for a pseudotachylite from the Alpine Fault Zone, New Zealand, *New Zeal. J. Geol. Geophys.*, *28*(3), 553–557, doi:10.1080/00288306.1985.10421207.

Seward, G. G. E., D. J. Prior, J. Wheeler, S. Celotto, D. J. M. Halliday, R. S. Paden, and M. R. Tye (2002), High-temperature electron backscatter diffraction and scanning electron microscopy imaging techniques: in-situ investigations of dynamic processes., *Scanning*, *24*(5), 232–40, doi:10.1002/sca.4950240503.

Seward, G. G. E., S. Celotto, D. J. Prior, J. Wheeler, and R. C. Pond (2004), In situ SEM-EBSD observations of the hcp to bcc phase transformation in commercially pure titanium, *Acta Mater.*, *52*(4), 821–832, doi:10.1016/j.actamat.2003.10.049.

Sharp, W. E. (1965), The deposition of hydrothermal quartz and calcite, *Econ. Geol.*, *60*(8), 1635–1644.

Shimamoto, T. (1989), The origin of S-C mylonites and a new fault-zone model, *J. Struct. Geol.*, *11*(1), 51–64, doi:10.1016/0191-8141(89)90035-7.

Shimamoto, T., and J. M. Logan (1981), Effects of simulated clay gouges on the sliding behavior of Tennessee sandston, *Tectonophysics*, *75*(3), 243–255, doi:10.1016/0040-1951(81)90276-6.

Shimamoto, T., and H. Nagahama (1992), An argument against the crush origin of pseudotachylytes based on the analysis of clast-size distribution, *J. Struct. Geol.*, *14*(8), 999–1006, doi:http://dx.doi.org/10.1016/0191-8141(92)90031-Q.

Sibson, R. H. (1973), Interactions between Temperature and Pore-Fluid Pressure during Earthquake Faulting and a Mechanism for Partial or Total Stress Relief, *Nat. Phys. Sci.*,

243(126), 66–68, doi:10.1038/physci243066a0.

Sibson, R. H. (1975), Generation of Pseudotachylyte by Ancient Seismic Faulting, *Geophys. J. R. Astron. Soc.*, *43*(3), 775–794, doi:10.1111/j.1365-246X.1975.tb06195.x.

Sibson, R. H. (1977), Fault rocks and fault mechanisms, *J. Geol. Soc. London.*, *133*(3), 191–213, doi:10.1144/gsjgs.133.3.0191.

Sibson, R. H. (1986), Earthquakes and Rock Deformation in Crustal Fault Zones, *Annu. Rev. Earth Planet. Sci.*, *14*(1), 149–175, doi:10.1146/annurev.ea.14.050186.001053.

Sibson, R. H. (1990), Conditions for fault-valve behaviour, *Geol. Soc. London, Spec. Publ.* , *54*(1), 15–28, doi:10.1144/GSL.SP.1990.054.01.02.

Sibson, R. H. (2003), Thickness of the Seismic Slip Zone, *Bull. Seismol. Soc. Am.* , *93*(3), 1169–1178, doi:10.1785/0120020061.

Sibson, R. H., and V. G. Toy (2006), The habitat of fault-generated pseudotachylyte: Presence vs. absence of friction-melt, , (Figure 1), 153–166, doi:10.1029/170GM16.

Sibson, R. H., J. M. M. Moore, and A. H. Rankin (1975), Seismic pumping—a hydrothermal fluid transport mechanism, *J. Geol. Soc. London.*, *131*(6), 653–659.

Sibson, R. H., S. H. White, and B. K. Atkinson (1981), Structure and distribution of fault rocks in the Alpine Fault Zone, New Zealand, *Geol. Soc. London, Spec. Publ.*, *9*(1), 197–210, doi:10.1144/GSL.SP.1981.009.01.18.

Simpson, C. (1985), Deformation of granitic rocks across the brittle-ductile transition, *J. Struct. Geol.*, *7*(5), 503–511, doi:10.1016/0191-8141(85)90023-9.

Skemer, P., I. Katayama, Z. Jiang, and S. Karato (2005), The misorientation index: Development of a new method for calculating the strength of lattice-preferred orientation, *Tectonophysics*, *411*(1), 157–167, doi:10.1016/j.tecto.2005.08.023.

Smith, A. P., M. P. Fischer, and M. A. Evans (2014), On the homogeneity of fluids forming bedding-parallel veins, *Geofluids*, *14*(1), 45–57, doi:10.1111/gfl.12040.

Smith, S. A. F., G. Di Toro, S. Kim, J. H. Ree, S. Nielsen, A. Billi, and R. Spiess (2013), Coseismic recrystallization during shallow earthquake slip, *Geology*, *41*(1), 63–66, doi:10.1130/G33588.1.

Snoke, A. W., J. Tullis, and V. R. Todd (1998), Fault-related Rocks: A Photographic Atlas, Princeton University Press, Princeton, New Jersey.

Spray, J. G. (1992), A physical basis for the frictional melting of some rock-forming minerals, *Tectonophysics*, *204*(3), 205–221, doi:10.1016/0040-1951(92)90308-S.

Spray, J. G. (1993), Viscosity determinations of some frictionally generated silicate melts: Implications for fault zone rheology at high strain rates, *J. Geophys. Res. Solid Earth*, *98*(B5), 8053–8068, doi:10.1029/93JB00020.

Spray, J. G. (1995), Pseudotachylyte controversy: fact or friction?, *Geology*, *23*(12), 1119–1122, doi:10.1130/0091-7613(1995)023<1119:PCFOF>2.3.CO.

Stern, T., S. Kleffmann, D. Okaya, M. Scherwath, and S. Bannister (2001), Low seismic-wave speeds and enhanced fluid pressure beneath the Southern Alps of New Zealand, *Geol.* , *29*(8), 679–682, doi:10.1130/0091-7613(2001)029<0679:LSWSAE>2.0.CO;2.

Stern, T., D. Okaya, S. Kleffmann, M. Scherwath, S. Henrys, and F. Davey (2007), Geophysical Exploration and Dynamics of the Alpine Fault Zone, in *A Continental Plate Boundary: Tectonics at South Island, New Zealand*, pp. 207–233, American Geophysical Union.

Stevens-Kalceff, M. A. (2009), Cathodoluminescence microcharacterization of point defects in α-quartz, *Mineral. Mag.*, *73*(4), 585–605.

Stevens-Kalceff, M. A. (2013), Cathodoluminescence microanalysis of silica and amorphized quartz, *Mineral. Petrol.*, *107*(3), 455–469, doi:10.1007/s00710-013-0275-5.

Sutherland, R. (1995), The Australia-Pacific boundary and Cenozoic plate motions in the SW Pacific: Some constraints from Geosat data, *Tectonics*, *14*(4), 819–831, doi:10.1029/95TC00930.

Sutherland, R. (1999a), Basement geology and tectonic development of the greater New Zealand region: an interpretation from regional magnetic data, *Tectonophysics*, *308*(3), 341–362, doi:10.1016/S0040-1951(99)00108-0.

Sutherland, R. (1999b), Cenozoic bending of New Zealand basement terranes and Alpine Fault displacement: A brief review, *New Zeal. J. Geol. Geophys.*, *42*(2), 295–301, doi:10.1080/00288306.1999.9514846.

Sutherland, R., F. Davey, and J. Beavan (2000), Plate boundary deformation in South Island, New Zealand, is related to inherited lithospheric structure, *Earth Planet. Sci. Lett.*, *177*(3–4), 141–151, doi:10.1016/S0012-821X(00)00043-1.

Sutherland, R. et al. (2007), Do great earthquakes occur on the Alpine Fault in central South Island, New Zealand?, edited by D. Okaya, T. Stern, and F. Davey, *A Cont. Plate Bound. Tectonics South Island, New Zeal.*, *175*, 235–251, doi:10.1029/175GM12.

Sutherland, R. et al. (2011), *Operations and well completion report for boreholes DFDP-1A and DFDP-1B, Deep Fault Drilling Project, Alpine Fault, Gaunt Creek, New Zealand*, Lower Hutt, NZ.

Sutherland, R. et al. (2012), Drilling reveals fluid control on architecture and rupture of the Alpine fault, New Zealand, *Geology*, *40*(12), 1143–1146, doi:10.1130/G33614.1.

Sutherland, R. et al. (2015), *Deep Fault Drilling Project (DFDP), Alpine Fault Boreholes DFDP-2A and DFDP-2B Technical Completion Report*.

Sutherland, R. et al. (2017), Extreme hydrothermal conditions at an active plate-bounding fault, *Nature*, *546*(7656), 137–140.

Swart, P. K. (1990), Calibration of the ion microprobe for the quantitative determination of strontium, iron, manganese, and magnesium in carbonate minerals, *Anal. Chem.*, *62*(7), 722–728, doi:10.1021/ac00206a015.

Tanikawa, W., H. Mukoyoshi, O. Tadai, T. Hirose, A. Tsutsumi, and W. Lin (2012), Velocity dependence of shear-induced permeability associated with frictional behavior in fault zones of the Nankai subduction zone, *J. Geophys. Res. Solid Earth*, *117*(B5), n/a-n/a, doi:10.1029/2011JB008956.

Tenthorey, E., and S. F. Cox (2006), Cohesive strengthening of fault zones during the interseismic period: An experimental study, *J. Geophys. Res. Solid Earth*, *111*(9), doi:10.1029/2005JB004122.

Tenthorey, E., S. F. Cox, and H. F. Todd (2003), Evolution of strength recovery and permeability during fluid-rock reaction in experimental fault zones, *Earth Planet. Sci. Lett.*, *206*(1–2), 161–172, doi:10.1016/S0012-821X(02)01082-8.

Thielmann, M., A. Rozel, B. J. P. Kaus, and Y. Ricard (2015), Intermediate-depth earthquake generation and shear zone formation caused by grain size reduction and shear heating, *Geology*, *43*(9), 791–794.

Tikoff, B., C. Teyssier, and C. Waters (2001), Clutch tectonics and the partial attachment of lithospheric layers, *Stephan Mueller Spec. Publ. Ser.*, *1*, 57–73, doi:10.5194/smsps-1-57-2002.

Tingle, T. N., H. W. Green, C. H. Scholz, and T. A. Koczynski (1993), The rheology of faults triggered by the olivine-spinel transformation in Mg2GeO4 and its implications for the mechanism of deep-focus earthquakes, *J. Struct. Geol.*, *15*(9), 1249–1256, doi:10.1016/0191-8141(93)90167-9.

The Engineering ToolBox. (2014), Water - Thermodynamic Properties, *Eng. ToolBox*. Available from: http://www.engineeringtoolbox.com/water-thermal-properties-d_162.html (Accessed 20 April 2016).

Townend, J., R. Sutherland, V. G. Toy, J. D. Eccles, C. Boulton, S. C. Cox, and D. McNamara (2013), Late-interseismic state of a continental plate-bounding fault: Petrophysical results from DFDP-1 wireline logging and core analysis, Alpine Fault, New Zealand, *Geochemistry, Geophys. Geosystems*, *14*(9), 3801–3820, doi:10.1002/ggge.20236.

Toy, V. G., D. J. Prior, and R. J. Norris (2008), Quartz fabrics in the Alpine Fault mylonites: Influence of pre-existing preferred orientations on fabric development during progressive uplift, *J. Struct. Geol.*, *30*(5), 602–621, doi:10.1016/j.jsg.2008.01.001.

Toy, V. G., D. Craw, A. F. Cooper, and R. J. Norris (2010), Thermal regime in the central Alpine Fault zone, New Zealand: Constraints from microstructures, biotite chemistry and fluid inclusion data, *Tectonophysics*, *485*(1–4), 178–192, doi:10.1016/j.tecto.2009.12.013.

Toy, V. G., S. Ritchie, and R. H. Sibson (2011), Diverse habitats of pseudotachylytes in the Alpine Fault Zone and relationships to current seismicity, *Geol. Soc. London, Spec. Publ.*, *359*(1), 115–133, doi:10.1144/SP359.7.

Toy, V. G., D. J. Prior, R. J. Norris, A. F. Cooper, and M. Walrond (2012), Relationships between kinematic indicators and strain during syn-deformational exhumation of an oblique slip, transpressive, plate boundary shear zone: The Alpine Fault, New Zealand, *Earth Planet. Sci. Lett.*, *333–334*, 282–292, doi:10.1016/j.epsl.2012.04.037.

Toy, V. G., R. J. Norris, D. J. Prior, M. Walrond, and A. F. Cooper (2013), How do lineations reflect the strain history of transpressive shear zones? The example of the active Alpine Fault zone, New Zealand, *J. Struct. Geol.*, *50*, 187–198, doi:10.1016/j.jsg.2012.06.006.

Toy, V. G., T. M. Mitchell, A. Druiventak, and R. Wirth (2015a), Crystallographic preferred orientations may develop in nanocrystalline materials on fault planes due to surface energy interactions, *Geochemistry, Geophys. Geosystems*, *16*(8), 2549–2563, doi:10.1002/2015GC005857.

Toy, V. G. et al. (2015b), Fault rock lithologies and architecture of the central Alpine fault, New Zealand, revealed by DFDP-1 drilling, *Lithosphere*, *7*(2), 155–173, doi:10.1130/l395.1.

Toy, V. V. G. (2007), Rheology of the Alpine Fault Mylonite Zone: deformation processes at and below the base of the seismogenic zone in a major plate boundary structure, University of Otago.

Tse, S. T., and J. R. Rice (1986), Crustal earthquake instability in relation to the depth variation of frictional slip properties, *J. Geophys. Res. Solid Earth*, *91*(B9), 9452–9472, doi:10.1029/JB091iB09p09452.

Tsutsumi, A., and T. Shimamoto (1997), High-velocity frictional properties of gabbro, *Geophys. Res. Lett.*, *24*(6), 699–702, doi:10.1029/97GL00503.

Tulloch, A. J. (1982), Mineralogical Observations on Carbonate Scaling in geothermal wells at Kawerau and Broadland, *New Zeal. Geotherm. Work. 4th*, 131–134.

Ujiie, K., A. Tsutsumi, and J. Kameda (2011), Reproduction of thermal pressurization and fluidization of clay-rich fault gouges by high-velocity friction experiments and implications for seismic slip in natural faults, *Geol. Soc. London, Spec. Publ.*, *359*(1), 267–285.

Upton, P., P. O. Koons, and C. P. Chamberlain (1995), Penetration of deformation-driven meteoric water into ductile rocks: Isotopic and model observations from the Southern Alps, New Zealand, *New Zeal. J. Geol. Geophys.*, *38*(4), 535–543, doi:10.1080/00288306.1995.9514680.

Verberne, B. A., C. J. Spiers, A. R. Niemeijer, J. H. P. De Bresser, D. A. M. De Winter, and O. Plümper (2014), Frictional Properties and Microstructure of Calcite-Rich Fault Gouges Sheared at Sub-Seismic Sliding Velocities, *Pure Appl. Geophys.*, *171*(10), 2617–2640, doi:10.1007/s00024-013-0760-0.

Vernon, R. H. (1981), Optical microstructure of partly recrystallized calcite in some naturally deformed marbles, *Tectonophysics*, *78*(1), 601–612, doi:10.1016/0040-1951(81)90031-7.

Vidale, J. E., and Y.-G. Li (2003), Damage to the shallow Landers fault from the nearby Hector Mine earthquake, *Nature*, *421*(6922), 524–526.

Viesca, R. C., and D. I. Garagash (2015), Ubiquitous weakening of faults due to thermal pressurization, *Nat. Geosci.*, *8*(11), 875–879, doi:10.1038/ngeo2554.

Violay, M., G. Di Toro, B. Gibert, S. Nielsen, E. Spagnuolo, P. Del Gaudio, P. Azais, and P. G. Scarlato (2014a), Effect of glass on the frictional behavior of basalts at seismic slip rates, *Geophys. Res. Lett.*, *41*(2), 348–355, doi:10.1002/2013GL058601.

Violay, M., S. Nielsen, B. Gibert, E. Spagnuolo, A. Cavallo, P. Azais, S. Vinciguerra, and G. Di Toro (2014b), Effect of water on the frictional behavior of cohesive rocks during earthquakes, *Geology*, *42*(1), 27–30.

Vry, J., R. Powell, K. M. Golden, and K. Petersen (2010), The role of exhumation in metamorphic dehydration and fluid production, *Nat. Geosci*, *3*(1), 31–35.

Vry, J. K., A. C. Storkey, and C. Harris (2001), Role of fluids in the metamorphism of the Alpine Fault Zone, New Zealand, *J. Metamorph. Geol.*, *19*(1), 21–31, doi:10.1046/j.0263-4929.2000.00299.x.

Walcott, R. I. (1998), Modes of oblique compression: Late Cenozoic tectonics of the south island of New Zealand, *Rev. Geophys.*, *36*(1), 1–26, doi:10.1029/97RG03084.

Wallace, R. C. (1976), Partial fusion along the Alpine Fault Zone, New Zealand, *Geol. Soc. Am. Bull.*, *87*(9), 1225–1228, doi:10.1130/0016-7606(1976)87<1225:PFATAF>2.0.CO;2.

Walther, J. V, and P. M. Orville (1982), Volatile production and transport in regional metamorphism, *Contrib. to Mineral. Petrol.*, *79*(3), 252–257,

doi:10.1007/BF00371516.

Wannamaker, P. E., G. R. Jiracek, J. A. Stodt, T. G. Caldwell, V. M. Gonzalez, J. D. McKnight, and A. D. Porter (2002), Fluid generation and pathways beneath an active compressional orogen, the New Zealand Southern Alps, inferred from magnetotelluric data, *J. Geophys. Res.*, *107*(B6), 1–21, doi:10.1029/2001JB000186.

Warr, L. N., and S. Cox (2001), Clay mineral transformations and weakening mechanisms along the Alpine Fault, New Zealand, *Geol. Soc. London, Spec. Publ.*, *186*(1), 85–101, doi:10.1144/GSL.SP.2001.186.01.06.

Warr, L. N., and B. A. van der Pluijm (2005), Crystal fractionation in the friction melts of seismic faults (Alpine Fault, New Zealand), *Tectonophysics*, *402*(1–4 SPEC. ISS), 111–124, doi:10.1016/j.tecto.2004.12.034.

Warr, L. N., B. A. van der Pluijm, D. R. Peacor, and C. M. Hall (2003), Frictional melt pulses during a ~1.1 Ma earthquake along the Alpine Fault, New Zealand, *Earth Planet. Sci. Lett.*, *209*(1–2), 39–52, doi:10.1016/S0012-821X(03)00070-0.

Warr, L. N., B. A. van der Pluijm, and S. Tourscher (2007), The age and depth of exhaumed friction melts along the Alpine fault, New Zealand, *Geology*, *35*(7), 603–606, doi:10.1130/G23541A.1.

Waychunas, G. A. (2014), Luminescence Spectroscopy, *Rev. Mineral. Geochemistry*, *78*(1), 175–217.

Wellman, H. (1953), Data for the study of Recent and late Pleistocene faulting in the South Island of New Zealand, *New Zeal. J. Sci. Technol.*, *34B*, 270 – 288.

Wells, A., M. D. Yetton, R. P. Duncan, and G. H. Stewart (1999), Prehistoric dates of the most recent Alpine fault earthquakes, New Zealand, *Geology*, *27*(11), 995, doi:10.1130/0091-7613(1999)027<0995:PDOTMR>2.3.CO;2.

Wendler, J., J. Köster, J. Götze, N. Kasch, N. Zisser, J. Kley, D. Pudlo, G. Nover, and R. Gaupp (2012), Carbonate diagenesis and feldspar alteration in fracture-related bleaching zones (Buntsandstein, central Germany): possible link to CO2-influenced fluid–mineral reactions, *Int. J. Earth Sci.*, *101*(1), 159–176, doi:10.1007/s00531-011-0671-1.

Wenk, H. R. (1978), Are pseudotachylites products of fracture or fusion?, *Geology*, *6*(8), 507–511.

Wheeler, J. (1992), Importance of pressure solution and coble creep in the deformation of polymineralic rocks, *J. Geophys. Res. Solid Earth*, *97*(B4), 4579–4586, doi:10.1029/91JB02476.

White, J. C., and S. H. White (1983), Semi-brittle deformation within the Alpine fault zone, New Zealand, *J. Struct. Geol.*, *5*(6), 579–589.

Whitney, D. L., and B. W. Evans (2010), Abbreviations for names of rock-forming minerals, *Am. Mineral.*, *95*(1), 185–187, doi:10.2138/am.2010.3371.

Wibberley, C. A. J. (2002), Hydraulic diffusivity of fault gouge zones and implications for thermal pressurization during seismic slip, *Earth, Planets Sp.*, *54*(11), 1153–1171, doi:10.1186/BF03353317.

Wibberley, C. A. J., and T. Shimamoto (2002), Internal structure and permeability of major strike-slip fault zones: The Median Tectonic Line in Mie Prefecture, Southwest Japan, *J. Struct. Geol.*, *25*(1), 59–78, doi:10.1016/S0191-8141(02)00014-7.

Wiersberg, T., and J. Erzinger (2007), A helium isotope cross-section study through the San Andreas Fault at seismogenic depths, *Geochemistry, Geophys. Geosystems*, *8*(1), doi:10.1029/2006GC001388.

Williams, J. N., V. G. Toy, C. Massiot, D. D. McNamara, and T. Wang (2016), Damaged beyond repair? Characterising the damage zone of a fault late in its interseismic cycle, the Alpine Fault, New Zealand, *J. Struct. Geol.*, *90*, 76–94,

doi:10.1016/j.jsg.2016.07.006.

Wilson, J. E., J. S. Chester, and F. M. Chester (2003), Microfracture analysis of fault growth and wear processes, Punchbowl Fault, San Andreas system, California, *J. Struct. Geol.*, *25*(11), 1855–1873, doi:10.1016/S0191-8141(03)00036-1.

Wiltschko, D. V, and J. W. Morse (2001), Crystallization pressure versus “crack seal” as the mechanism for banded veins, *Geol.* , *29*(1), 79–82, doi:10.1130/0091-7613(2001)029<0079:CPVCSA>2.0.CO;2.

Wintsch, R. P. (1975), Feldspathization as a result of deformation, *Bull. Geol. Soc. Am.*, *86*(1), 35–38, doi:10.1130/0016-7606(1975)86<35:FAAROD>2.0.CO;2.

Wintsch, R. P., and M.-W. Yeh (2013), Oscillating brittle and viscous behavior through the earthquake cycle in the Red River Shear Zone: Monitoring flips between reaction and textural softening and hardening, *Tectonophysics*, *587*, 46–62, doi:10.1016/j.tecto.2012.09.019.

Wintsch, R. P., R. Christoffersen, and A. K. Kronenberg (1995), Fluid-rock reaction weakening of fault zones, *J. Geophys. Res. Solid Earth*, *100*(B7), 13021–13032, doi:10.1029/94JB02622.

Wogelius, R. A., D. G. Fraser, G. R. T. Wall, and G. W. Grime (1997), Trace element and isotopic zonation in vein calcite from the Mendip Hills, UK, with spatial-process correlation analysis, *Geochim. Cosmochim. Acta*, *61*(10), 2037–2051, doi:10.1016/S0016-7037(97)00065-3.

Woodcock, N. H., and K. Mort (2008), Classification of fault breccias and related fault rocks, *Geol. Mag.*, *145*(3), 435–440, doi:10.1017/S0016756808004883.

Wu, F. T., L. Blatter, and H. Roberson (1975), Clay gouges in the San Andreas Fault System and their possible implications, *Pure Appl. Geophys. PAGEOPH*, *113*(1), 87–95, doi:10.1007/BF01592901.

Xue, L. et al. (2013), Continuous Permeability Measurements Record Healing Inside the Wenchuan Earthquake Fault Zone, *Science (80-.).*, *340*(6140), 1555–1559.

Yamaji, A. (2015), How tightly does calcite e-twin constrain stress?, *J. Struct. Geol.*, *72*, 83–95, doi:10.1016/j.jsg.2015.01.008.

Yardley, B. W. D. (1997), The Evolution of Fluids Through the Metamorphic Cycle, in *Fluid Flow and Transport in Rocks: Mechanisms and effects*, edited by B. Jamtveit and B. W. D. Yardley, pp. 99–121, Springer Netherlands, Dordrecht.

Yund, R. A., M. L. Blanpied, T. E. Tullis, and J. D. Weeks (1990), Amorphous material in high strain experimental fault gouges, *J. Geophys. Res. Solid Earth*, *95*(B10), 15589–15602, doi:10.1029/JB095iB10p15589.

Zoback, M., S. Hickman, W. Ellsworth, and S. S. Team (2011), Scientific Drilling Into the San Andreas Fault Zone-An Overview of SAFOD's First Five Years, *Sci. Drill.*, (11, March 2011), 14–28, doi:10.2204/iodp.sd.11.02.2011.